


12-2014

A COMPREHENSIVE ASSESSMENT METHODOLOGY BASED ON LIFE CYCLE ANALYSIS FOR ON-BOARD PHOTOVOLTAIC SOLAR MODULES IN VEHICLES

Mahmoud Abdelhamid
Clemson University, mabdelh@g.clemson.edu

Follow this and additional works at: https://tigerprints.clemson.edu/all_dissertations

 Part of the [Electrical and Computer Engineering Commons](#), [Environmental Sciences Commons](#),
and the [Operations Research, Systems Engineering and Industrial Engineering Commons](#)

Recommended Citation

Abdelhamid, Mahmoud, "A COMPREHENSIVE ASSESSMENT METHODOLOGY BASED ON LIFE CYCLE ANALYSIS FOR ON-BOARD PHOTOVOLTAIC SOLAR MODULES IN VEHICLES" (2014). *All Dissertations*. 1458.
https://tigerprints.clemson.edu/all_dissertations/1458

This Dissertation is brought to you for free and open access by the Dissertations at TigerPrints. It has been accepted for inclusion in All Dissertations by an authorized administrator of TigerPrints. For more information, please contact kokeefe@clemson.edu.

A COMPREHENSIVE ASSESSMENT METHODOLOGY BASED ON LIFE CYCLE
ANALYSIS FOR ON-BOARD PHOTOVOLTAIC SOLAR MODULES IN VEHICLES

A Dissertation
Presented to
the Graduate School of
Clemson University

In Partial Fulfillment
of the Requirements for the Degree
Doctor of Philosophy
Automotive Engineering

by
Mahmoud Masad Abdelhamid
December 2014

Accepted by:
Dr. Imtiaz Haque, Committee Chair
Dr. Rajendra Singh, Co-Chair
Dr. Zoran Filipi
Dr. Srikanth Pilla

ABSTRACT

This dissertation presents a novel comprehensive assessment methodology for using on-board photovoltaic (PV) solar technologies in vehicle applications. A well-to-wheels life cycle analysis based on a unique energy, greenhouse gas (GHG) emission, and economic perspective is carried out in the context of meeting corporate average fuel economy (CAFE) standards through 2025 along with providing an alternative energy path for the purpose of sustainable transportation.

The study includes 14 different vehicles, 3 different travel patterns, in 12 U.S. states and 16 nations using 19 different cost analysis scenarios for determining the challenges and benefits of using on-board photovoltaic (PV) solar technologies in vehicle applications. It develops a tool for decision-makers and presents a series of design requirements for the implementation of on-board PV in automobiles to use during the conceptual design stage, since its results are capable of reflecting the changes in fuel consumption, greenhouse gas emission, and cost for different locations, technological, and vehicle sizes.

The decision-supports systems developed include (i) a unique decision support systems for selecting the optimal PV type for vehicle applications using quality function deployment, analytic hierarchy process, and fuzzy axiomatic design, (ii) a unique system for evaluating all non-destructive inspection systems for defects in the PV device to select the optimum system suitable for an automated PV production line. (iii) The development of a comprehensive PV system model that for predicting the impact of using

on-board PV based on life cycle assessment perspective. This comprehensive assessment methodology is a novel in three respects. First, the proposed work develops a comprehensive PV system model and optimizes the solar energy to DC electrical power output ratio. Next, it predicts the actual contribution of the on-board PV to reduce fuel consumption, particularly for meeting corporate average fuel economy (CAFE) 2020 and 2025 standards in different scenarios. The model also estimates vehicle range extension via on-board PV and enhances the current understanding regarding the applicability and effective use of on-board PV modules in individual automobiles. Finally, it develops a life cycle assessment (LCA) model (well-to-wheels analysis) for this application. This enables a comprehensive assessment of the effectiveness of an on-board PV vehicle application from an energy consumption, Greenhouse Gas (GHG) emission, and cost life-cycle perspective.

The results show that by adding on-board PVs to cover less than 50% of the projected horizontal surface area of a typical passenger vehicle, up to 50% of the total daily miles traveled by a person in the U.S. could be driven by solar energy if using a typical mid-size vehicle, and up to 174% if using a very lightweight and aerodynamically efficient vehicle. In addition, the increase in fuel economy in terms of combined mile per gallon (MPG) at noon for heavy vehicles is between 2.9% to 9.5%. There is a very significant increase for lightweight and aerodynamic efficient vehicles, with MPG increase in the range of 10.7% to 42.2%, depending on location and time of year.

Although the results show that the plug-in electric vehicles (EVs) do not always have a positive environmental impact over similar gasoline vehicles considering the well-to-

wheel span, the addition of an on-board PV system for both vehicle configurations, significantly reduces cycle emissions (e.g., the equivalent savings of what an average U.S. home produces in a 20 month period). The lifetime driving cost (\$ per mile) of a gasoline vehicle with adding on-board PV, compared to a pure gasoline vehicle, is lower in regions with more sunlight (e.g., Arizona) even of the current gasoline price in the U.S. (\$4.0 per gallon) assuming battery costs will decline over time. Lifetime driving cost (\$ per mile) of a plug-in EV with added PV versus pure plug-in EV (assuming electricity price 0.18 \$/kWh) is at least similar, but mostly lower, even in regions with less sunlight (e.g., Massachusetts). In places with low electricity prices (0.13 \$/kWh), and with more sunlight, the costs of operating an EV with PV are naturally lower.

The study reports a unique observation that placing PV systems on-board for existing vehicles is in some cases superior to the lightweighting approach regarding full fuel-cycle emissions.

An added benefit of on-board PV applications is the ability to incorporate additional functionality into vehicles. Results show that an on-board PV system operating in Phoenix, AZ can generate in its lifetime, energy that is the equivalent of what an American average household residential utility customer consumes over a three-year period. However, if the proposed system operates in New Delhi, India, the PV could generate energy in its lifetime that is the equivalent of what an Indian average household residential utility customer consumes over a 33-year period. Consequently, this proposed application transforms, in times of no-use, into a flexible energy generation system that can be fed into the grid and used to power electrical devices in homes and offices. The

fact that the output of this system is direct current (DC) electricity rather than alternative current (AC) electricity reduces the wasted energy cost in the generation, transmission, and conversion losses between AC-DC electricity to reach the grid. Thus, this system can potentially reduce the dependency on the grid in third world countries where the energy consumption per home is limited and the grid is unstable or unreliable, or even unavailable.

DEDICATION

I lovingly dedicate this dissertation to my wonderful family, who supported me through each step of the way. Particularly, to my brilliant and beautiful wife, Ala Qattawi, for her endless support and encouragement, and to my sons Kareem and Ameer, who filled our lives with joy and excitement. I also dedicate this work to my great parents, Masad and Inam, who provided me with endless support and encouragement during my whole life, and to my siblings, Rania, Alaa, Mohammed, and Roaa, for their boundless friendship and delightful encouragement.

ACKNOWLEDGMENTS

First of all, I would like to acknowledge my advisor, Dr. Imtiaz Haque, and my co-adviser, Dr. Rajendra Singh, for their guidance and encouragement during my graduate study and throughout this work, their technical knowledge and expertise has provided me with the tools that I needed to complete my research and I am extremely thankful. I appreciated every moment that Dr. Haque spent with me for not only to guide this work, but also for his immense care of my professional development, though his extremely busy schedule. I also appreciated the continuous support from Dr. Singh, his class was very valuable and beneficial and I greatly appreciate it.

I also would like to thank my committee members, Dr. Zoran Filipi and Dr. Srikanth Pilla for their valuable suggestions and input on my research. Their technical knowledge and expertise has helped to improve the quality of this work and I am extremely thankful.

Many thanks are required for Dr. Mohammed Omar, who guided me during my start at CU-ICAR. Dr. Omar supported and encouraged me to pursue the PhD degree and gave me the technical knowledge and motivation that I needed to take that first step. Special thanks to Dr. Pierluigi Pisu, his class was very valuable and beneficial and I greatly appreciate it.

Special thanks to my sister-in-law, Shaima Qattawi, who assisted my family and took care of everything in the last few months and I am extremely thankful.

Last but not least, I feel privileged to have been surrounded by brilliant colleagues- Dr. Ala Qattawi, Dr. Amin Bibo, Dr. Ali Alahmer, Mr. Abdelrahim Khal, Mr. Bashar Alzuwayer, Mr. Hakan Kazan, and Mr. Rakan Alturk. I thank all of them for making my life as a graduate student a memorable one. I appreciate any help from other coworkers and friends that made this work possible.

TABLE OF CONTENTS

	Page
ABSTRACT	ii
DEDICATION	vi
ACKNOWLEDGMENTS	vii
LIST OF TABLES	xiv
LIST OF FIGURES	xvi
CHAPTER ONE	1
INTRODUCTION	1
1.1 Motivation	1
1.2 Problem Statement	2
1.3 Research Questions (RQs) and Objective	7
1.4 Approach	8
1.5 Dissertation Organization.....	10
CHAPTER TWO	12
EVALUATION OF ON-BOARD PHOTOVOLTAIC MODULES OPTIONS FOR ELECTRIC VEHICLES	12
2.1 Introduction	12
2.2 Literature Review	13
2.3 Methodology	15
2.3.1 Stage I: QFD	15
2.3.2 Stage II: PV Search Domain	18
2.3.3 Stage III: AHP.....	25
2.4 Electric Vehicles Powered by PV modules.....	28
2.4.1 Best Case Scenario.....	30
2.4.2 Intermediate Case Scenario.....	32
2.4.3 Worst Case Scenario	32
2.4.4 CO ₂ Reduction	33
2.5 Summary	34

Table of Contents (Continued)	Page
CHAPTER THREE.....	36
COMPARISON OF ANALYTICAL HIERARCHY PROCESS AND FUZZY AXIOMATIC DESIGN FOR SELECTING APPROPRIATE PHOTOVOLTAIC MODULES FOR ON-BOARD VEHICLE DESIGN.....	36
3.1 Introduction	36
3.2 Background of AHP, Fuzzy AD, QFD	39
3.3 Methodology	42
3.3.1 PV Module Types	42
3.3.2 The QFD & AHP Approach	49
3.3.3 The Fuzzy AD Approach.....	56
3.4 Discussion	62
3.5 Summary	64
CHAPTER FOUR.....	65
REVIEW OF MICRO CRACK DETECTION TECHNIQUES FOR SILICON SOLAR CELLS.....	65
4.1 Introduction	65
4.2 Origin and Root Causes of Micro Cracks	68
4.3 Classifications of micro cracks	71
4.4 Impact of the micro cracks on the performance and reliability of solar	72
4.4.1 Impact of micro cracks on the electrical characteristics of solar cells.....	72
4.4.2 Impact of the wafer thickness on cell breakage in mc-Si wafers.....	74
4.5 Micro Crack Detection Techniques	75
4.5.1 Optical Transmission	76
4.5.2 Infrared Ultrasound Lock-in Thermography (ULT)	79
4.5.3 Scanning Acoustic Microscopy (SAM)	80
4.5.4 Impact Testing	80
4.5.5 Resonance Ultrasonic Vibration (RUV)	81
4.5.6 Electronic Speckle Pattern Interferometry (ESPI)	82
4.5.7 Lamb Wave Air Coupled Ultrasonic Testing (LAC-UT)	82
4.5.8 Lock-in Thermography (LIT)	83
4.5.9 Electroluminescence (EL) imaging and Photoluminescence (PL) imaging	84

Table of Contents (Continued)	Page
4.6 Comparison between Micro Crack Detection Techniques.....	87
4.7 NDT Tool Selection Study.....	90
4.8 Summary	95
CHAPTER FIVE.....	96
MODELING PV SYSTEM FOR ON-BOARD VEHICLE APPLICATION	96
5.1 Introduction	96
5.2 Crystalline Silicon PV Module Structure.....	98
5.3 The electrical performance of PV solar module	100
5.4 Modeling PV module circuit.....	105
5.5 The thermal performance of a PV solar module	115
5.6 Modeling solar data.....	118
5.7 Maximum power point tracking (MPPT) algorithm	130
5.8 Modeling Energy Storage	134
5.9 Optimized PV Energy Output	145
5.9.1 Mounting configuration effect on PV temperature	145
5.9.2 Shadow and Sky Clearness	150
5.9.3 PV Tilt Angle and Orientation.....	156
5.9.4 Angling PV on Vehicle Surface.....	160
5.9.5 Battery Size.....	162
5.10 Modeling PV System Results.....	170
5.11 Summary	180
CHAPTER SIX	181
VEHICLE MODEL WITH ON-BOARD PV (TANK TO WHEEL ANALYSIS)	181
6.1 Introduction.....	181
6.2 Benchmarked Electric Vehicle (EV).....	184
6.3 Benchmarked Solar Vehicle.....	187
6.4 Modeling Vehicle Energy at Wheels	189
6.5 Sensitivity Analysis and MPG calculation.....	198
6.5 MPG Calculations	205
6.6 CAFE Standards with Projected Horizontal Vehicle Surface.....	209

Table of Contents (Continued)	Page
6.7 Driving Pattern Scenarios	213
6.8 Summary	214
CHAPTER SEVEN.....	215
LIFE CYCLE ASSESSMENT MODEL (CRADLE-TO-GATE ANALYSIS)	215
7.1 Introduction	215
7.2 Defining LCA Study Methodology.....	218
7.3 LCA for PV Modules	222
7.4 Embodied Energy.....	234
7.5 LCA for PV Balance of System (BOS)	238
7.5.1 Battery.....	238
7.5.2 Other BOS components	239
7.6 Estimation of PV Performance Ratio for On-board PV for Vehicle Application	240
7.7 PV lifetime Energy in US and the World.....	246
7.8 LCA for Gasoline Fuel.....	250
7.9 LCA for Electricity from Grid in US and the World	251
7.10 Reduction of Life Cycle Grid Emission by using PV	258
7.11 Limitations and Data Uncertainty	261
7.12 Summary	263
CHAPTER EIGHT	264
ASSESSMENT METHODOLOGY RESULTS.....	264
8.1 Introduction	264
8.2 Contribution of On-board PV toward CAFE 2025	266
8.3 Pure PV Solar Daily Driving Ranges (PV Range Extender)	272
8.4 How green is Pure Solar Vehicle	274
8.5 Life Cycle Emission Reduction for On-board PV with Gasoline Vehicle.....	279
8.6 Life Cycle Emission Reduction for On-board PV with Plug-in Electric Vehicle	283
8.7 Cost Analysis	289
8.7.1 Cost Analysis of Pure Solar PV Vehicle.....	289
8.7.2 Cost Analysis of Pure Gasoline Vehicle Vs. Gasoline vehicle with PV	292

Table of Contents (Continued)	Page
8.7.3 Cost Analysis of Pure Plug-in EV vs. Plug-in EV with PV	302
8.8 Comparison of On-board PV vs. Vehicle Lightweighting	311
8.9 Challenges of Vehicle Design with On-board PV	315
8.10 Summary	316
CHAPTER NINE	318
CONCLUSION	318
9.1 Conclusion	318
9.2 Contribution	327
9.3 Limitation and Future Works	329
REFERENCES	331

LIST OF TABLES

	Page
Table 2. 1 Decision-Making Pairwise matrix	22
Table 2. 2 LCC of electricity of different PV module options	24
Table 2. 3 Assumptions for EV with PV	30
Table 3. 1 Performance Data from PV Manufacturers' Datasheets and LCC Results	48
Table 3. 2 LCC Calculations with Respect to Multi-Si PV Module	49
Table 3. 3 Proposed QFD Structure	51
Table 3. 4 Pairwise Comparison Matrix Related to Power Density	54
Table 3. 5 System Range for AD Approach	58
Table 3. 6 Information Contents for Alternatives	62
Table 3. 7 Comparison between AHP/QFD with Fuzzy AD/QFD	63
Table 4. 1 Comparison between different NDT techniques	89
Table 5. 1 Empirically determined coefficients to predict PV module temperature [212]	117
Table 5. 2 Recommended average days for months [216]	121
Table 5. 3 Mismatch power losses for angling PV module on vehicle surface	162
Table 6. 1 Combined miles on a charge, the time to charge the battery, and motor description for selected EVs.	186
Table 7. 1 IEA Guidelines for PV LCAs [274], [275]	220
Table 7. 2 Summaries of published LCA estimated emission for multi-Si PV manufacturing	225
Table 7. 3 Summaries of published LCA estimated emission for mono-Si PV manufacturing	226
Table 7. 4 Summaries of published LCA estimated emission for a-Si PV manufacturing	227
Table 7. 5 Summaries of published LCA estimated emission for CIGS PV manufacturing	228
Table 7. 6 Summaries of published LCA estimated emission for CdTe PV manufacturing	229
Table 7. 7 The calculated emission of PV manufacturing stage.	231
Table 7. 8 PV LCA studies are excluded in this study due to grid electricity not in Europe	233
Table 7. 9 Embodied energy of PV manufacturing in terms of MJ/m ²	235
Table 7. 10 LCA Emission and Embodied Energy for Lithium-ion battery	239
Table 7. 11 Average monthly irradiation in Phoenix, AZ and Boston, MA	242
Table 7. 12 Estimated PR in Phoenix, AZ	244
Table 7. 13 Estimated PR in Boston, MA	244
Table 7. 14 Electricity production energy sources in some countries in Africa [314], [315]	251

Table 7. 15 Electricity production energy sources in some countries in America [314], [315].	251
Table 7. 16 Electricity production energy sources in some countries in Asia [314], [315].	252
Table 7. 17 Electricity production energy sources in some countries in Europe [314], [315].	253
Table 7. 18 Electricity losses on low voltage level for some countries [316]	254
Table 7. 19 CED at low level voltage at Grid [316]	255
Table 7. 20 GHG at low level voltage at Grid, calculated IPCC global warming potential 2007 100 , GWP) [316]	257
Table 7. 21 The proposed LCA emission estimation of on-board PV system for vehicle application	258
Table 8. 1 The key assumptions used for assessment results	265
Table 8. 2 Assumptions for cost analysis of pure solar vehicle.....	291
Table 8. 3 Assumptions for cost analysis of pure gasoline vehicle	293
Table 8. 4 Proposed cost scenarios of Gasoline vehicle with and without PV	295
Table 8. 5 Cost analysis of gasoline vehicle with PV (Scenario 1)	296
Table 8. 6 Cost analysis of gasoline vehicle with PV (Scenario 2)	297
Table 8. 7 Cost analysis of gasoline vehicle with PV (Scenario 3)	298
Table 8. 8 Cost analysis of gasoline vehicle with PV (Scenario 4)	299
Table 8. 9 Proposed scenarios of plug-in electric vehicle with and without PV	303
Table 8. 10 Lifetime cost analysis for pure electric vehicles of different scenarios....	304
Table 8. 11 Life cycle cost analysis of EV with PV (scenario 1)	305
Table 8. 12 Life cycle cost analysis of EV with PV (scenario 2)	305
Table 8. 13 Life cycle cost analysis of EV with PV (scenario 3)	306
Table 8. 14 Life cycle cost analysis of EV with PV (scenario 4)	306
Table 8. 15 Life cycle cost analysis of EV with PV (scenario 5)	307
Table 8. 16 Life cycle cost analysis of EV with PV (scenario 6)	307
Table 8. 17 Lightweighting approach vs. adding on-board PV (gasoline vehicle).....	314
Table 8. 18 Lightweighting approaches Versus adding on-board PV (electric vehicle)	315
Table 8. 19 Weight analysis by added PV on-board to gasoline vehicle.....	316

LIST OF FIGURES

	Page
Figure 1. 1 The United States Energy Flow Trends in 2013 [2].....	3
Figure 1. 2 United States Carbon Emission in 2013 [3]	4
Figure 1. 3 Fuel Economy Target (CAFE) per Passenger Vehicle (ft ²) [4] (edited for clearness).....	5
Figure 1. 4 Different Research Approaches and Current Study Approach to Reduce Well-to-Wheel Emission and Meet CAFE 2025	6
Figure 1. 5 Dissertation Approach and Organization	8
Figure 2. 1 The Proposed Methodology to Select the Optimum PV Module Option to Power On-board EVs.....	16
Figure 2. 2 Proposed QFD	16
Figure 2. 3 Power Density and Specific Weight of Different PV Options from Different Manufactures.....	21
Figure 2. 4 Efficiency and PTC of Different PV Options from Different Manufactures	22
Figure 2. 5 Pairwise comparison matrix related to specific weight.....	26
Figure 2. 6 Rank of different PV module types for EV application	28
Figure 2. 7 Performance sensitivity analysis	28
Figure 2. 8 Driving cycle and power demand at wheel	31
Figure 2. 9 (a) Daily Vehicle Ranges of Three Scenarios. (b) CO ₂ Reduction Compare to Equivalent Gasoline Vehicle.....	33
Figure 3. 1 Power Density and Efficiency Factors of the Commercial PV Module Types.....	47
Figure 3. 2 Specific Weight and PC Factors of the Commercial PV Module Types	48
Figure 3. 3 Steps of Applying QFD with AHP	50
Figure 3. 4 Hierarchical Problem Construction	53
Figure 3. 5 Rank of Different PV Module Types for Vehicle Application using AHP/QFD	55
Figure 3. 6 Sensitivity Analysis of AHP/QFD Rank Results	56
Figure 3. 7 The Proposed Approach for Fuzzy AD	57
Figure 3. 8 Triangular Fuzzy Number	59
Figure 3. 9 Design Ranges for AD Approach.....	60
Figure 3. 10 FR3 (PC Factor) with Respect to a-Si PV Module.....	61
Figure 4. 1 Some types of cell defects in wafer based silicon solar cells	66
Figure 4. 2 Key processing steps used in manufacturing of crystalline and poly silicon PV modules	70
Figure 4. 3 Classification of Cracks.....	73
Figure 4. 4 Wafer thickness of previous and current generations of silicon solar cells [147].....	75

Figure 4. 5 The proposed criteria and relative weight used in this work.....	91
Figure 4. 6 Alternatives are based on (a) Optical Transmission, (b) EL imaging, (c) PL imaging, and (d) RUV	92
Figure 4. 7 Pairwise comparison between main selection criteria.....	93
Figure 4. 8 The sensitivity for different constraint with respect to the ultimate goal	93
Figure 4. 9 The sensitivity for different constraint with respect to the ultimate goal	94
Figure 5. 1 Annual Potential for Renewable Energies vs. Total Resources for Finite Energies (Source: Perez & Perez, 2009a [185])	97
Figure 5. 2 Basic Component of PV Cell (Source: Clean & Green, 2012 [186]).....	98
Figure 5. 3 Cross Section of a Commercial Monocrystalline Silicon Solar Cell [187].	99
Figure 5. 4 Typical I-V Curve [189].....	101
Figure 5. 5 ASTM G173-03 Reference Spectra Global Tilt (data from NREL [191])	103
Figure 5. 6 SUNPOWER Mono-Si PV Model [192].....	104
Figure 5. 7 Ideal and practical PV equivalent circuit.....	105
Figure 5. 8 Preliminary Results I-V Curves: Actual vs. Predicted ($n=1$)	110
Figure 5. 9 Preliminary Results I-V Curves: Actual vs. Predicted ($n=2$)	111
Figure 5. 10 Preliminary Results I-V Curves: Actual vs. Predicted ($n=1.1$)	111
Figure 5. 11 Preliminary Results I-V Curves: Actual vs. Predicted ($n=1.33$).....	112
Figure 5. 12 Preliminary results I-V curves actual vs. predicted (different R_s).....	112
Figure 5. 13 I-V Curves (Actual data vs. model results)	113
Figure 5. 14 P-V Curves in Different Solar Irradiance.	114
Figure 5. 15 P-V Curves at Different PV Temperature.	114
Figure 5. 16 The ambient temperature ($^{\circ}\text{C}$) in Phoenix, AZ in both June and December (weather data in [213])	118
Figure 5. 17 Define Angle of Incidence.....	120
Figure 5. 18 Define Tilt Angle and Azimuth Angle	121
Figure 5. 19 Annually global horizontal irradiation in US states [217].....	122
Figure 5. 20 Average daily GHI per month in Phoenix, AZ and Boston, MA (Source data from [213])	124
Figure 5. 21 Average Daily GHI Per Month in Phoenix, AZ and Boston, MA (Source data from [213])	125
Figure 5. 22 The angle of incidence (Θ) of beam radiation on a surface- June 11 Phoenix-AZ.....	127
Figure 5. 23 The angle of incidence (Θ) of beam radiation on a surface in Dec, 10 (Phoenix, AZ).....	127
Figure 5. 24 DNI, DHI, and GHI for Phoenix, AZ in June	128
Figure 5. 25 Predicted and Actual GHI	129
Figure 5. 26 Error between Actual and Predicted GHI.....	129
Figure 5. 27 P-V curves of PV model and MPP	130

Figure 5. 28 Optimum PV module output power and PV efficiency in June in Phoenix, AZ.....	132
Figure 5. 29 Optimum PV module output power and PV efficiency in December in Phoenix, AZ.....	132
Figure 5. 30 Optimum PV Output Voltage in June and December in Phoenix, AZ....	133
Figure 5. 31 Energy storage classification [221]	134
Figure 5. 32 Specific energy and specific power of different cell types [222]	135
Figure 5. 33 Battery Simple Model Electric Circuit	137
Figure 5. 34 Digitized Battery Manufacturer Charging Curves	138
Figure 5. 35 Digitized Battery Manufacturer Discharging Curves	139
Figure 5. 36 Validate the Model: Discharging curves (Solid lines actual data & Circles represent model output).....	140
Figure 5. 37 Validate the model: Charging curves (Solid lines actual data & stars represent model output	141
Figure 5. 38 Single Cell Electric Equation	142
Figure 5. 39 Battery Electric Equation	142
Figure 5. 40 Estimation Battery Parameters	143
Figure 5. 41 Effects of mounting configuration on PV cell temp in June (Phoenix, AZ)	146
Figure 5. 42 Effects of mounting configuration options in PV output power in June in Phoenix, AZ	147
Figure 5. 43 Output Power Loss (%) in June, Phoenix, AZ for Different Mounting Configurations	148
Figure 5. 44 Effects of mounting configuration options in PV efficiency in June in Phoenix, AZ.....	149
Figure 5. 45 GHI in Phoenix, AZ in June for different α & Ψ values	152
Figure 5. 46 GHI in Phoenix, AZ in Dec for different α & Ψ values	153
Figure 5. 47 Total incident radiation on June in Phoenix, AZ for Different Shadow scenarios.....	154
Figure 5. 48 Total incident radiation on December in Phoenix, AZ for Different Shadow Scenarios	155
Figure 5. 49 Total incident radiation vs. tilt angle (June, Phoenix, AZ)	156
Figure 5. 50 Total incident radiation vs. tilt angle (Dec, Phoenix, AZ)	157
Figure 5. 51 Total incident radiation in December Phoenix, AZ in different tilt & azimuth angles	158
Figure 5. 52 Entire DNI and Cosine component DNI in June, Phoenix, AZ.....	160
Figure 5. 53 Angling PV on Vehicle Surface	161
Figure 5. 54 Optimum PV module voltage and battery voltage for battery cells in Phoenix, AZ in June.	163
Figure 5. 55 Solar Energy to Battery Charging Efficiency.....	164
Figure 5. 56 Optimum ratio between V_{mp} and battery voltage.....	165

Figure 5. 57 (a) Charging current and (b) battery voltage	166
Figure 5. 58 Battery SOC with time by charging with PV module	167
Figure 5. 59 Internal resistor (R) and open voltage (E) in battery charging mode as a functions of time	168
Figure 5. 60 Battery charging efficiency	169
Figure 5. 61 Total energy in kWh stored in battery with using typical PV module in Phoenix, AZ in June	170
Figure 5. 62 Total daily Energy Stored (Wh) in Battery by PV module in Phoenix, AZ (June)	171
Figure 5. 63 Total daily Energy Stored (Wh) in Battery by PV module in Phoenix, AZ (December)	172
Figure 5. 64 Hourly Energy Stored (Wh) in Battery by PV module in Phoenix, AZ (June)	173
Figure 5. 65 Hourly Energy Stored (Wh) in battery (as function of time and efficiency) by PV module in Phoenix, AZ (June)	174
Figure 5. 66 Hourly Energy Stored (Wh) in battery (as function of time and efficiency) by PV module in Phoenix, AZ (December)	175
Figure 5. 67 Hourly Energy Stored (Wh) in battery (as a function of time and efficiency) by PV module in Boston, MA (June)	176
Figure 5. 68 Hourly Energy Stored (Wh) in battery (as function of time and efficiency) by PV module in Boston, MA (December)	177
Figure 5. 69 Daily Energy (Wh) stored in battery for different scenarios	178
Figure 5. 70 Hourly energy (Wh) stored in battery for different scenarios	179
Figure 6. 1 Snapshot from GREET Model: Energy Pathway [245]	183
Figure 6. 2 Selected Electric vehicle for Benchmarked.....	184
Figure 6. 3 Curb weight and battery size for selected EVs.....	185
Figure 6. 4 Energy consumption per mile (Wh/mile) of selected EVs.....	187
Figure 6. 5 C-MAX Solar Energi Concept, Ford Motor Company [257].....	189
Figure 6. 6 Speed profile in FUDS driving cycle	194
Figure 6. 7 Speed profile in FHDS driving cycle	195
Figure 6. 8 Speed profile in 10+15 Japanese driving cycle	196
Figure 6. 9 Traction and braking power in FUDS for specific vehicle.....	200
Figure 6. 10 Traction and braking power in FHDS for specific vehicle.....	201
Figure 6. 11 Traction and braking power in 10+15 for specific vehicle.....	202
Figure 6. 12 Energy required at wheels per 100 km for different driving cycle for the assumed vehicle	203
Figure 6. 13 Sensitivity analysis based on 5% reduction in parameter yields x% reduction in required energy consumption at wheels (perfect 100% regeneration).....	204
Figure 6. 14 Sensitivity analysis based on 5% reduction in parameter yields x% reduction in required energy consumption at wheels (80% regeneration)	205

Figure 6. 15 Combined MPG/MPGe based on Tank to wheel efficiency and curb weight (No regeneration)	207
Figure 6. 16 Zooming snapshot of combined MPG/MPGe based on Tank to wheel efficiency and curb weight (No regeneration)	208
Figure 6. 17 CAFE (MPG) Standard Curves for Passenger Cars [266], edited for clearness	209
Figure 6. 18 Predicted projected horizontal surface based on vehicle footprint for selected 2014 EVs	211
Figure 6. 19 Differences between projected horizontal surfaces (actual Vs. predicted) for selected EVs	212
Figure 6. 20 The percent of trips by day [Data from [267]]	213
Figure 7. 1 Percentage of total PV cells/modules production per region [268]	215
Figure 7. 2 Global PV Module Production by region (MW) in 2013 [269]	216
Figure 7. 3 Percentages by the country to the total global PV installation [268]	217
Figure 7. 4 Experience curve of doubling of PV module manufacturing and cost reduction by 20 % and extension to 2035 [270]	218
Figure 7. 5 Phases of an LCA (Source: ISO, 1997 [273])	219
Figure 7. 6 Proposed On-board PV LCA study	222
Figure 7. 7 GHG emission (kg CO ₂ -eq) in PV manufacturing stage	232
Figure 7. 8 Embodied energy of PV manufacturing in terms of MJ/m ²	236
Figure 7. 9 Annual solar irradiation kWh/m ² (Estimated and Actual) in Phoenix, AZ	243
Figure 7. 10 Annual solar irradiation kWh/m ² (Estimated and Actual) in Boston, MA	243
Figure 7. 11 Estimated PR for On-board PV system for Vehicle application	245
Figure 7. 12 Average lifetime PV efficiency (%)	246
Figure 7. 13 Lifetime generated PV Energy in MWh in U.S. states	247
Figure 7. 14 Lifetime generated PV Energy in MWh in selected countries in the World	248
Figure 7. 15 Gasoline with additives (E10) [Source: GREET [309]]	250
Figure 7. 16 Reduction of Life Cycle g CO ₂ -eq emission per kWh by using PV vs. Grid	260
Figure 8. 1 On-board PV contribution in fuel economy (MPG) at 9-10 am scenario	269
Figure 8. 2 On-board PV contribution in fuel economy (MPG) at 12-1 pm scenario	270
Figure 8. 3 On-board PV contribution in fuel economy (MPG) at 4-5 pm scenario	271
Figure 8. 4 Daily pure solar driving ranges	273
Figure 8. 5 Life cycle emission for pure solar vehicle in US (Assumed vehicle 2)	275
Figure 8. 6 Life cycle emission for pure solar vehicle in US (Assumed vehicle 1)	276
Figure 8. 7 Life cycle emission for pure solar vehicle in US (Vehicle with efficiency similar to Nissan Leaf 2014 or Mitsubishi i-MiEV 2014)	277

Figure 8. 8 Life cycle emission for pure solar vehicle in the US (Vehicle similar to Tesla Model S2013).....	278
Figure 8. 9 LCA emission in terms of (g CO ₂ -eq per mile) for gasoline vehicle versus gasoline vehicle with PV	280
Figure 8. 10 LCA metric tons of CO ₂ -eq reduction ranges by incorporating the proposed on-board PV to different gasoline vehicles	282
Figure 8. 11 grams CO ₂ -eq reduction by incorporating on-board PV to pure plug-in electric vehicle (U.S. Grid)	286
Figure 8. 12 grams CO ₂ -eq reduction by incorporating on-board PV to pure plug-in electric vehicle (India Grid)	287
Figure 8. 13 Metric tons of grams CO ₂ -eq reduction by incorporating on-board PV to pure plug-in electric vehicle (U.S. Grid vs. India Grid)	288
Figure 8. 14 Planned 2020 Gigafactory Production [329].....	290
Figure 8. 15 The battery cost forecast based on Tesla Motor's proposed production [330]	290
Figure 8. 16 Lifetime cost of driving (¢ per mile) for pure gasoline vehicle versus gasoline vehicle with PV [gasoline price 4 \$/gallon]	300
Figure 8. 17 Lifetime cost of driving (¢ per mile) for pure gasoline vehicle vs. gasoline vehicle with PV [gasoline price \$8/gallon].....	301
Figure 8. 18 Lifetime cost of driving (¢ per mile) of pure plug-in EV vs. plug-in EV with PV [Electricity price 0.13 \$/kWh]	308
Figure 8. 19 Lifetime cost of driving (¢ per mile) for pure plug-in EV vs. plug-in EV with PV [Electricity price \$0.18/kWh]	309
Figure 8. 20 Lifetime cost of driving (¢ per mile) for pure plug-in EV vs. plug-in EV with PV [Electricity price \$0.35/kWh]	310
Figure 8. 21 Effect of mass-reduction technology on CO ₂ emission rate for constant performance [336]	312

CHAPTER ONE

INTRODUCTION

1.1 Motivation

The solar photovoltaic is a promising technology for managing the on-board power systems of Hybrid Electric (HEVs) and Plug-In Hybrid Electric Vehicles (PHEVs). The widespread use of solar energy, which is a free, sustainable, renewable, and clean source, will ensure U.S. energy independence and a low environmental impact in the manufacture of fuel-efficient automobiles. In addition, most vehicles are rarely driven for long distances in the US, with the average vehicle trip approximately 36 miles and the average driving duration of less than an hour [1]. Consequently, such a novel system will serve as a ready reserve of energy that can be tapped in times of intensive use.

Although the continuous technological advances have increased the efficiency and reduced the cost of photovoltaics, which could accelerate their inclusion into the automobile design process, many challenges must be resolved before a PV powered automobile can be manufactured and marketed.

The current lack of thorough decision-making methodologies to select the most appropriate PV module for vehicle applications is perhaps the most urgent of these problems. There is also an incomplete understanding about the actual contribution of the on-board PV in reducing fuel consumption, particularly as regards to meeting corporate average fuel economy (CAFE) standards for different vehicle sizes. Compounding these difficulties is an absence of literature on the well-to-wheels life cycle assessment (LCA)

for vehicles with on-board PV, which can serve as a useful study to compare the “green” ratings of vehicles powered entirely by solar PV with vehicles partially powered by solar PV technologies with other energy paths used to power vehicles.

Therefore, all these challenges motivate a strong need to develop novel comprehensive assessment methodology of using on-board PV solar modules to enhance automotive fuel economies to meet CAFE standards through 2025 along with providing an alternative energy path for the purpose of sustainable transportation, which is proposed in this study. Specifically, the proposed work could be used to develop a tool for decision-makers to use during the conceptual design stage, since its results are capable of reflecting the changes in fuel consumption, greenhouse gas (GHG) emission, and cost for different locations, technological, and vehicle sizes to facilitate the deployment of a sustainable transportation system.

1.2 Problem Statement

Today’s energy and automotive sectors face the following challenges from different aspects:

- 1) Energy Demand: there is a high-energy demand in the transportation sector, which as indicated in Figure 1.1, represented the second greatest consumer of the energy used in the US in 2013 [2]. In addition, the transportation sector represented the greatest consumer of petroleum in the US in 2013 [2], a non-

sustainable energy source subject to large and unpredictable fluctuations in price, which is also steadily increasing.

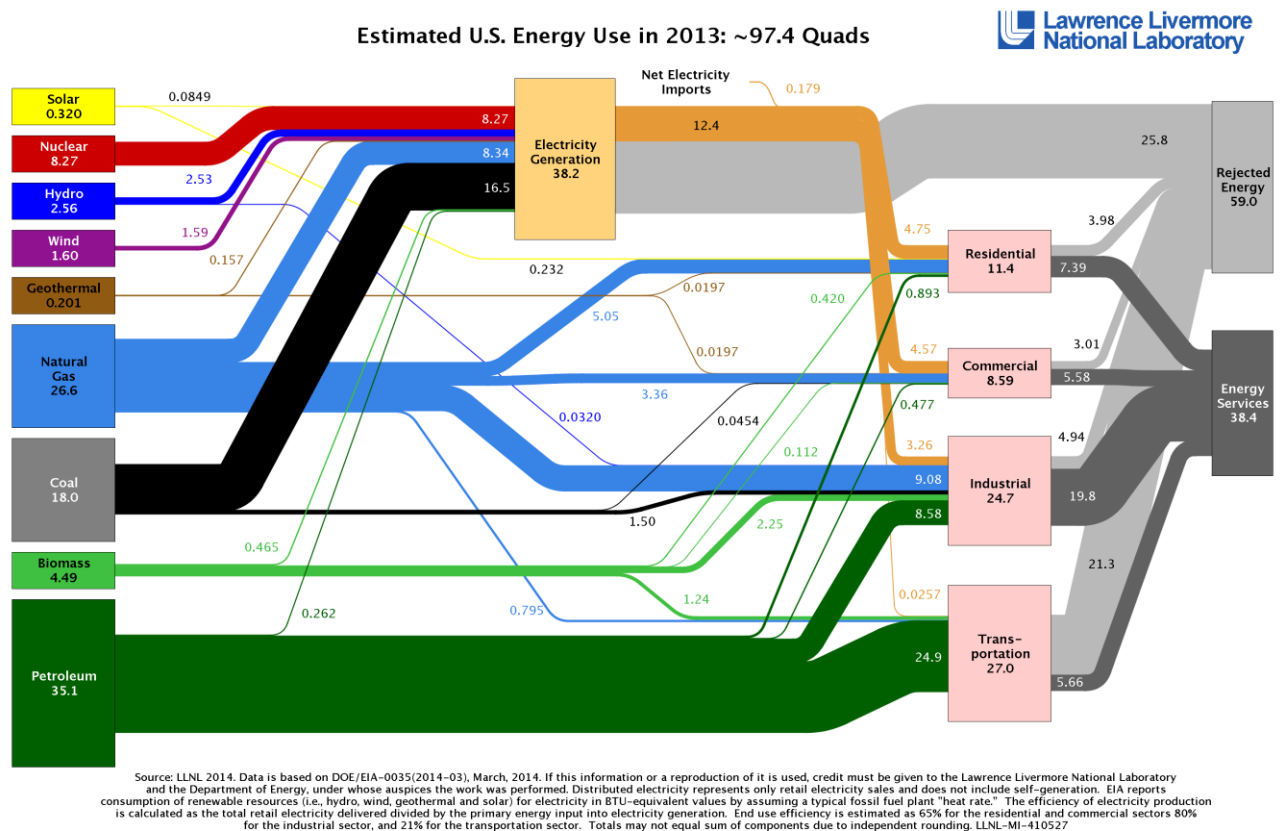


Figure 1. 1 The United States Energy Flow Trends in 2013 [2]

- 2) The environment impact: one of the greatest adverse effects to the earth's climate is the total energy-related CO₂ vehicular emissions released annually. As shown in Figure 1.2 [3], the level of emissions generated by the transportation sector, which is the second largest emitter of greenhouse gases, was around 34% of the total emissions in the U.S. in 2013. The electrical generation in the US was the

highest emitter of greenhouse gases in 2013 with 38% of the total emissions in 2013, all of which was the byproduct of coal and natural gas.

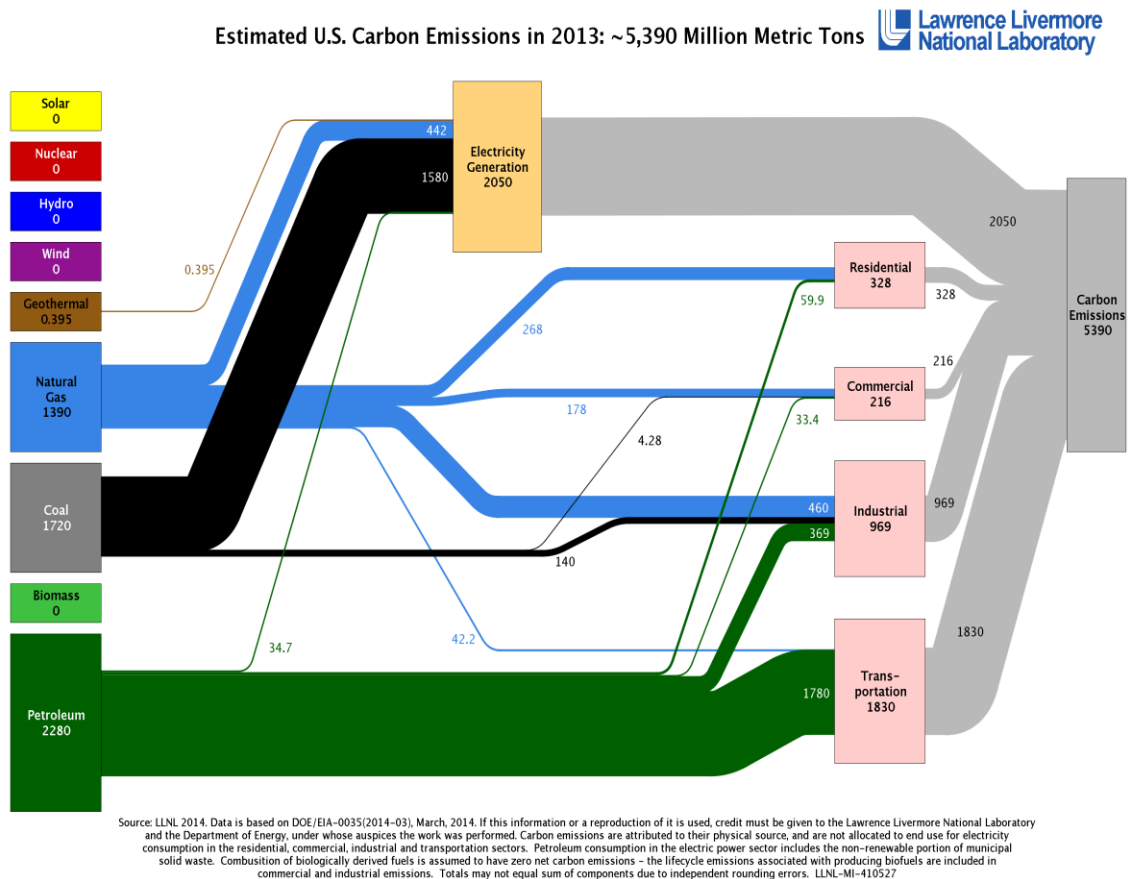


Figure 1. 2 United States Carbon Emission in 2013 [3]

- 3) Policy: to adhere to these climatic control standards and to increase fuel economy, US automakers must meet annual corporate average fuel economy (CAFE) standards as mandated by the National Highway Traffic Safety Administration (NHTSA) and the Environmental Protection Agency (EPA) (See Figure 1.3 [4]).

For example, the CAFE target for vehicles with 41-ft² footprint size or lesser is at least 38 mpg in 2014 and increase to 61 mpg in 2025. Meeting these targets has been most challenging. Indeed, the failure of the US auto industry to meet or exceed these fleet CAFE targets has resulted in total fines of more than \$844 million collected so far from manufacturers [5].

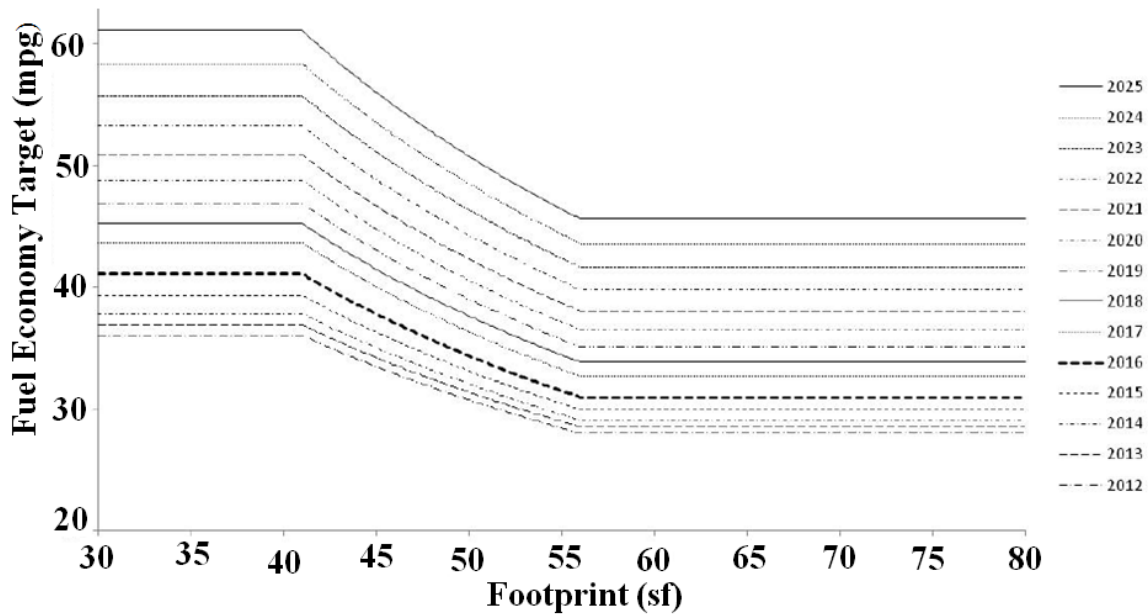


Figure 1. 3 Fuel Economy Target (CAFE) per Passenger Vehicle (ft²) [4] (edited for clearness)

To solve these challenges, the research community has been engaged in developing a multitude of options to mitigate this alarming rate of emissions and to meet CAFE target, some of which are highlighted in Figure 1.4.

Despite this effort, there has been no comprehensive study to determine the efficacy of on-board PV technologies in vehicles for solving these challenges. The problem statement of this study is to develop a comprehensive assessment methodology for determining the challenges and benefits of using on-board photovoltaic (PV) solar

technologies in vehicle applications toward meeting the CAFE standards through 2025 along with providing an alternative energy path for the purpose of sustainable transportation.

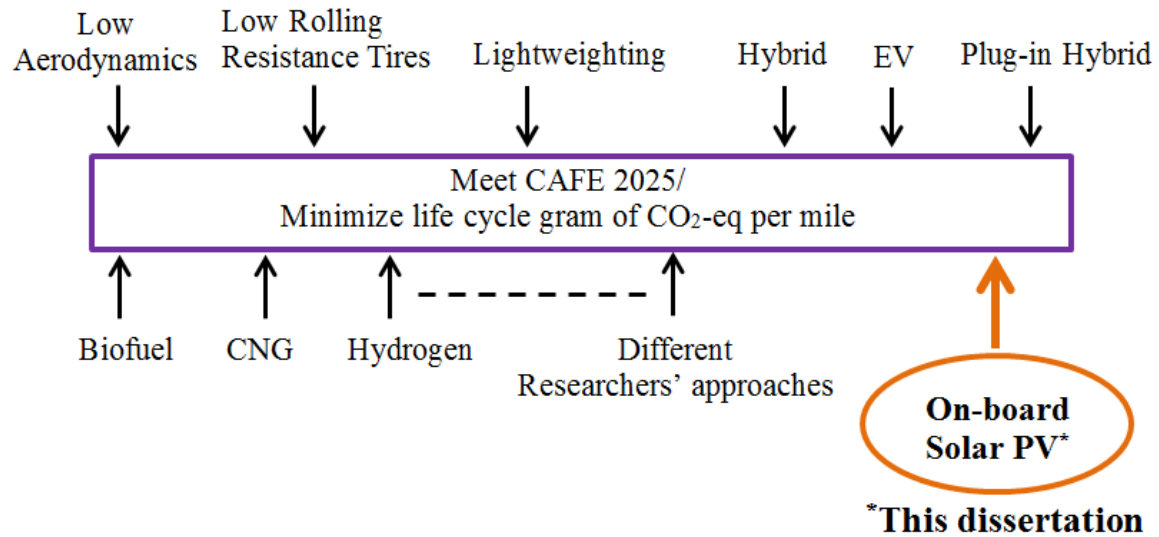


Figure 1. 4 Different Research Approaches and Current Study Approach to Reduce Well-to-Wheel Emission and Meet CAFE 2025

1.3 Research Questions (RQs) and Objective

The objective of this research is to answer the following Research Questions (RQs):

- ❖ **RQ.1:** Which PV module type is the most appropriate for the on-board vehicle application? How can we evaluate and select the best PV module?
- ❖ **RQ.2:** What are the factors that influence the reliability and the performance of PV module?
- ❖ **RQ.3:** How much contribution does on-board PV make toward supply energy? How can the solar energy to direct current (DC) electrical power ratio be optimized?
- ❖ **RQ.4:** To what degree can on-board PVs minimize energy consumption in the vehicle? What is the maximum contribution towards meeting CAFE? Is it vehicle dependent?
- ❖ **RQ.5:** How green is the solar vehicle and how green are other vehicles with PVs? Is it a cost effective solution to add on-board PVs?

1.4 Approach

The proposed approach of this dissertation is to develop a comprehensive methodology based on life cycle assessment to answer the RQs. Figure 1.5 highlights the dissertation's approach.

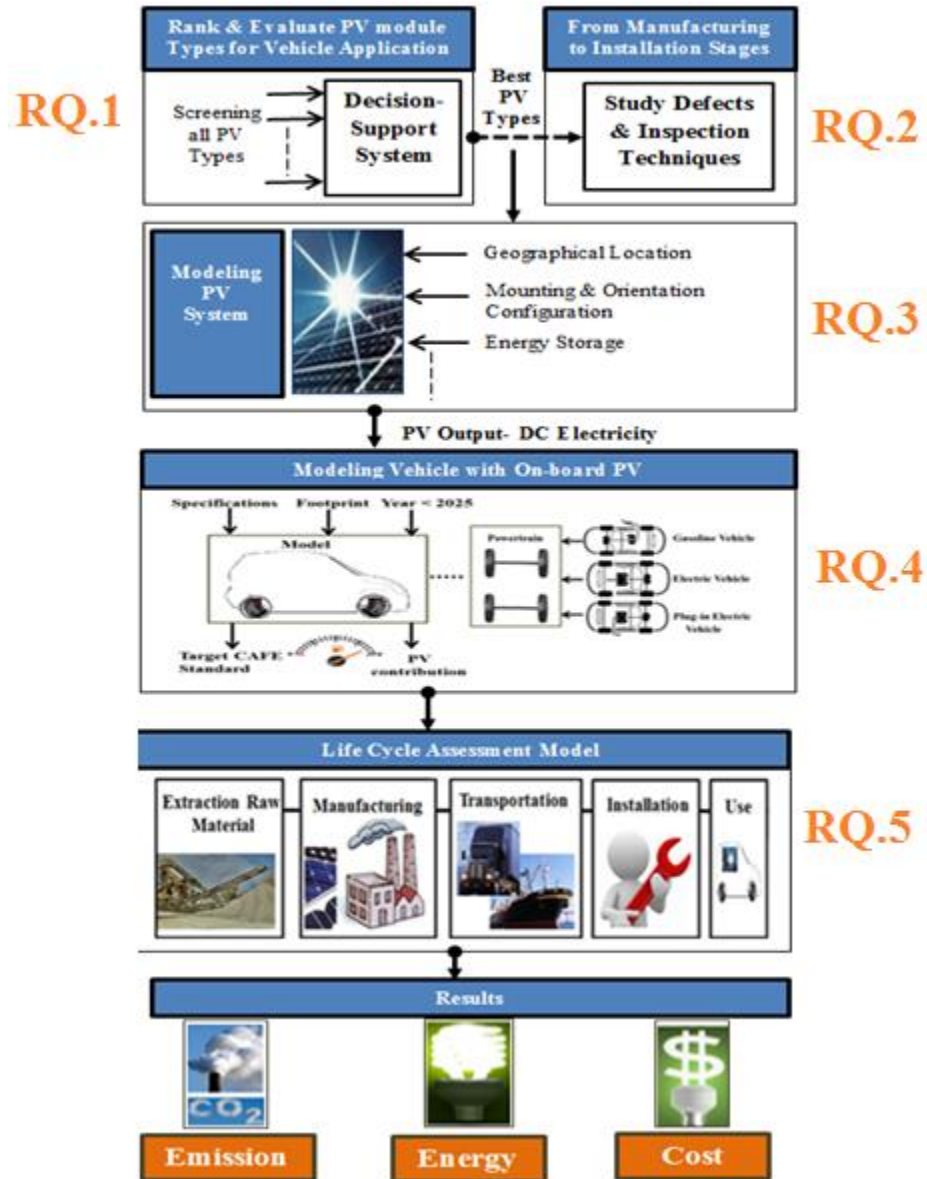


Figure 1. 5 Dissertation Approach and Organization

A novel five-step process is used in this comprehensive assessment methodology of on-board photovoltaic (PV) solar technologies in vehicle applications. The assessment results of this work are based on emission, energy, and cost perspective. In this work, more than 25 PV types screened, 10 Inspection techniques are reviewed, and more than 200 LCA studies screened. In addition, more than 14 different vehicles are analyzed with two Powertrain configurations; pure gasoline and pure plug-in electric vehicles. The proposed assessment methodology includes 3 different travel patterns in 12 U.S. states and 16 countries covering 19 different cost analysis scenarios for current and future prices.

First, two decision-support systems are developed for evaluating and selecting the optimal PV module type option for vehicle applications. The first approach involves a combination of quality function deployment (QFD) and analytical hierarchy process (AHP) and the second approach entails the use of QFD and fuzzy axiomatic design.

Second, the defects in the PV device from the manufacturing to the installation stage are studied along with a concurrent review of the related inspection tools. This work is transformative in that a unique decision-support system is proposed for evaluating all related non-destructive inspection systems to select the optimum one suitable for an automated PV production line to increase the PV module reliability and efficiency in the field, as well as reduce PV manufacturing cost.

Third, a comprehensive PV system model for on-board vehicle application is developed and the solar energy to the DC electrical power output ratio is optimized.

Forth, the vehicle model with on-board PVs is proposed to assess how well using on-board PV technologies assist in powering different vehicle configurations to enhance the automotive fuel economy and meet CAFE standards.

Fifth, the novel life cycle assessment (LCA) model is developed with a particular emphasis on energy, emission, and cost factors of using on-board PV technologies for automotive application.

This study covers well-to-tank analysis, tank-to-wheel analysis, and wheels-to-miles of pure PV solar vehicles, pure gasoline vehicles, gasoline vehicles with PVs, pure plug-in electric vehicles, and plug-in electric vehicles with PVs.

1.5 Dissertation Organization

Chapter 1 presents the motivation, problem statement, research questions, objective, approaches of the dissertation, and outlines its organization.

From Chapter 2 to Chapter 7, five major processes, Photovoltaic (PV) decision-support systems for vehicle application, PV defects and inspection techniques, modeling PV system for on-board vehicle application, modeling vehicle with on-board PV, and the life cycle assessment model are discussed - see Figure 1.5.

Chapters 2 and 3 develop two decisions-support systems based on analytic hierarchy process (AHP) and fuzzy axiomatic design (AD) to rank and evaluate all PV options for vehicle application.

Chapter 4 studies the PV defects from manufacturing to installation stage, reviews the main inspection techniques to detect them so the PV reliability and efficiency is increased, as well as manufacturing cost is decreased.

Chapter 5 develops a comprehensive PV system model for on-board vehicle application and optimizes the solar energy to the DC electrical power ratio (well-to-tank analysis).

Chapter 6 presents the vehicle model with on-board PV, this includes tank-to-wheel analysis and wheel-to-mile analysis.

Chapter 7 presents the life cycle assessment model, includes PV system, gasoline, and grid electricity.

Chapter 8 presents the results of the proposed assessment methodology after the above major sections are integrated, includes environmental, energy, and economic analysis for using on-board PV with different vehicle Powertrain options. The results include the contribution of on-board PV toward CAFE, PV range extender estimation, how green is solar vehicle, LCA (well-to-mile analysis) of gasoline vehicle with and without on-board PVs, LCA (well-to-mile analysis) of plug-in electric vehicle with and without on-board PVs in the U.S. and in India, economic analysis (lifetime cost analysis) of using PV on-board for gasoline and electric vehicles, comparison between the proposed on-board PV approach over vehicle Lightweighting approach, and the current challenges for this vehicle design.

Finally, Chapter 9 wraps up the entire dissertation and presents the conclusion, contributions, limitations, and future work.

CHAPTER TWO

EVALUATION OF ON-BOARD PHOTOVOLTAIC MODULES OPTIONS FOR ELECTRIC VEHICLES

2.1 Introduction

The non-sustainable nature of fossil fuels and the increasing awareness about environmental pollution has resulted the creation of vehicles that use alternative fuel sources such as: electric vehicles (EVs), hybrid electric vehicles (HEVs), and plug-in hybrid electric vehicles (PHEVs). Photovoltaic (PV) technologies, in which solar energy is captured and converted to direct current (DC) electricity, have also been developed because of the availability of resources to create such technologies, and because of the ubiquitous nature and zero cost of solar energy. The PV module, which is a packaged assembly of individual PV cells, can provide energy to the vehicle via either on-board or off-board methods. In off-board applications, the PV is the source of energy for the charging station. In on-board applications, the PV modules are vehicle mounted or integrated either to assist in propulsion or to run a specific vehicle application [6]-[9]. There has been substantial interest in developing PV technologies for transportation because of the rapid evolution of these technologies in terms of increased efficiency and

* © [2014] IEEE. Reprinted, with permission, from [Abdelhamid, M.; Singh, R.; Qattawi, A.; Omar, M.; Haque, I., Evaluation of On-Board Photovoltaic Modules Options for Electric Vehicles, *IEEE Journal of Photovoltaics*, Nov/2014]

reduction in cost. The approaches vary in terms of the PV module type, specifications, and configuration of the system.

However, thus far, no research has been undertaken to determine the efficiency of decision-making methodologies to evaluate and select the optimum commercial PV module option of on-board EVs. In this study, we propose evaluation factors, constraints, and the decision-making criteria necessary to assess PV module's suitability for this application. We also present an overview of different commercial PV modules options. The proposed decision-making methodology is a combination of the quality function deployment (QFD) [10] and the analytical hierarchy process (AHP) [11]. This research reduces the subjectivity of these methods used with the inclusion of commercial PV market data for comparison, and not from experts' experiences as in traditional research. It is also innovative in that we add QFD as an input stage to correlate EV customers' needs with PV module capabilities. The balance of this chapter is organized as follows: in Section 2.2, we provide a literature review, followed by our proposed methodology in Section 2.3. In Section 2.4, we provide our range of results for an EV powered by PV modules, and provide a summary in Section 2.5.

2.2 Literature Review

Based upon a combination of qualitative and quantitative approaches, the AHP is a multi-criteria decision-making (MCDM) method used to evaluate multiple and conflicting criteria. In the qualitative sense, it decomposes an unstructured problem into a systematic decision hierarchy. A quantitative ranking using numerical ranks and weights

in which a pairwise comparison is then employed to determine the local and the global priority weights and finally the overall ranking of proposed alternatives. The AHP approach has been recently used to rank various renewable and non-renewable electricity production technologies [12], for determining the best possible solar tracking mechanism [13], for selecting the most appropriate package of solar home system (SHS) for rural electrification [14], for selecting the solar-thermal power plant investment projects [15], for determining the best sequence of switching [16], and in evaluating different power plants [17]. As part of this dissertation, we use the AHP for selecting the best micro-crack inspection technique for an automated PV production line [18].

The QFD is a systematic method that the designer may use to develop a new product or service by learning about the needs of the customer, also known as the voice of the customer (VOC). The aim of QFD is to incorporate the VOC into the engineering characteristics of a specific product or a service. The planners can then prioritize each product or service attributes to set the levels necessary for achieving these characteristics. The QFD is used for various applications, and the combined AHP-QFD is applied to various situations [19], [20]. A QFD and AHP combination as a decision-making tool used for material selection of automobile bodies [21] and used to develop a knowledge-based system for designing an automotive production line [22].

There are many other MCDM models, all of which have their strengths, weaknesses, and areas of application, and none of which is truly superior [23]. The most common disadvantage between the MCDM tools is the subjectivity where the decision maker uses his/her experience to rank alternatives.

Our proposed methodology minimizes the subjectivity and provides robust results. We chose the AHP decision-making for these reasons: (i) selecting the optimum PV module option for on-board EV is an MCDM problem with conflicting objectives, (ii) the AHP is based on pairwise comparison and provides a robust decision tool if precise data are used, (iii) the ability to incorporate QFD as an input stage so that weights are assigned according to EV customer's preference and reducing the subjectivity found in traditional AHP method.

2.3 Methodology

The methodology used in this study is shown in Fig. 2.1. The objective is to select the optimum PV module options to power on-board EVs. We divide this approach in three main stages as discussed in the following sub-sections.

2.3.1 Stage I: QFD

There are five key components in our QFD matrix (see Fig. 2.2). First, the “How” window is used to specify the engineering requirements. Here, we propose the decision-making criteria necessary to assess a PV module's suitability for commercial use for EV, which are the six PV functional requirements as specific weight, power density, efficiency, power temperature coefficient (PTC), life cycle cost (LCC) of electricity, and material concern.

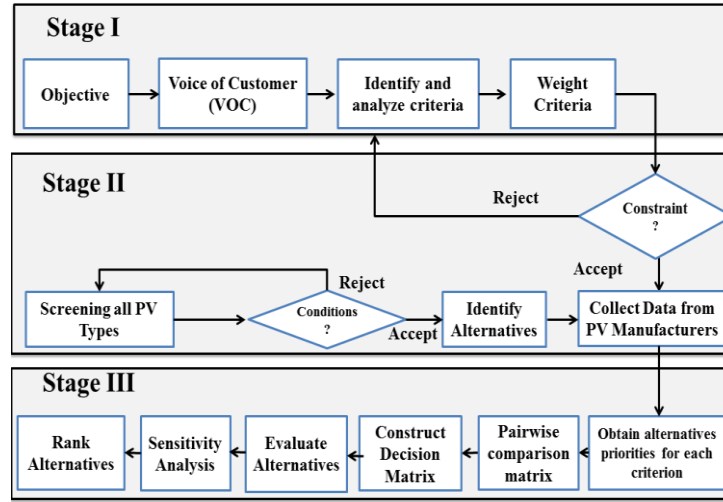


Figure 2. 1 The Proposed Methodology to Select the Optimum PV Module Option to Power On-board EVs

Row #	Importance (α)	<div> <div>PV Modules Functional Requirement ("Hows")</div> <div>EV Requirements ("Whats")</div> </div>	Column #	1	2	3	4	5	6
				Power Density (W/m ²)	Specific weight (W/kg)	Efficiency (%)	Power Temperature Coefficient (-%/°C)	Cost (€/kWh)	Material
1	25.0	High Performance		9	9	9	3	1	1
2	25.0	High Milage		9	9	9	3	1	1
3	20.0	Economy		3	1	3	1	9	1
4	15.0	Stability and reliability		1	1	1	3	3	9
5	15.0	Temperature Durability		1	1	1	9	1	9
Sum	100.0								
		Evaluation= $\sum \alpha_{j1} \beta_{ij}$ i= 1,2,...,No.Hows j= 1,2,...,No. Whats		540.0	500.0	540.0	350.0	290.0	340.0
		Relative Weight(%) = Evaluation / \sum Evaluations		21.09	19.53	21.09	13.67	11.33	13.28

Figure 2. 2 Proposed QFD

The specific power is defined as the total power generated by the PV module divided by the module weight and expressed in watts per kilogram (W/kg). For use in EVs, the specific power of the PV module should be high, as the installation of PV modules will increase the vehicle curb weight, which affects vehicle performance. The power density is the total power generated divided by the area of the module with units of watts per meter-squared (W/m^2). Higher density modules are preferred for EVs with limited surface areas. The efficiency of the PV module is defined as the total power generated per unit area (m^2) divided by $1,000 \text{ W/m}^2$ and multiplied by 100. The efficiency of the PV module should also be high to provide maximum output power for given weather conditions and given module area. PTC is expressed as $\text{-\%/}^\circ\text{C}$. An increase in temperature in turn causes a corresponding decrease in all types of PV module performance, with a lower PTC indicating improved performance. Finally, both cost and material criteria will be discussed later.

Second, the “What” window is used to determine VOC preference in an EV. Third, the “Importance” window is used to weigh the VOC preferences as percentages. The higher percentage score represents the most important customer need. Fourth, the “Hows” and “Whats” are combined using a relation matrix that consists of three different scores (1, 3, and 9) to define the relationship between the customer needs and the engineering metrics. Score 1 indicates a low impact between the specific column in the “How” window and a specific row in “What” window; score 3 is the mean medium impact, and score 9 indicates a strong effect. For instance, a score of “25 out of 100” is assigned for “High performance” as a high valued customer need for those EVs. Any high performance EV

must have a PV with strong power density, specific weight, and PV efficiency, with the medium and weak impacts for the other factors. Correspondingly, the rest of the relationship matrix completed. Although these values cause decision inconsistency, it can be reduced by establishing many customer-oriented questionnaires and by incorporating a team of engineering, marketing, and research professionals.

At the bottom, or fifth position of the OFD matrix is the outcome, which is the relative weight. The returned relative weights indicate the relative importance for all PV modules requirements and are used as input to the AHP stage. The relative weight is calculated using (2.1):

$$\text{Evaluation} = \sum_{ij} \alpha_i \times \beta_{ij} \quad (2.1)$$

Where, i =number of rows (from 1 to 5), j =number of columns (from 1 to 6), α_i is the importance and β is the score (the value from the relationship matrix for the given “How”/”What” pair). That is to say, the evaluation in first column (power density) is calculated as $=25 \times 9 + 25 \times 9 + 20 \times 3 + 15 \times 1 + 15 \times 1 = 540$.

The relative evaluation is calculated as the specific evaluation divided by the sum of all evaluations that is equal to $540/2560 = 21.09\%$.

2.3.2 Stage II: PV Search Domain

Here, we highlight the possible search space for the selection process and provide an overview of the different commercial PV technologies with main emphasis on the strengths and challenges of each type of PV module. Although many PV cell types are

available, cost, availability of raw materials, reliability, stability, and lifetime limitations limit their widespread availability [24].

The current commercial PV modules are based on bulk silicon (wafer based) and thin films could be deposited on either rigid or flexible substrates. Bulk silicon PV modules in the form of either mono-or multi-crystalline silicon (mono-Si or multi-Si) are superior to other PV materials. They are composed of silicon, the second most abundant element in the earth's crust and a well-researched and understood element in the periodic table. Consequently, this element is the predominant material of silicon based solar cells that compose the \$350 billion semiconductor industry. E.g., in 2013, the silicon bulk PV module shipped was 89.58% of a 40 GW total, with thin films (cadmium telluride (CdTe), copper indium gallium selenide (CIGS), and amorphous silicon (a-Si)) solar cells comprising the remaining 10.42% [25]-[28]. Laboratory tests also show that bulk silicon based single junction cells can achieve an efficiency of 25% [24]. The challenges for CdTe PV modules are that cadmium is toxic and there is a limited supply of Te [29]. Some companies recycle the product to mitigate environmental toxicity of CdTe modules, but the cost of reclamation is quite prohibitive. CIGS have small amounts of cadmium sulfide making them relatively safer than CdTe PV modules. Unfortunately, CIGS has limited use in that it requires indium, an element that is both rare and expensive [29]. The advantages of a-Si PV module, in addition to the abundance of silicon, is that both the manufacturing tools and techniques used to deposit a-Si and related materials are similar to that used in liquid-crystal display (LCD) manufacturing. They are also superior to bulk silicon PV modules in terms of PTC. The main disadvantage of a-Si PV module is

low efficiency, which can be increased, however, with the use of multiple junction a-Si solar cells.

In this work, we analyzed six different PV module options: mono-Si, multi-Si (poly-Si), a-Si single junction, double junctions' a-Si/micro-Si, CdTe, and CIGS. We did not analyze single and multi-junction gallium arsenide (GaAs) (with or without concentration technology), organic photovoltaic (OPV), dye-sensitized solar cell (DSSC), and quantum dot cells. Although GaAs-based solar cells are the most efficient PV type, they are the most expensive and are mainly used in space applications. The relatively low efficiencies of OPVs, DSSCs, and quantum dot cells make them particularly poor candidates for the large-scale PV generation of electricity. Specifically, DSSCs do not exceed 17 cm², which makes it very difficult to build large-area energy modules because of the large amount of energy that is lost during their connection [30]. OPV is unreliable with a cell lifetime of only 3 to 4 years [31] compared to other commercial PV module options, which have a lifespan of 20-30 years. Unless there is a fundamental breakthrough in the material synthesis and performance of these types, it is not possible that the PV modules based on these types of solar cells will be ever used for bulk power generation [30].

In order to test the different types of PV module options, we collected the performance specifications for each using manufacturer Datasheets and analyzed these data in terms of our decision criteria (see Figs 2.3 and 2.4). Over than 20 top PV manufacturers are included in this study, where the best PV module option per manufacturer in terms of maximum power rating is used for analysis that serve as the basis for the evaluation. All PV modules included here are rigid. The manufacturer's PV module power ratings are for

standard test conditions (STC) ($1,000 \text{ W/m}^2$ solar irradiance) at 25°C . Fig. 2.3 shows the specific weight and the power density of the various PV modules from different manufacturers. Note both the highest specific weight and the highest power density in the case of mono-Si of approximately 18.5 W/kg and 211.6 W/m^2 respectively. Fig. 2.4 shows the efficiency and PTC of various PV modules, the efficiency varies from a low value of 5.9% for a-Si modules to a high value of 21.5% for mono-Si. The best PTC value is $-0.2\%/^\circ\text{C}$ for a-Si module and the worst is $-0.452\%/^\circ\text{C}$ for a multi-Si module. In Table 2.1, we provide all the values used for the pairwise comparison in stage III. The first four criteria values are the average values shown previously in Figs. 2.3 and 2.4. E.g., the average specific weight for mono-Si is equal to 14.4 W/kg where this value is the average for all specific weights of mono-Si modules from different mono-Si manufacturers in Fig. 2.3.

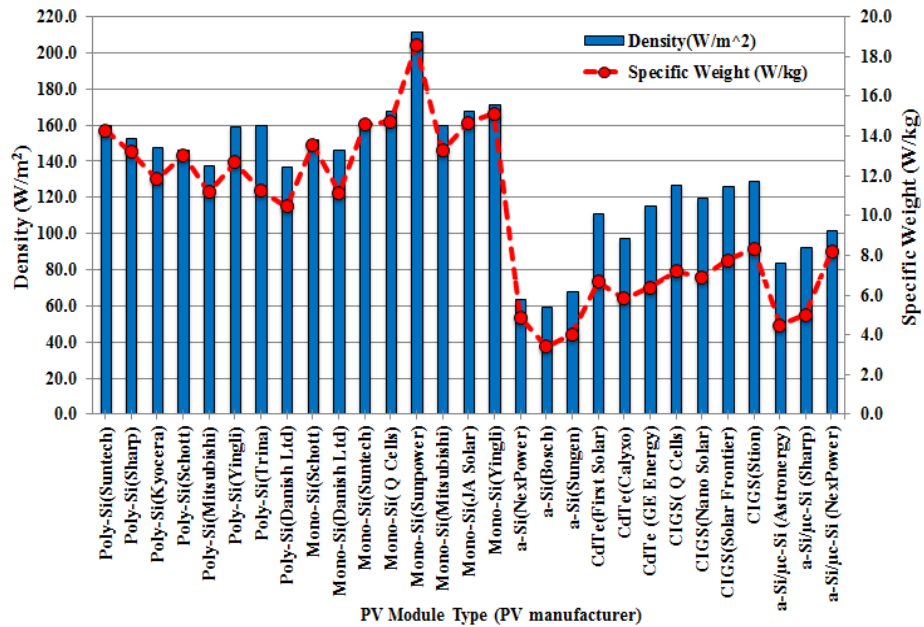


Figure 2. 3 Power Density and Specific Weight of Different PV Options from Different Manufactures

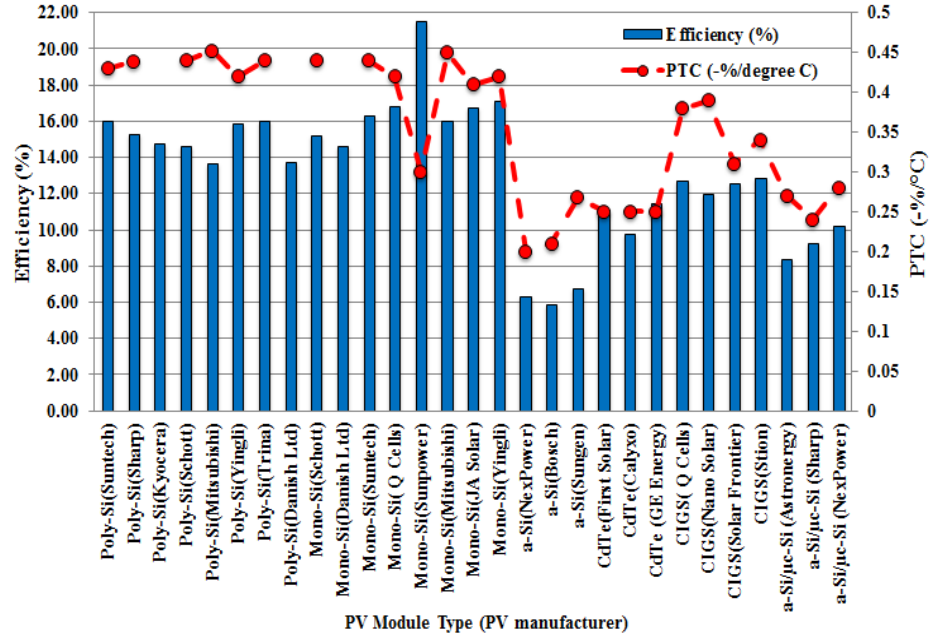


Figure 2. 4 Efficiency and PTC of Different PV Options from Different Manufactures

Table 2. 1 Decision-Making Pairwise matrix

		Alternative					
		Multi-Si	Mono-Si	a-Si	CdTe	CIGS	a-Si/μ-Si
Criteria	Power Density (W/m ²)	150.1	167.5	63.7	107.9	125.4	92.8
	Specific Weight (W/kg)	12.2	14.4	4.1	6.3	7.5	5.9
	Efficiency (%)	15.01	16.79	6.35	10.80	12.55	9.30
	PTC (-%/°C)	0.437	0.411	0.226	0.250	0.355	0.263
	Cost (¢/kWh)	1.871	1.853	1.660	1.652	1.769	1.650
	Material	“Excellent”	“Excellent”	“Excellent”	“Least”	“Moderate”	“Excellent”

We used this average to (i) enhance the robust nature of our pairwise comparison to reflect actual PV market data, and (ii) reduce the subjectivity in the traditional AHP method by making the pairwise comparison depend on manufacturer's actual data and not on the evaluations of the decision maker using the 1-to-9 scale [11].

For values of the cost criterion in Table 2.1, we used a life cycle cost (LCC) of electricity indicator for comparison since the constraint here is the installation surface area of the vehicle. The LCC is defined as the total cost of PV system per total energy generated through PV system in the life cycle in unit (\$/kWh). The LCC is calculated using [32, eq. (2.2)-(2.3)].

$$LCC (\$/kWh) = \frac{\text{Cost} \sum [\text{PV Module} + \text{installation} + \text{land} + \text{Energy storage} + \text{maintenance}]}{\text{Total energy generated}} \quad (2.2)$$

$$\text{Total energy generated} = I \times \eta \times PR \times LT \times A' \quad (2.3)$$

Where, I is the irradiation ($kWh/m^2/yr$) which the average energy flux from the sun and depends on the installation location. η is the lifetime average module efficiency (%), PR is the performance ratio, LT is the system lifespan (year), and A is the total module area (m^2). We did not factor in a cost of land since the PV module integrates into the vehicle body. We also assumed that the installation, maintenance, and energy storage costs were similar for all PV module types. The current prices of commercial PV modules (excluding tax) in (\$/W) for the bulk silicon solar modules are 0.55, 0.655, and 0.92, while for thin film solar modules are slightly less as 0.49, 0.583, and 0.87 for low, average and, high scenarios respectively [33]. These prices are set by the manufacturers,

with Chinese made PV modules the least expensive. The cost of PV module per energy generated is calculated using average module prices, the details of which are in Table 2.2. The cost of PV module per m^2 is calculated using the average module density value (Table 1). The PV module lifetime efficiency is calculated based on degrade over the system lifetime by 0.5% relative to the initial efficiency shown in Table 2 per year [34]. The total energy generated is calculated with assumed parameters are $I=1800 \text{ kWh/m}^2/\text{yr}$ based on US location, $PR=0.75$, $n=30$ years [34].

The use of silicon, which unlike Cd based CdTe PV modules are neither hazardous to humans nor the environment, obviates any difficulties in the supply chain. Indeed, the CdTe module is not the preferred choice worldwide and may be banned in several countries [35].

Table 2. 2 LCC of electricity of different PV module options

	Multi-Si	Mono-Si	a-Si	CdTe	CIGS	a-Si/ μ -Si
PV Module price (\$/W) (Excluded Tax) [33]	0.655	0.655	0.583	0.583	0.583	0.583
PV Module price (\$/W) (with sales tax=7%)	0.701	0.701	0.624	0.624	0.624	0.624
Cost PV Module (\$/m ²)	105.198	117.392	39.737	67.309	78.226	57.890
PV Module Average Lifetime efficiency (%)	13.880	15.640	5.910	10.060	10.920	8.661
Total energy generated (KWh)	5621.400	6334.20	2393.55	4074.3	4422.60	3507.826
Cost PV per Total Energy (¢/KWh)	1.871	1.853	1.660	1.652	1.769	1.650

Based on material availability/concern, we rank PV module using the traditional 1-to-9 AHP scale [11].

In order to adequately evaluate the PV options, the three constraints (geographical location, mounting configuration, and tracking/orientation option) should be identical in any comparison, which is beyond the scope of this section.

2.3.3 Stage III: AHP

Unlike traditional AHP models, our system evaluates the alternatives differently by first establishing a relationship between the objective function with criterion created by giving related weights to each, which we obtain from the QFD stage I output. The relationship between each criterion and each alternative is then established by a pairwise comparison between two elements simultaneously. Table 2.1 shows the alternatives, criteria, and the values used in the decision. The pairwise comparison matrix A in traditional AHP is obtained based on the decision maker's judgments a_{ij} using the 1-to-9 scale criteria [11, eq. (2.4)]

$$A = \begin{bmatrix} 1 & a_{12} & \dots & a_{1n} \\ a_{21} & 1 & \dots & a_{2n} \\ \vdots & \vdots & \dots & \vdots \\ a_{n1} & . & \dots & 1 \end{bmatrix}, \text{ Where } a_{ij} = 1 / a_{ji}, i, j = 1, \dots, n \quad (2.4)$$

In our proposed methodology, the decision matrix based on average values from actual manufactures data sheets [Table 2.1]. E.g., the pairwise comparison matrix for “specific weight criterion” shown in Fig. 2.5, has a multi-Si and mono-Si comparison equal to

1.18. This value is calculated by referring to the average specific weights for mono-Si and poly-Si, which are equal to 14.4 W/kg and 12.2 W/kg respectively. By dividing these two numbers, we get 1.18. All comparisons are performed in this manner. Although time consuming, this process yields very accurate results because no personal experiences and opinions of the decision-makers are used.

	Multi-Si	Mono-Si	a-Si	CdTe	CIGS	a-Si/micro-Si
Multi-Si	1	1.18	0.336	0.516	0.6146	0.4835
Mono-Si	0.847	1	0.2847	0.4374	0.5208	0.4096
a-Si	2.976	3.512	1	1.537	1.829	1.439
CdTe	1.937	2.286	0.6506	1	1.19	0.9363
CIGS	1.627	1.920	0.5467	0.84	1	0.78678
a-Si/micro-Si	2.068	2.441	0.6949	1.068	1.271	1

Consistency index (C.I.)=0.00

Figure 2. 5 Pairwise comparison matrix related to specific weight

This innovative approach in turn yields a robust decision tool. As the consistency index (C.I.) is zero, as shown in Fig 2.5, we can then calculate the *C.I.* using the method below [11, 36, eq. (2.5)]

$$CI = \frac{\lambda_{\max} - n}{n - 1} \quad (2.5)$$

Where, λ_{\max} is the maximum eigenvalue of the comparison matrix and n is the number of attributes in the square matrix. In the typical AHP, the conclusion of *C.I.* can be drawn by using a comparison to the consistency ratio (CR) to check the judgment of inconsistencies [36, eq. (2.6)].

$$CR = \frac{CI}{RI} \quad (2.6)$$

Where, RI (random index) is an experimental value, which depends on n and represents an average CI for a huge number of randomly generated matrices of the same order. Therefore, CR is the ratio between $C.I.$ (the calculated value) and the $R.I.$ (the expected value). The bigger $C.R.$ requires the decision maker to revise judgments to reduce the inconsistencies. Typically, if the value of $C.R.$ is less than or equal 0.1, the decision is acceptable [11], [36]. In our case (Fig. 2.5), since $n=6$, then $RI=1.25$ (The full table of RI values can be found in [36]. Therefore, in a typical AHP, if the CI is less than or equal 0.125, the decision maker accepts the results. In our proposed methodology the CI is zero, however, which reflects the robust and accurate decision-making results. In our final ranking of all the alternatives for the ultimate goal, we found that the crystalline silicon (mono and multi) modules yielded the best overall results, with the CdTe and a-Si PV modules have the lowest results (see Fig. 2.6).

The performance sensitivity analysis for our problem, shown in Fig. 2.7, clearly indicates conflicting objectives. Although the mono-Si PV module option yields the best power density, specific weight, and efficiency factors, it is the worst in term of the cost and the second worst in terms of PTC after multi-Si. Any inclusion of a thin film on a flexible substrate will result in these modules having a higher specific weight. We do not expect these results to vary greatly, however. In addition, any inclusion of semi-flexible PV modules with mono- and multi-crystalline PV cells between polymer sheets will increase the superiority of these modules as the specific weight of these modules will

increase further but with the assumption, the cost is still competitive with commercial bulk PV modules.

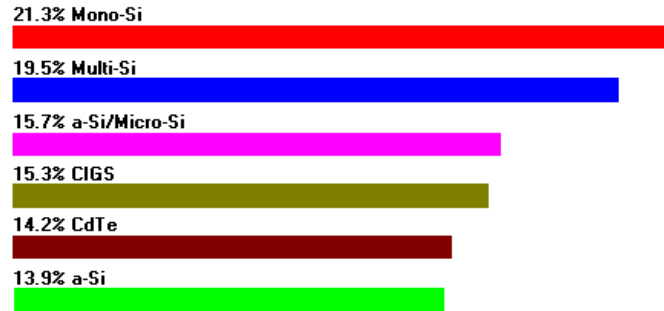


Figure 2. 6 Rank of different PV module types for EV application

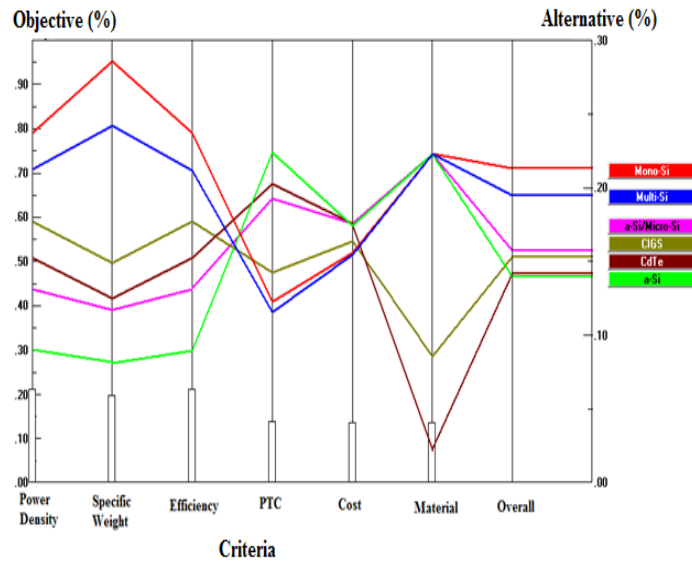


Figure 2. 7 Performance sensitivity analysis

2.4 Electric Vehicles Powered by PV modules

Here, we estimate the potential driving ranges for EV powered only by PV modules based on mono-Si PV option, which was ranked first in our study. We also categorized the three scenarios as best, intermediate, and worst cases. The proposed EV is lightweight

with an efficient aerodynamic design. For all scenarios, we also assumed that the EV owner has two sets of PV modules and batteries. The first set is of the PV modules are assumed to cover a total surface area of 2 m² on the vehicle roof to charge the on-board battery. The other set is assumed to cover an area of 5 m², which will be used to charge batteries at home. The assumptions of the vehicle, PV module, operating location, and battery are in Table 2.3. For the given vehicle, we calculate the power demands (P_w) at the wheel using the Japan 10+15 driving cycle using [37, eq. (2.7)-(2.11)].

$$P_w = \frac{1}{2} \rho C_d A_f V^3 + C_r M g V + M_{eff} V \frac{dV}{dt} \quad (2.7)$$

$$M_{eff} = M + M_r \approx 1.1M \quad (2.8)$$

Here M_{eff} is the effective mass, M_r is the rotational inertia, and V is the vehicle speed, which depends on the driving cycle. The energy to be provided at the wheel over the driving cycle is calculated by (2.9).

$$E_w = \int_{Cycle} P_w dt = \frac{1}{2} \rho C_d A_f \int_{Cycle} V^3 dt + C_r M g \int_{Cycle} V dt + M_{eff} \int_{Cycle} V \frac{dV}{dt} \quad (2.9)$$

Fig. 8 shows the power demands at the wheel and the driving cycle. The driving range (R) is calculated as (2.10)

$$R = \frac{E_w / D}{E_{batt}} \quad (2.10)$$

Where, D is driving cycle distance and E_{batt} is the amount of battery energy that reaches wheel, which is given by (2.11).

$$E_{batt} = \eta \times \Delta SOC \times E_{int} \quad (2.11)$$

Here, η is the traction efficiency and is equal to the product of that efficiency of each component: motor, batteries, etc. ΔSOC is operating window of the battery state of charge, and E_{int} is the initial energy stored in the battery from the PV, which differs in the three proposed scenarios.

Table 2. 3 Assumptions for EV with PV

PV Module SUNPOWER Model: SPR-327 NE-WHT-D	Specifications at 25 °C, Specific weight=17.58 W/kg, Density=200 W/m ² , PTC=-0.38 %/°C Efficiency=20.1%. Total weight of on-board PV with support structure = 25.00 kg Area of on-board PV=2 m ² (the constraint is the available installation area on the vehicle) Area of off-board PV=5 m ² (the constraint is the required area to charge the battery fully in the best case scenario)
Assumptions for scenarios	Best scenario: The temperature in both on-board & off-board PV modules at STC (25 °C) Intermediate scenario: On-board PV module at (45°C) & off-board PV modules at STC (25 °C) Worst scenario: The temperature in both on-board & off-board PV modules at 45 °C
PV Module Configuration	Horizontal
Operating Location	Insolation = 5 kWh/m ² /day (Average in US) [34]
Typical Lead-acid Battery [38]	Specific energy=40 Wh/kg Capacity=7 kWh, Operating window of the battery state of charge (SOC) >20% & < 80% Batteries weight= 175 kg
Typical lightweight Vehicle Specifications [37]	Traction efficiency (η)=0.8 Drag coefficient (C_d) X frontal area (A_f)=0.5 Air density (ρ) = 1.225 kg/m ³ Coefficient of rolling resistance (C_r) = 0.008 Gravitational constant=9.81 m/s ² Total weight (M)=curb weight + PV weight + driver=668 kg

2.4.1 Best Case Scenario

The assumptions of the different scenarios are tabulated in Table 2.3. Here, it is assumed that either with or without efficient cooling, the average temperature on both PV modules is kept at an STC of 25°C. The power generated by the PV modules at home is

equal to 1000 W. In the assumed location, the energy generated by the PV is approximately equal to 5000 Wh per day.

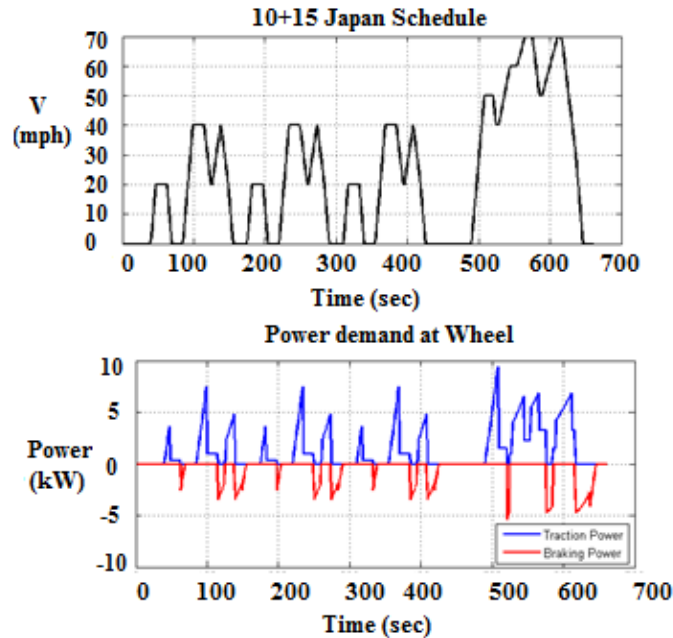


Figure 2. 8 Driving cycle and power demand at wheel

Assuming an ideal case, on the first day the fully charged EV batteries will provide 5000 Wh of energy storage. On the second day, the second set of PV modules, which is mounted on the car roof, generates 400 W and the total weight of the modules is 22.75 kg. While driving the EV, the batteries will discharge and will recharge again using the on-board PV modules mounted on the EV. During driving, the EV may not be exposed to sun or the weather may be rainy or cloudy. For these reasons, the amount of energy generated by PV modules mounted on the EV will vary daily. We assume that the PV modules mounted on the EV charge the batteries for 0, 1, 2, 3, 4, or 5 hours daily. Adding these additional charges to fully charged batteries provides the EV with the total energy

equal to 5000, 5400, 5800, 6200, 6600, or 7000 Wh, respectively. To keep the cost of PV-powered EV low, we used lead-acid batteries in this analysis based on [38]. For more sophisticated battery model approach, (see [39]). The expected daily vehicle ranges are shown in Fig. 2.9(a).

2.4.2 Intermediate Case Scenario

Here, the PV modules mounted on EV are not cooled. The average temperature at this location is assumed approximately 45°C. Consequently, the PV modules mounted on the EV will provide less electrical power compare to on-board PV module in the best - case scenario. The new efficiency of these PV modules is equal to 12.5% with each generating around 250 W and the car batteries providing additional energy storage of 0, 250, 500, 750, 1000, and 1250 Wh for 0, 1, 2, 3, 4, or 5 hours per day respectively. The expected daily vehicle ranges as a function of vehicle speed is shown in Fig. 2.9(a).

2.4.3 Worst Case Scenario

Here, the average temperature in both cases (home or if mounted on an EV) is assumed equal to 45 °C. The batteries charged at home provided less energy as compared to the previous cases. The modules will generate 625 W and the full day charged batteries would store 3125 Wh. The additional charge provided by the PV modules mounted to the battery is identical to the intermediate case scenario. The expected daily vehicle ranges as a function of vehicle speed are in Fig. 2.9(a).

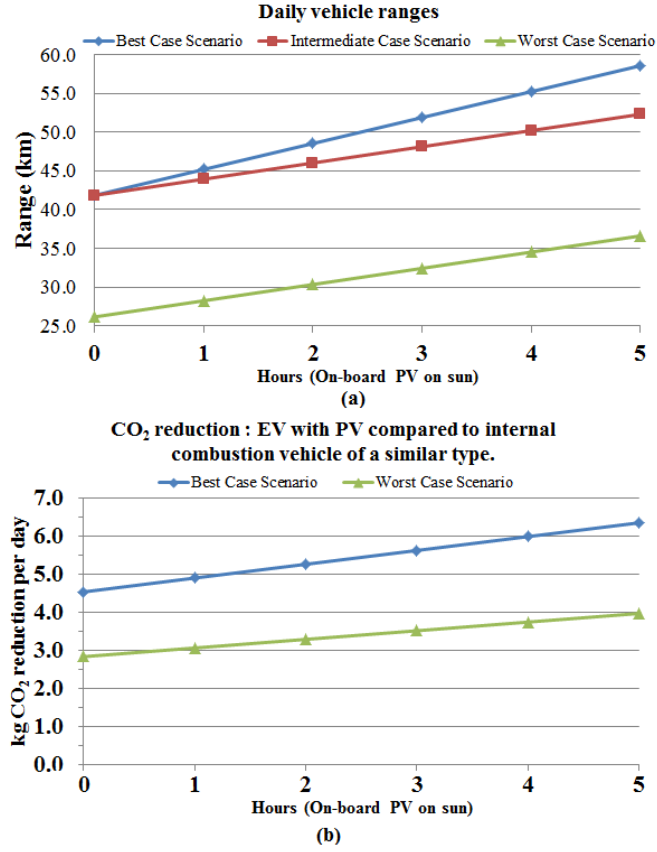


Figure 2. 9 (a) Daily Vehicle Ranges of Three Scenarios. (b) CO₂ Reduction Compare to Equivalent Gasoline Vehicle

2.4.4 CO₂ Reduction

In Fig. 2.9 (b), we estimate the amount of CO₂ reductions per day for this assumed vehicle compared to an equivalent gasoline vehicle. We estimated the equivalent mile per gallon (MPG) for the assumed vehicle in the given driving cycle as 51 MPG. The calculations are based on [37, eq. (2.12)]

$$MPG = \eta_{T2W} \times \frac{\rho_{gasoline}}{E_{Cycle}} \cdot I_{Cycle} \times 2.352 \quad (2.12)$$

Where, η_{T2W} is tank to wheel efficiency (assumed 15%), $\rho_{gasoline}$ is volumetric energy density (assumed 30 MJ/L), E_{cycle} is the energy need for given cycle in MJ, I_{cycle} is the driving cycle length in km, and the 2.352 is the conversion factor. Each gallon of gasoline emits approximately 8,887 grams of CO₂ [40]. Based on that, our calculation shows that the CO₂ emissions were reduced between 3 and 6.5 kg, compared to internal combustion vehicles of a similar type.

2.5 Summary

Sales of low speed EVs are expected to increase in the next few years to 695,000 units sold by 2017, a growth of 45% that is not confined to any region of the world [41]. The increase of consumers worldwide who can afford cars makes it more urgent to develop green transportation alternatives. The continued reduction in the cost of PV modules coupled with increase PV module efficiency are the primary impetus for developing electricity generated PV modules to meet the 21st century transportation needs. In this work, with the sole purpose of driving EVs powered only on PV generated energy, we used a unique QFD-AHP hybrid decision making approach to select the best commercially available PV modules. Unlike traditional methodologies, this unique approach evaluates and ranks the different PV modules by reconciling the conflicting objectives and multi-attribute restraints to solve the problem. The subjectivity inherent in dealing with such tools was reduced with the incorporation of QFD into the input stage to weigh the criteria based on customer's needs and through the use of commercial PV market data for pairwise comparison between alternatives. The subjectivity also can be

further limited by establishing a customer-oriented questionnaire and by incorporating a team with members from the engineering, marketing, R&D departments. The proposed decision-making methodology is robust since we depend on precise data. However, this approach is still useful even in the absence of accurate data. The same methodology can still be applied by making the pairwise comparison between alternatives based on decision maker's experiences. Incorporating many decision-makers will reduce the decision subjectivity as well. We found bulk silicon PV modules to be the most appropriate for estimating the driving range for a given set of PV modules and batteries. PV modules are an excellent option powering the next generation of small, lightweight, and aerodynamically efficient vehicles EVs. Future designs for EVs, PV modules and energy storage units are expected to lead to the commercialization of low-cost EVs powered exclusively by PV for the entire EV transport industry, making it fully sustainable.

CHAPTER THREE

COMPARISON OF ANALYTICAL HIERARCHY PROCESS AND FUZZY AXIOMATIC DESIGN FOR SELECTING APPROPRIATE PHOTOVOLTAIC MODULES FOR ON-BOARD VEHICLE DESIGN

3.1 Introduction

Gasoline powered internal combustion engines have been the mainstay of the automobile industry for over a century. For example, the United States (US) transportation sector consumes approximately 71% of the total petroleum used in 2013 [42]. Unfortunately, this technology is now a fundamental hindrance to global economic growth and is entirely inadequate for meeting the long-term energy needs of a growing world economy.

The World's population will reach nearly 9 billion in 2040 [43], with a concurrent increase in the number of individuals who can afford vehicles. This population growth will in turn lead to an increase in energy demands, a problem further complicated by the expected increase in petroleum products combined with large and unpredictable fluctuations in availability.

* Abdelhamid, M., Qattawi, A., Singh, R., and Haque, I., "Comparison of Analytical Hierarchy Process and Fuzzy Axiomatic Design for Selecting Appropriate Photovoltaic Modules for On-board Vehicle Design", *Accepted in International journal of modern engineering*

Perhaps the greatest adverse effect to the earth's climate is the total energy-related CO₂ vehicular emissions released in that each vehicle emits around 5.1 metric tons of CO₂ annually [44]. Switching from the present transportation system to one that uses sustainable, renewable, and clean energy sources will ensure US energy independence with a corresponding low environmental impact. Solar generated electricity is a prominent candidate for replacing current US energy supplies because of its clean nature, abundance, and supply of inexhaustible and cost free sunlight. Solar electricity could be generated by photovoltaic (PV) cells, which is a specialized semiconductor diode (PN-Junction) that converts electromagnetic radiation near the visible range into direct current (DC) electricity.

The PV module is a packaged assembly of individual PV cells. The cost of PV modules has declined significantly over the past 20 years, from \$5.7 per watt in the early nineties to approximately \$0.65 per watt currently [45]. The solar electricity cost will be competitive with other sources of energy by 2020 [46]. As such, the cumulative installed solar PV capacity is firmly moving to the terawatt scale and it is a prominent candidate to solving 21st century energy challenges [47]-[51]. The continuing increases in PV cell efficiencies [52], improving manufacturing and inspection technologies to make defect-free PV modules [53], coupled with reductions in cost are made PVs particularly useful in powering the next generation of individual transportation solutions.

The PV modules can provide energy to the vehicle via either on-board or off-board applications. In off-board applications, the PV is the source of energy for the charging station. In on-board applications, the PV modules are vehicle mounted either to assist in

propulsion or to run a specific vehicle application. Applications for on-board PV modules have been the subject of much research. The approaches vary in terms of the configuration and the specifications of the system [54]-[58].

Thus far, however, no research has been undertaken to determine the decision-making methodology for selecting the best commercial PV module type for on-board vehicle applications. The objective of this chapter is to provide an overview of different commercial PV module options to power vehicle application, and that of the decision-making criteria for selecting the optimum PV module types for on-board vehicle applications.

In this work two different decision-making methodologies are proposed: the analytical hierarchy process (AHP) [59], and the fuzzy axiomatic design (AD) [60], [61]. In both approaches, the quality function deployment (QFD) [62] is incorporated as the input stage to capture customer requirements for vehicle application with PV module capabilities. The novel use of these approaches will benchmark each other to minimize subjectivity, which usually is the most difficult challenge. This chapter is organized as follows: a background of AHP, fuzzy AD, and QFD are presented in Section 3.2, the methodologies are presented in section 3.3. Sections 3.4 and 3.5 discuss the results and provides a comparison between both approaches and the summary is presented.

3.2 Background of AHP, Fuzzy AD, QFD

The AHP and fuzzy AD are multi-criteria decision-making (MCDM) methods used to evaluate multiple and conflicting criteria. Selecting the best PV module for vehicle application shares the common MCDM problem characteristics [63] in that the conflicting objective or attribute criteria, and the incommensurable unit of measurements, require choosing a solution from a list of alternatives.

The AHP lets decision makers to structure the decision-making case in attribute hierarchies. These establish a relationship between objective function and criteria in the first hierarchy level and between the criteria and alternatives in the second. The AHP is superior in that it combines both qualitative and quantitative approaches. In the qualitative sense, it decomposes an unstructured problem into a systematic decision hierarchy, followed by a quantitative ranking using numerical ranks and weights in which a pairwise comparison determines the local and the global priority weights to obtain a ranking of proposed alternatives.

Some of the most recent applications of AHP are in ranking various renewable and non-renewable electricity production technologies [64], in selecting the most appropriate package of solar home system for rural electrification [65], in selecting the solar-thermal power plant investment projects [66], and in evaluating different power plants [67]. We used AHP to rank the different micro-crack non-destructive inspection tools for automated PV production stages [68].

Designers can use the AD approach to create a theoretical foundation based on logical and rational thought process to reduce the random search and trial-and-error process, and determine the best design among those proposed designs [60]. The most important concept in AD is the existence of the design axioms [60], [61]. The first axiom, which is the independence axiom, maintains the independence of functional requirements (FRs). The second axiom is the information axiom, which involves minimizing the information content. The FR is the minimum set of independent requirements that the design must satisfy. The first axiom states that design solution should provide such that each one of the FRs do not affect the other FRs. The second axiom provides the theoretical basis for design optimization by providing a quantitative measure of the merits of a given design. The design with the least information content is the best choice. The AD has been recently applied to a fuzzy environment in which there is fuzzy instead of precise data. Some of the applications of fuzzy AD to decision-making problems were selected from renewable energy alternatives [69]; evaluation energy policies [70], ergonomic compatibility evaluation of advanced manufacturing technology [71], and for the best green supplier manufacturing companies [72].

The QFD [62] is a method that the designer may use to develop a new product or service by learning about customer needs, which in QFD is known as the voice of the customer (VOC). The aim of QFD is to incorporate the VOC into the engineering characteristics of a specific product or a service. The planners can then prioritize each product or service attributes to set the levels necessary for achieving these characteristics. The QFD tool has been used for many different applications [73]. Some authors have

been used QFD with the AHP tool for various situations as reviewed in [74]. The QFD and AHP combination are implemented as decision-making tool for selecting materials for automobile bodies [75] and for developing a knowledge-based system to design an automotive production line [76].

Kahraman and his colleagues [77] undertook a comparative study of fuzzy AHP and fuzzy AD and used this approach for selecting the best renewable energy sources, both of which were used in a fuzzy environment, with all evaluations based on expert linguistic terms or fuzzy numbers. The proposed approach goes beyond that work. Unlike conventional fuzzy studies, (i) the AHP and fuzzy AD are used for the PV module selection for on-board vehicle application; (ii) the pairwise comparison in the AHP depends on data collected from PV manufacturers' datasheets and not numbers from experts as in typical fuzzy AHP. (iii), the fuzzy data applied to AD is from the same dataset, which the authors collected from PV manufacturers; (iv) and the authors conduct the comparative study between the two approaches after adding the QFD as the input stage. There are many other MCDM models, all of which have their strengths, weaknesses, and areas of application, and none of which is truly superior [78].

Thus far, no MCMD has been applied to this current problem and the proposed approach will fill this gap in the literature. In this study, the AHP and the fuzzy AD are chosen as the proposed decision-making methodologies for these reasons; (a) it allows selection the optimum PV module type for on-board vehicle use, which is an MCMD problem with conflicting objectives; (b) it use precise data for a robust pairwise comparison of the AHP decision tool; (c) the fuzzy AD approach can be used to conduct

evaluations in fuzzy environment to capture the entire commercial PV market data; (d) the QFD can be incorporated in the input stage for both approaches reflecting the VOC and reducing the subjectivity of traditional methods; and finally (e) the authors can use the gathered data from PV manufactures' datasheets in proposed evaluation thus reducing subjectivity and permits benchmarking both approaches using data that is both precise and fuzzy.

3.3 Methodology

3.3.1 PV Module Types

Though more than 25 PV cell types exist [52], not all are available for commercial use. They are also unsuitable for vehicle applications because of cost, availability of raw materials, reliability, stability, and lifetime limitations. Here, the authors outline the different commercial PV technologies, emphasizing the strengths and challenges of each PV module type. This overview is essential for decision-making as it highlights the possible search space for the MCDM tools. The current commercial PV modules are bulk Silicon (wafer based) or thin films could be deposited on rigid or flexible substrates.

The total global PV module production in 2013 was 40 GW, the Silicon bulk PV module (mono-crystalline silicon (Mono-Si) and multi-crystalline silicon (Multi-Si) shipped was 89.58% of a total, with thin films (cadmium telluride (CdTe), copper indium gallium selenide (CIGS), and amorphous silicon (a-Si)) solar cells comprising the

remaining 10.42% [79]. Mono-Si and Multi-Si PV modules are advantageous in that they use silicon, the second most abundant element in the earth's crust. Silicon is also a well-researched and understood element in the periodic table due to its use of \$350 billion semiconductor industry. The dominance of silicon as a PV material is predicted in [80], [81], that abundance of raw material is a key requirement for terrestrial PV.

CdTe PV modules have the inherent deficiency of using Cd, which is toxic combined with a limited supply of Te [48]. To handle CdTe module toxicity, some companies recycle this material, but reclamation is both difficult and expensive. CIGS PV modules are much safer than CdTe because of the miniscule amounts of cadmium sulfide. The most critical drawback of CIGS modules is the very limited supply and expense of Indium, which constitutes the primary element of this module [48].

The advantages of a-Si PV module, in addition to their silicon abundance, is that the manufacturing techniques and tools used to deposit a-Si and related materials are similar to liquid crystal display (LCD) manufacturing. a-Si PV modules also have the advantage of operating well in both hot and cloudy climates. a-Si PV modules are also compatible with building-integrated PV. The disordered structure of a-Si initially degrades the a-Si PV module efficiency, which stabilizes at some point. The efficiency of stabilized commercial single junction a-Si PV modules is much lower than the single junction CdTe and CIGS PV modules. However, the performance of commercial double junction a-Si PV modules is comparable with CdTe and CIGS PV modules.

In this study, the top five commercial PV types are analyzed. Other PV module types as (multi-junction cells and single junction Gallium arsenide (GaAs), organic photovoltaic

(OPV), dye-sensitized solar cell (DSSC), and quantum dot cells) are excluded in this study for the following reasons: although the GaAs is the most efficient PV type, it is also the most expensive, mainly use in space applications. The relatively low efficiencies of OPVs, DSSCs, and quantum dot cells make them particularly poor candidates for the large-scale PV generation of electricity. Specifically, DSSCs do not exceed 7 cm^2 , which makes it very difficult to build large-area modules because of the large amount of energy lost during connection [49]. OPV is unreliable with a cell lifetime of only 3 to 4 years [82] compare to other PV types, which have a 20-30 year life span.

In this work, six evaluation criteria are proposed based on QFD as will show later for benchmarking and evaluating PV modules for vehicle applications as below:

- (i)- Power density, which is defined as PV module power generated per area (W/m^2) at standard test conditions (STC). Limited vehicle surface areas make higher density modules are preferable. This factor is related to PV module efficiency, which is the PV watt generated per area divided by 1000 W/m^2 at STC.
- (ii)- Specific weight, which is the PV module Watt generated per weight (W/kg). A high specific weight is required, since the installation of PV modules adds extra weight of an automobile body and increases the vehicle curb weight, affecting vehicle performance.
- (iii)-Power temperature coefficient (PC), is measured as $-\%$ per $^\circ\text{C}$, this is related to PV module reliability. Temperature increases reduce the performance of all PV module types. The module with a lower PC factor is more reliable.
- (iv)- Flexibility, flexible substrates are used with thin films technology, making the installation of PV modules on the vehicle body easier.

(v)- Health and Safety Consideration, using silicon obviates any supply chain difficulties. Unlike silicon, Cd based CdTe PV modules present environmental and human hazards. For that, the CdTe module could be banned in future in few countries and is not even a preferred choice worldwide [83].

(vi)- Life cycle cost (LCC) of electricity is defined as the total cost of PV system per total energy generated through PV system in the life cycle in unit (¢ per kWh). Since the constraint, here is the installation surface area of the vehicle.

The LCC is calculated using Equations (3.1), (3.2) [84], [85]:

$$LCC (\$/kWh) = \frac{\text{Cost} \sum [\text{PV Module} + \text{installation} + \text{land} + \text{Energy storage} + \text{maintenance}]}{\text{Total energy generated}} \quad (3.1)$$

The total energy generated through a system lifetime is calculated as Equation (3.2).

$$\text{Total energy generated} = I \times \eta \times PR \times LT \times A \quad (2)$$

Where, I is the irradiation ($kWh/m^2/yr$) which the average energy flux from the sun and depends on the installation location. η is the lifetime average module efficiency (%), PR is the performance ratio, LT is the system lifetime in a year, and A is the total module area (m^2).

In order to adequately evaluate the PV options, the following constraints (geographical location, mounting configuration, and tracking/orientation option) should be identical in any comparison. In addition, the structural design of the solar panels should fulfill many load demands since the solar panels may be subject to strong wind, snow, and many other

effects. Aly and Bitsuamlak [86], [87] have evaluated wind induced pressure on solar panels, which are beyond the scope of this work. To evaluate the different PV module types, the authors collected the required performance specifications for each PV module that reflect each of the proposed evaluation factors using datasheets from many PV manufacturers (See Figures 3.1 and 3.2. The data gathered from 27 PV manufacturers (8 Multi-Si, 8 Mono-Si, 3 a-Si, 3 CdTe, and 5 CIGS) reflects the current PV market. Based on Figures 3.1 and 3.2, the results for power density, specific weight, and PC factors are tabulated in Table 3.1. Table 3.1 data have manufacturers' data on the minimum, maximum values, and the average value for each PV type.

The flexibility and health/safety concern are non-numerical values. The bulk-silicon PV types are rigid, and the thin film PVs deposited on rigid or flexible substrates depend on packaging. The results in regards to LCC of electricity (see Table 3.2) are calculated with the following assumptions; the cost of land is not factored since the PV modules mount on the vehicle body. In addition, the installation, maintenance, and energy storage costs were assumed similar for all PV module types. The current prices of commercial PV modules (excluding tax) in (\$/W) for the bulk silicon solar modules are 0.55, 0.657, and 0.92, while for thin film solar modules are slightly less as 0.49, 0.583, and 0.87 for low, average and, high scenarios respectively [88]. These prices are set by the manufacturers, with Chinese made PV modules the least expensive.

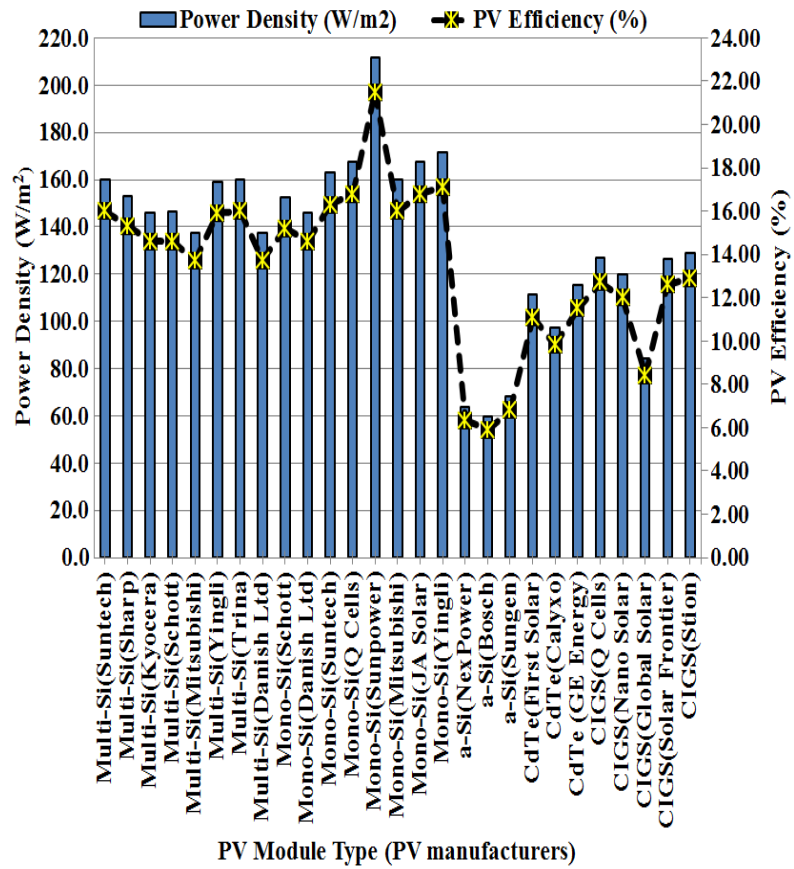


**Figure 3. 1 Power Density and Efficiency Factors of the Commercial
PV Module Types**

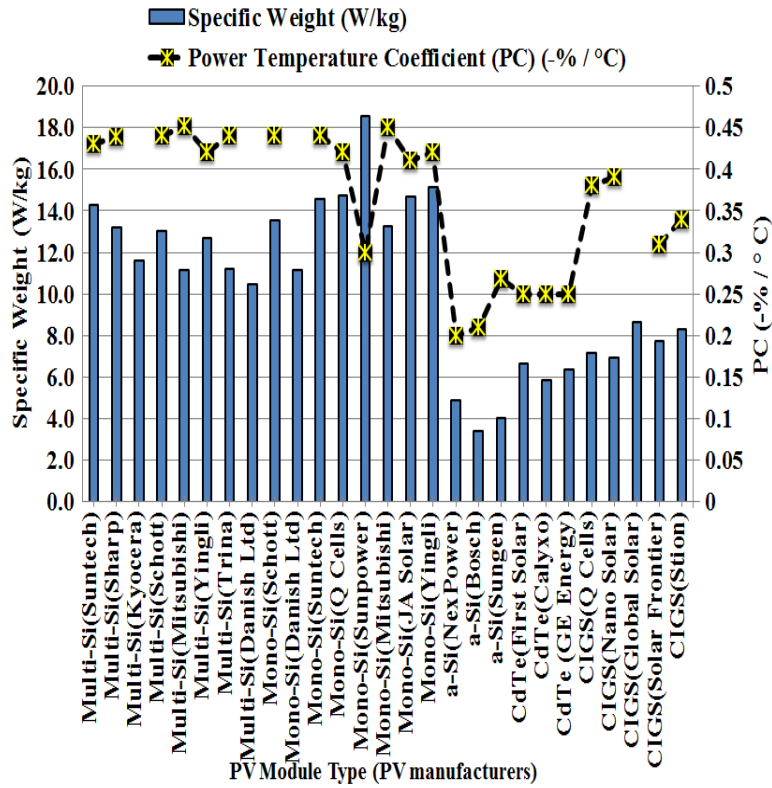


Figure 3. 2 Specific Weight and PC Factors of the Commercial PV Module Types

Table 3. 1 Performance Data from PV Manufacturers' Datasheets and LCC Results

PV Module Type	Power Density (W/m ²)			Specific Weight (W/kg)			PC (-%/°C)			Life cycle cost (LCC) of electricity(¢/kWh)		
	Min.	Max	Avg.	Min.	Max	Avg.	Min.	Max	Avg.	Min.	Max	Avg.
Multi-Si	137.2	159.8	149.9	10.5	14.3	12.2	0.42	0.452	0.4368	1.570	2.625	1.875
Mono-Si	146.1	211.6	167.5	11.1	18.5	14.4	0.3	0.44	0.411	1.557	2.603	1.859
a-Si	59.4	68.2	63.7	3.4	4.9	4.1	0.268	0.2	0.226	1.394	2.477	1.660
CdTe	97.2	115.3	107.9	5.8	6.7	6.3	0.25	0.25	0.25	1.389	2.465	1.652
CIGS	84.1	128.9	117.1	6.9	8.6	7.8	0.31	0.39	0.355	1.389	2.465	1.652

Table 3. 2 LCC Calculations with Respect to Multi-Si PV Module

PV Module Type	Module price (\$/W) (excluded tax) [88]	Module price after 7 % sales tax (\$/W)	PV Module Average Power Density (W/m ²) [Table 1]	Cost PV Module (\$/m ²)	PV Module Average initial efficiency (%) [Figure 1]	PV Module Average Lifetime efficiency (%)	Total energy generated (KWh)	Cost PV per Total Energy (¢/KWh)
Low LCC Scenario	0.550	0.589	149.900	88.216	14.900	13.877	5620	1.570
Average LCC Scenario	0.657	0.703	149.900	105.378	14.900	13.877	5620	1.875
High LCC Scenario	0.920	0.984	149.900	147.562	14.900	13.877	5620	2.625

The cost of PV module per energy generated is calculated using three scenarios as best, intermediate, and worst-case scenarios. The calculation is based on Equations 3.1 and 3.2, and the assumed parameters are $I=1800 \text{ kWh/m}^2/\text{yr}$ based on US location, $PR=0.75$, $n=30$ years [89]. η is based on degrade over the system lifetime by 0.5% (relative to the initial efficiency) per year [89]. The initial PV efficiency is considered equal to the average PV efficiency in Table 3.1. Example of LCC calculations are shown in Table 3.2 with respect to Multi-Si PV module, the LCC values for all other PV types is done in similar way and tabulated in Table 3.1.

3.3.2 The QFD & AHP Approach

The incorporation of the QFD and the AHP are done through three-step process to overcome the well-known dependence of AHP on subjective pairwise comparisons. A knowledge-based database is used in the pairwise comparison, where the comparison of each criterion based upon manufacturers datasheets. To make the pairwise comparison

more robust, the authors compared the average values from different manufacturers of each PV module type in Table 3.1. Finally, the QFD is incorporated as an input stage to the AHP to assign weights per vehicle customer preference. Figure 3.3 shows the proposed OFD/AHP combination procedure. The QFD structure is in Table 3.3. There are five QFD components. The first is the engineering requirements specified by the “How” window, which are the PV FRs.

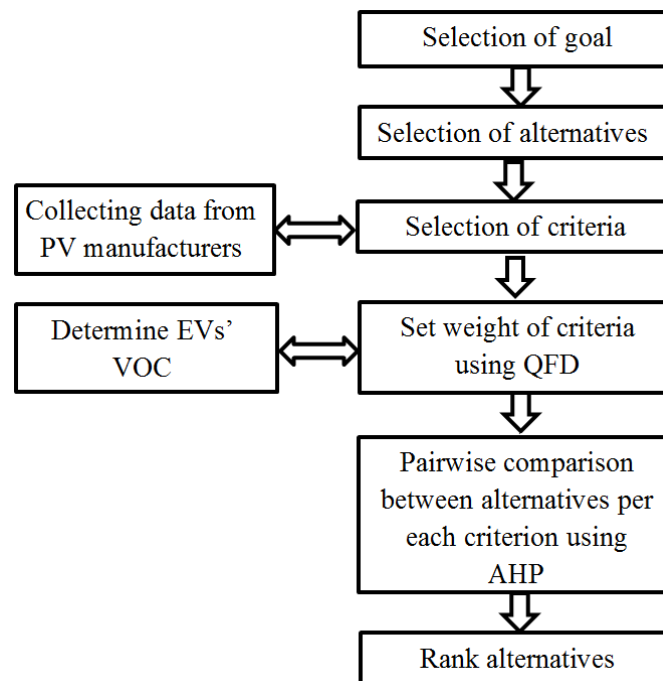


Figure 3. 3 Steps of Applying QFD with AHP

Next is the customer need (VOC) represented by the vehicle requirements and specified by the “what” window. Third are the weights for customer needs shown as an importance percentage of specific vehicle requirements, with the total importance weights for all VOC requirements equaling 100%. Fourth is the combined HOWs and WHATs using a relation matrix of three scores (1, 3, and 9) with score 1 the lowest

between the specific column in the “How” window and the specific row in the “What” window, score 3 the mean medium impact and score 9 a strong impact.

Table 3. 3 Proposed QFD Structure

Relative Weight (%)	Customer Importance	Functional Requirement (FR) EV Customer Needs	Power Density (W/m ²)	Specific Weight (W/kg)	Reliability to Temp.	Envir./ health/ safety	Flexibility	Cost (\$/kWh)
20	3	High Range	9	3	3			
30	2	Help Save Money	9	3	3			9
35	1	Eco-Friendly				9		
15	4	Aesthetic (Good looking)					9	
		Evaluation	450	150	150	315	135	270
		Relative Evaluation (%)	30.6	10.2	10.2	21.4	9.2	18.4

For instance, a score of “35” is assigned for “Eco-friendly” as a high valued customer need for those EVs. “Eco-friendly EV” customer requirement have only strong impact with environmental, health, and safety concern factor. Correspondingly, the rest of the relationship matrix completed. Although these values cause decision inconsistency, it can be reduced by establishing many customer-oriented questionnaires and by incorporating a team of engineering, marketing, and research professionals. Finally, is the outcome at the bottom of the QFD matrix of the relative evaluations (weights). In the present approach,

the QFD output correlates the PV module FRs with vehicle requirements. The returned relative evaluations (weights) are the relative importance of all PV module requirements and are the input for the AHP stage. The evaluation is calculated using Equation (3.3) [21]:

$$Evaluation = \sum \alpha_i \beta_{ij} \quad (3.3)$$

Where, i =number of rows (from 1 to 4), j =number of columns (from 1 to 6), α is the importance, β is score in specific Hows. The evaluation in the first column (power density) is calculated as $= 20 \times 9 + 30 \times 9 = 450$. The relative evaluation is calculated as the specific evaluation divided by the sum of all evaluations equal to $450/1470 = 0.306$ (30.6%).

The last step in this approach entails using AHP to rank alternatives. Figure 3.4 shows the construction of the problem as top-level hierarchy, as the objective function of the problem. The second level represents the criteria for evaluations, which is the same “Hows” window in the QFD stage. The third hierarchy level is the alternatives, which are the five PV module candidates.

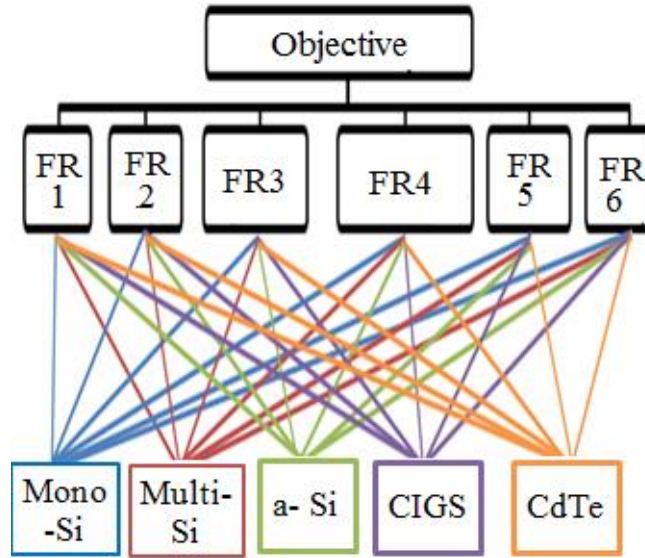


Figure 3. 4 Hierarchical Problem Construction

The proposed AHP model evaluates the alternatives different from traditional AHP [59]. First, the authors create the relationship between the objective function and each criterion in the first hierarchy, giving related weights for each criterion, which is the output of QFD stage. Second, the pairwise comparison matrix A in traditional AHP in the second hierarchy is obtained based on the decision maker's judgments a_{ij} from scale 1-to-9 using Equation (3.4) [59]. In the proposed methodology, the decision matrix based on averaging values from actual manufactures datasheets in Table 3.1. Table 3.4 shows an example of comparison of PV alternatives with respect to power density criterion. The comparison between Mono-Si and Poly-Si yielded a value of "1.117".

$$A = \begin{bmatrix} 1 & a_{12} & \dots & a_{1n} \\ a_{21} & 1 & \dots & a_{2n} \\ \vdots & \vdots & \dots & \vdots \\ a_{n1} & \dots & \dots & 1 \end{bmatrix}, \text{Where } a_{ij} = 1 / a_{ji}, i, j = 1, \dots, n \quad (3.4)$$

Table 3. 4 Pairwise Comparison Matrix Related to Power Density

	Mono-Si	Multi-Si	a-Si	CdTe	CIGS
Mono-Si	1.0	1.117	2.629	1.43	1.552
Multi-Si	0.89526	1.0	2.353	1.28	1.389
a-Si	0.38037	0.42499	1.0	0.544	0.590
CdTe	0.6993	0.78125	1.8382	1.0	1.085
CIGS	0.64433	0.71994	1.6949	0.92166	1.0

Consistency index (C.I.) = 0.00

The average power densities from datasheets, listed in Table 3.1 for mono-Si and poly-Si equal to 167.5 and 149.9 W/m², respectively. By dividing these two numbers, the value of “1.117” is obtained (Table 3.4). All comparisons were performed in this manner. Although time consuming, the results are very accurate as no personal experiences of the designers are used. The consistency index (*C.I*) is calculated as Equation (3.5) [90].

$$CI = \frac{\lambda_{\max} - n}{n - 1} \quad (3.5)$$

Where, λ_{\max} is the maximal eigenvalue of comparison matrix and n is the number of attribute in the square matrix. In this case $n=5$ as shown in Table 3.4, since the authors depend only on the actual manufacturer datasheets, the calculated λ_{\max} is equal 5.00 and the *C.I* is equal 0.00 as shown in Table 4. In typical AHP, the conclusion about *C.I* can be

drawn comparing it by consistency ratio (CR) to check the judgment inconsistencies using Equation (3.6) [49].

$$CR = \frac{CI}{RI} \quad (3.6)$$

Where, RI is the random index, which is an experimental value depends on n . In this case, $n=5$, then $RI=1.11$ (The full table of RI value can be found in [90]. In typical AHP if the CI less than or equal 0.111, the decision maker accepts the results, but in the proposed methodology the CI is zero, which reflects the high accuracy of the methodology used in this study. The final step is to rank all the alternatives as shown in Figure 3.5. The results show that mono-Si PV modules rank first with a score of 22.9 of 100 points, followed by multi-Si modules with a score of 21.5 out of 100. The third, fourth, and fifth ranked PV modules are a-Si, CIGS, and CdTe, respectively. The sensitivity analysis of the problem is shown in Figure 3.6. It clearly indicates that the problem has conflicting objectives. For example, a-Si PV module has the best results in regards to PC factor and the worst in both power density and specific weight factors.

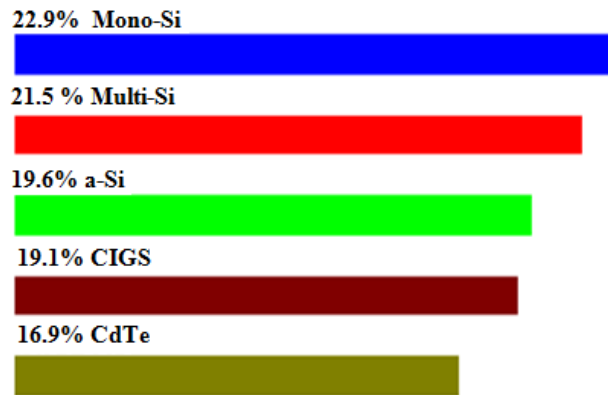


Figure 3. 5 Rank of Different PV Module Types for Vehicle Application using AHP/QFD

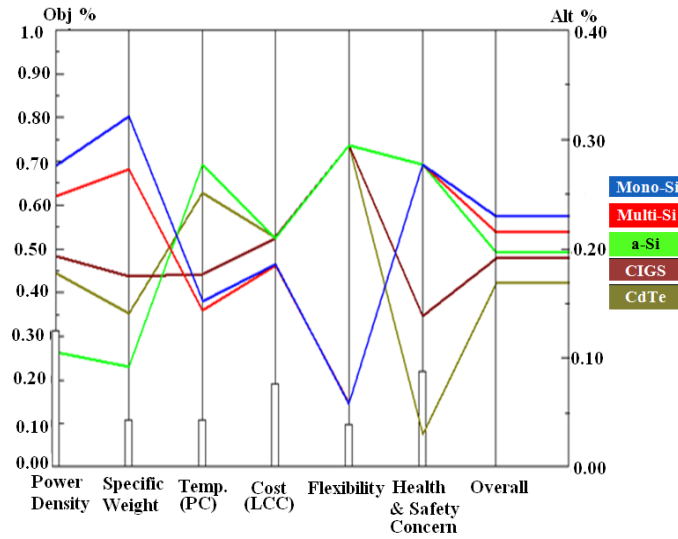


Figure 3. 6 Sensitivity Analysis of AHP/QFD Rank Results

3.3.3 The Fuzzy AD Approach

In the second decision-making methodology, the fuzzy AD combined with QFD is proposed. The method is based on independence axioms, with information axioms as the decision-selection tool.

Figure 3.7 lists the steps applied to the fuzzy AD method. The selection of the goal and alternatives are the same as discussed in the AHP decision-making method. Although the FRs are identical as in the QFD stage, the first axiom is satisfied. FRs are chosen to ensure independence from one another. The system range is set by converting the data in Table 3.1 to triangular fuzzy number (TFN) in Table 5. The maximum value is converted to a scale of 10 and the remaining values to scale from 0-10. The benefits are in two-folds: it allows benchmarking the AHP/QFD since it uses same data set; and provides a

robust decision process because it captures the entire commercial PV market data, and not just the average value used in pairwise comparison as in the AHP. Consequently, decision-makers have more freedom to determine which specific PV type satisfies the design range.

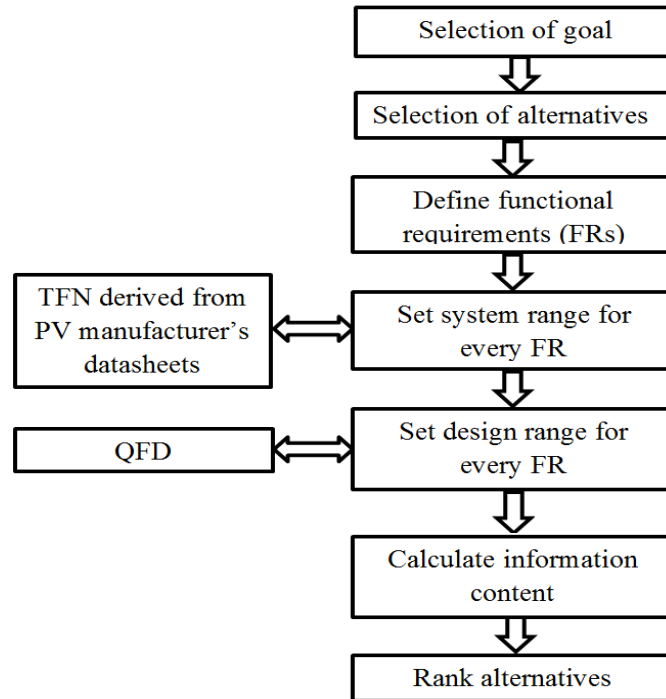


Figure 3. 7 The Proposed Approach for Fuzzy AD

Table 3. 5 System Range for AD Approach

Criteria	Power Density			Specific Weight			PC			Cost			Flexibility			Health and Safety Consideration		
	Min	Max	Avg	Min	Max	Avg	Min	Max	Avg	Min	Max	Avg	Min	Max	Avg	Min	Max	Avg
PV Types																		
Multi-Si	6.5	7.6	7.1	5.7	7.7	6.6	9.3	10.0	9.7	5.98	10.00	7.14	0.0	1.0	1.0	0.0	1.0	1.0
Mono-Si	6.9	10.0	7.9	6.0	10.0	7.8	6.6	9.7	9.1	5.93	9.92	7.08	0.0	1.0	1.0	0.0	1.0	1.0
a-Si	2.8	3.2	3.0	1.8	2.6	2.2	5.9	4.4	5.0	5.31	9.44	6.32	0.0	10.0	5.0	0.0	1.0	1.0
CdTe	4.6	5.4	5.1	3.1	3.6	3.4	5.5	5.5	5.5	5.29	9.39	6.29	0.0	10.0	5.0	7.0	10.0	10.0
CIGS	4.0	6.1	5.5	3.7	4.6	4.2	6.9	8.6	7.9	5.29	9.39	6.29	0.0	10.0	5.0	4.0	10.0	10.0

In Table 3.5, the flexibility is set to “0-1-1” if the module is rigid and set to “1-5-10” if it depends upon packaging. For the health and safety concern value “0” is the best, indicating little adverse environmental consequences. TFN can be defined by a triplet (n_1 , n_2 , and n_3) shown in Figure 3.8. The membership function $\mu(x)$ is defined using Equation (3.7) [91]. For, the design ranges for every FR, a wider selection is provided to choose the most appropriate alternative for each FR based on QFD. For (power density, specific weight, and flexibly) factors, the highest values are the best for the proposed application. While, for all remaining factors (PC, health& safety concern, and LCC) it is the opposite.

$$\mu(x) = \begin{cases} 0, & x < n_1 \\ \frac{x-n_1}{n_2-n_1} & n_1 \leq x \leq n_2 \\ \frac{x-n_3}{n_2-n_3} & n_2 \leq x \leq n_3 \\ 0 & x > n_3 \end{cases} \quad (3.7)$$

The proposed design ranges in this study are shown in Figure 3.9. The information content (I_i) for the specific (FR_i) is defined in terms of probability per Shannon's theory [92], in Equation 3.8.

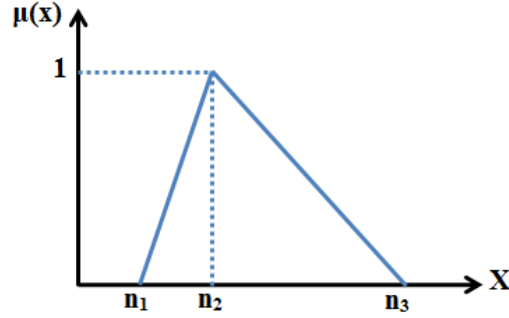


Figure 3. 8 Triangular Fuzzy Number

$$I_i = \log_2 \frac{1}{P_i} \quad (3.8)$$

Where, the information I is in unit of bits, P is the probability from the AD perspective P_i is the probability of achieving specific FR_i . The information content for the entire system is calculated using the Equation (3.9) [60], [61]:

$$I_{sys} = \sum_{i=1}^m I_i = -\sum_{i=1}^m \log_2 P_i \quad (3.9)$$

Where, m is the number of independent FRs. If the I approach is infinity, the probability is zero and the system will never function. If I is zero, however, the probability is that the system will function perfectly (Axiom 2). In the AD approach, the designer wishes a high probability of success in terms of design range (tolerance) and system range, which reflects overall system capability. The information content is calculated using Equation (3.10) [93].

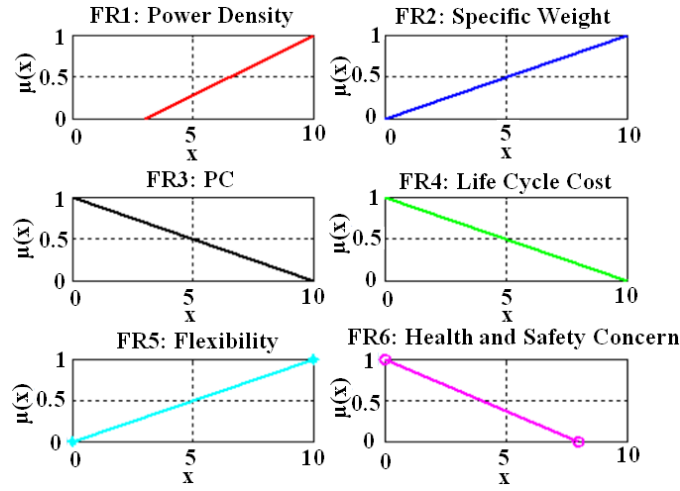


Figure 3. 9 Design Ranges for AD Approach

$$P_i = \frac{\text{Area of common range}}{\text{Area of system design}} \quad (3.10)$$

Here, the common range is the overlap between the design and system range. For example, the information content is calculated for the “FR3: PC” with respect to “a-Si PV module” as an alternative (in Figure 3.10), which indicates the design ranges (Figure 3.9) and system ranges (Table 3.5). By solving the intersection, the following parameters are determined:

$$(x_1, \mu_1) = (4.7159, 0.5284)$$

$$(x_2, \mu_2) = (5.4946, 0.4505)$$

$$A_{\text{common}} = 0.5559$$

$$P_i = \frac{0.5559}{\frac{1}{2} \times (5.9 - 4.4) \times 1} = 0.7412$$

$$I_i = \log_2(0.7412) = 0.432$$

The same procedure is repeated for each FR and each alternative. The calculations for all FRs with respect to all alternatives are tabulated in Table 3.6. In total, the mono-Si PV module is ranked first as it contains the lowest information content followed by the CIGS and Multi-Si PV modules, respectively. The a-Si and CdTe PV modules are fourth and fifth respectively. The green color in Table 3.6 indicates the best PV module option for specific FR.

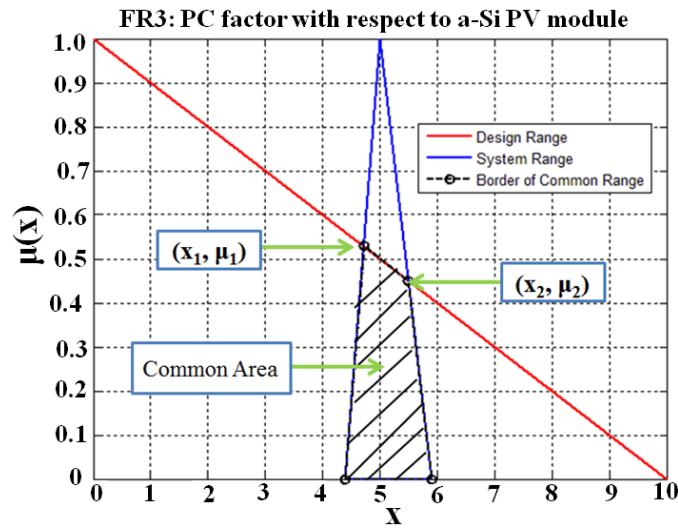


Figure 3. 10 FR3 (PC Factor) with Respect to a-Si PV Module

Table 3. 6 Information Contents for Alternatives

PV Type	Power Density	Specific Weight	PC	LCC of electricity	Flexibility	Health and Safety Concern	Total
Mult i-Si	0.26	0.175	3.89	1.43	4.32	0.02	10.1
Mon o-Si	0.12	0.08	1.76	1.4	4.32	0.02	7.7
a-Si	6.18	1.36	0.43	1.11	2.00	0.02	11.1
CdTe	1.01	0.84	1.15	1.06	2.00	5.05	11.1
CIG S	0.96	0.60	1.36	1.08	2.00	2.39	8.4

■ Green color indicates the lowest information content and the best option for specific FR

3.4 Discussion

Two decision-making methodologies are proposed to determine the optimum commercially available PV module type for use in vehicle design: (i) a QFD/AHP combination and (ii) a QFD/Fuzzy AD combination. The novel use of both approaches permitted a mutual benchmarking of each and minimal subjectivity, which is the most difficult challenge.

In both approaches, the QFD is incorporated to correlate the PV module FRs with vehicle requirements. Both are superior to current methods in that the evaluation depends on data collected from PV manufacturer datasheets reflects current PV market data, which yields a very robust methodology. The gathered data is used in a pairwise comparison between various alternatives in the AHP methodology and to derive TFN to

implement the system range for the fuzzy AD based approach to capture the complete commercial PV market. The results from the fuzzy AD approach agreed with the AHP results; for both approaches, the most suitable PV was mono-Si and the least suitable CdTe. The difference was that, in the AHP approach, the Multi-Si PV modules were Rank number 2 but in fuzzy AD the CIGS is ranked number 2. If the aesthetics are deemed less important as assumed here, then the crystalline PV is the most appropriate selection. A comparison of both approaches is provided in Table 3.7.

Table 3. 7 Comparison between AHP/QFD with Fuzzy AD/QFD

Methodology	AHP/QFD	Fuzzy AD/QFD
Approach	Depends upon pairwise comparison based on average value obtained from many PV manufacturer's data sheets	Depends on all ranges obtained from PV manufacture Datasheets. Fuzzy data is from the minimum, average, and maximum values in all datasheets.
Way to minimize subjectivity	Each criterion is compared based on actual manufacturer datasheets and not anecdotal decisions. To improve the pairwise comparison, many datasheets are collected from different manufactures with the average for each criterion calculated for each alternative. The QFD is used to weigh all criteria based on customer need and incorporated into the AHP stage.	The FRs and the design range are derived in the QFD stage. System range is derived from manufacturer datasheets in TFN form.
Strength	The inconsistent error is too low. Accurate data are needed to improve the selection of the best PV module.	The robust decision-making tool works in a fuzzy environment

3.5 Summary

This chapter is an overview of the available commercial photovoltaic (PV) module options for powering on-board vehicle applications. We used two decision-making methodologies to determine the evaluation factors and the decision-making criteria necessary for assessing the suitability of the particular PV module type. In both (i) the analytical hierarchy process (AHP), and (ii) the fuzzy axiomatic design (AD), the authors used at the input stage, quality function deployment (QFD) to determine customer requirements for a vehicle with PV module capabilities. This approach is innovative in that evaluation depended upon data collected from PV manufacturers' datasheets. This approach is novel in that (i) the AHP and fuzzy AD are used as decision-making methodologies to select the optimum PV module type to power a vehicle, (ii) compared the QFD & AHP hybrid approach with the QFD & fuzzy AD hybrid approach, and (iii) used commercial PV market data in for comparison, and not from experts as in traditional research. A benchmark of both approaches determined differing results if the evaluation was conducted with both methods using identical data with different natures (i.e. Precise vs. fuzzy). Results show that for on-board vehicle applications, the most suitable PV module option is mono-crystalline silicon and the least suitable option is cadmium telluride.

CHAPTER FOUR

REVIEW OF MICRO CRACK DETECTION TECHNIQUES FOR SILICON SOLAR CELLS

4.1 Introduction

Globally, the cumulative installed solar photovoltaic (PV) capacity has topped the 100-gigawatt (GW) milestone [94]. The current growth in the PV is not confined to any one region of the globe, however, but rather distributed worldwide [95]. As compared to the 35 GW markets of 2013, the PV market with a value of \$155.5 Billion is projected to grow to 61.7 GW by the year 2018 [96]. The past success of the PV industry indicates that, for sustained global economic growth, PV offers a unique opportunity to solve the 21st century's electricity generation problem because solar energy is essentially unlimited and PV systems can provide electricity for rich and poor, alike [97]. The average selling prices of PV panels have dropped to \$0.65/Wp [98].

Silicon based solar cells have dominated the PV market and accounts for about 90 % of the PV market. For example, in 2012, silicon bulk PV module shipments represented 89% of the total amount of 31.3 GW, while thin films (CdTe, CuInSe/CuInGaSe, and a-Si) solar cells contributed to the remaining 11% [99].

[#] © [2014] IEEE. Reprinted, with permission, from [Abdelhamid, M.; Singh, R.; Omar, M, Review of Microcrack Detection Techniques for Silicon Solar Cells, *IEEE Journal of Photovoltaics*, Jan/2014]

Dominated by the second-most abundant element in the earth's crust [100], the PV industry is based mostly on mono- and poly-crystalline silicon solar cells and is firmly moving toward the terawatt scale [101]. The highest efficiencies of silicon solar cells and silicon PV modules are 25 % [102] and 21.5 % [103], respectively.

Researchers have been investigating the possible solutions to reduce the gap between the efficiency of a silicon solar cell and that of the PV module. One possibility entails eliminating the shunts, which are internal short-circuits where localized current significantly exceeds the homogeneously flowing current. Other solutions consider reducing defects that affect the quality of the solar cell or reduce energy conversion efficiency of the PV module. Fig. 4.1 shows some examples of the defects in solar cells [104]-[113], categorized as either processed induced or material induced.

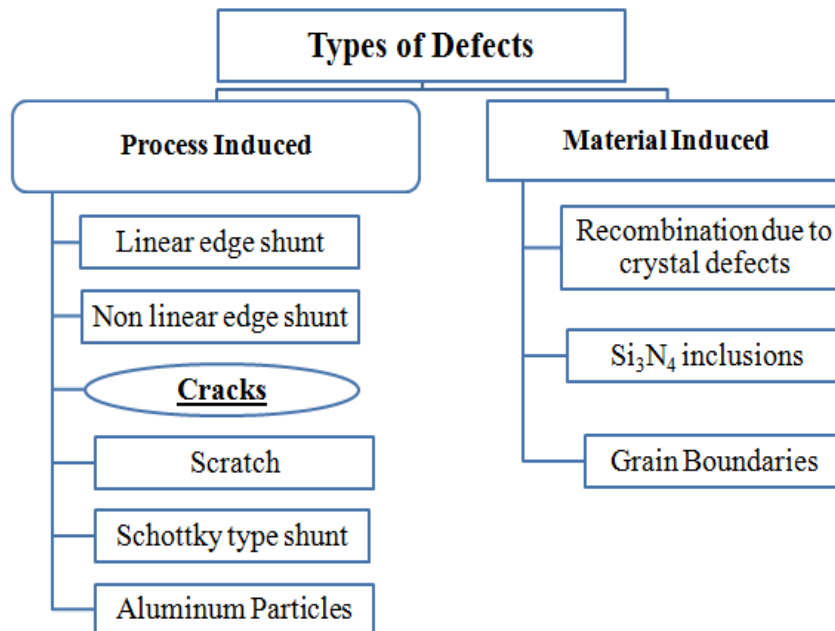


Figure 4. 1 Some types of cell defects in wafer based silicon solar cells

In this chapter, we have focused solely on defects caused by micro cracks because wafer breakage decreases the optimal utilization of the production line and leads to the waste of costly production material. The losses resulting from micro crack defects can be as high as 5–10% in a typical manufacturing facility [114]. According to 2011 production costs and wafer prices, 1% wafer breakage rate costs about \$656,700 annually for an 80 Megawatt production line [115]. Cracked solar cells lead to the loss of yield in manufacturing production line with a consequent increase in production costs.

The micro crack defects not only reduce cell efficiency in the field, but also reduce the cell reliability. Due to the economic importance of micro crack defects, we have reviewed the current inspection techniques that have been used to detect micro crack defects. Though the authors [116] have published a review of micro crack detection methods, it has a limited technical scope. Specifically, they did not (a) address other types of defects that are related to the origin of cracks, (b) classify cracks, (c) engage in a fundamental comparison between various methods, (d) explain all methods for crack detection, and (e) most importantly provided no description of a method to select the best tool for micro crack detection.

In this chapter, we have reviewed six integral aspects regarding micro cracks: (i) as part of the defects of silicon wafers; (ii) their origins, (iii) their root causes, (iv) their full impacts in terms of electrical and mechanical issues, (v) their classification, and (vi) the suitable methods used to detect various types of micro-cracks. For the first time, we have used the multi-attribute decision-making tools using the analytical hierarchy process

(AHP) to assist in the evaluation and selection of currently available inspection tools used for micro crack detection.

In section 4.2, we discuss the origin and root causes of micro cracks followed by the classification of cracks in section 4.3. The impact of the micro cracks on the mechanical and electrical properties of solar cells is discussed in section 4.4. A survey of the main techniques used to detect the micro cracks is presented in section 4.5. The advantages and disadvantages of various non-destructive testing (NDT) techniques are discussed in section 4.6. The approach used for selecting inspection tools is discussed in section 4.7, and we sum up the summary in section 4.8.

4.2 Origin and Root Causes of Micro Cracks

The silicon atoms in a crystalline silicon solar cell arrange in a diamond lattice unit cell with a lattice constant equal to 0.357 nanometers. The diamond-crystal lattice is characterized by four covalently bonded atoms. The fracture in PV cells occurs when the energy available for crack enlargement is sufficient to overcome the resistance of the material. The typical thickness of silicon wafers used for solar cell applications is around 180 μm . These wafers are also quite fragile in that the silicon material used in their construction is most brittle at room temperature, and is characterized by two principle planes of cleavage: $\{111\}$ and $\{110\}$ [117], [118], and [119]. In various studies undertaken to observe the direction of crack propagation in these materials, the preferred propagation direction was in the $\langle 110 \rangle$ direction on both planes [118].

The cleavage plane $\{111\}$ is the easier plane in which a crack may propagate as it has the lowest energy and the lowest fracture energy, which for this plane, is reported as 2.2 J/m^2 . The energy needed for fracturing silicon material with defects is even lower [119], [120]. In both poly and single crystalline silicon solar cells, crack propagation in the direction of depth of the wafer typically either terminates or is strongly reduced at the interface between the silicon layer and back contact layer of Al because Al–Si eutectic layer has high fracture toughness [121], [122].

The thermal stress generated during various thermal processing steps is the main cause of microcracking. Fig. 4.2 shows the main processing steps used in the manufacturing of crystalline and poly silicon PV modules. The feedstock is melted at high temperatures. Overly long melting and holding periods combined with the high temperatures prior to crystallization can lead to higher impurity transfer between the ingot and crucible. During the block sawing stage, the produced heat can cause thermally induced stress, which in addition to the sawing forces can cause the initiation and propagation of cracks, mostly particularly from the saw damages to the block [123]. Micro cracks are usually introduced at the wire sawing stage of blocks/ingots [124]. If the cracked wafers are processed as normal wafers, more cracks occur introduced during the thermal processing steps used in the cell production. The biggest challenge is the detection of micro cracks generated during this sawing process, since these defects are hidden within the bulk of the wafer.

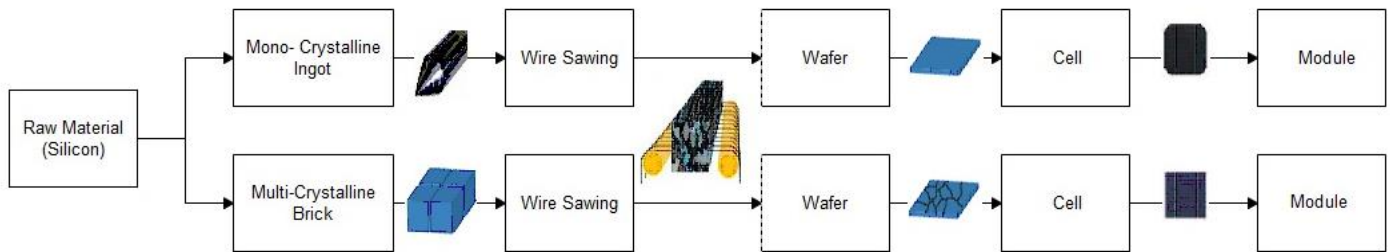


Figure 4. 2 Key processing steps used in manufacturing of crystalline and poly silicon PV modules

Saw-damage etching, a procedure performed in order to remove the surface damage caused by wire sawing, is another production process that causes micro cracking [125]. Different methods for chemical etching and texturing are used in solar cell manufacturing. In their study of the effect of saw-damage etching on micro cracks, Larsson *et al.*, [126] reported that neither alkaline nor acidic saw-damage etching increased the micro cracks length, but did decrease the shallow parts of the cracks since the surrounding silicon is etched away. If the initial crack is large enough, the crack can widen and deepen after etching, possibly by etching the edges of the fracture.

The etching time and consequently the etching depth is a major process parameter influencing the mechanical stability of the wafer [127], [128]. In [127], the authors reported alkaline etching and diffusion processes enhance the mechanical stability by approximately 11 %, and that mechanical edge isolation by sawing and contact formation led to a reduction of approximately 10-30% in the mechanical stability. With the trend to reduce the wafer thickness, the problem of over- etching will be more challenging since the stability of the wafer will be reduced. If the wafers contain micro cracks the problem

will be more critical and increase the breakage rate particularly where the screen printers are involved. Another important source of micro cracks is the physical stress generated during transportation [129] and handling [130], [131].

4.3 Classifications of micro cracks

The classification of micro cracks can be based upon either the crack direction [118], or the propagation speed [119]. In this chapter, we have classified cracks as either macro or micro cracks (μ -cracks) according to the crack width sizes. The crack with size smaller than 30 μm in width is usually referred to as a μ -crack [132]. The cracks are further classified according to their position as either facial or sub-facial cracks. The classification scheme is shown in Fig. 4.3.

Cracks occurring upon the surface of a silicon wafer are referred as facial cracks. Depending on the size, it is difficult to quantify these facial cracks by the naked eye. Cracks that lie beneath the surface of a wafer or either start on the surface and propagate in the depth direction are referred as sub facial cracks. Based upon the depth of the crack, sub facial cracks can further be classified as either deep-layer or shallow-layer cracks.

4.4 Impact of the micro cracks on the performance and reliability of solar

Micro cracks affect the electrical and mechanical properties of solar cells. Here, we discuss how these cracks affect the performance and reliability of solar cells.

4.4.1 Impact of micro cracks on the electrical characteristics of solar cells

In their study of solar cell cracking, Breitenstein *et al.*, [104], [133] reported that such cracks could act as a linear or nonlinear edge shunt, and that cracks in processed solar cells led to a weak nonlinear edge recombination current, similar to nonlinear edge shunts. However, micro cracks present in the starting wafer or occurring during processing prior to screen-printing metallization, may behave as severe ohmic shunts.

The faulty cell or group of cells can generate hot spot heating problems in a module, which occurs when the operating current of a module exceeds the reduced short circuit current of faulty cell. Here, the cell is forced into reverse bias and must dissipate power. Indeed, if the dissipation power is great enough, this reverse biased cell can overheat and melt the solder or cause deterioration of the backsheet. Hot spot cells either exhibit low shunt resistance where the reverse-bias performance is current-limited or high shunt resistance where the reverse-bias performance is voltage-limited [134].

To determine the influence of the position of the cracks on the electrical parameters of the individual cells, Grunow *et al.*, applied artificially varying cracks patterns to single cell modules [135]. If the crack were parallel and centered between the bus bars, a mere

power drop of less than 4% occurred. Most strikingly, however, if the cracks were parallel on both sides of the both bus bars a substantial power drop of 60% occurred. Similarly, in their detailed study of micro cracks, Köntges *et al.*, concluded that if the location of the cracks is parallel to the bus bar significant reduction of the module power output is observed [136], [137]. Similarly, in their study of the direct impact of micro cracks on the reliability of solar cells, they observed that the power stability of the PV module is directly related to the maximum cell area that might become electrically separated. They also [138] reported the immediate effect of micro cracks on the module power reduction is less than 2.5% if the crack does not hinder the electrical contact between the cell fragments.

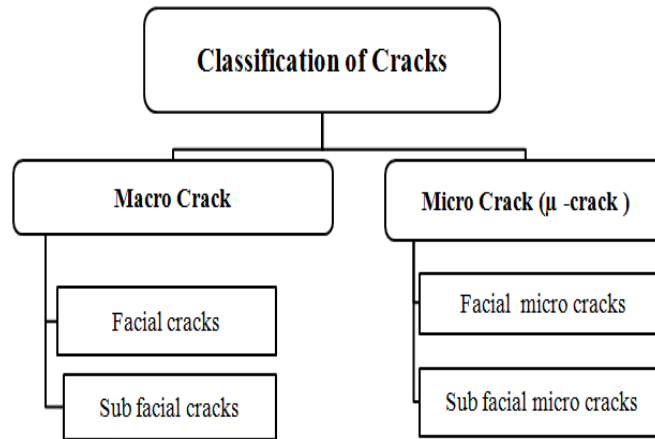


Figure 4. 3 Classification of Cracks

Also, if the solar cell with micro cracks separates a part of less than 8% of the cell area, no power loss occurred. Conversely, if the inactive area of a single cell is approximately 12 to 50%, the power loss increased nearly linearly from zero to the power of one double string of the PV module [138].

The unknown propagation rate for cracks in the wafer to cell metallization makes it difficult to predict the impact of the cracks on the efficiency of the PV module during its field life [139], [140]. Accelerated aging tests of PV modules with micro cracks clearly indicates that cell cracks cause irregularly shaped dark regions, which reduces both the life and output of the PV module [141].

4.4.2 Impact of the wafer thickness on cell breakage in mc-Si wafers

The fracture strength of multi crystalline silicon wafers depends upon both material-intrinsic properties (e.g., grain size, grain boundaries, and crystal orientation) and the extrinsic variables (e.g., micro cracks) [142]. These surface and edge micro cracks are the most important sources of degradation of mechanical strength. Reducing the potential micro cracks can in turn increase the fracture strength [143]. Jorgen *et al.*, [144] reported that the micro cracks located at the edge of the wafer induce breakage at lower forces than micro cracks located in the interior. These micro cracks normally propagate along the weakest lattice directions over grains and change direction at grain boundaries. At room temperature, silicon shows elastic behavior with almost no observed plastic deformation [145]. In their study of the mechanical stability of wafers with thicknesses varying between 120 and 320 μm , Coletti *et al.*, [146] reported a linear relationship between breakage force and wafer thickness. These results suggest that the micro crack defects will be more critical with smaller wafer thicknesses. Though the trend is to reduce

this wafer thickness, as shown in Fig. 4.4, the mechanical requirements necessary for that reduction will be challenging.

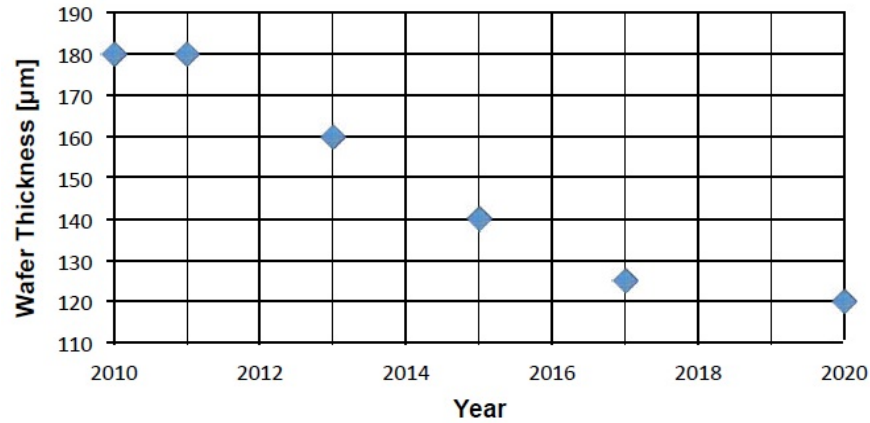


Figure 4. 4 Wafer thickness of previous and current generations of silicon solar cells [147]

4.5 Micro Crack Detection Techniques

As mentioned in section 4.4, micro-cracks can seriously impede solar cell performance and reliability. Because the PV industry requires a fast and precise in-line method of crack detection and characterization, many NDT techniques have been used for detecting micro cracks in silicon wafers and silicon solar cells. In this section, we review these NDT techniques.

4.5.1 Optical Transmission

In optical transmission, the silicon wafer is placed above a broad-spectrum flashlight or laser diode and the CCD camera is used to detect the optical transmission through the wafer. The micro cracks inside the wafer affect the infrared portion of the light that passes through. The resolution of the CCD camera determines the minimum crack width that can be detected by this method.

Li *et al.*, [148] proposed the use of a general CCD camera with a laser diode as an automatic inspection technique for facial crack detection. Though useful in detecting the facial cracks, it fails to detect hidden cracks in the awkward shaped plaques and cracks exhibiting snow-like point spread features. In addition to an infrared CCD camera and lamps behind the solar wafer, Aghamohammadi *et al.* [149] used a programmable logic controller (PLC) to acquire the signal from the computer to select a rejection line if any crack is via the image analysis system. The crack size is calculated by counting the associated dark gray pixels and the detected crack is classified based on the position of the bus bar using Fuzzy logic. The advantage of this approach [149] is that it can be applied to noisy images, thus obviating the need to use pre-processing steps to filter the noise image.

Rueland *et al.*, [150] used the transmission of a high intensity flashlight through the wafer and high-resolution CCD camera to capture the image. A thin crack scatters the light and appears as a dark line on the image while wider cracks let the light through the wafer and appear as white lines. The micro crack lengths are calculated by measuring the

number of pixels that represent the crack. The optical transmission method is unsuitable for crack detection for finished solar cell due to the interference of the aluminum on the reverse side of the cell.

Xu *et al.*, [151] used a cubic parametric spline curve to fit the cracks on the solar panel, which was useful in finding a broken edge location by using the ‘min’ filter to obtain the gray value of cracks to note the coincident pixel location. This method has a considerably small curve fitting error compared to the least square polynomial curve fitting. The approach of Zhuang *et al.*, [152] is based on the images taken from regular visible camera, and uses image processing techniques like gray transform, image adjustment, and contour detection. Though the micro crack is defined based upon the change in gray value of the crack pixels to the remaining pixels in the solar wafer, the visible camera and simple image processing theory of this technique permits only the detection of elemental simple cracks. It can distinguish cracks from its surroundings only if the gray level is distinct from their surroundings.

Another technique involves the use of an LED light source (940 nm) with CCD camera to inspect and mark the position of micro cracks in polycrystalline silicon wafers [153], [154]. Here, a tunable exposing system enabled the detection of micro cracks even with inconstant thicknesses of the multi-crystalline silicon wafer. Furthermore, once the cracks were detected, image-processing algorithms based upon histogram equalization, morphology methods, and a particles filter, were incorporated to mark the position of micro cracks. Reported detection times were less than 1 second. Though the micro cracks

were defined as low gray level and high gradient in sensed image, this method could not discern the difference between a micro crack and a mere scratch.

Du-Ming *et al.*, [155] developed a machine vision scheme for detecting micro-crack defects in a polycrystalline silicon wafer. The proposed method is based on anisotropic diffusion scheme, which smooths the suspected defect region and preserves the original gray-levels of the faultless background patterns. The authors adjusted diffusion factors in the proposed method based on a low gray value and high gradient characteristics of a micro crack in a sensed image. Though effective in detecting cracks within 0.09 sec for image size of 640 X 480 pixels, it could not detect sub facial cracks as it must visualize the crack on the sensed image. It also had inadequate resolution for detecting such facial micro cracks based on crack characteristics.

Yang [156] proposed a real-time in-line scanning method, which is based on short-time discrete wavelet transform (STDWT) to determine reflective characteristics of micro cracks. Assuming the far-field condition, the operation of this system is based on the emission of a continuous pulse laser beam of 656.3 nm wavelength, through the beam is spread out by linear optics to form a line directly striking the surface of the silicon wafer. The reflected optical signal is collected by a spatial probe array and STDWT is incorporated into the post signal-processing unit. The advantage of this approach is that the entire wafer can be inspected without image processing technology. However, the disadvantage is the tradeoff between the spatial resolution and the STDWT parameters. Though the selection of a small window size increases the spatial resolution for the

proposed system, it causes an irregular pattern of the STDWT curve, making automatic identification useless.

4.5.2 Infrared Ultrasound Lock-in Thermography (ULT)

Rakotoniaina *et al.*, [157] used the ultrasound lock-in thermography (ULT) method to detect facial cracks in silicon wafers and solar cells. Based on the periodic introduction of ultrasound energy (USE) into the wafer the principle of ULT is based upon the detection of heat created by friction at the edges of the crack as the USE is driven into the wafer. USE is generated by a transducer at a fixed frequency of 20 kHz. A special resonant ultrasound coupler is used to feed-in USE into the Si wafer. Heat is detected by the IR camera and converted into an image by the lock-in thermography (LIT) system. Using 30 minutes measure time, the LIT system allows imaging of periodic surface temperature modulations having an effective value as low as 10 mK. The special resolution of this method depends on the quality of IR camera incorporated into the ULT setup. This method can detect cracks with lengths as small as 100 μm . One of the disadvantages of this technique is that the long processing time makes it unsuitable for in-line production. An additional disadvantage is that the etched cracks do not lead to local heat generation and might require covering the wafer surface with black paint, which considerably enhances the IR signal.

4.5.3 Scanning Acoustic Microscopy (SAM)

Belyaev *et al.*, [158] used scanning acoustic microscope (SAM) method for the detection of facial micro cracks. Here a focused high-frequency acoustic beam operating in a pulsed mode is scanned over the front surface of the wafer. These pulses are transmitted through the Si wafer at the sound velocity and are reflected at various interfaces, including the front and back surfaces of the wafer. The pulse echo technique operates at frequencies up to 250 MHz and the cracks are visualized through material discontinuity due to acoustic impedance mismatch caused by the micro cracks. The time required to scan a 100 mm by 100 mm wafer, which is between 10 to 15 minutes, makes this method not suitable for mass production. Additionally, the wafer must be submerged in a water bath or covered with a water droplet because the high-frequency acoustic waves are attenuated quickly in air, requiring the placement of wafers in a coupling medium. However, this approach does allow the detection of cracks as small as 5–10 μm .

4.5.4 Impact Testing

In this method, the acoustic measurements are obtained by mechanically exciting vibratory modes in single-crystalline silicon wafers to detect the location and types of micro cracks [159]. This method depends on the audible impact response from cracked wafer sounds, which differ from a cracked free wafer. The setup is based on applying impacts to the wafer using a miniature piezoelectric impact hammer with a vinyl tip, weight of 2.9 g and length of 10 cm and generating up to 2,000 Hz waves. The impact

response is measured with a microphone mounted 2 cm above the test wafer. The reported results showed dependence of natural frequencies, peak amplitudes and damping levels with the crack type and location. However, this approach is used in detecting only facial cracks and the force applied for the impact could initiate cracks even in crack free solar cells. Impact testing allows identification of cracks with total length of 10 mm only.

4.5.5 Resonance Ultrasonic Vibration (RUV)

The Resonance Ultrasonic Vibrations (RUV) technique developed by Belyaev *et al.*, [160] is used for fast micro crack detection in solar grade crystalline silicon wafers. In this method, ultrasonic vibrations of a tunable frequency and adjustable amplitude are applied to the silicon wafer using an external piezoelectric transducer in the frequency range of 20 to 90 kHz. The transducer contains a central hole allowing a reliable vacuum coupling between the wafer and transducer by applying 50 kPa negative pressure to the backside of the wafer. Belyaev *et al.*, [160] reported that for C-Si wafers the increased crack length leads to decrease in peak frequency and increase in peak bandwidth. A typical RUV system can detect cracks up to sub-millimeter lengths. Dallas *et al.*, [161] used finite element analysis (FEA) modeling to select proper vibration mode to optimize the crack detection and increase the sensitivity of RUV technique.

4.5.6 Electronic Speckle Pattern Interferometry (ESPI)

Wen and Yin [162] developed a non-contact approach for detecting cracks in mono and poly crystalline solar cells using electronic speckle pattern interferometry (ESPI). In this method, speckle interference patterns are produced by real-time subtraction of sequential speckle images captured before and after an imposed deformation. This method depends on the variation of strain distribution due to thermal deformation in the solar cell, which is caused by discontinuities in material properties or the crystal lattice. A high resolution 2448×2050 pixels CCD camera and a DPSS laser with 532 nm wavelength are used in this method. A temperature-controllable planar heater was also used to apply a heat flux to the specimen. The ESPI image was taken from the back of the solar cells because ESPI is more suited for detecting rough rather than smooth surfaces. The authors reported that under similar constraints and temperature rise, defect free specimens and specimens with micro cracks shows different results [162]. This approach is used to detect both facial and sub facial cracks and can distinguish between crack and scratch.

4.5.7 Lamb Wave Air Coupled Ultrasonic Testing (LAC-UT)

Lamb wave air coupled ultrasonic testing (LAC-UT) [163], [164] is used as non-contact rapid inspection technique for detecting cracks in silicon wafers. An air coupled transducer is used to excite and detect the anti-symmetric (A0) Lamb wave mode in polycrystalline silicon wafers. The transducer is excited with an electrical spike of 900 V by a parametric pulsar/receiver with a central frequency of 200 KHz. The transmitter

emits an ultrasound wave into the surrounding air and then enters the silicon wafer, and is converted into the Lamb wave. The Lamb wave travels through the thickness of the silicon wafer, which is captured by a receiving transducer. The reported distance between the transmitter and receiver is 100 mm. The large acoustic-impedance mismatch between the solar cell specimen and air interface, which reflects that part of that energy into the solar cell limits the usefulness of the air coupling technique, however. Depending upon the orientation of cracks, the propagation of A0 mode is blocked and the receiver will receive little or no signal compared to defect free solar cell. The proposed system is automated for crack detection with scanning time less than 15 seconds for each wafer. This methodology can only be used for accepting or rejecting wafers during in-line processing because it offers rapid screening without finding the crack location. Clearly, this approach also cannot distinguish between real micro cracks and other defects, since any defect could block the A0 mode.

4.5.8 Lock-in Thermography (LIT)

Unlike Infrared (IR) thermography that utilizes the photon in the infrared range of the electromagnetic spectrum to produce images of a specific temperature pattern, lock-in thermography uses modulated excitation to periodically excite carriers. The sample is imaged by an IR camera running at a certain frame rate, and all images captured in a certain acquisition time are sent to the processing machine for evaluation and averaging [165], [166].

There are two main types of lock-in thermography; Dark Lock-in Thermography (DLIT) and Illuminated Lock-in Thermography (ILIT) where the former is used by applying either a reverse bias to concentrate current in shunts or a forward bias to sense shunts and the latter uses light instead of voltage applied by contacts to drive currents through the shunts [167], [168].

St-Laurent *et al.*, [169] used IR thermography for detecting sub facial micro cracks. The limitation of this technique is that only cracks with shape as triangular with large mouths at the surface and tiny tips are detected. This method has not been tested to detect different shapes of micro cracks, and has been used only for off-line inspection.

4.5.9 Electroluminescence (EL) imaging and Photoluminescence (PL) imaging

Luminescence results from light emissions from non-thermal energy sources. Electroluminescence (EL) imaging for solar cell characterization was introduced by Fuyuki *et al.*, in 2005 [170] where the excess carriers are injected across the junction of a solar cell using an applied forward bias. The EL imaging system is a contact technique, which is only applicable for a finished solar cell.

Photoluminescence (PL) imaging is another form of luminescence that was introduced by Trupke *et al.*, in 2006 [171]. PL imaging is contactless technique with an acquisition time of typically less than one second used to capture luminescence images of unprocessed and partially processed wafers and finished solar cells. In the PL imaging

setup, the entire surface of the sample is illuminated homogeneously with an external optical energy that is equal or greater than the semiconductor band gap to create excess electron and hole pairs. The luminescent samples are imaged by a CCD camera with help of an IR filter. In other words, photoluminescence is the measure of radiative recombination that depends upon the defects and impurities in the semiconductor. The photoluminescence intensity is also proportional to the carrier concentration. The photoluminescence associated with crack is weaker due to the localized increased non-radiative recombination at crack surfaces, which makes the crack appears darker in the luminescent samples.

Both PL imaging and EL imaging systems are used for micro crack detection [172]. Breitenstein *et al.*, [173] reported that the luminescence methods are better than lock-in thermography for crack inspection because luminescence imaging is usually based on a Si-detector camera that is less expensive than LIT and it does not suffer from thermal blurring, and it usually needs a lower acquisition time than LIT.

Jong- Hann *et al.*, [174] developed software and hardware for an automatic optical inspection system for inspecting the facial cracks of polycrystalline silicon solar cells or modules. They used the EL imaging technique with a CCD interlaced camera with 768×494 pixels resolution with optical lens mounted and illumination unit [174]. The software [174] is based on the use of windows-based user interface to implement the average gray level tool and the binary large object (BLOB) tool. However, it is difficult to distinguish between micro cracks and other type of defects like scratches using this approach. EL equipment with CCD camera plus lens filter has been used to capture the emissions and

filter out visible spectrum for automatic detection of sub facial cracks in solar cells [175]. An image processing scheme is used to count and recognize dark area in sensed image as micro cracks. This approach cannot distinguish between the micro cracks or any defects that appear as dark region in sensed EL image, however. Also, lengthy exposure times, of about 30 seconds, are required. As a contact technique, the EL imaging approach can be applied only on complete solar cells and is not applicable to wafers.

Using the EL imaging system with a cooled infrared (IR) camera, Tsai, *et al.*, [176] proposed a Fourier image reconstruction scheme to detect sub facial cracks in multi crystalline silicon solar cells. Based on the fact that the defects in solar cell appear as line or bar shaped objects in EL image, the proposed scheme can detect defects as long as they appear darker than its surroundings in the EL image, Tsai, *et al.*, [176] reported that the defect contrast is not required to be larger than the grain boundary contrast. However, in order to have better quality results for particular cases there should be an adaptive control approach that depends on the image parameters such as image size and resolution. The authors [176] have not reported the minimum micro crack size that can be detected using this approach.

The PL imaging system proposed by Yih-Chih *et al.*, [132] has been used to detect invisible sub facial micro cracks down to 13.4 μm . Image processing was used to extract the micro cracks. The setup used near infrared (NIR) camera with a homemade dome illuminator, which consisted of 32 pieces of 940 nm LEDs. Two different algorithms were used to extract the micro cracks. The first μ -crack extraction method was based on Niblack's local segmentation algorithm [177]. The second method is based on region

growing technique. The use of second algorithm proved to be more suitable approach for in-line applications. The sensed micro crack is assumed significantly darker than the crystal grains under infrared light. However, with this method, a dark and thin elongated crystal grain in the defect free multi crystalline silicon wafer could be falsely identified as a micro crack. Though this approach was highly accurate, the speed of inspection was low due to the low resolution of the NIR camera. The minimum detectable crack width, or the minimum detectable distance of two opposing internal micro crack surfaces is given by the wavelength of the light used in NIR. In addition, the reflection is distorted for distances smaller than the wavelength, and the minimum detectable area of the micro crack planes depends on the resolution of the digital camera. Consequently, this approach is unsuitable for detecting very slender micro cracks.

4.6 Comparison between Micro Crack Detection Techniques

Micro cracks adversely affect the manufacturing cost and reliability of PV modules. In Table 4.1, we have compared the weakness and strength of different NDT techniques to detect micro cracks in mono and poly crystalline silicon wafers and solar cells. As we have discussed in the previous section, there are many types of inspection tools for detecting micro cracks. If the production line is fully automated, the inspection tools must be fast and precise. Only tools based on PL imaging, EL imaging, optical transmission, and RUV meet these requirements. However, if there is a need to detect micro cracks

only in the finished solar cell stage, we can use an inspection tool based only on EL imaging and not tools based on optical transmission. Should an inspection tool be required during the wafer and finished solar cell manufacturing stages, we can use PL imaging or RUV based inspection tools. Some commercial inspection tools that use Photoluminescence (PL) imaging technology, such as that created by the BT Imaging Company formed by Bardos and Trupke [178], provide many products for inline inspection tools for both wafer and solar cells. The throughput for this tool is up to 3600 measurements per hour where the throughput for the commercial RUV system [179] is between 1200-1800 measurements per hour. There are many methods for micro crack inspections, each of which have their advantages and disadvantages. In the following section, we describe, for the first time, our use of a methodology to rank these various micro-crack inspection tools.

Table 4. 1 Comparison between different NDT techniques

Method	Advantage	Disadvantage	References
Optical Transmission	Detect small crack ~ few μm , High Throughput ~ 1 wafer per sec, Can be used as online inspection tool	Use in production stages prior to metallization , inapplicable in finished solar cell	[148] – [156]
Infrared Lock-in Ultrasound Thermography (ULT)	Can be used both for wafers and solar cells	Long acquisition time ~ 30 minutes, might require covering the wafer surface with black paint. standalone tool	[157]
Scanning Acoustic Microscopy (SAM)	Detect cracks as small as 5–10 μm	Long acquisition time ~ 10-15 minutes, wafer has to be covered with water, used as standalone tool	[158]
Impact Testing	High Throughput	Use of impact could introduce cracks, detect cracks with total length of 10 mm only, used as standalone system	[159]
Resonance Ultrasonic Vibration (RUV)	High Throughout ~ 2 sec/ wafer. no interference with defects due to scratches	Sensitivity to crack length and crack location, used only to reject or accept wafers, does not identify the location of cracks	[160], [161]
Electronic Speckle Pattern Interferometry (ESPI)	No interference with defects due to scratches	Resolution to measure the crack length is 2.65 mm for 25 mm long crack.	[162]
Lamb Wave Air Coupled Ultrasonic Testing (LAC-UT)	Scanning time < 15 sec/ wafer, ability to quantify the cracks in terms of length	Only used for accepting or rejecting wafers during online processing, can't distinguish between real crack and any defect could block the A0 mode.	[163], [164]
Lock-in Thermography (LIT)	High resolution imaging of defects	Offline inspection only, long acquisition time, suffer from thermal blurring	[165]-[169]
Electroluminescence (EL) imaging	High Throughput	Interference with other defects (e.g. scratches), contacted method , can be used only with finished solar cell, standalone system	[170], [172], [173]-[176]
Photoluminescence (PL) imaging	High Throughput, contactless can be used as online inspection tool for both wafers and solar cells	Interference with other defects such as scratches	[171], [172], [132]

4.7 NDT Tool Selection Study

Our objective is to rank different crack detection tools reviewed in this chapter for a specific PV production line. Our decision-making tool is based on the analytical hierarchy process (AHP) to rank different inspection tools based on given selection criteria. AHP [180] provides a comprehensive framework for structuring a system of objectives, criteria, and alternatives. AHP hierarchy is used to establish a relation in the first hierarchy level between objective function and between criteria and alternatives in the second hierarchy level. AHP is used in a number of decision-making applications, e.g., Bun [181] used AHP to provide a structure on decision-making for car purchase. Bhattacharyay *et al.*, [182] have used AHP for robot selection. The AHP also is used to assist in the material selection for the automotive Body-In-White (BiW) panels at the conceptual design stage [183] and for automotive production line design [184].

Our proposed approach for using AHP is based on the following specifications:

- 1) The ultimate goal is to choose best micro crack detection tool for specific mono and poly crystalline photovoltaic production line. This is the first level in AHP.
- 2) The second level in AHP, known as criteria, is dependent upon the requirements of a specific production line. We assume that the specific production line requires an inspection tool, which can work on multiple production stages (wafer and cell), with high throughput and can be incorporated into a fully automated PV production line. Initial equipment cost is perhaps the highest priority, followed by the sensitivity to discern small crack length. The inspection tool must also be precise in identifying micro-cracks without

any concern of false detection. Fig. 4.5 shows the criteria with relative weight, where the highest priority criterion has the highest weight and the total weights for all criteria are equal 100%.

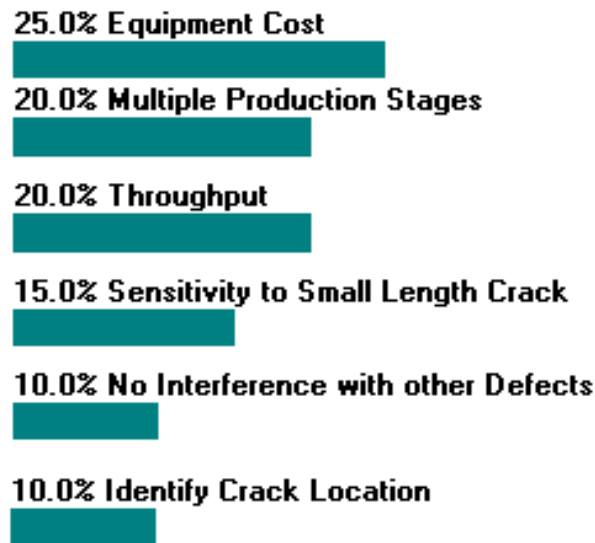


Figure 4. 5 The proposed criteria and relative weight used in this work

3) The third level of hierarchy, known as alternatives or competitors, represents the four inspection tools. Fig. 4.6 shows the setup for the alternatives.

4) The relation between each criterion and each alternative in the second hierarchy level is established by a pairwise comparison between two elements simultaneously. For each criterion, i.e. multiple production stages, we compare between two alternatives at a time. For example, we start with a comparison between PL and EL imaging systems. After comparing the alternatives, it should be repeated for different criterion using the same procedure.

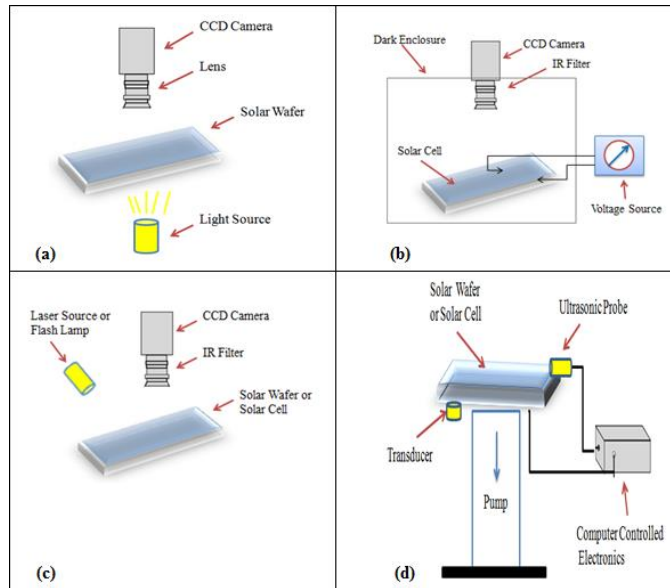


Figure 4. 6 Alternatives are based on (a) Optical Transmission, (b) EL imaging, (c) PL imaging, and (d) RUV

Figure 4.7 shows pairwise comparisons between PL imaging and optical transmission based on multiple production stages. As displayed in Fig. 4.7, the result of this comparison is equal 2, which implies that the ratio between the PL imaging systems to optical transmission is equal to 2:1. Our calculations in this step are based on Table 1, which is the summary of the literature data presented in this work. The PL imaging system is capable of detecting micro cracks in unprocessed and partially processed wafers and finished solar cells, but the optical transmission can detect micro cracks only in the production stages prior to metallization. Since it is inapplicable for finished solar cells, it results in a ratio of 2:1. If the comparison is between PL imaging and EL imaging for use in a multiple production stages criterion, the ratio will be 3:1 since EL imaging is only applicable for the inspection of finished solar cells.

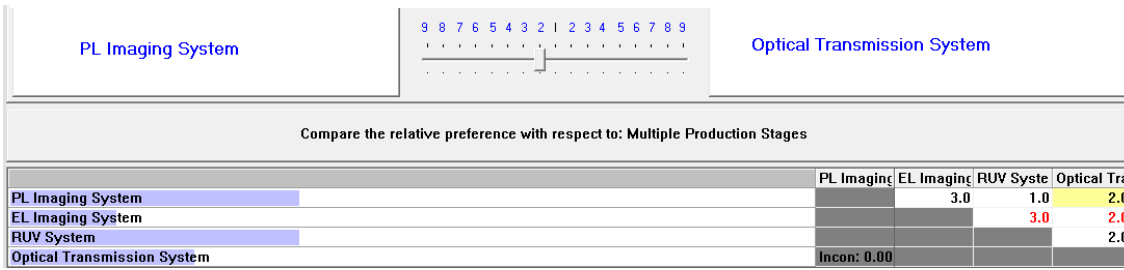


Figure 4. 7 Pairwise comparison between main selection criteria

5) The final step is to rank all the alternatives (micro crack inspection tools) based upon the overall criteria (production line requirements) to satisfy the ultimate goal of selecting the best micro crack detection tool. The results shown in Fig. 4.8 indicate that the PL imaging system is the best system, with a 27.3 % rate of effectiveness, making it the best for this production line. The second ranked system is the optical transmission system followed by the RUV system in third place. EL imaging system is the last ranked tool.

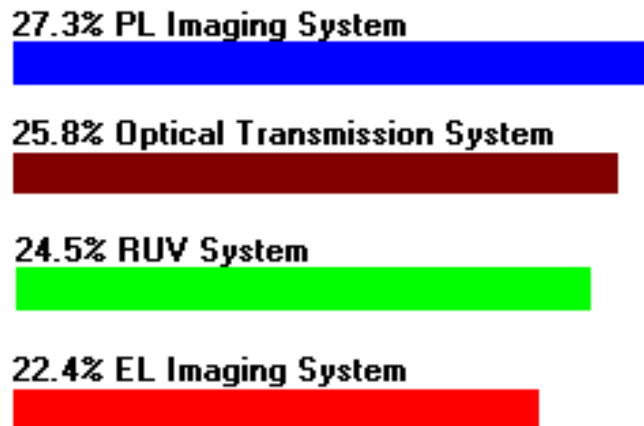


Figure 4. 8 The sensitivity for different constraint with respect to the ultimate goal

Fig. 4.9 shows the rank for all alternatives based on each of the selection criterion and shows the sensitivity for different constraint in respect to the ultimate goal. Fig. 4.9 also shows the values for each alternative with regards to each constraint. As shown in Fig. 4.9 the problem has conflicting objectives and multi-attribute constraints (e.g., no interference with other defects criterion, RUV system has the best rank, but has the lowest rank as regards to throughput).

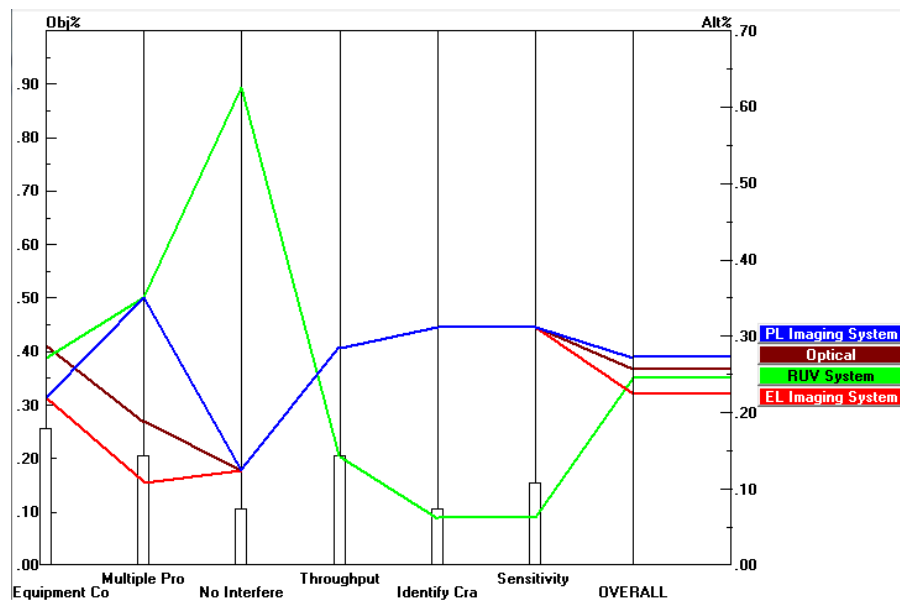


Figure 4. 9 The sensitivity for different constraint with respect to the ultimate goal

4.8 Summary

In this chapter, we reviewed the origin and root causes of micro cracks in mono and poly crystalline silicon wafers and solar cells, and the strengths and weaknesses of various non-destructive techniques used for the detection of micro cracks. For automated manufacturing plants, the optimum micro crack detection techniques must satisfy conflicting objectives and multi-attribute constraints. We used the decision- making tool based on the analytical hierarchy process (AHP) to rank various inspection tools based upon specific criteria. Our results indicate that the micro crack detection system based upon the photoluminescence (PL) imaging system was superior to all others and ideally suited for automated production lines.

CHAPTER FIVE

MODELING PV SYSTEM FOR ON-BOARD VEHICLE APPLICATION

5.1 Introduction

Why should we use Photovoltaic solar On-board in transportation?

- i. Solar energy is an unlimited renewable energy source. The total solar irradiation of the sun reaches the earth's surface is about 1.8×10^{14} kW. In Figure 5.1, a comparison of the potential energy (in a year) that is possible from different renewable energies versus the total resources that are possible from conventional finite sources of energy.
- ii. Solar energy has zero energy cost.
- iii. There is no emission of PV during operation.
- iv. PV is reliable and noise free because there are no moving parts.
- v. PV could be used in many applications in the vehicle applications from small to large applications.
- vi. The output of the PV is direct current (DC) electricity, which could minimize the AC-to-DC conversion though the traditional grid electricity generation and transmission.
- vii. It is flexible energy charging source.
- viii. Most of time, the vehicle is in parking, and even the diffuse light can be transformed to electricity through PV.

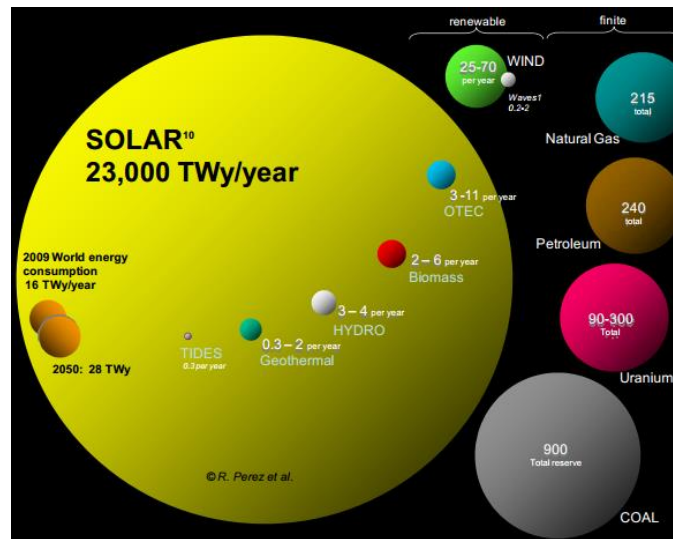


Figure 5. 1 Annual Potential for Renewable Energies vs. Total Resources for Finite Energies (Source: Perez & Perez, 2009a [185])

What are the major disadvantages?

- i. PV has low conversion energy density compared to other energy sources have been used in vehicles.
- ii. Electricity production depends on the weather conditions.
- iii. The installation areas on the vehicle surface are limited.
- iv. The energy storage devices are still costly.

5.2 Crystalline Silicon PV Module Structure

A solar cell is an electronic device converts sunlight into direct current (DC) electricity. This process requires firstly, a material in which the absorption of light raises an electron to a higher energy state, and secondly, the movement of this higher energy electron from the solar cell into an external circuit (load). The electron then dissipates its energy in the load (produces current and voltage) and returns to the solar cell [186]. In the previous chapters, the mono-crystalline silicon (mono-Si) PV cell type is selected as the optimum type for the on-board vehicle application. Figures 5.2 and 5.3 show the basic component and the cross section of mono-Si solar cell, respectively.

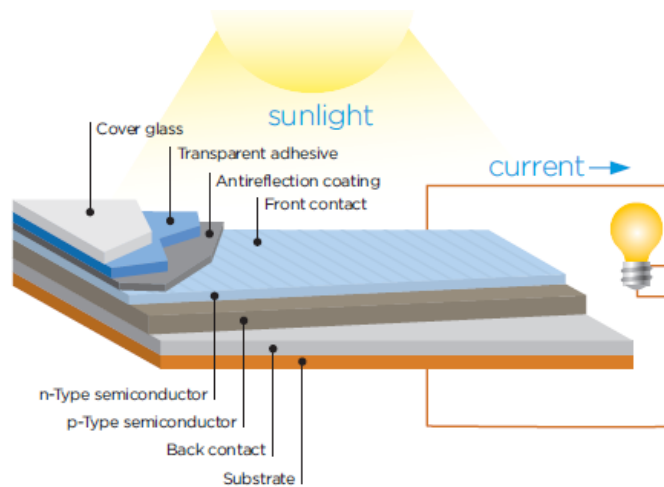


Figure 5. 2 Basic Component of PV Cell (Source: Clean & Green, 2012 [186])

The production process of a typical commercial crystalline silicon solar cell is discussed in chapter four.

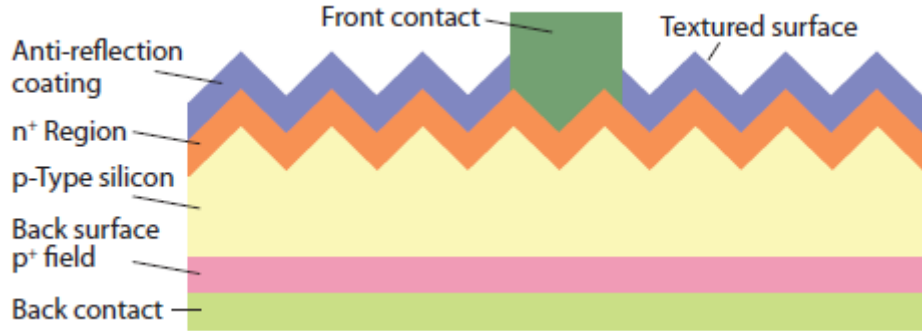


Figure 5. 3 Cross Section of a Commercial Monocrystalline Silicon Solar Cell [187]

The front surface of the cell is covered with micrometer sized pyramid structures (textured surface) to reduce reflection loss of incident light. An anti-reflection coating (ARC) of silicon nitride (SiN_x) or titanium oxide (TiO_x) is overlaid on the textured silicon surface to reduce further the reflection loss [187]. Crystalline silicon solar cells have highly phosphorous-doped n^+ (electron-producing) regions on the front surface of boron-doped p -type (electron-accepting) substrates to form p - n junctions. Back-surface p^+ field (BSF) regions are formed on the back surface of the silicon substrate to suppress recombination of minority carriers (photo-generated electrons). The carriers (electrons) generated in the silicon bulk and diffusion layers are collected by silver contacts (electrodes) formed on the front and back silicon surfaces. The front contact consists of gridlines connected by a busbar to form a comb-shaped structure. The back contact is usually a series of silver stripes connected to the front bus bar of the adjacent cell via soldered copper interconnects [187].

The substrate thickness used in most standard crystalline cells is between 160 to 240 μm and the trend to reduce it to less than 120 μm as discussed in the previous chapter.

The solar cells are assembled into modules by soldering and laminating to a front glass panel using ethylene vinyl acetate as an encapsulant. The energy conversion efficiency of the best commercial mono-Si modules of standard mono-Si solar cells are around 3-4% lower than the best individual cell efficiency [188].

The energy conversion efficiency of solar cells is another important issue because the efficiency influences the entire value-chain cost of the PV system, from material production to system installation. The solar cell efficiency is limited by the three loss mechanisms [187].

- a) Photon losses due to surface reflection, silicon bulk transmission and back contact absorption.
- b) Minority carrier (electrons in the p region and holes in the n region) loss due to recombination in the silicon bulk and at the surface.
- c) Heating joule loss due to series resistance in the gridlines and busbars, at the interface between the contact and silicon, and in the silicon bulk and diffusion region.

5.3 The electrical performance of PV solar module

The electrical performance of a PV solar cell is determined by the following basic points; short circuit current (I_{sc}), open-circuit voltage (V_{oc}), current at the maximum power point (I_{mp}), the voltage at the maximum power point (V_{mp}). The other important PV points are maximum power (P_{max}), fill factor (FF) and energy conversion efficiency (η). Figure 5.4 shows the typical current (I)-voltage (V) curve, highlighted the basic points.

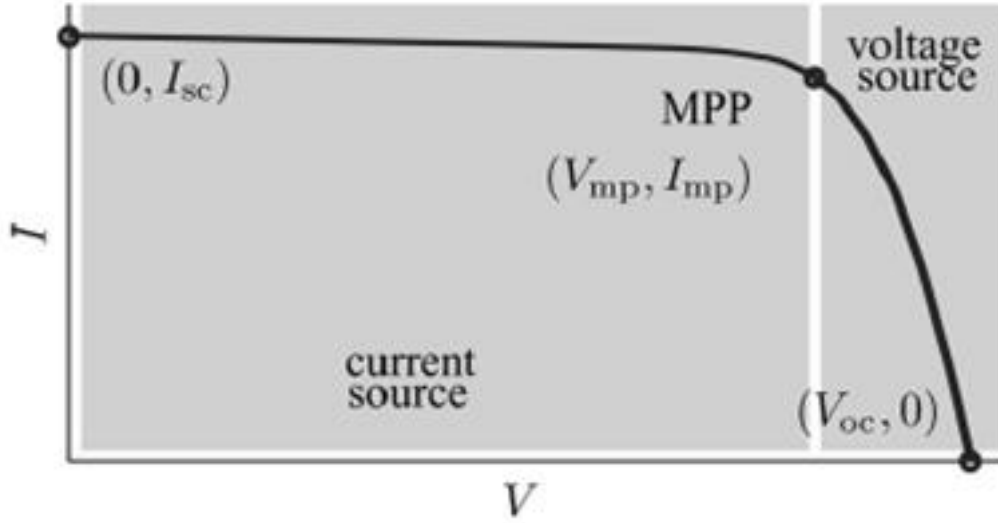


Figure 5. 4 Typical I-V Curve [189]

The V_{oc} is the maximum available voltage from the PV cell, at this point the current (I) is equal zero. The V_{oc} corresponds to the amount of forward bias on the solar cell due to the bias of the solar cell junction with the light-generated current increases logarithmically with the ambient irradiation [190]. The I_{sc} is the largest current that can be drawn from a PV cell at this point the voltage across the PV cell is zero. I_{sc} is a linear function of the ambient irradiation. The I_{mp} and V_{mp} is the optimum operating point which will discuss later. The FF is the ratio between maximum power from the PV cell to ideally maximum power. The FF is calculated using equations (5.1 and 5.2) below:

$$FF = \frac{P_{\max} [W]}{I_{sc} [A] \times V_{oc} [V]} \quad (5.1)$$

$$P_{\max} [W] = I_{mp} [A] \times V_{mp} [V] \quad (5.2)$$

The PV energy conversion efficiency (η) is defined as the ratio (the fraction) of incident power from the sun, which is converted to electricity and is defined using equation (5.3):

$$\eta[\%] = \frac{P_{\max} [W] \times 100}{1,000 [Wm^{-2}] \times Cell \text{ area } [m^2]} \quad (5.3)$$

The PV cell area (in m^2) and the 1,000 Watt per m^2 is the maximum solar energy reach the earth for terrestrial PV application. Terrestrial solar cells are measured under air mass 1.5 ($AM_{1.5}$) spectrum condition and at a temperature of 25 °C. Solar cells intended for space use are measured under AM_0 conditions. The $AM_{1.5}$ condition is defined as 1.5 times the spectral absorbance of Earth's atmosphere. In contrast, the spectral absorbance for space is zero (air mass zero, AM_0).

The solar energy under the $AM_{1.5}$ condition is used as the input energy for calculation of solar cell efficiency. Figure 5.5 shows the reference solar spectrum (with units of $W.m^{-2}.nm^{-1}$) from NREL [191] (the complete solar spectrum from 280 nm till 4000 nm). Based on PV cell material, the fraction of this solar spectrum can be absorbed and converted to electricity. The ETR (the black curve in Figure 5.5) referred to extraterrestrial radiation (solar spectrum at top of atmosphere) means Earth-Sun distance, which is used for space application. The red and blue curves used in the proposed application with the difference is the blue reflects the global and the red is the direct radiation. More details about these terms will be discussed later.

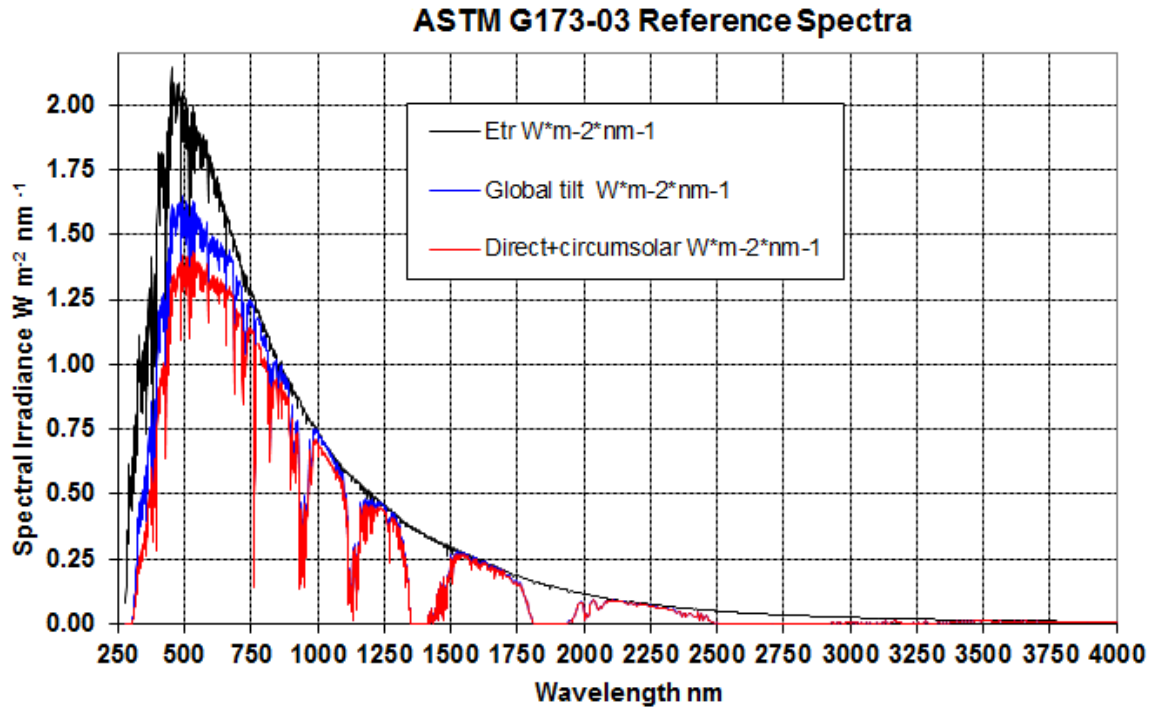


Figure 5. 5 ASTM G173-03 Reference Spectra Global Tilt (with units of $W\ m^{-2}\ nm^{-1}$), (data from NREL [191])

Typically, the above PV solar cell electrical performance points are given by PV manufacturer at STC. Figure 5.6 shows example of mono-Si PV module datasheet from SUNPOWER Company [192], which is used through this study to validate the model results.

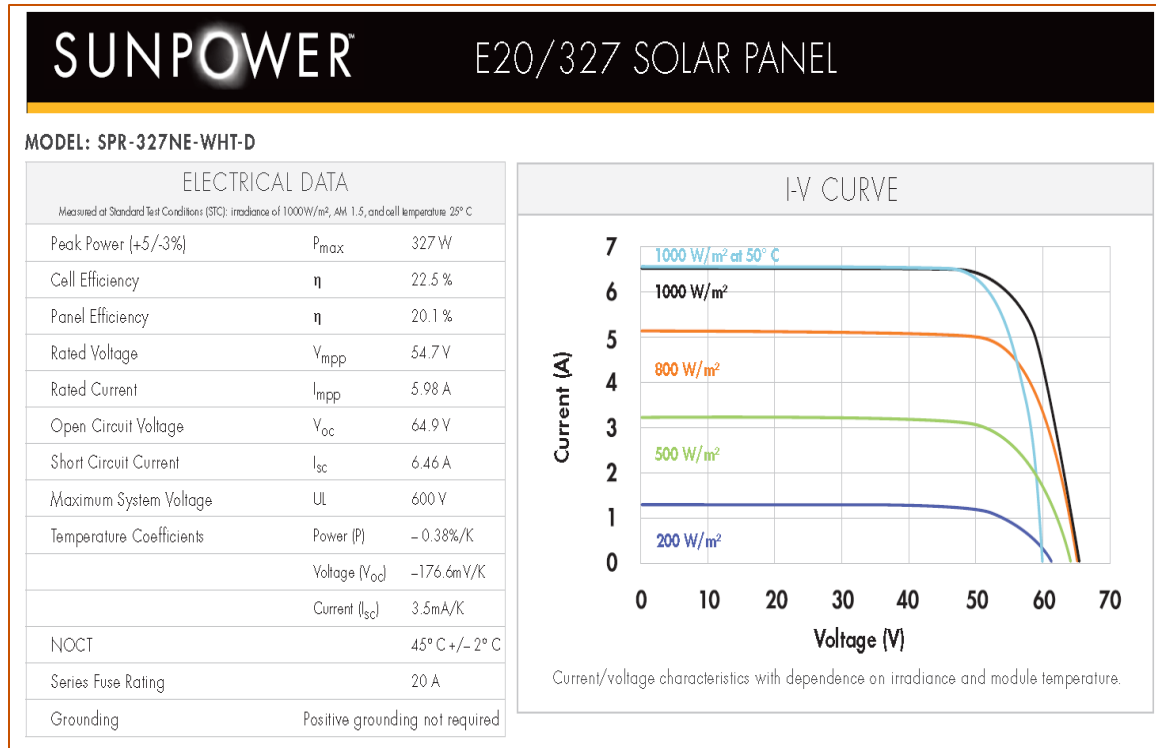


Figure 5. 6 SUNPOWER Mono-Si PV Model [192]

The area of this PV module equal 1.631 m², the other specifications in terms of PTC, weight, etc. are discussed in chapter 2. The I-V curves depend on both solar irradiance and module temperature. The manufacturers of PV module provide the above I-V curves at STC with only some experimental data reflects the modules electrical and thermal characteristics. In order to capture the PV module behaviors in terms of I , V , P , η at all conditions, the PV device is modeled in the next section.

5.4 Modeling PV module circuit

The ideal and practical PV cell circuit is shown in Figure 5.7. The ideal PV cell consists of current source and parallel diode(s). The current generated by incident light (I_{pv}) which depends on sun irradiation and the diode current based on the Shockley diode equation. The practical PV device has a series resistance (R_s) and a parallel resistance (R_p). The R_s reflects the internal resistances in the gridlines, busbar, the interference between silicon and the contacts, and the movement of current through the emitter and base of the PV cell [193]. The R_p or sometimes is called shunt resistance (R_{SH}) is typically due to the manufacturing defects. In Chapter Four, the main defect types are reviewed and the effects on the PV performance are discussed.

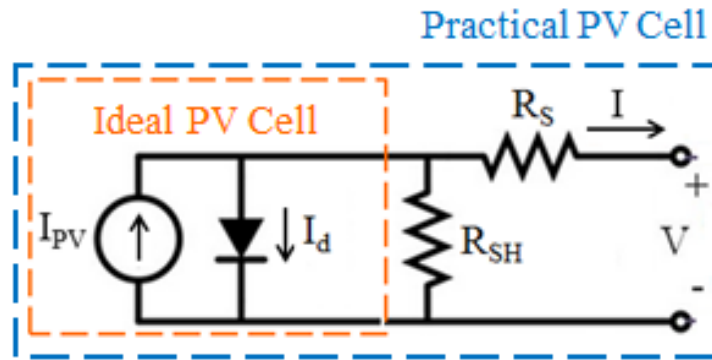


Figure 5. 7 Ideal and practical PV equivalent circuit

Several authors in previous work modeled PV device circuit using single-diode model [194], two-diode model [195]- [198], and three-diode model [199]. The different model approaches are reviewed in [200].

The values of R_p and R_s are measured through flash test. The R_p can be estimated using the I-V curve as the inverse of the slope $-dV/dI$ around the I_{sc} value using equation 5.4 or equation 5.5 [201].

$$R_p = -\left(\frac{dV}{dI}\right)^{-1} \Big|_{I=I_{sc}} \quad (5.4)$$

The value of R_p , is calculated as the fraction of the slope $(I_{sc}-I_{mpp}) / V_{mpp}$

$$R_p = \frac{I_{sc} - I_{mpp}}{V_{mpp}} \quad (5.5)$$

By looking to I-V curve (Figure 5.4), the curve in “current source region” is almost flat and the differences between the two approaches are not crucial. However, the value of R_p is generally too high and some authors neglect this resistance to simplify the model [202]-[204].

Some authors estimated the value of R_s as the inverse of the slope $-dV/dI$ around V_{oc} using equation 5.6 below, which is known as the "apparent" series resistance and is greater than R_s as it includes the contribution of the slope of the diode exponential at the V_{oc} point [201].

$$R_s = -\left(\frac{dV}{dI}\right)^{-1} \Big|_{V=V_{oc}} \quad (5.6)$$

Other authors estimated R_s using equations 5.7 and 5.8 below [205].

$$R_s = -\left(\frac{dV}{dI}\right) \Big|_{V=V_{oc}} - \frac{1}{X_V} \quad (5.7)$$

$$X_V = \frac{I_0(T_1) \times q}{n \times K \times T_1} \times \exp\left(\frac{q \times V_{oc}(T_1)}{n \times K \times T_1}\right) \quad (5.8)$$

The parameters are defined below. Other author estimated R_s and R_p based on characteristic resistance (R_{ch}) [206] as equations 5.9, 5.10, and 5.11. The reported value of R_s for silicon PV could be less than $0.50 \, \Omega$ [207], [208]. However, the value of R_s is very low, and sometimes this parameter is neglected too [209], [210].

$$R_{ch} = \frac{V_{oc}}{I_{sc}} \quad (5.9)$$

$$R_p = 1000 \times R_{ch} \quad (5.10)$$

$$R_s = 0.1 \times R_{ch} \quad (5.11)$$

In this work, the PV circuit is modeled using single-diode model approach with moderate complexity, since it offers a good compromise between simplicity and accuracy. The equations bellows are used for modeling [205], [211].

$$I = I_{PV} - I_d - \frac{V + R_s \cdot I}{R_p} \quad (5.12)$$

$$I_{PV}(T) = \frac{G}{G(nom)} [I_{sc}(T_{1,nom}) + K_0(T - T_1)] \quad (5.13)$$

$$K_0 = \frac{I_{sc}(T_2) - I_{sc}(T_1)}{(T_2 - T_1)} \quad (5.14)$$

$$I_d = I_0 \left(e^{\frac{q(V + I \cdot R_s)}{nkT}} - 1 \right) \quad (5.15)$$

$$I_0 = I_0(T_1) \times \left(\frac{T}{T_1} \right)^{\frac{3}{n}} \times e^{\frac{q \cdot V_g(T_1)}{nk \left(\frac{1}{T} - \frac{1}{T_1} \right)}} \quad (5.16)$$

$$I_0(T_1) = \frac{I_{SC}(T_1)}{\left(e^{\frac{q \cdot V_{OC}(T_1)}{nkT_1} - 1} \right)} \quad (5.17)$$

Where;

I : PV cell current

V : Voltage across PV cell

I_{PV} : Current generated by the incident light, directly proportional to solar irradiance G

I_d : Current diode (Shockley diode equation)

I_0 : Reverse saturation current, which is the measure of recombination. For better material quality, the recombination is less, and then I_0 is low. In addition, I_0 is increasing as PV cell temperature increasing.

K_0 : Current temperature coefficient, which is equal 3.5 mA/k in Figure 5.6.

V_g : Band gap energy (eV). Depends on PV cell material, is the minimum energy required to excite an electron that is stuck in its bound state into a free state where it can participate in conduction. For crystalline PV module around 1.12 eV and for amorphous silicon around 1.75 eV.

V_{th} : Thermal voltage ($=nKT/q$), for ideal diode $n=1$, then at $T=300$ k, $V_{th}=25.85$ mV.

K : Boltzmann constant, equal 1.38066×10^{-23} J/k.

T : Cell temperature (in Kelvin)

T_1 : reference temperature = 25° C.

n : Diode ideality factor, ranging from 1 to 2, the n value near 1 at high current and near 2 at low current.

q : electron charge = 1.60218×10^{-19} coulombs

G : Solar irradiation is the rate at which radiant energy is incident on a surface, per unit area of surface in unit (W/m^2)

$G(\text{nom})$ nominal irradiation = 1000 W/m^2

R_s : Series resistance in (Ω).

R_{sh} : Shunt resistance in (Ω).

To increase the PV voltage, the PV module consists of different PV cells connected in series. To increase the current different PV cells are connected in parallel. Suppose, the number of PV cells connected in series is (N_s) and the number of parallel PV cells are (N_p), then:

$$V_t (\text{module}) = N_s \times V_t (\text{cell}) \quad (5.18)$$

$$I_{pv} (\text{module}) = I_{pv} (\text{cell}) \times N_p \quad (5.19)$$

$$I_o (\text{module}) = I_o (\text{cell}) \times N_p \quad (5.20)$$

By substituting all above equations in equation (5.12), the final equation is called transcendental equation, since it does not have a direct solution because it is in the form (5.21) and (5.22) below.

$$I = f(G, T, V_g, n, R_s, R_{sh}, I, V) \quad (5.21)$$

$$I - f(G, T, V_g, n, R_s, R_{sh}, I, V) = 0 \quad (5.22)$$

The numerical solution is done by minimizing the error $I - f(I, V) = 0$ for a set of V values to find the corresponding I values. The proposed model is based on Matlab Simulink[®] using four-parameter approach, this mean the R_p is assumed infinite and ignored, the other unknown parameters (I_L and I_o) are calculated using equations above.

The V_g is set to 1.12, which is a typical value for crystalline silicon PV module. The other parameters (n and R_s) are estimated using curve-fitting approach where these parameters' values are tuned with the objective function is to minimize the maximum PV module power to be within the accuracy range for the reported peak power in PV manufacturer data (e.g., +5/-3%, See Figure 5.6).

The proposed PV module is used to validate the results by comparing the actual manufacturer' datasheet and the model predicted results. The Figures 5.8- 5.11 show preliminary results for different iterations of n .

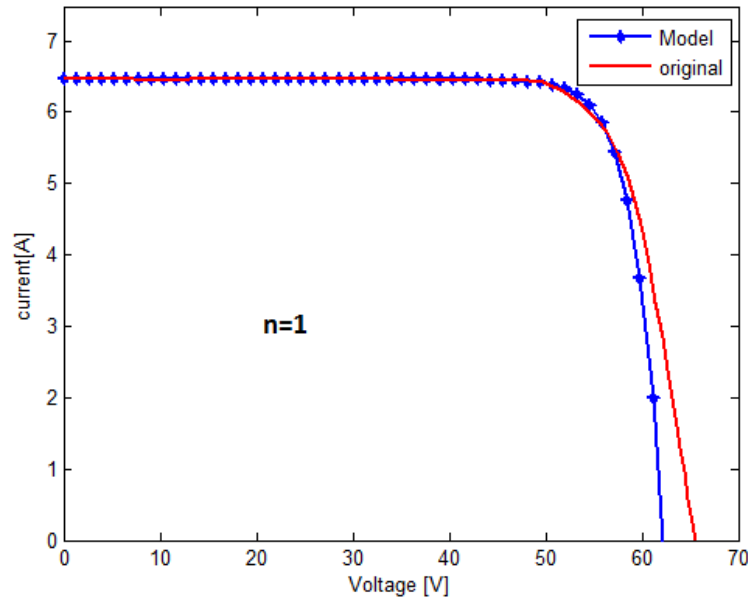


Figure 5. 8 Preliminary Results I-V Curves: Actual vs. Predicted ($n=1$)

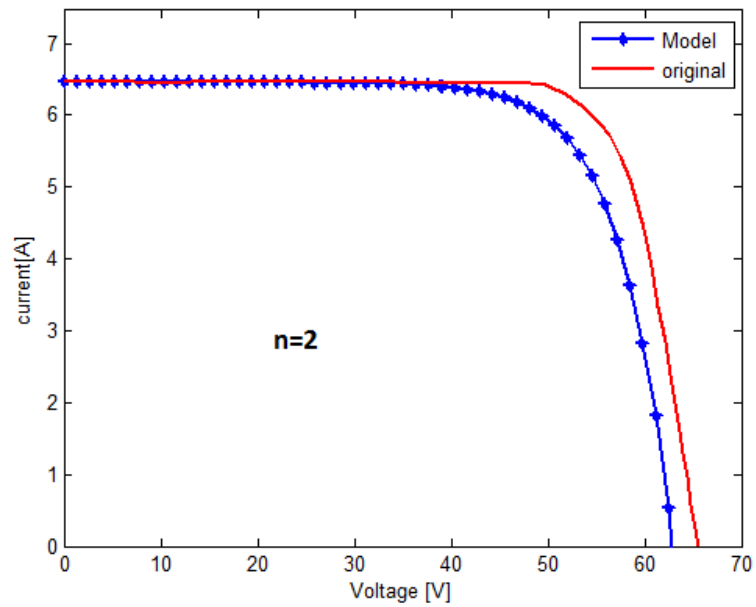


Figure 5. 9 Preliminary Results I-V Curves: Actual vs. Predicted ($n=2$)

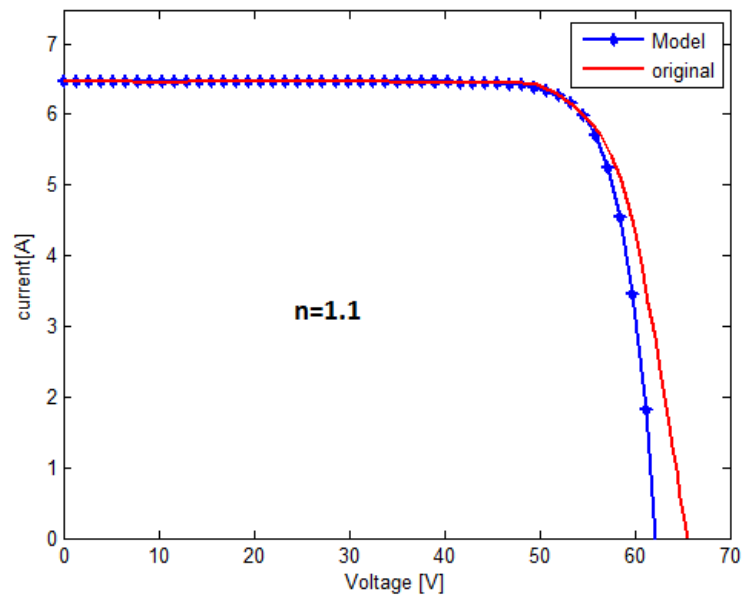


Figure 5. 10 Preliminary Results I-V Curves: Actual vs. Predicted ($n=1.1$)

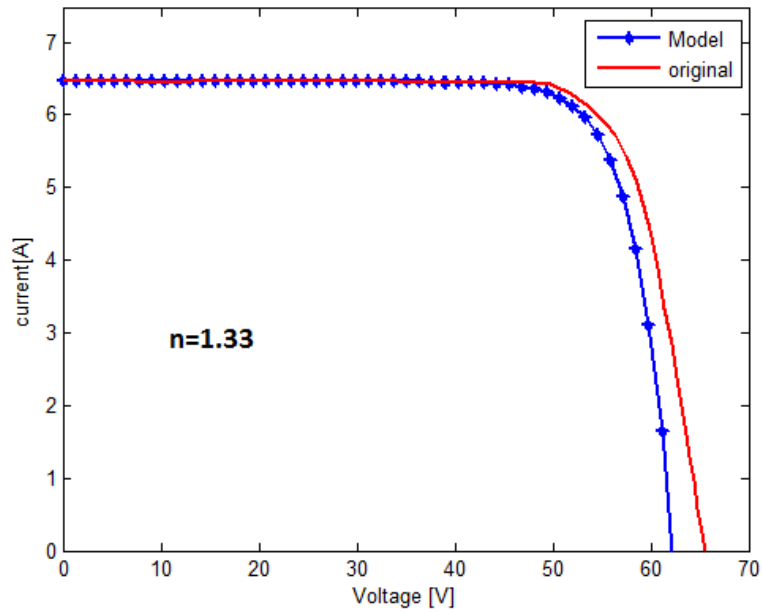


Figure 5. 11 Preliminary Results I-V Curves: Actual vs. Predicted ($n=1.33$)

The Figure 5.12 shows the R_s tuning and how it affects the I-V curve shape. The solid black curve is the actual curve while the other curves for different R_s values.

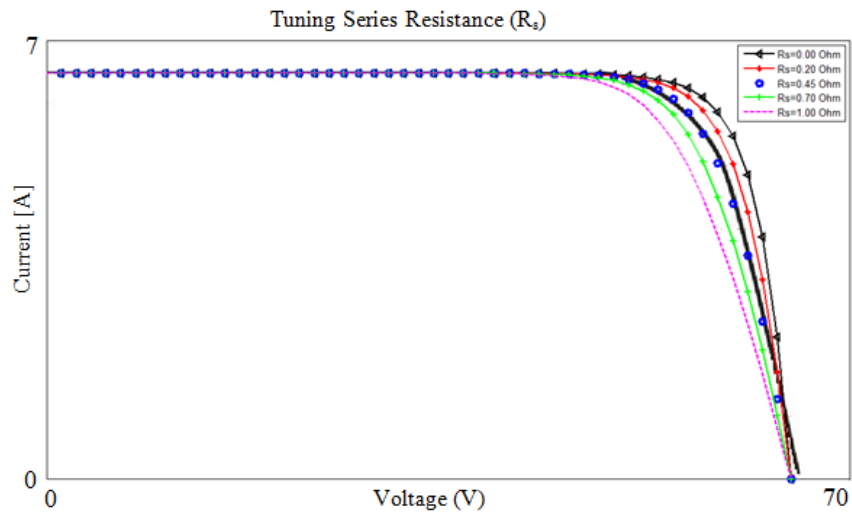


Figure 5. 12 Preliminary results I-V curves actual vs. predicted (different R_s)

The minimum error is found when ($R_s=0.45 \Omega$ and $n=1.1$). The Figure 5.13 shows the final model result. The solid lines represented the actual I-V curves reported by manufacturers and the “triangle and circle” are the proposed model results.

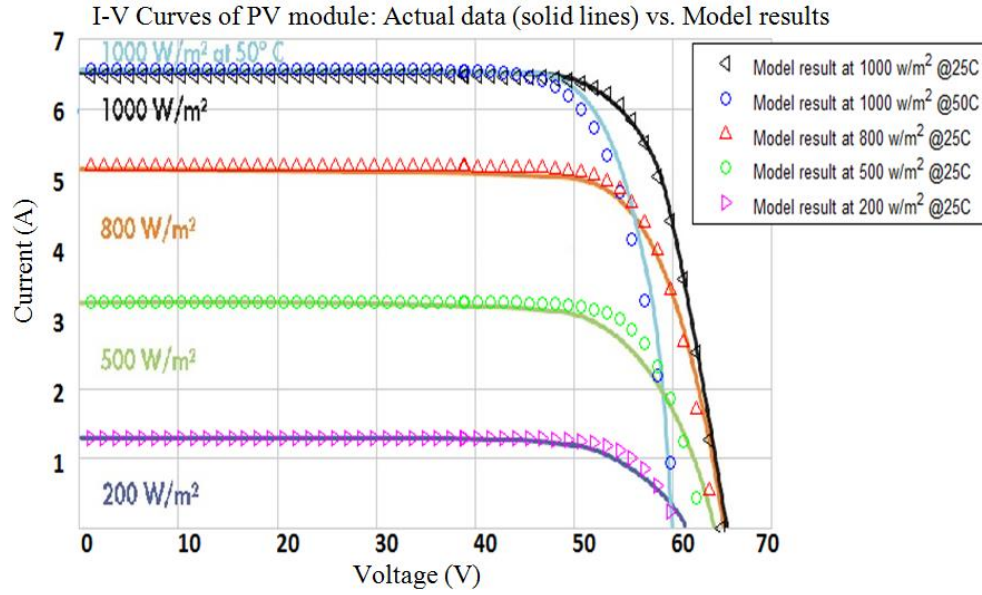


Figure 5. 13 I-V Curves (Actual data vs. model results)

Figure 5.14 shows the output of the proposed PV module in terms of power-voltage curves with different solar irradiance at fixed temperature. The maximum power output is reduced as the solar irradiance reduced.

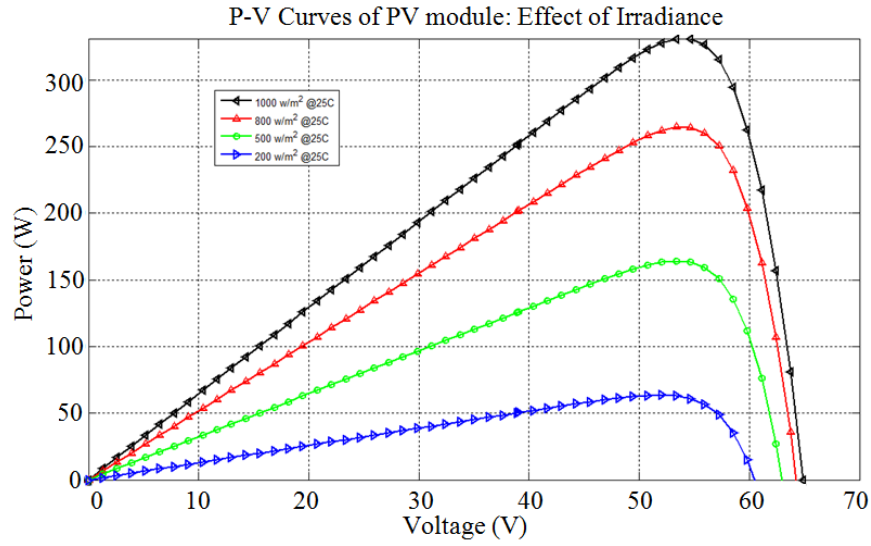


Figure 5. 14 P-V Curves in Different Solar Irradiance.

Figure 5.15 shows the output of the proposed PV module in terms of power-voltage curves with different temperature at a fixed solar irradiance. The maximum power output is reduced as the PV temperature is increased.

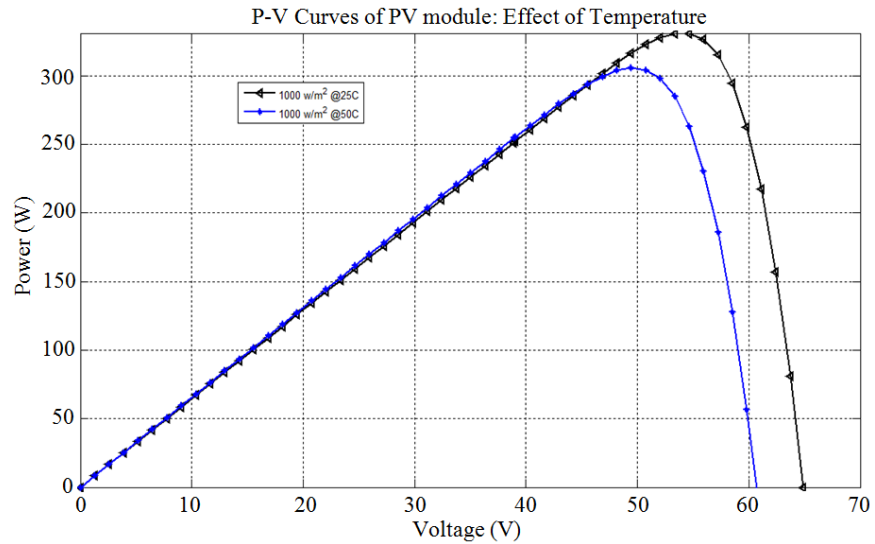


Figure 5. 15 P-V Curves at Different PV Temperature.

The parameters “ T & G ” in equation 5.13 still need further modeling stages, which will discuss later in the following sub-sections. Since, “ T ” represents the PV module temperature, which is different from ambient temperature. “ G ” is the effective solar irradiance, which depends on location, season, time, and module configuration and orientation.

5.5 The thermal performance of a PV solar module

As discussed previously, the performance of all PV module types reduces as the PV module temperature increase. There is no thermal model in the open literature to predict the PV module temperature for vehicle application installation. For that, the empirically based thermal model developed by Sandia Lab [212] is used to predict the PV cell model temperature based on the ambient temperature (see equations 5.23 and 5.24 [212]). The accuracy of this model is reported to be within $\pm 5^\circ \text{C}$ which corresponding to less than a 3% effect on the PV module power. By testing thousands of temperature measurements recorded over several different days, the empirical factors a , b , and ΔT are reported for every mounting configuration and module type.

The back-surface PV module temperature (T_m) is calculated using equation (5.23). This equation depends on ambient temperature, wind speed, solar irradiance, and couple of empirical parameters (a & b).

$$T_m = E \cdot (e^{a+b \cdot W_s}) + T_a \quad (5.23)$$

Where,

T_m : Back-surface module temperature ($^\circ\text{C}$)

T_a : Ambient air temperature (°C)

E : Solar irradiance incident on the module surface (W/m²) same as (G) in the proposed model.

WS : Wind speed measured at standard 10-m height (m/s)

a & b : Empirically determined coefficient

The equation (5.23) related the PV module temperature (T) with T_m , using equation (5.24).

$$T = T_m + \frac{G}{G(nom)} \Delta T \quad (5.24)$$

Where,

T : Cell temperature inside module (°C)

T_m : Measured back-surface module temperature (°C)

G : Measured solar irradiance on module (W/m²)

$G(nom)$: Reference solar irradiance on module (1000 W/m²) same as $G(nom)$

ΔT : Empirically determined coefficients

Table (5.1) shows the empirically determined coefficients of different module types and configuration type.

Table 5. 1 Empirically determined coefficients to predict PV module temperature [212]

Module Type	Mount	a	b	$\Delta T (^{\circ}\text{C})$
Glass/cell/glass	Open rack	-3.47	-0.0594	3
Glass/cell/glass	Close roof mount	-2.98	-0.0471	1
Glass/cell/polymer sheet	Open rack	-3.56	-0.0750	3
Glass/cell/polymer sheet	Insulated back	-2.81	-0.0455	0
Polymer/thin-film/steel	Open rack	-3.58	-0.113	3

The open rack configuration is allowed the air to circulate freely around the PV module. The close roof mount means the module is mounted in rack with little clearance between the surface and the module back, which allow less air to flow over the module. The insulated back means there is no clearance and there is no free air circulate behind the module, that is why the “ $\Delta T=0$ ” for this option, since there is no temperature differences between the back of the module and inside the module. Figure 5.16 shows the ambient temperature ($^{\circ}\text{C}$) in Phoenix, AZ in both June and December (Data source in [213]).

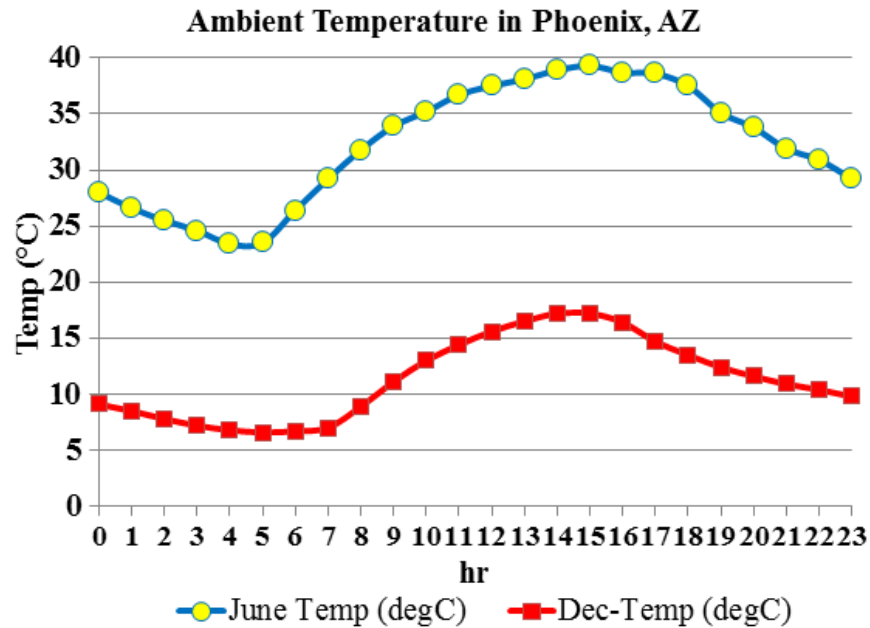


Figure 5. 16 The ambient temperature (°C) in Phoenix, AZ in both June and December (weather data in [213])

5.6 Modeling solar data

In this section, the model is estimated “G” or called “global horizontal irradiance (GHI)”, which is the total incident solar radiation reach the ground in unit kWh per m² for specific period e.g., day or year. The GHI reaches the ground in three ways: direct normal radiation (DNI), diffuse horizontal irradiance (DHI), and reflected. The DNI represents the solar energy reach the ground in a straight line from the sun. The DHI represents the amount of solar energy that does not arrive the ground on a direct path from the sun. The DHI component is arrived after scattering or diffused by molecules and particles in the atmosphere.

The “reflected component” represents the total solar radiation reflects to the PV module from the ground. Typically, the value of the reflected part is too small, which is dependent on ground nature (e.g., snow-covered ground different from grassy ground) and ignored [214]. In the proposed application, this component will be much smaller because the PV module will cover the vehicle body and far away from the ground, so it is ignored here.

The GHI is computed based on the equation (5.25), which is the summation of DHI and the cosine (θ) component of DNI [214]. The “ θ ” (see Figure 5.17) is the angle of incidence, which is defined as the angle between the beam radiation on a surface and the normal to that surface.

$$\text{GHI} = \text{DHI} + \text{DNI} \times \cos(\theta) \quad (5.25)$$

The $\cos(\theta)$ is estimated using the equations 5.26 & 5.27 below [214].

$$\begin{aligned} \cos(\theta) = & \sin(\delta) \sin(\phi) \cos(\beta) - \sin(\delta) \cos(\phi) \sin(\beta) \cos(\gamma) + \\ & \cos(\delta) \cos(\phi) \cos(\beta) \cos(\omega) + \cos(\delta) \sin(\phi) \sin(\beta) \cos(\gamma) \cos(\omega) \\ & + \cos(\delta) \sin(\beta) \sin(\gamma) \sin(\omega) \end{aligned} \quad (5.26)$$

$$\delta = 23.45 \sin\left(360 \frac{284 + n}{365}\right) \quad (5.27)$$

Where,

ϕ : Latitude, the angular location north or south of the equator, north positive.

δ : Declination, the angular position of the sun at solar noon (i.e., when the sun is on the local meridian) with respect to the plane of the equator (North positive). The Declination

is calculated using equation (5.27) [215], where n : is the number of day in year. The Table 5.2 displayed the recommended average days for months [216].

β : Tilt angle, the angle between the plane of the surface and the horizontal; . ($\beta = 0^\circ$ means that the PV surface is horizontal), ($\beta = 90^\circ$ means that the PV surface is vertical), and ($\beta > 90^\circ$ means that the surface has a downward facing components). This applies to fixed PV and PV with one-axis tracker.

γ : Surface azimuth angle, the deviation of the projection on a horizontal plane on the normal to the surface from the local meridian, with zero due south, -ve is east, +ve is west. These directions may be different if the geometry assumptions are changed.

This only applies for fixed PV module with tilt angle with no tracker option.

ω : Hour angle, the angular displacement of the sun east or west of the local meridian due to rotation of the earth on its axis at 15° per hour, morning is -ve and afternoon +ve.

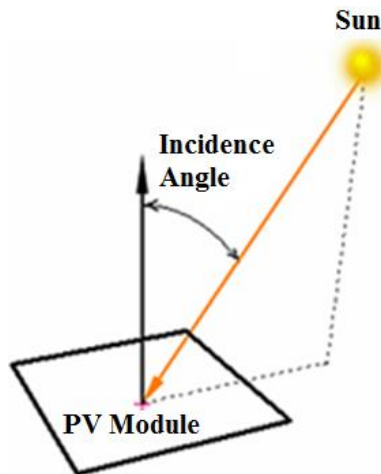


Figure 5. 17 Define Angle of Incidence

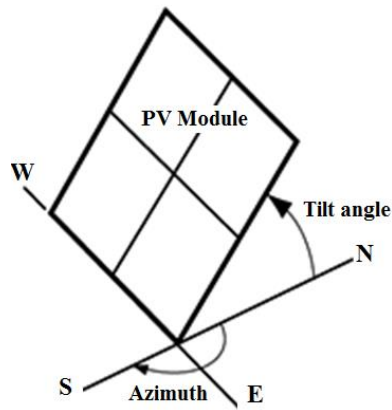


Figure 5. 18 Define Tilt Angle and Azimuth Angle

Table 5. 2 Recommended average days for months [216]

Month	Average Day of the month	Day of Year (n)
Jan	17	17
Feb	16	47
March	16	75
Apr	15	105
May	15	135
Jun	11	162
Jul	17	198
Aug	16	228
Sep	15	258
Oct	15	288
Nov	14	318
Dec	10	344

The weather data (in terms of ambient temperature, wind speed) and irradiance data (in terms of DHI and DNI), and geographical data (in terms of latitude and longitude) are input to the proposed model. These data are either directly measured or as here taken from reliable databases.

The annually GHI US solar map is shown below (see Figure 5.19 [217]). The highest solar energy in the U.S. in the places located in west south where the GHI is bigger than $1,900 \text{ kWh/m}^2/\text{year}$ and could reach more $2,300 \text{ kWh/m}^2/\text{year}$, this means the daily global solar between is roughly between 5.2 to 6.3 kWh/m^2 in these areas. There is less solar energy in the east south areas and the least solar energy is in the north and the northeast.

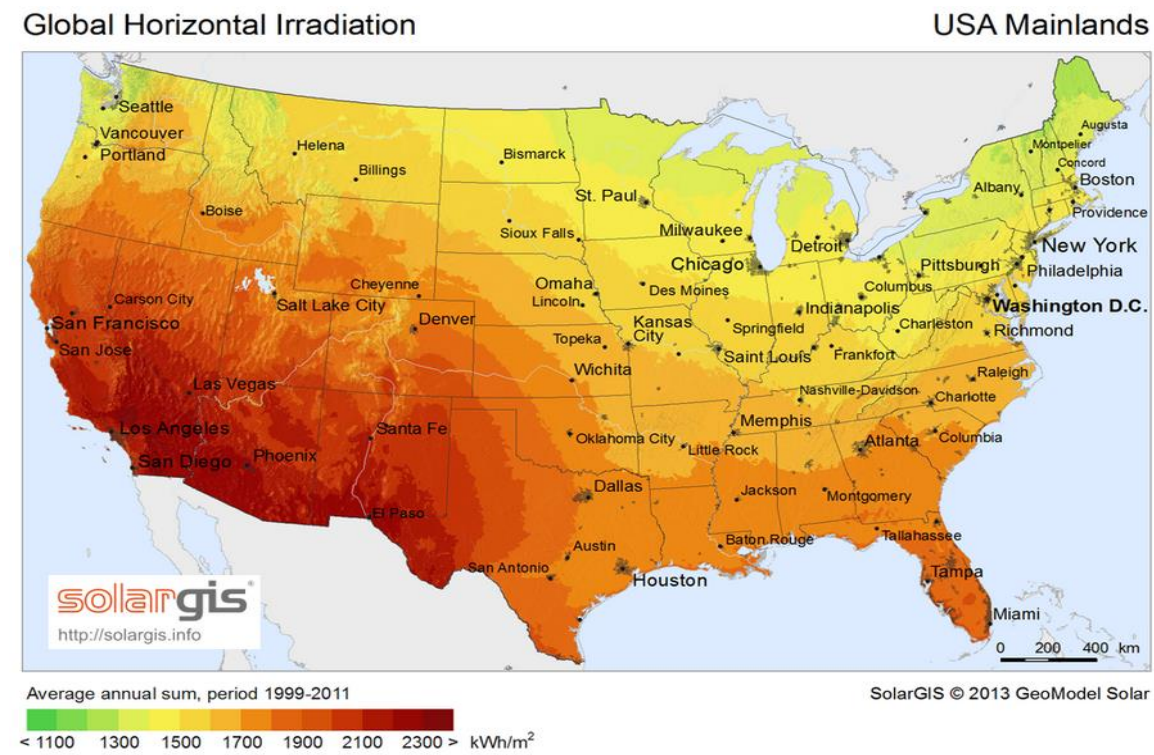


Figure 5. 19 Annually global horizontal irradiation in US states [217]

Two cities in the US are selected for full analysis through this work, which are represented the extreme cases, in terms of available solar energy; (i) Phoenix, Arizona and (ii) Boston, Massachusetts. For better understanding about how the average daily

solar is changed from month to month in these two cities, the average daily GHI are collected using weather data in [213]. Figure 5.20 shows the analysis of the gathered solar data. The highest average daily GHI in Phoenix, AZ and Boston, MA are occurring in June as 8.3 kWh/m^2 and 6.0 kWh/m^2 respectively. Whereas, the lowest daily GHI found in December in both cities as 3 and 1.6 kWh/m^2 in Phoenix and Boston, respectively. As expected, per each time (e.g., month) there are differences in solar data per location in the U.S. In addition, per each geographical location (e.g., city) there is difference in solar data per time (in this case month).

In addition, the solar data will be different per hour as shown in Figure 5.21. Figure 5.21 shows GHI in Phoenix, AZ hourly in June and December. In June, there is solar energy starts from 5 am increasing gradually to reach the maximum at noon, which around 1 kWh per m^2 , then decreasing until the sunset around 7 pm. In December, the maximum solar energy also at noon, but equal less than 0.5 kWh with availability of solar energy only from 7 am to 5 pm.

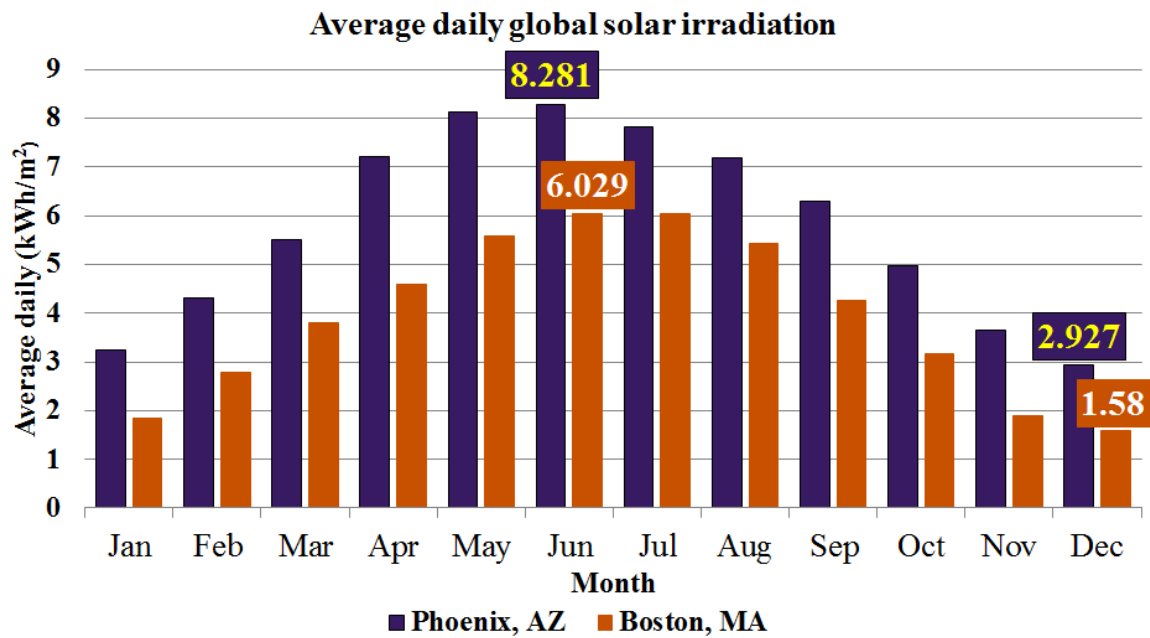


Figure 5. 20 Average daily GHI per month in Phoenix, AZ and Boston, MA (Source data from [213])

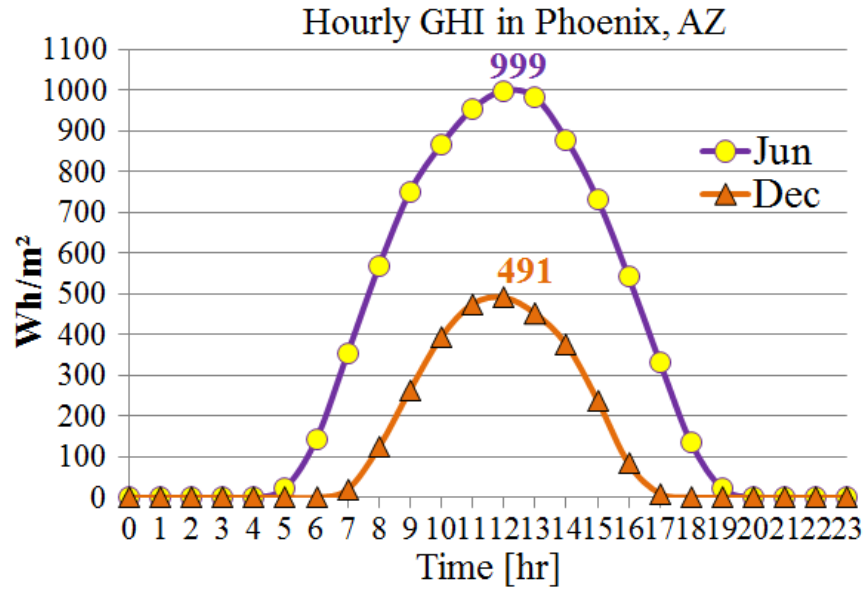


Figure 5. 21 Average Daily GHI Per Month in Phoenix, AZ and Boston, MA (Source data from [213])

There is a difference between local clock time and solar time. The solar time is based on the apparent angular motion of the sun across the sky, with solar noon the time the sun crosses the meridian of the observer and calculated using equation (5.28) [214]. The differences between solar time and standard time (in minutes) are based on the correction factor (E) based on the number of the day in a year and the fact of that the sun takes 4 minutes to transverse 1° of longitude.

$$\text{Solar time} - \text{Standard time} = 4(L_{st} - L_{loc}) + E \quad (5.28)$$

Where,

L_{st} is the standard meridian for local time zone. The L_{st} of U.S. time zones is for Eastern (75°W), Central (90°W), Mountain (105°W), and Pacific (120°W).

L_{loc} is the longitude of the location in degrees west.

E is the called the correction factor (in minutes) calculated using equations (5.29) and (5.30) [218], [219].

$$E = 229.2 (0.000075 + 0.001868 \cos(B) - 0.032077 \sin(B) - 0.014615 \cos(2B) - 0.04089 \sin(2B)) \quad (5.29)$$

$$B = (n - 1) \times \frac{360}{365} \quad (5.30)$$

Where, B in degree and n is the day of the year (same as in Table 5.2)

Example of the calculations, suppose the PV module is located in Phoenix, AZ in June. Phoenix follow Mountain time zone, so $L_{st} = 105^\circ W$, $L_{loc} = 112.071^\circ$, and $n = 162$. So, $B = 158.8^\circ$ and $E \approx 0$ minute. The solar time is equal the standard time minus 7.07 minute. The calculated δ is 23.1° and the latitude in this location is equal $\phi = 33.45^\circ$. Suppose the orientation of the PV module is horizontal and is faced to the south. For that, the calculated angle of incidence (θ) is shown in Figure (5.22). In June in Phoenix-AZ, at noon the sun is almost perpendicular with (θ) is around 10° and θ is bigger than 50° before 8 am and after 4 pm. Figure (5.23) shows θ in same location Phonex-AZ, but in December. The θ in December is at least 60° , which is much higher than June is as displayed.

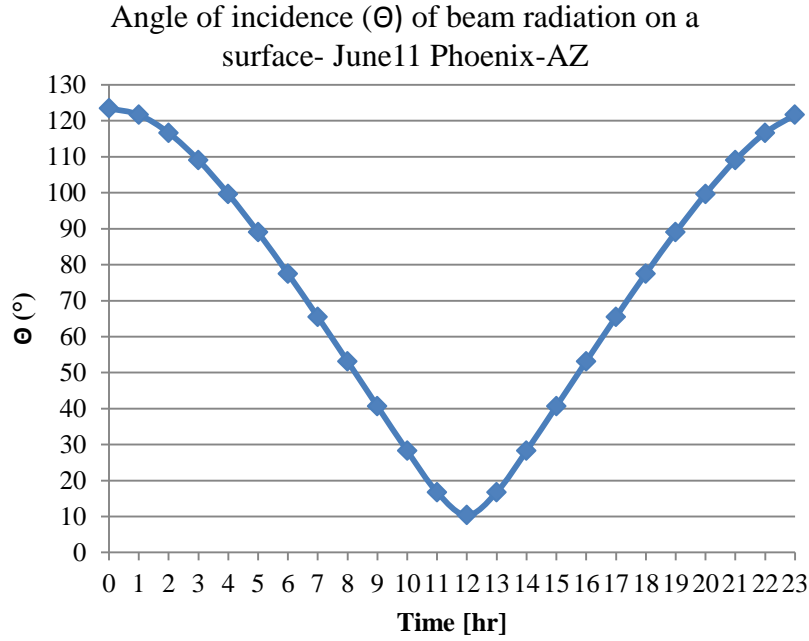


Figure 5. 22 The angle of incidence (Θ) of beam radiation on a surface- June 11 Phoenix-AZ

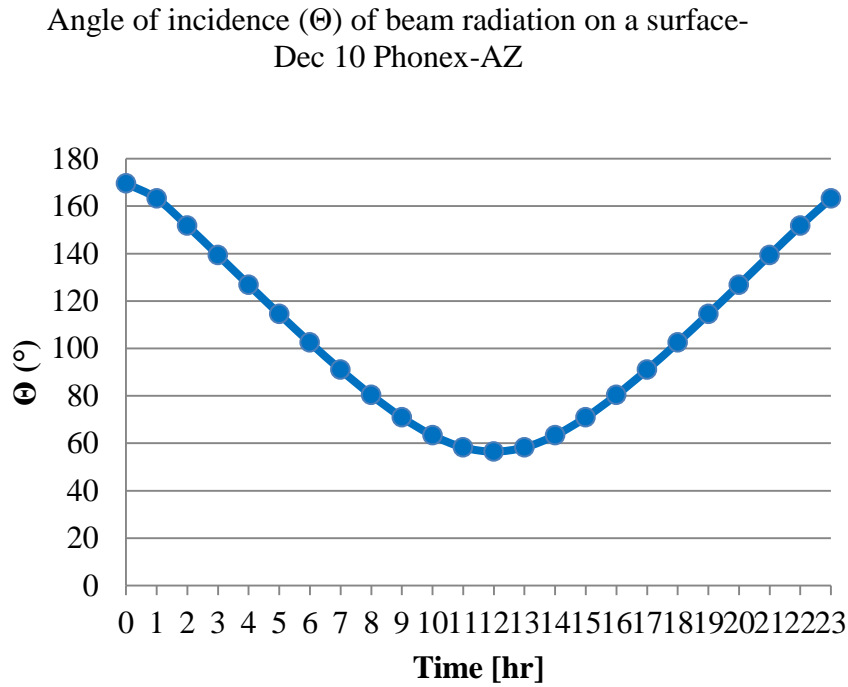


Figure 5. 23 The angle of incidence (Θ) of beam radiation on a surface in Dec, 10 (Phoenix, AZ)

By substituting the published DHI and DNI for June in Phoenix-AZ [213] in Equation (5.25), the GHI is calculated and displayed in Figure (5.24) .

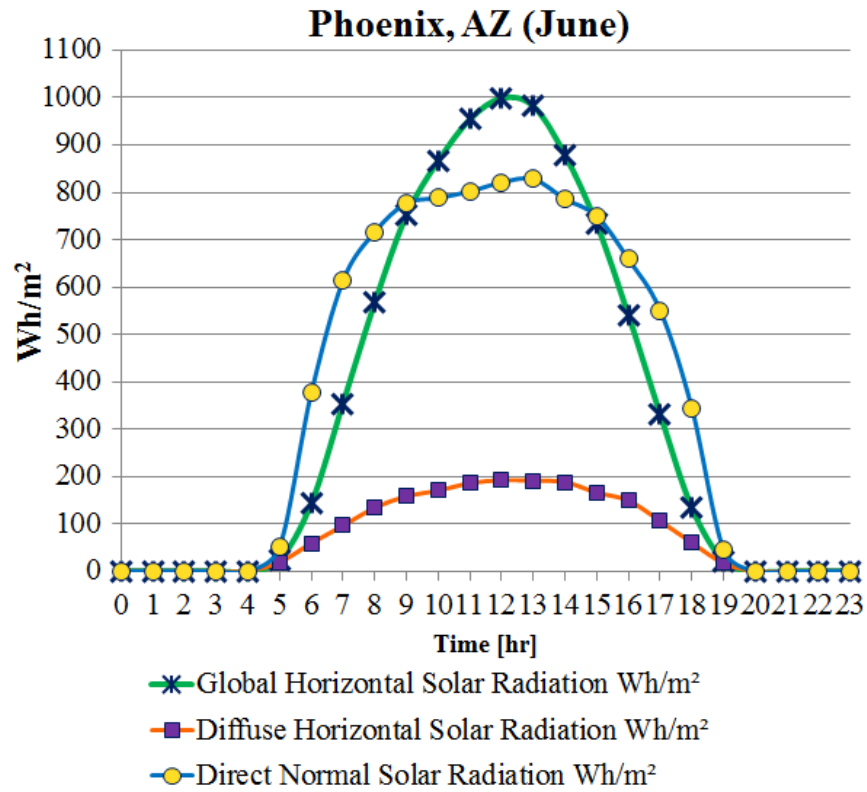


Figure 5. 24 DNI, DHI, and GHI for Phoenix, AZ in June

The output of the proposed model in terms of predicted GHI is compared with the actual published GHI and displayed in Figures 5.25. The error between both values is shown in Figure 5.26 with maximum and minimum error around $-3/+4 \text{ Wh/m}^2$.

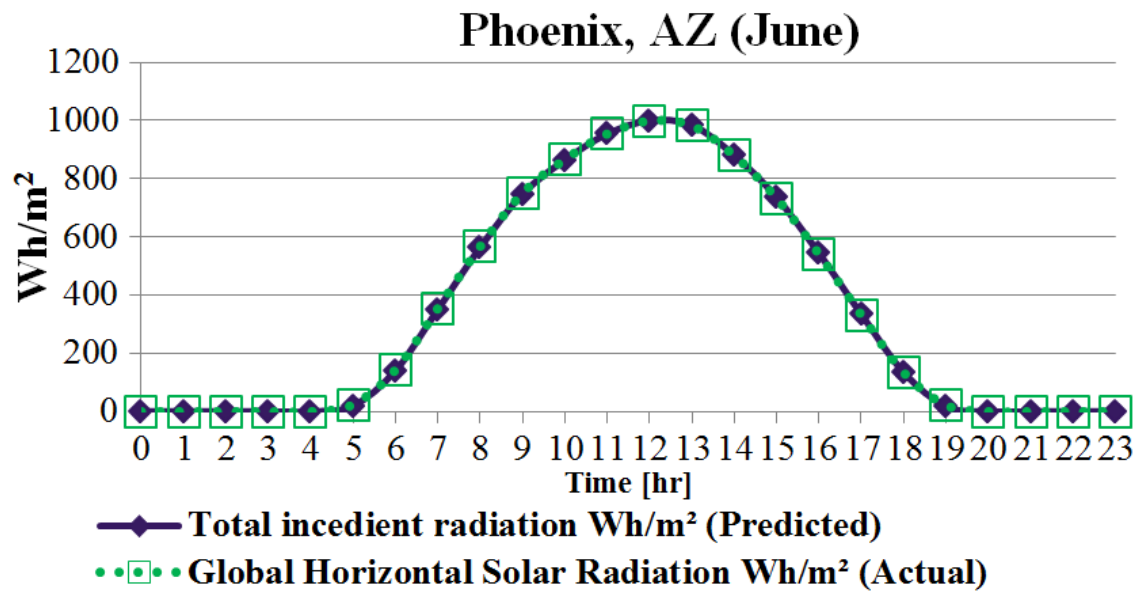


Figure 5. 25 Predicted and Actual GHI

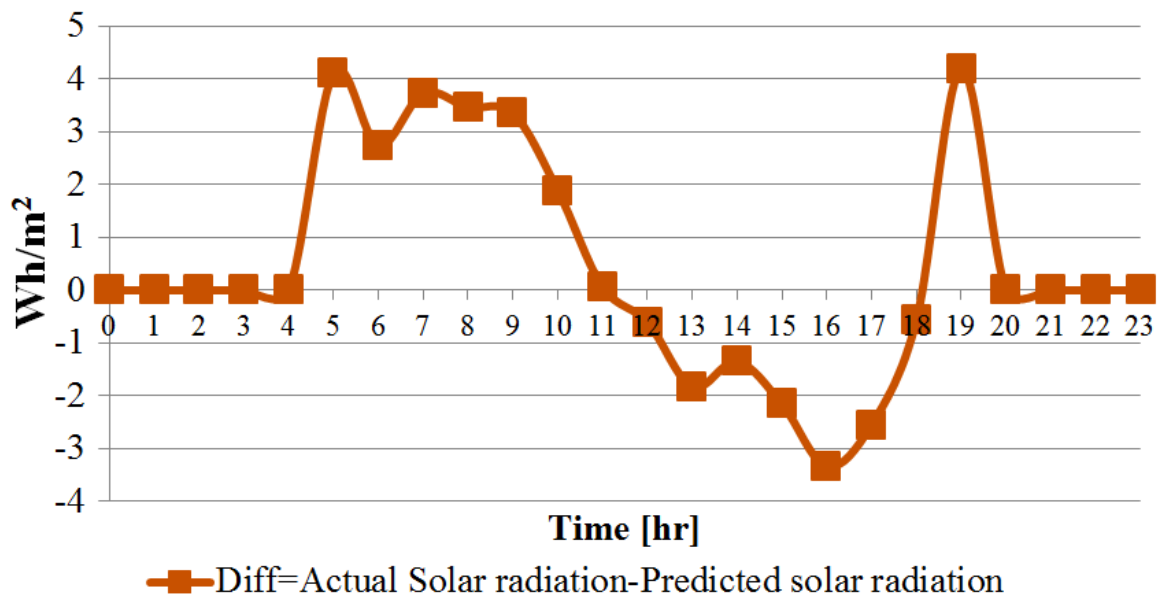


Figure 5. 26 Error between Actual and Predicted GHI

5.7 Maximum power point tracking (MPPT) algorithm

The MPPT algorithm is implemented to track the optimum operating points (the orange/ yellow dots in Figure (5.27)) in terms of maximum operating power. In every solar irradiance and/or every PV module temperature, the MPP is changed and the algorithm needs to keep track it. The MPP implies optimum voltage and optimum current the PV system needs to work on.

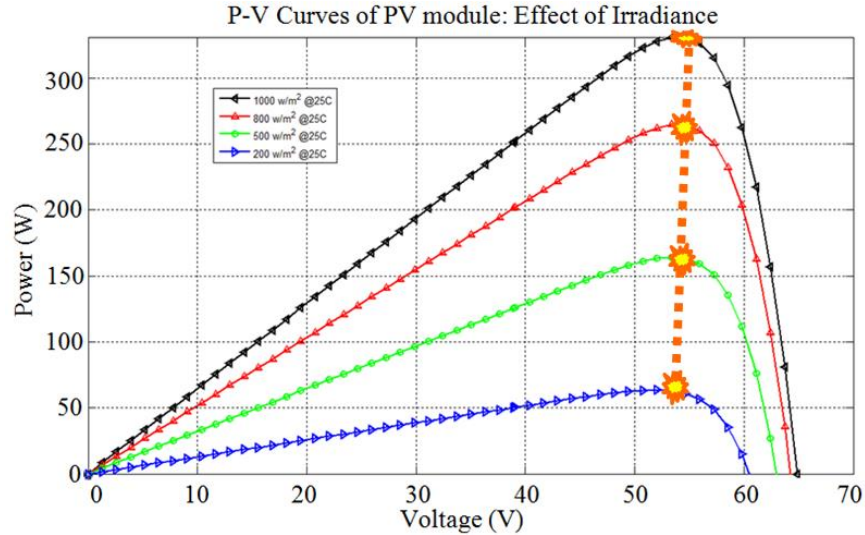


Figure 5. 27 P-V curves of PV model and MPP

In this work, the incremental conductance (IncCond) algorithm [220] is implemented to track MPP points. This algorithm is based on tracking the sign of the power-voltage derivative “ dP/dV ” for every curve. If the sign is “+ve” this mean this point is located to the left of MPP “left of solid orange line”. But, if the sign is “-ve”, this indicates that this point is located to the right of MPP. The algorithm keeps track the MPP by increasing or decreasing the search point depends on their location to the actual MPP until the

“ $dP/dV=0$ ”, at this point, the MPP is located. The equations (5.31) to (5.33) [220] show the math behind this algorithm.

$$P = I \times V \quad (5.31)$$

$$\frac{dp}{dV} = \frac{d(IV)}{dV} = I + V \times \frac{dI}{dV} \quad (5.32)$$

$$\begin{cases} \frac{dp}{dV} = 0 & , \text{at the MPOP} \\ \frac{dp}{dV} > 0 & , \text{to the left of the MPOP} \\ \frac{dp}{dV} < 0 & , \text{to the right of the MPOP} \end{cases} \quad (5.33)$$

For ideal case scenario, assuming the PV module temperature is equal the ambient temperature. After applying the MPPT algorithm, the optimum PV power and efficiency in Phoenix, AZ in both June and December months are shown in Figures 5.28 and Figure 5.29. Even, in the ideal scenario the optimum output power in Phoenix, AZ does not reach the peak power reported by PV manufacturer under STC (Figure 5.6). The reported P_{max} under STC is equal 327 W while the maximum power are founded at noon are 317 and 165 watts for June and December, respectively. The founded PV module efficiencies are lesser than the reported efficiency by PV manufacturer at STC. Only at noon, it reaches 19.46% and 10.11 % in June and December, respectively.

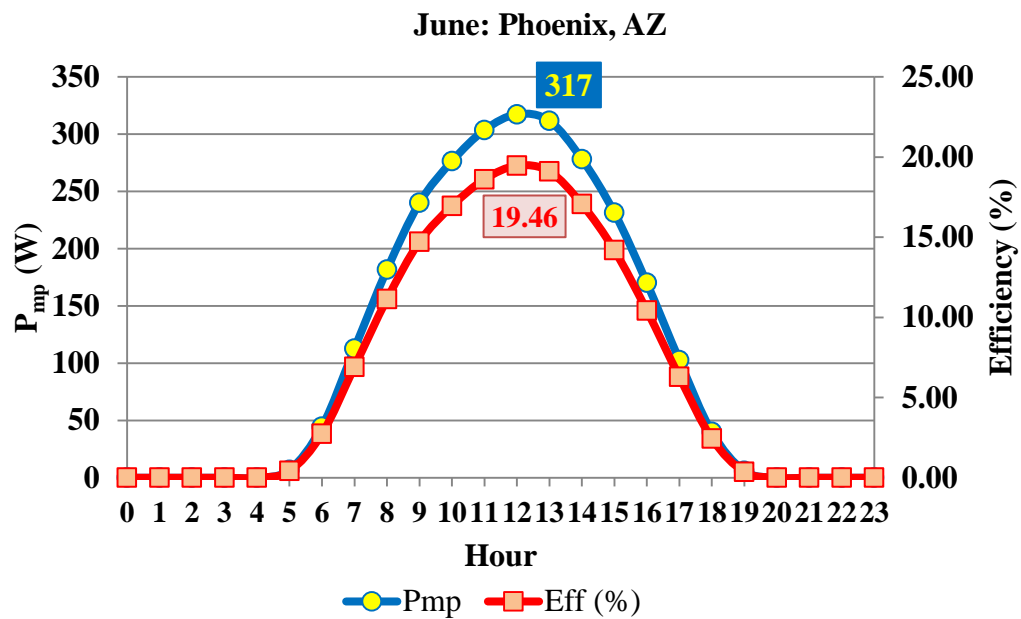


Figure 5. 28 Optimum PV module output power and PV efficiency in June in Phoenix, AZ

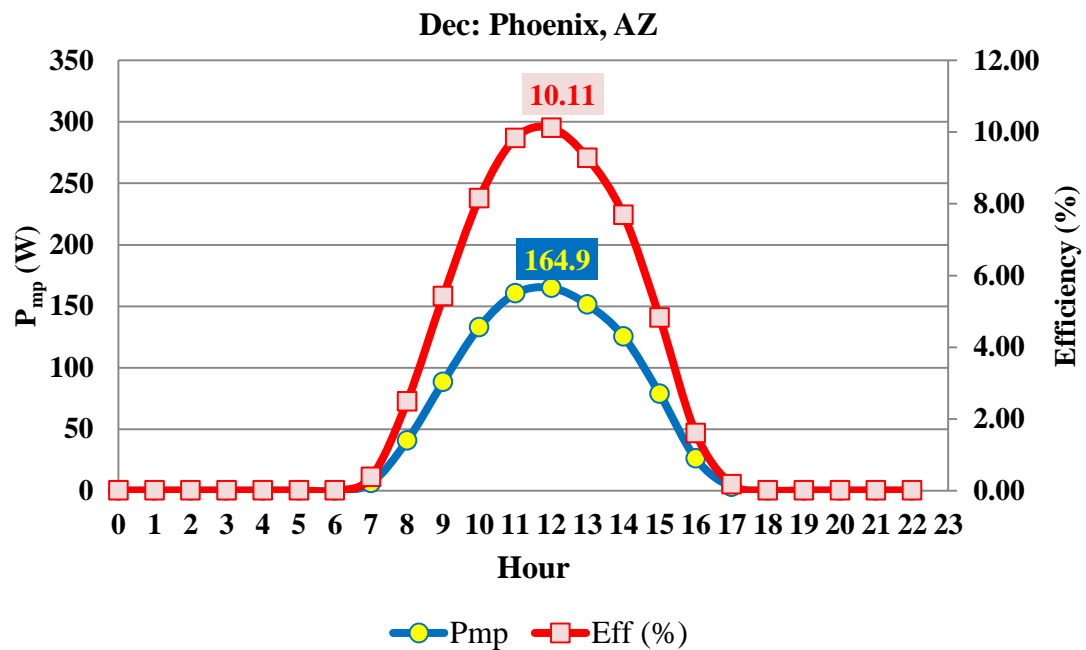


Figure 5. 29 Optimum PV module output power and PV efficiency in December in Phoenix, AZ

The Figure 5.30 shows the optimum output voltage in both December and June in Phoenix, AZ. The output voltage is almost constant when there is available solar, however, this voltage should be matched with battery voltage as will discuss later.

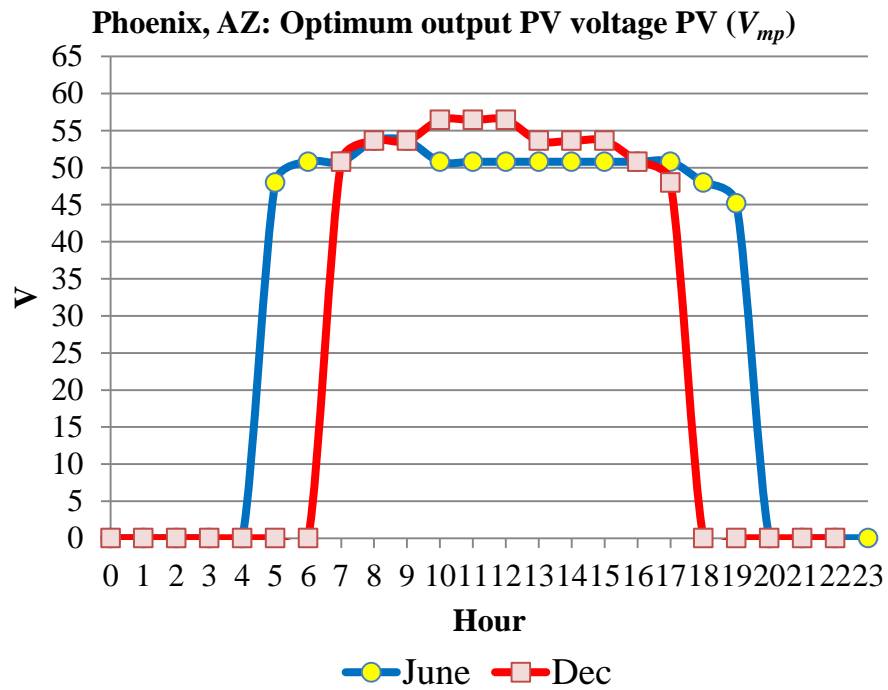


Figure 5. 30 Optimum PV Output Voltage in June and December in Phoenix, AZ

5.8 Modeling Energy Storage

The on-board PV module converts the solar energy to direct current (DC) electricity to power the vehicle propulsion. In most cases, the available energy cannot be used directly to the wheels of the vehicle so the ability to store the energy on-board is required.

In general, many energy storage technologies include batteries, flywheel, super-capacitor, compressed air, hydraulic fluid, etc. Figure (5.31) shows the main types of electrical energy storage systems [221].

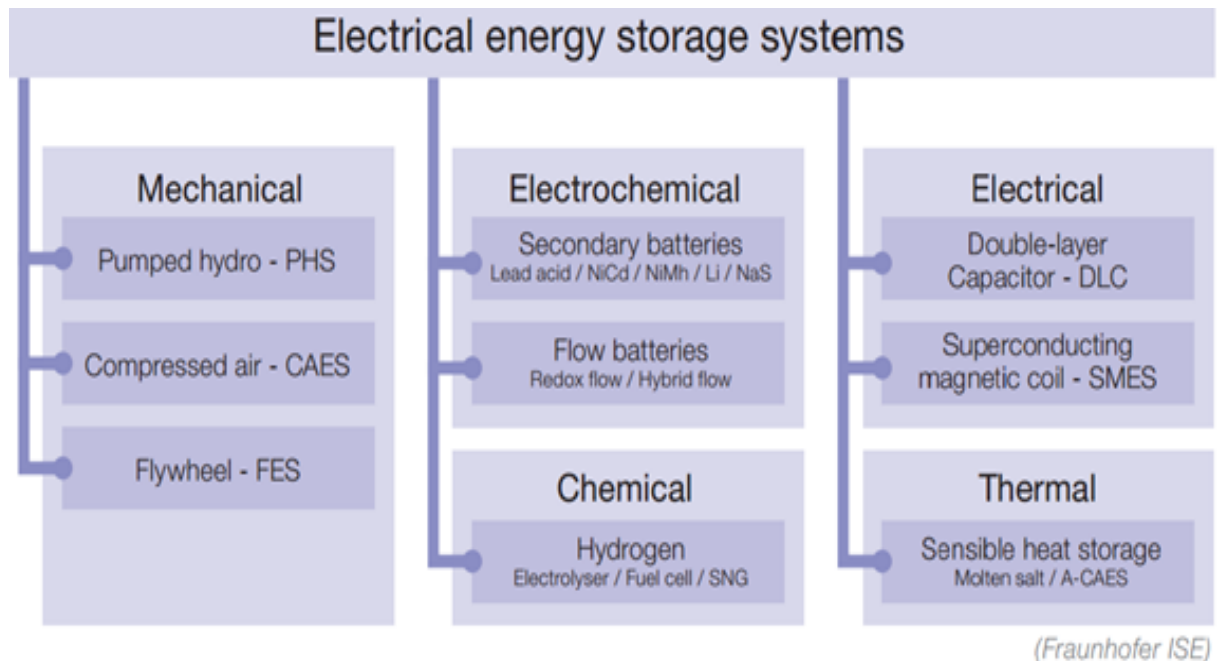


Figure 5. 31 Energy storage classification [221]

The secondary batteries have commonly been used in PV applications. The batteries are electrochemical storage devices composed of individual cells. Depending on the

application, multiple batteries are connected in series and called battery string (bank). If the battery is non-rechargeable it is called primary battery, while it is called secondary battery when it is rechargeable. There are many secondary battery types (see Figure 5.32 [222]) include Lead acid, NiCd, NiMH, Li-ion, etc. The batteries are different in terms of material, weight energy density, volume energy density, cost, lifetime span, capacity, and discharge time [223]-[225]. Figure (5.32) shows the specific energy and specific weight for different secondary battery cell types. The values correspond to the cell level and not including cooling system, electrical system, etc.

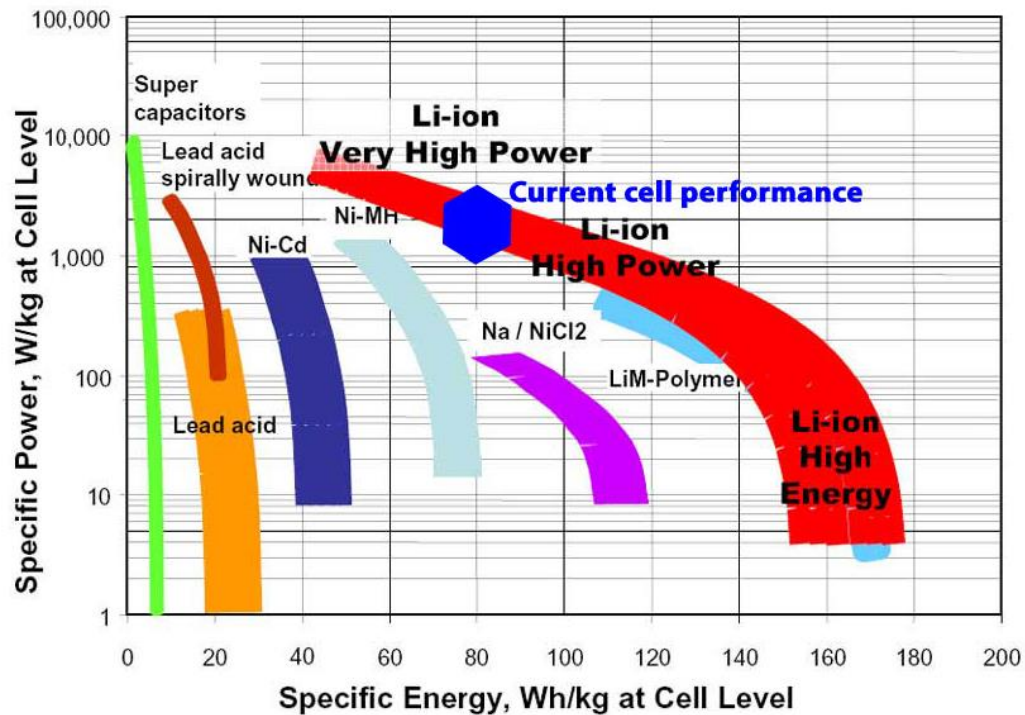


Figure 5. 32 Specific energy and specific power of different cell types [222]

The specific energy or it is called energy density is important for a pure EV since it controls the driving range of the vehicle. On the other hand, it is also important to have a high specific power since it controls the performance of the vehicle. The Lead-acid

battery is the most common battery and the cheapest one, but as shown in Figure 5.32 , it has relatively the lowest specific energy. In general, for standalone PV application the lead acid batteries are used to minimize the cost as weight is not a constraint. Charging lead acid batteries by PV is discussed previously in Chapter 2. For automotive application, the weight is a critical issue, for that mostly many types of the Lithium-ion (Li-ion) batteries are used in vehicles.

The Li-ion batteries [226] used to charge the solar PV experimentally in [227]. In this work, the Lithium Ion Polymer battery is modeled. The cathode is based on LiFePO_4 and the anode is Carbon-based. This type is relatively recent and currently viewed as one of the promising battery technologies for future EV and HEV market. Li-Ion polymer eliminates the liquid electrolytes and can be molded into different shapes. The full specifications of the battery system are found in previous publications [228], [229].

The battery model here is based on simple model (See Figure 5.33) consists of open circuit voltage (E_0) and a series resistance (R). This model is called a static model or 0th order model since it does not capture the dynamic of the battery, but it does provide accurate result given the simplicity in the absence of experimental testing data, since here the battery internal characteristics is not the scope of this study. To capture the dynamics of the battery 1st, 2nd, 3rd, etc... order(s) model can be used. The differences in modeling are that in addition to the model has ideal voltage source and internal resistance (simple model), the dynamic model will have resistance-capacitor RC circuit(s). The behaviors of (E) and (R) are different in charging and discharging modes and are varying with battery state of charge (SOC) and temperature (T).



Figure 5. 33 Battery Simple Model Electric Circuit

The Equations 5.34 and 5.35 below show the relation between batteries current and voltage in charging and discharging stages.

$$V_{disch} = E_{disch} - R_{disch} \times I_{disch} \quad (5.34)$$

$$V_{ch} = E_{ch} + R_{ch} \times I_{ch} \quad (5.35)$$

Where,

V_{ch} , the battery voltage in charging

V_{disch} , the battery voltage in discharging

E_{disch} , the open circuit battery voltage in discharging

E_{ch} , the open circuit battery voltage in charging

I_{disch} , the battery discharging current

I_{ch} , the battery charging current

R_{disch} , the internal battery resistance in discharging

R_{ch} ,the internal battery resistance in charging

These equations are fitted using battery's manufacturer charging and discharging curves to determine E_{disch} , E_{ch} , R_{disch} , and R_{ch} using these steps:

First, digitized the discharging and charging curves published by battery manufacturer. The Figures 5.34 and 5.35 shows the generated plot based on image processing techniques by reading and rewriting the manufacturer published plots related battery capacity with battery voltage.

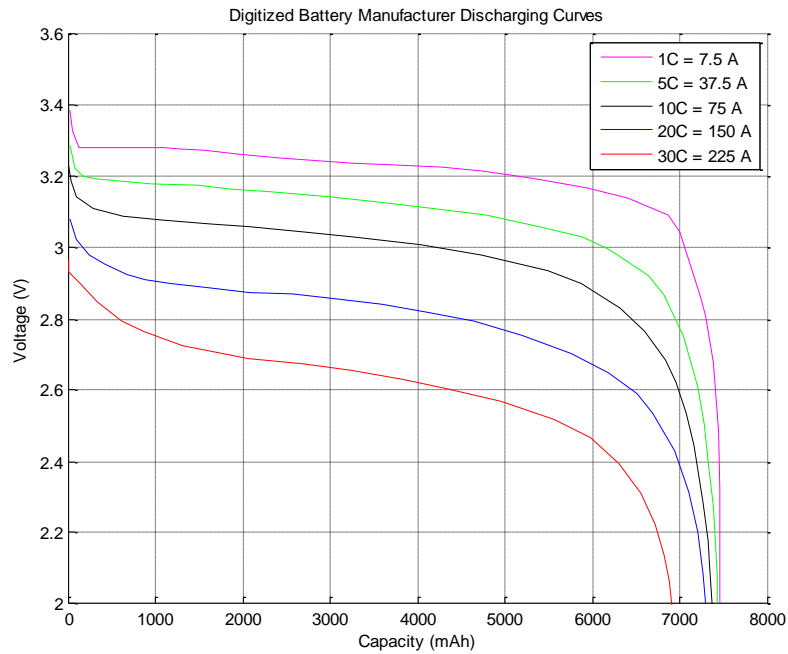


Figure 5. 34 Digitized Battery Manufacturer Charging Curves

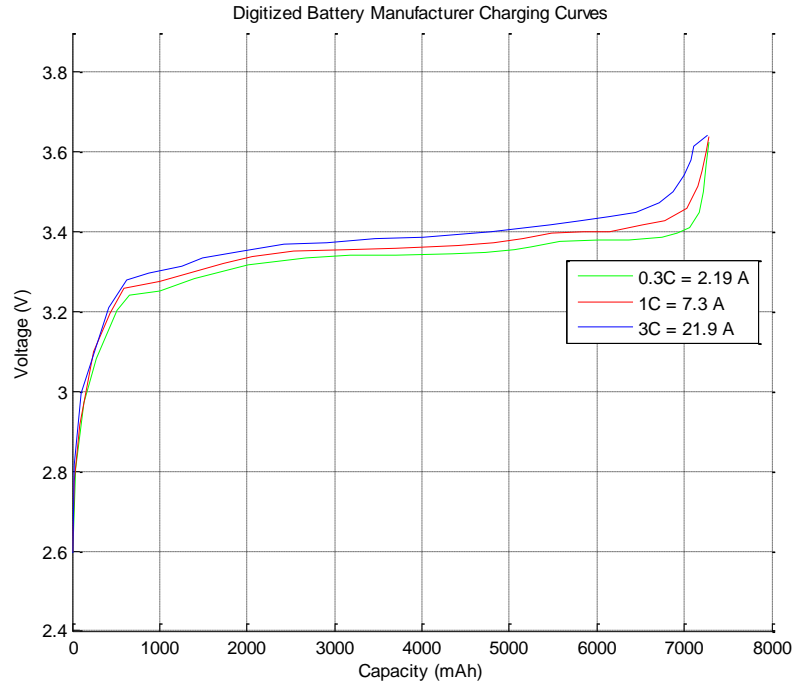


Figure 5.35 Digitized Battery Manufacturer Discharging Curves

The Peukert effect is included for discharging curve using Equation (5.36) to find the normalize battery SOC.

$$\Delta SOC_I \% = - \left(\int \frac{I}{C_I} dt \right) \times 100 \quad (5.36)$$

The fitting is done in the linear region using the following Equations (5.37)-(5.40):

$$E_{disch} = \alpha_0 + \alpha_1 \times SOC + \alpha_2 \times T \quad (5.37)$$

$$R_{disch} = \beta_0 + \beta_1 \times SOC + \beta_2 \times T \quad (5.38)$$

$$E_{ch} = \alpha_0 + \alpha_1 \times SOC \quad (5.39)$$

$$R_{ch} = \beta_0 + \beta_1 \times SOC \quad (5.40)$$

Where,

α_i, β_i ($i=0,1$, and 2) parameters for discharging mode found by curve fitting.

α_j, β_j ($j=0$ and 1) parameters for charging mode found by curve fitting.

Typically, the E_{ch} and R_{ch} are also functions of both SOC and T but since the manufacturer does not publish the behavior of charging voltage under different temperatures, the fitting is done with dependent on SOC only. If the fitting consider fixed temperature, the fitting matrix result will be close to singular, which makes the results may be not accurate. The Figures 5.36 and 5.37 validates the model results by comparing the predicted output versus the actual (published) values.

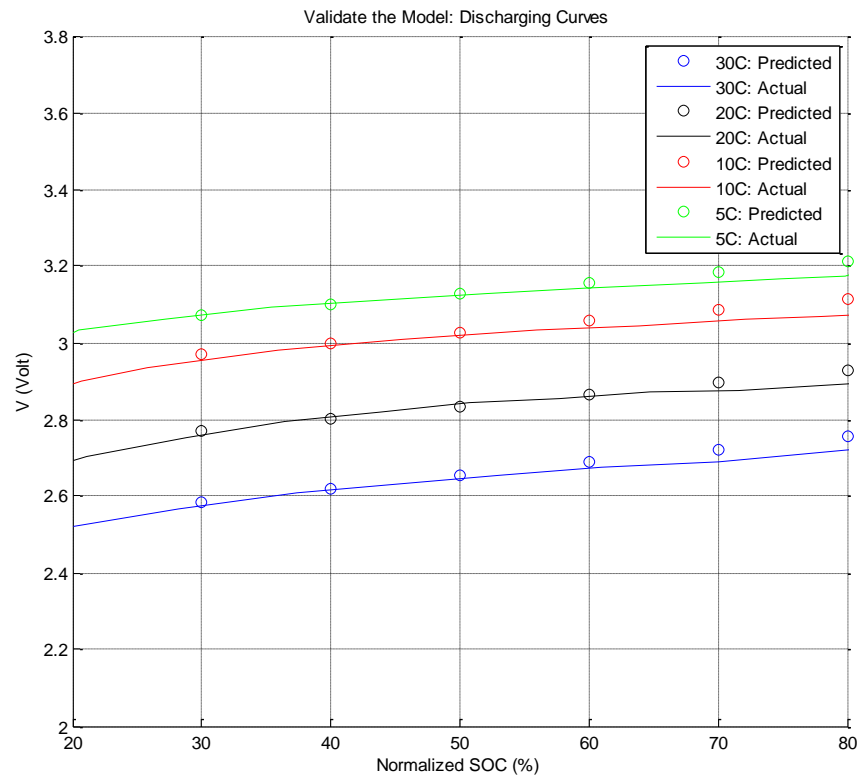


Figure 5. 36 Validate the Model: Discharging curves (Solid lines actual data & Circles represent model output)

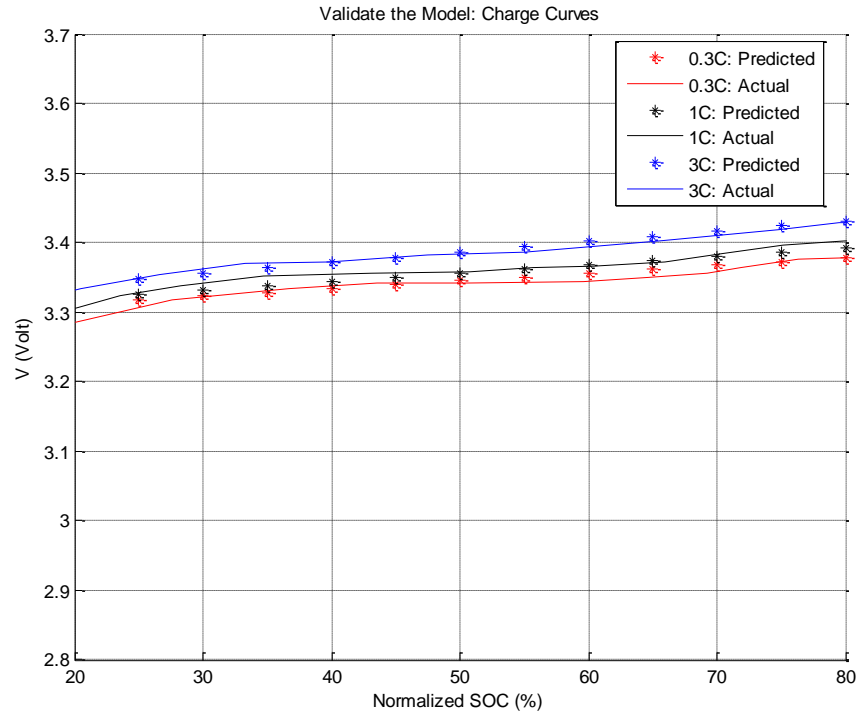


Figure 5. 37 Validate the model: Charging curves (Solid lines actual data & stars represent model output

The Simulink[®]/Matlab[®] is used to model the battery. The Figures 5.38, 5.39, and 5.40 show the model steps. The electric model is shown in Figure 5.38 is related to the single cell battery, and N is the number of cells. Multiply the N with single battery to determine battery voltage (size). In the following subsection, the optimum battery size for charging from PV module is discussed.

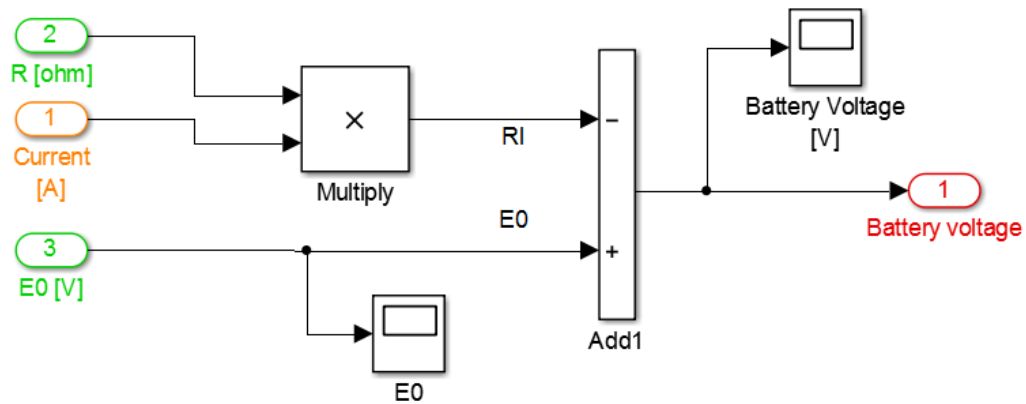


Figure 5.38 Single Cell Electric Equation

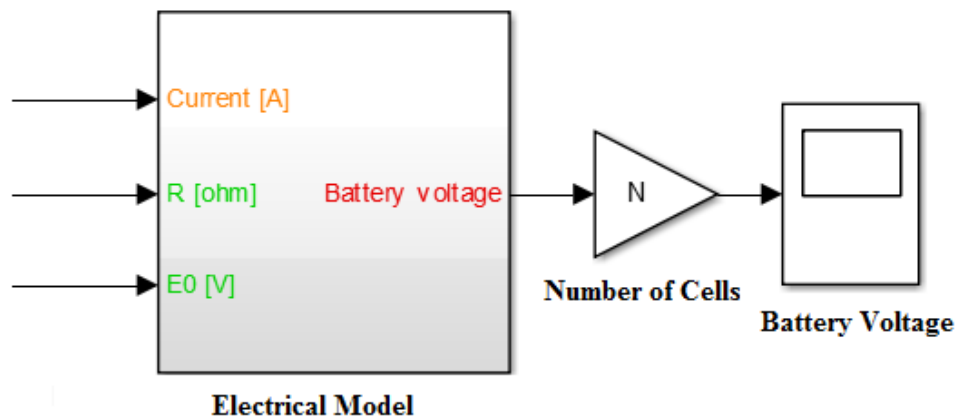


Figure 5.39 Battery Electric Equation

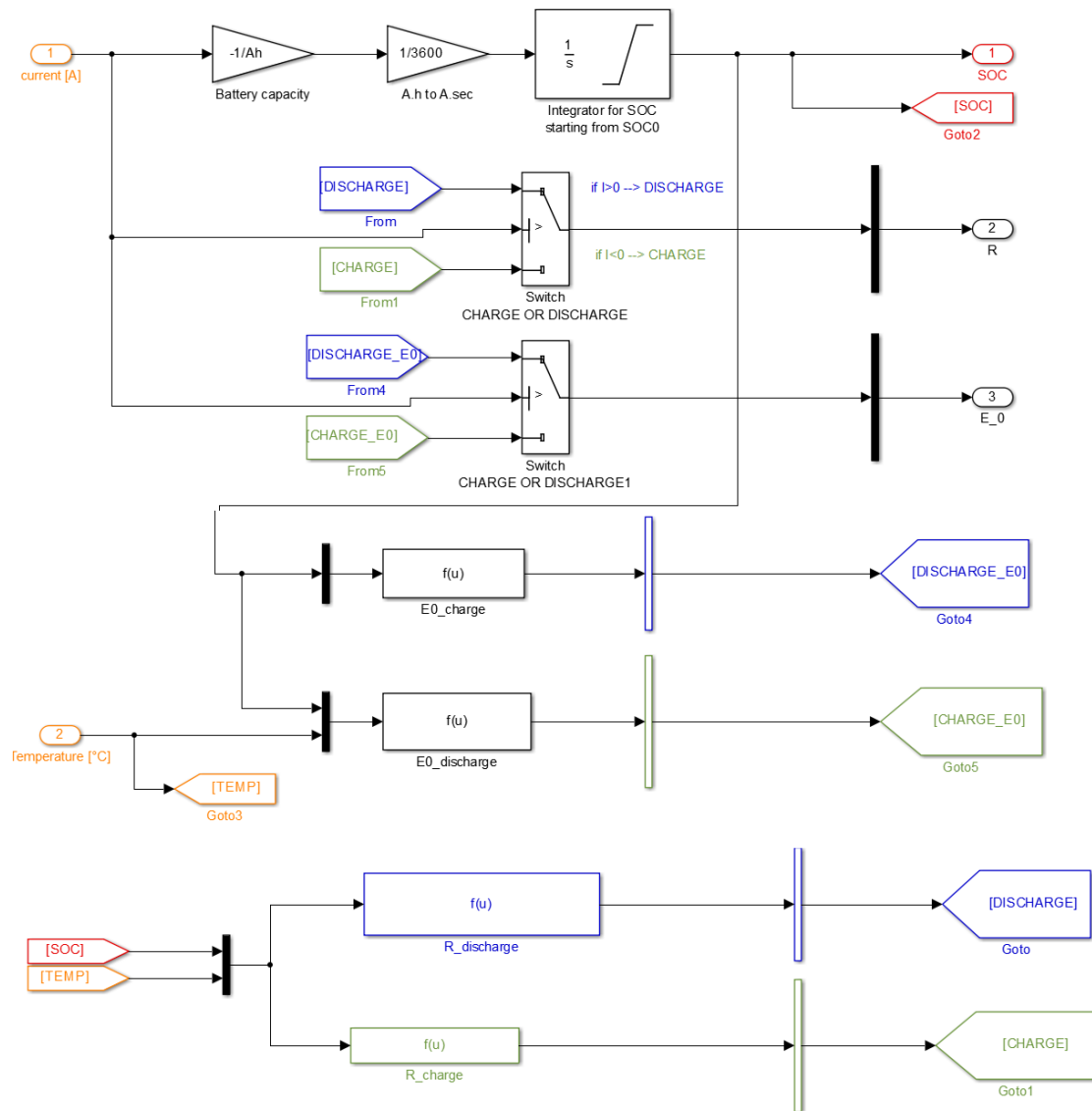


Figure 5. 40 Estimation Battery Parameters

The SOC (in Figure 5.40) are calculated based on current integration method using Equation (5.41):

$$SOC(t) = SOC_0 - \frac{\int_0^t \eta(t) \times I(t) dt}{E_{nom}} \quad (5.41)$$

Where,

SOC_0 , is the initial state of charge of the battery

E_{nom} , is the nominal battery capacity (Ah)

η , is the battery efficiency and calculated using Equations (5.42) and (5.43):

$$\overline{\eta}_{ch} = \frac{\int_{I<0} (E_0 \cdot I) dt}{\int_{I<0} (V \cdot I) dt} \quad (5.42)$$

$$\overline{\eta}_{disch} = \frac{\int_{I>0} (V \cdot I) dt}{\int_{I>0} (E_0 \cdot I) dt} \quad (5.43)$$

5.9 Optimized PV Energy Output

In this section, many parameters are investigated with the purpose to optimize PV energy output for vehicle application by optimize the ratio of solar energy to the DC electricity output.

5.9.1 Mounting configuration effect on PV temperature

Figure 5.41 shows the effects of the different mounting configuration on PV module temperature in June month in Phoenix, AZ. In general, the open rack configuration is preferred to keep the PV module temperature as low as possible. The glass/cell/polymer sheet configuration has both the highest and lowest PV temperature depends on mounting option. The lowest (best) when open rack is used and the highest (worst) in insulated back option. For other scenarios, the PV temperature will be lesser, so this show the extreme case.

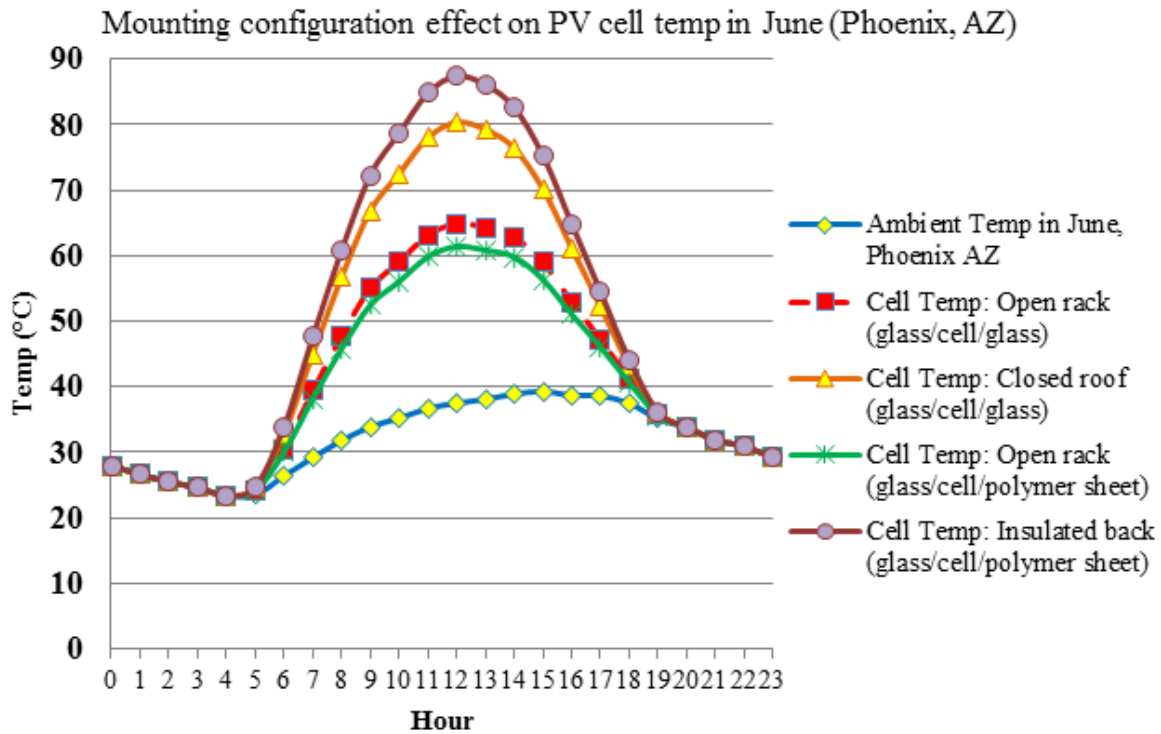


Figure 5. 41 Effects of mounting configuration on PV cell temp in June (Phoenix, AZ)

Figure (5.42) shows the PV output power for three different scenarios in June (Phoenix, AZ); (i) the best (theoretical) scenario is when the PV cell temperature is equal ambient temperature, (ii) using the best mounting option (open rack), and (iii) using the worst option (insulated back).

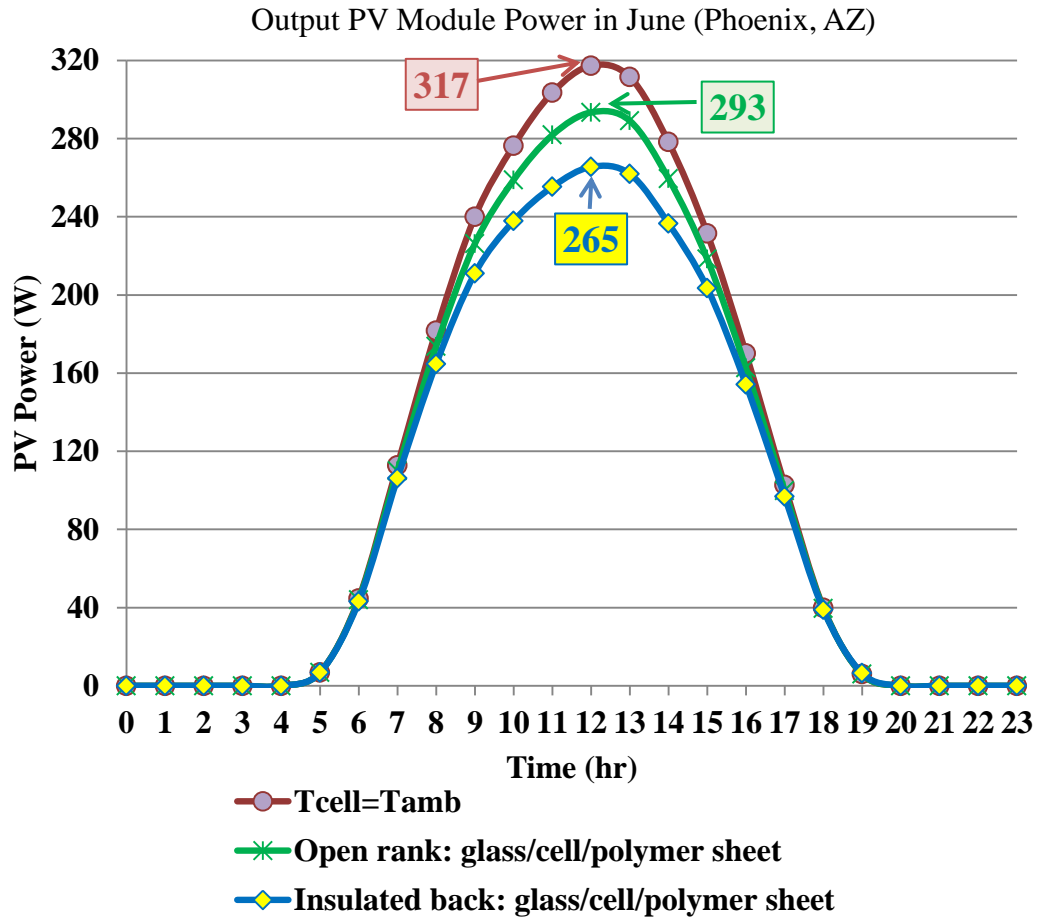


Figure 5. 42 Effects of mounting configuration options in PV output power in June in Phoenix, AZ

As displayed the maximum power is further reduced than scenario (i) and the power loss is varying between 8 to 16 % depends on mounting configuration. Figure 5.43 shows the power output losses in the extreme case.

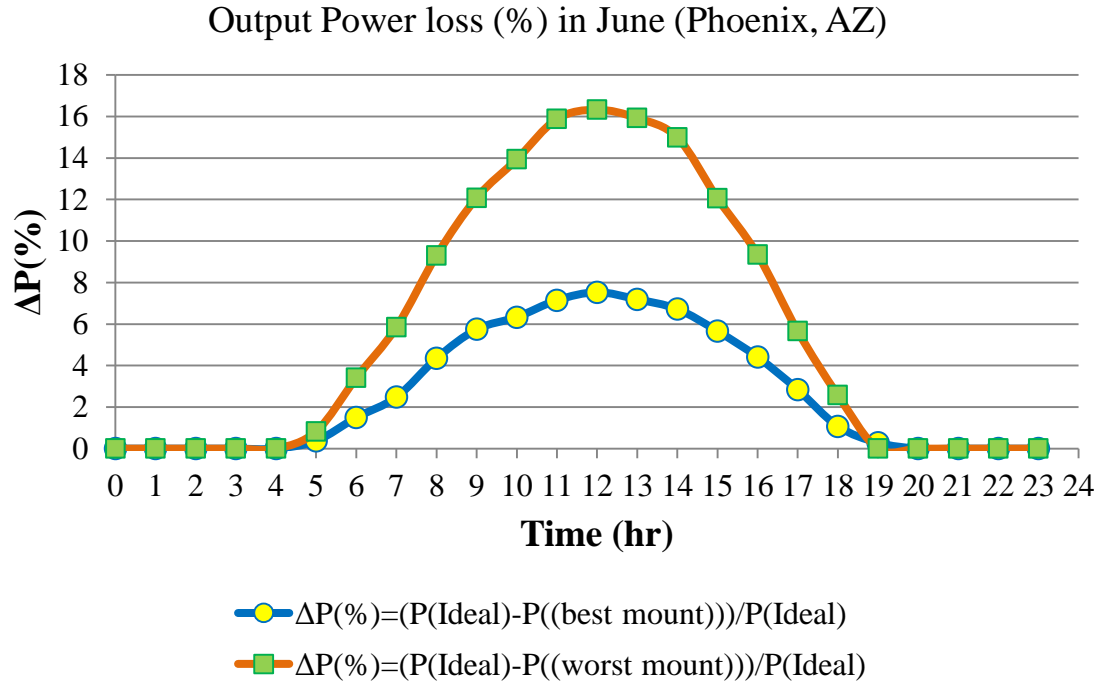


Figure 5. 43 Output Power Loss (%) in June, Phoenix, AZ for Different Mounting Configurations

Figure 5.44 shows the PV module efficiency for three previous different scenarios in June (Phoenix, AZ). The maximum PV efficiency occurred at noon and reduced from the rating manufacturer in the datasheet (20.1%) to (19.46% in the ideal case scenario) to around 17.99% or 16.26% depends on mounting options.

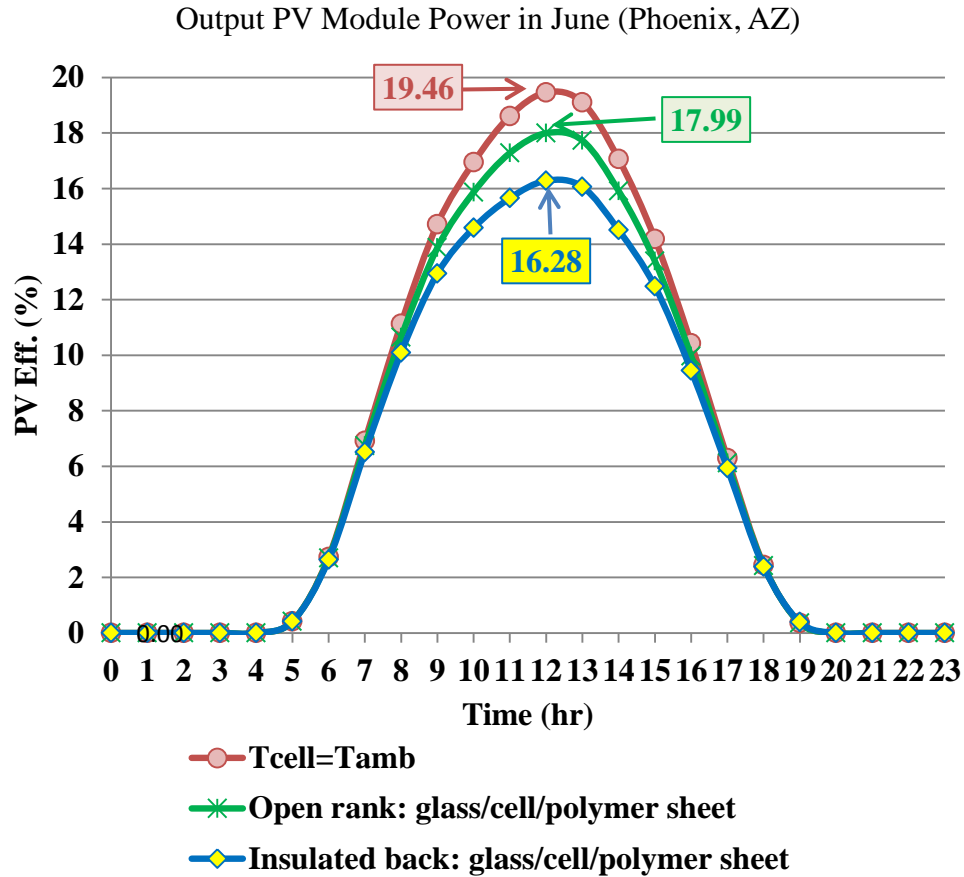


Figure 5. 44 Effects of mounting configuration options in PV efficiency in June in Phoenix, AZ

The temperature of PV module could be minimized if cooling system is implemented, either active cooling or passive cooling. In the active cooling, researchers have been used water-cooling [230]-[233] or forced air [234]. In passive cooling, researchers have been used aluminum heat sink [235] or Silicon oil [236].

Typically, without active cooling is implemented, the temperature of PV module could not be dropped to less than ambient temperature. Previously, the limit for this option is discussed. In other hand, if the active cooling is implemented the PV temperature

decrease further, but the active cooling will consume energy. However, implementing any specific cooling system for any PV system, the net energy gain should be estimated versus the additional cost to decide if it's worthy considered it.

5.9.2 Shadow and Sky Clearness

Generally, if the designers need to increase the PV output voltage, the series connection is used. But, to increase PV output current the parallel connection is used. This depends on the load and other system constraints as will discuss later. Suppose, the PV system is used two PV modules in series connection, then the same current passes through the two modules. For that, it is important that the two PV modules have same I_{mp} to make the two modules works in their optimum power. As an example, suppose I_{mp1} , V_{mp1} , and P_{mp1} are related to PV module 1 and I_{mp2} , V_{mp2} , and P_{mp2} related to PV module 2. If the two PV modules in series and the $I_{mp1} \neq I_{mp2}$, then the output PV power equal the lowest current multiply by the summation of the two voltages. If $I_{mp1} < I_{mp2}$, then the PV output loss is equal , $\Delta I \times (V_{mp1} + V_{mp2})$, where $\Delta I = I_{mp2} - I_{mp1}$.

Sometimes, even if the series PV modules are selected perfectly to have same I_{mp} , the PV system could be forced to work under different conditions. For example, if the shadow affects the PV system partially, then the above similar power losses may happen. Suppose, portion or entire of PV module number 1 is under shadow, then the current generated by the incident light (I_{pv1}) will be reduced. Then, $I_L < I_{mp1}$ and the PV system output power is lesser than the optimum power.

As discussed previously, the two components comprised GHI are DHI and DNI. The direct component DNI reaches the PV module affected if there are any shadows on the PV module (e.g., shadow created by nearby buildings, large vans, trees, etc.). The DHI component could be affected and minimized based on the sky clearness, which is the factor that the sky is obstructed. The Equations (5.44) and (5.45) represent the GHI in both parking and driving modes.

$$GHI_{\text{Parking Mode}} = \alpha_p \times DNI \times \cos(\theta) + \Psi_p \times DHI \quad (5.44)$$

$$GHI_{\text{Driving Mode}} = \alpha_d \times DNI \times \cos(\theta) + \Psi_d \times DHI \quad (5.45)$$

Where,

α ,is the shadow factor varying between $0 \leq \alpha \leq 1$

Ψ ,is the sky clearness factor varying between $0 \leq \Psi \leq 1$

If $\alpha = 1$, there is no shadow while if $\alpha = 0$ means there is complete shadow. If $\Psi = 1$ means the sky is clear, while $\Psi = 0$ means the clearness of the sky is completely blocked. Generally, α & Ψ factors are changed with time and depends on many factors as weather, surroundings, locations, etc. In addition, α & Ψ could affect the PV module partially and not the entire module and could have different values in different sections of the module. For that, the PV module designs have bypass diodes connected in parallel with each group of series PV cells to separate the shaded or bad cells and not affected the entire PV module. Depending on the case for a specific time, the PV power output could be predicted.

Assuming $\alpha_p = \alpha_d$ and $\Psi_p = \Psi_d$ and the α & Ψ affected the entire PV module uniformly, the Figures 5.45 and 5.46 shows the GHI in Phoenix, AZ in June and December months for different α & Ψ values.

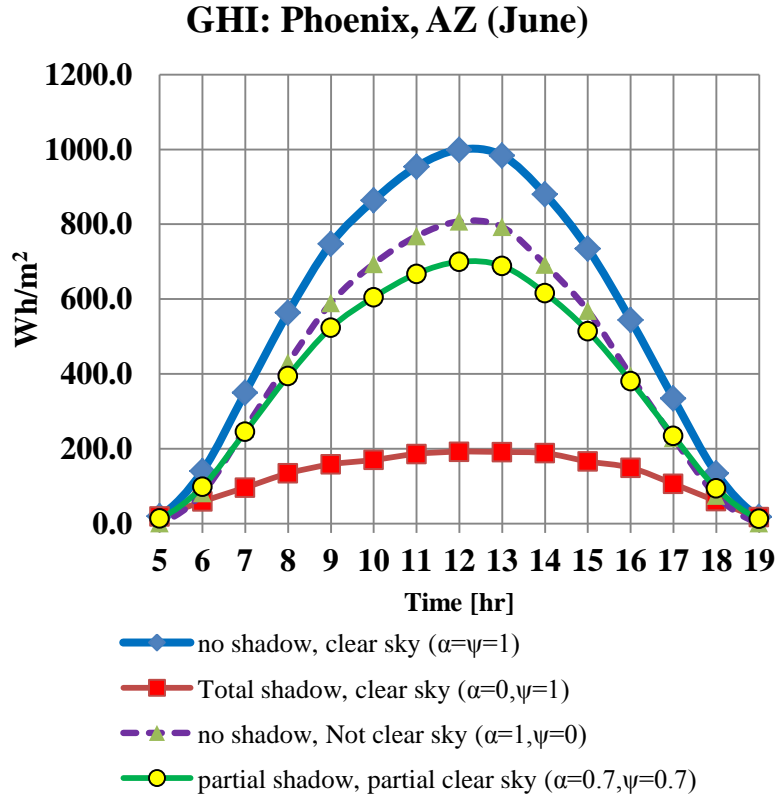


Figure 5. 45 GHI in Phoenix, AZ in June for different α & Ψ values

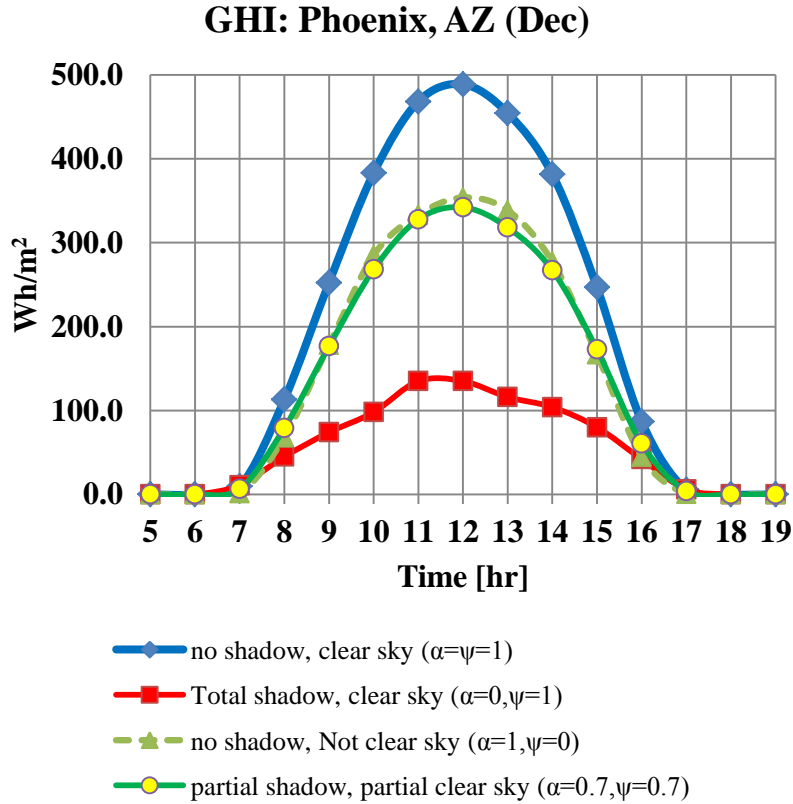


Figure 5. 46 GHI in Phoenix, AZ in Dec for different α & Ψ values

Figures 5.47 and 5.48 show the total incident radiation in June and December, respectively, for the same α & Ψ assumptions. In the case, $\alpha = \Psi = 1$, the PV module is in the sun for all periods and the sky is clear. If $\alpha = 1$ & $\Psi = 0$, the PV module is in the sun, but the sky is not clear at all. If $\alpha = 0$ & $\Psi = 1$, the sky is totally clear, but the PV module is under complete shadow for all the time. Based on the above calculations, even if the PV module is totally located in the shadows all the time, the GHI still reaches 23% of the maximum GHI if the sky is clear. If there are partial shadow and partial sky clearness (e.g., $\alpha = 0.7$ & $\Psi = 0.7$) the GHI is reduced to 77% compared to the ideal case.

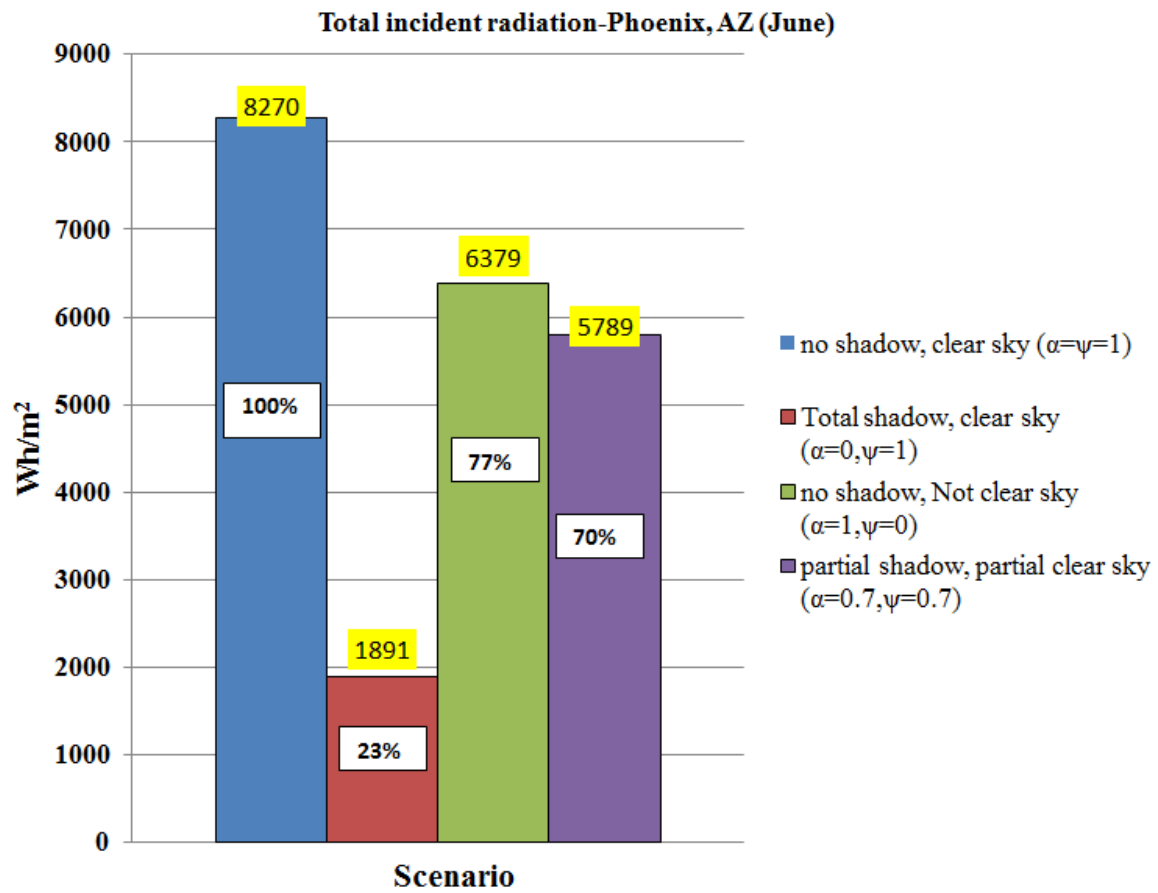


Figure 5. 47 Total incident radiation on June in Phoenix, AZ for Different Shadow scenarios

For the same above location, but in December, if the assumption is partial shadow and partial sky clearness (e.g., $\alpha=0.7$ & $\Psi=0.7$) the GHI reduced to 70% the ideal case.

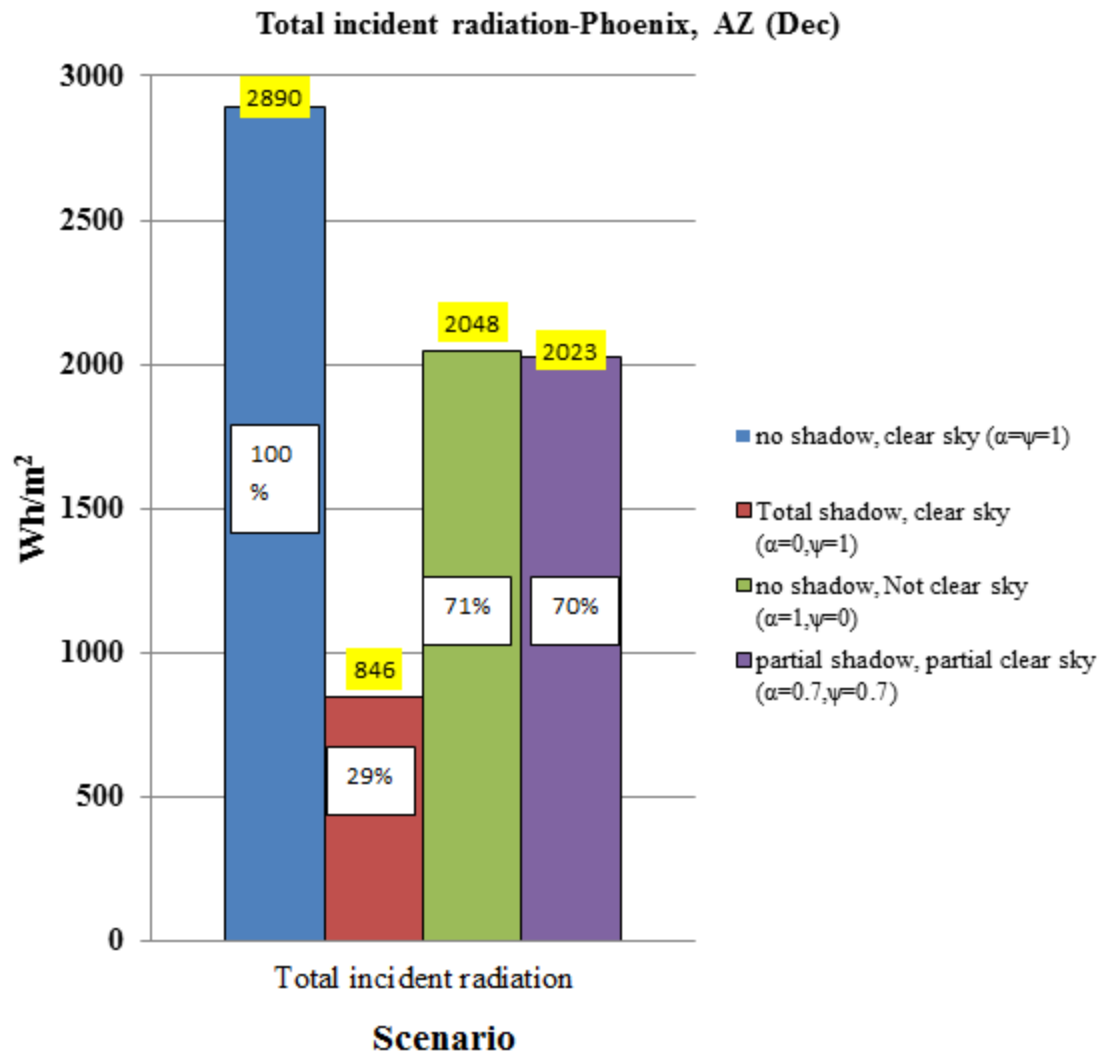


Figure 5. 48 Total incident radiation on December in Phoenix, AZ for Different Shadow Scenarios

5.9.3 PV Tilt Angle and Orientation

Assuming the PV module is fixed and is oriented to the south (Azimuth=180°) as shown in Figure 5.18, the total incident irradiation is changed based on the value of the tilt angle. Assuming the tilt angle is varying between 0° (horizontal configuration) to 90° (vertical configuration), the Figures 5.49 and 5.50 show the total incident irradiation in Phoenix, AZ in both June and December months.

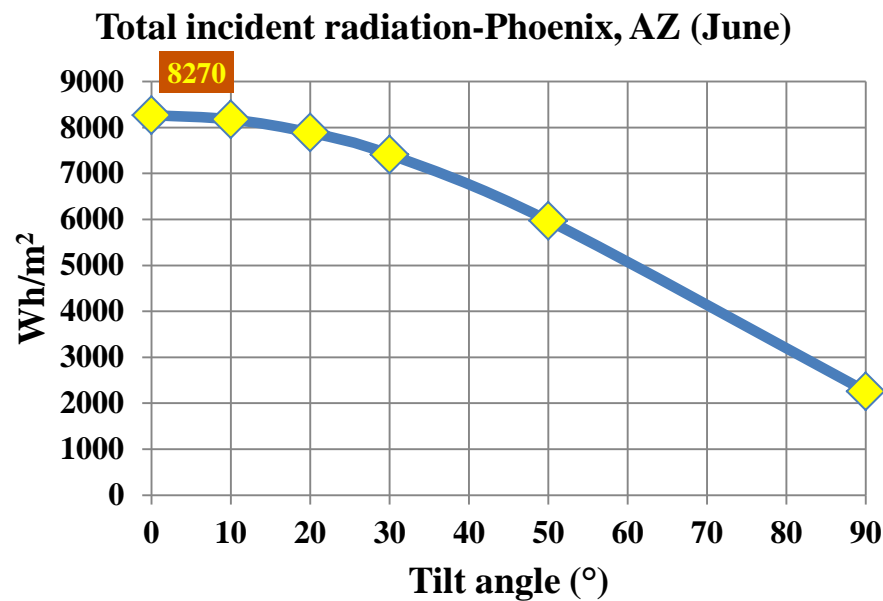


Figure 5. 49 Total incident radiation vs. tilt angle (June, Phoenix, AZ)

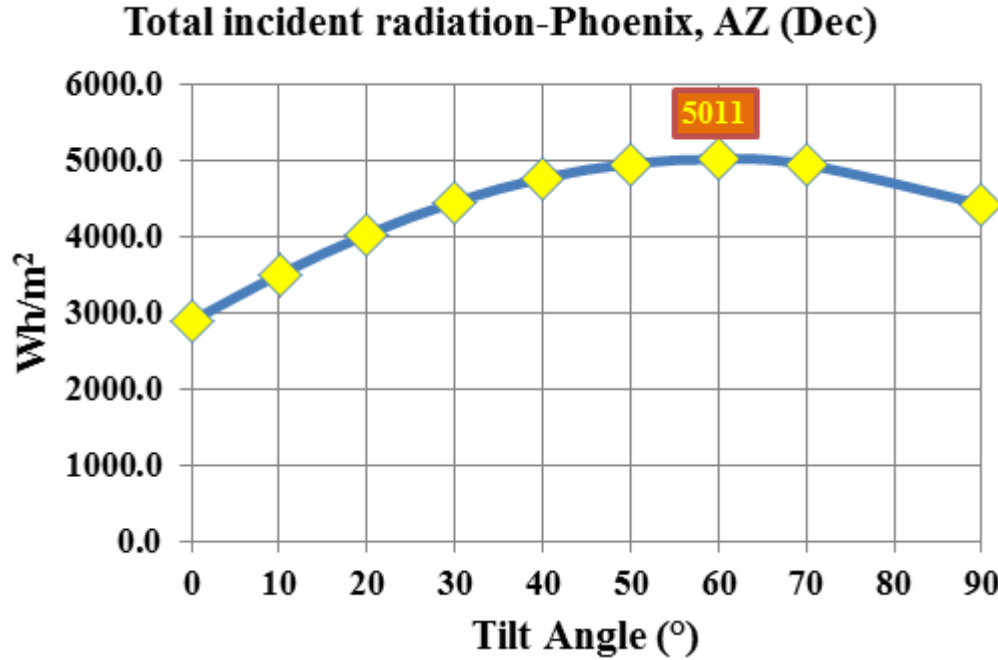


Figure 5. 50 Total incident radiation vs. tilt angle (Dec, Phoenix, AZ)

As shown in Figures 5.49 and 5.50, for each tilt and azimuth angles the total incident radiation is changed based on the time in a year (in this case June & Dec) for the same location. In addition, for every time in a year in specific location, the incident radiation is changed based on tilt angle. For example, the maximum incident solar energy in June is equal 8,270 Wh per m^2 and this occurred when the tilt angle is 0° . The reason is typically in June the position of the sun is mostly perpendicular. In December, the lowest solar energy incident when the tilt angle is 0° , while the maximum is found when the optimum tilt angle is 60° . Under these circumstances, in December the energy gain between optimum tilt angle and horizontal configuration is found around $(5011 - 2890) / 2890 = 73\%$.

Typically, the rule of thumb for PV application, if the PV module is fixed the optimum tilt angle through a year is equal the latitude of the location. Figures 5.49 and 5.50 are generated by the assumption is that the PV faces the south all the time. For vehicle application, this assumption is not valid if the PV module is fixed, typically the PV module in parking and driving modes will face all the directions. Figure 5.51 shows the total incident radiation in Phoenix, AZ in December for different tilt & angles.

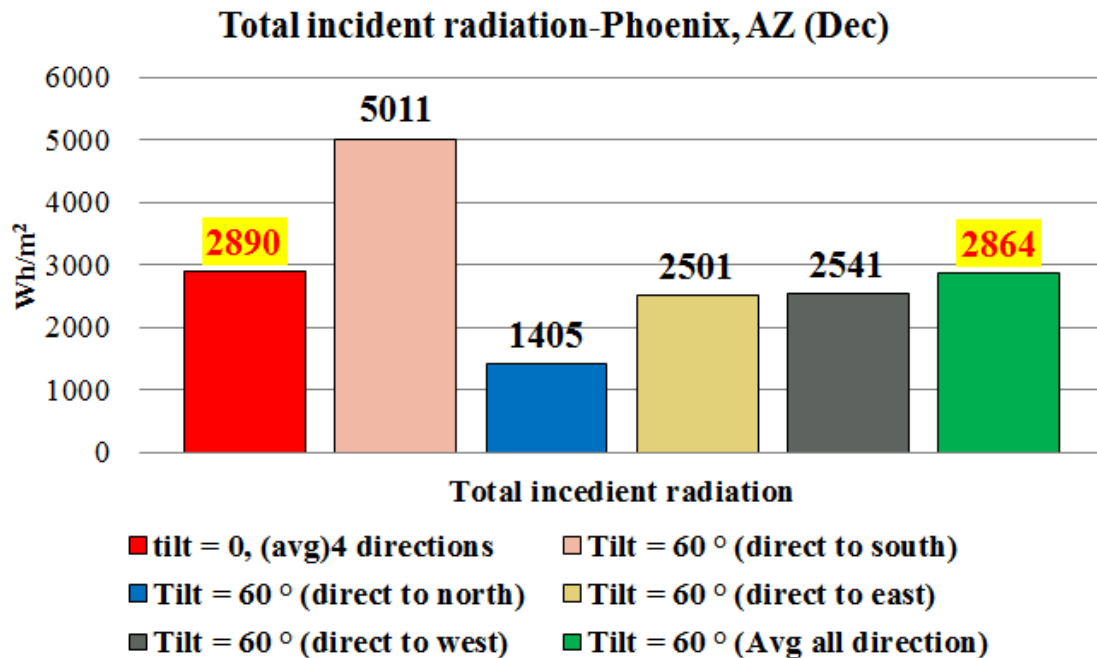


Figure 5. 51 Total incident radiation in December Phoenix, AZ in different tilt & azimuth angles

If the tilt angle is 0°, this means the module is horizontal mounted. Actually, the azimuth angle will not affected the incident radiation in this case. The total incident radiation in this case is equal 2,890 Wh per m². For the optimum tilt angle, which is equal

60° by assuming the PV module faces all the four cardinal directions equally through a month, the average incident solar radiation is found equal 2,864 Wh per m² which is slightly less than the horizontal case.

This study showed that for vehicle application, if the PV module is fixed the optimum tilt angle is horizontal. This also will eliminate any problem could be based on aerodynamic issue.

The one-axis or two-axis trackers could be used to track the sun to increase solar yield by keeping the PV module normal to incoming radiation to minimize θ . Figure 5.52 shows the fraction of DNI in Wh per m² incident on fixed PV in June in Phoenix, AZ calculated as DNI multiply by cosine incidence angle compared to the entire DNI incident on PV in the same case. Ideally, this entire curve (green-yellow) could be captured if ideal 2-axis tracker is used. The challenges with using tracker are additional cost and weight will add to the PV system. In addition, the effect of the tracker in vehicle aerodynamics should be considered for that the feasibility for tracker to use only in parking mode. Another challenge is that the installation geometry surface (e.g., on vehicle roof) could add a constraint so the tracker could not work perfectly as discussed in [237]. For that, implementing the tracker in a vehicle application needs to address all these issues to predict the net energy gain versus complexity and cost issues.

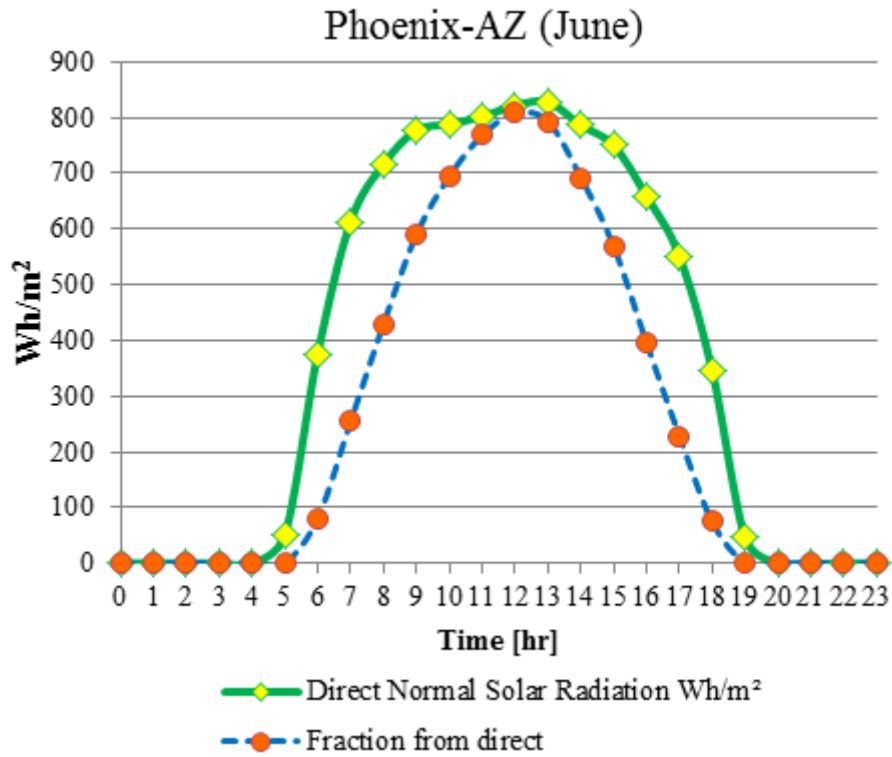


Figure 5. 52 Entire DNI and Cosine component DNI in June, Phoenix, AZ

5.9.4 Angling PV on Vehicle Surface

If the PV module(s) places on a curved vehicle surface, different PV cells or modules have different angles of incidence (θ) with respect to the sun. If these modules on series connection, probably some of the module will be forced to work with different current than the optimum. This will generate the same mismatch problem discussed previously in section 5.9.2. As discussed previously, the DNI depends on (θ) and the power mismatch between modules will be related to the difference between these angles.

For example, Figure 5.53 shows two PV modules placed on a curved vehicle surface. The θ_1 and θ_2 are angle of incidences of PV modules 1 and 2, respectively. The mismatch power between the two PV modules is calculated using Equation (5.46).

$$\text{Mismatch power loss} = [\cos(\theta_1) - \cos(\theta_2)] \times 100\% \quad (5.46)$$

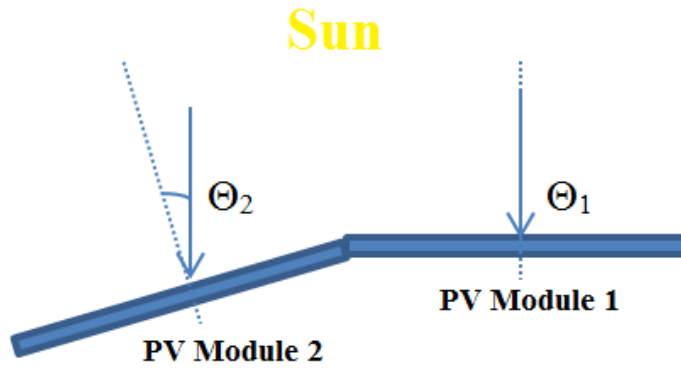


Figure 5. 53 Angling PV on Vehicle Surface

Assume, the curvature of vehicle surface between the two regions where the PV modules 1 and 2 are installed introduced angles differences as 2° , 4° , or 10° . Then, if the sun is perfectly perpendicular to the first PV module ($\theta_1=0^\circ$), then the mismatch power losses in all cases will be minor at most less than 1.52% as shown in Table 5.3. In other case, if $\theta_1=50^\circ$, then the losses are bigger as shown in Table 5.3. If the vehicle is used in June, 11 in Phoenix, Arizona, θ_1 at noon is less than 10° , so the losses will be minor. However, θ_1 is bigger than 50° in early morning and late evening (See Figures 5.22 and 5.23 for θ all that day) and the losses are significant. Ideally, the PV modules should be parallel as possible.

Table 5. 3 Mismatch power losses for angling PV module on vehicle surface

Case (1)			Case (2)		
θ_1	θ_2	Mismatch power losses	θ_1	θ_2	Mismatch power losses
0°	2°	0.061%	50°	52°	2.71%
0°	4°	0.244%	50°	54°	5.5%
0°	10°	1.519%	50°	60°	14.279%

5.9.5 Battery Size

The battery size for the on-board PV of vehicle application is determined based on many constraints as total stored energy, cost, weight, space for packaging, etc. In addition, it is important that the battery voltage is matched PV module voltage and the MPPT. Ideally, the voltage of the PV module should be slightly higher than battery voltage to use step down DC-DC, which is more efficient than step up.

The single cell battery nominal voltage used in battery model is equal 3.2 V as discussed previously. By using the proposed PV and battery models, the PV output current is used to charge the battery. Figure 5.54 shows the optimum PV module voltage and battery voltage for different number of battery cells with time from 5 am to 7 pm in Phoenix, AZ in June.

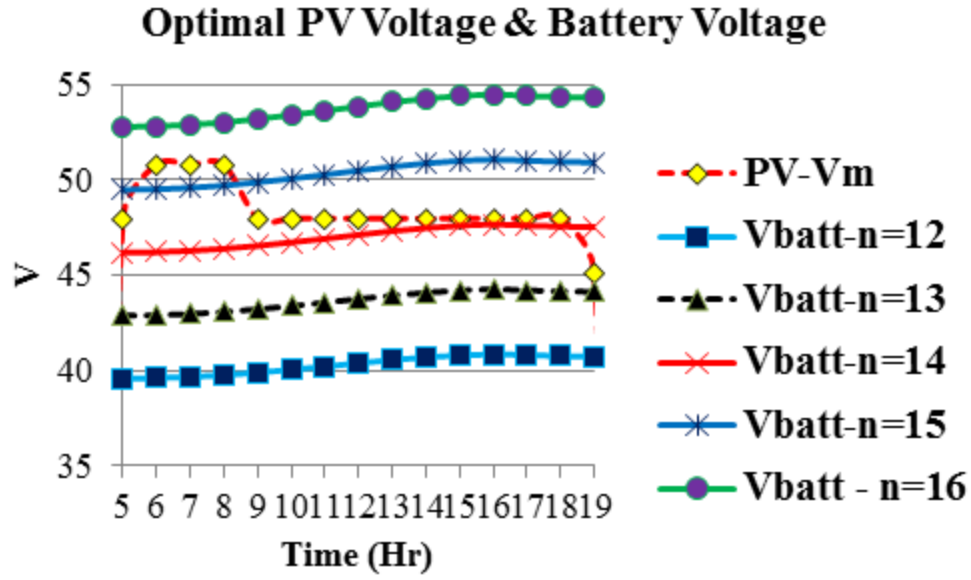


Figure 5. 54 Optimum PV module' voltage and battery voltage for battery cells in Phoenix, AZ in June.

From Figure 5.54, the optimum PV voltage is around 48 V and this is when number of battery cells equal 14, the charging battery voltage is slightly less than PV module. The solar energy to battery charging efficiency is calculated using equations (5.47) and (5.48) [43].

$$\text{efficiency (\%)} = \frac{\text{avg. voltage (V)} \times \text{charge increase (Ah)} \times \text{battery charging (\%)}}{\text{avg. solar irradiance (W/m}^2\text{)} \times \text{PV area (m}^2\text{)} \times \text{time interval (hr)}} \quad (5.47)$$

$$\text{Charge increase} = \text{current} \times \text{time} \quad (5.48)$$

The solar energy to battery charging efficiency with number of battery cells equal 12, 13, and 14 are shown in Figure 5.55. As expected, the maximum efficiency is found when $N=14$ cells, which is around 17-18 %.

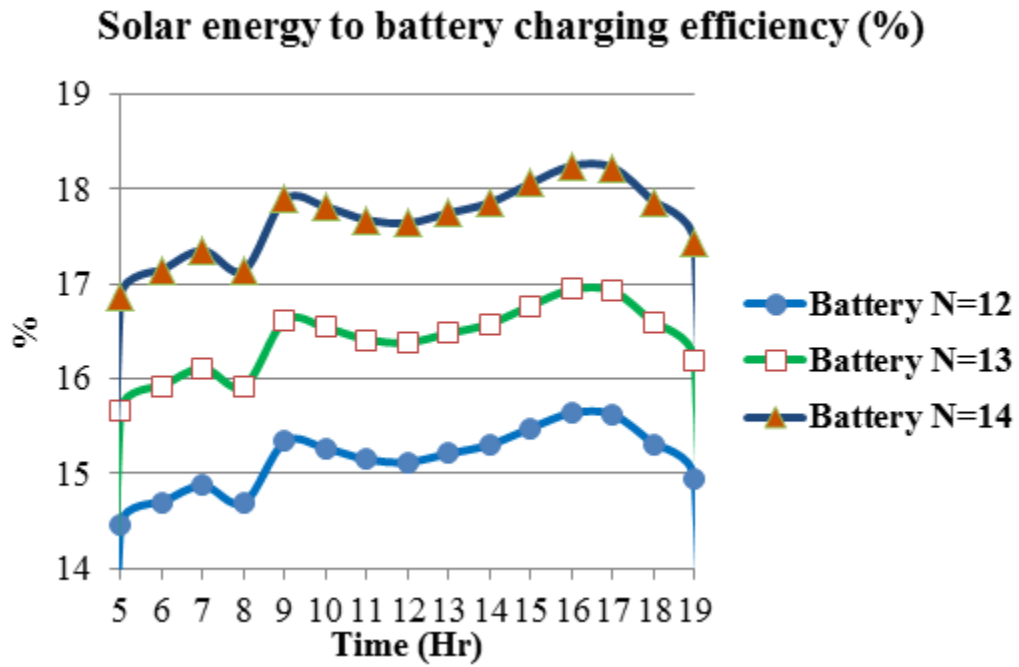


Figure 5. 55 Solar Energy to Battery Charging Efficiency

The solar to battery charging is optimized when the PV voltage is slightly higher than battery voltage. To determine specific value, the ratio of optimum PV output voltage (V_{mp}) to battery voltage is calculated and displayed in Figure 5.56. For the best efficiency it is found that the optimum ratio V_{mp} to battery voltage is equal 1.029.

Ratio of V_{mp} of PV to Battery Charging Voltage

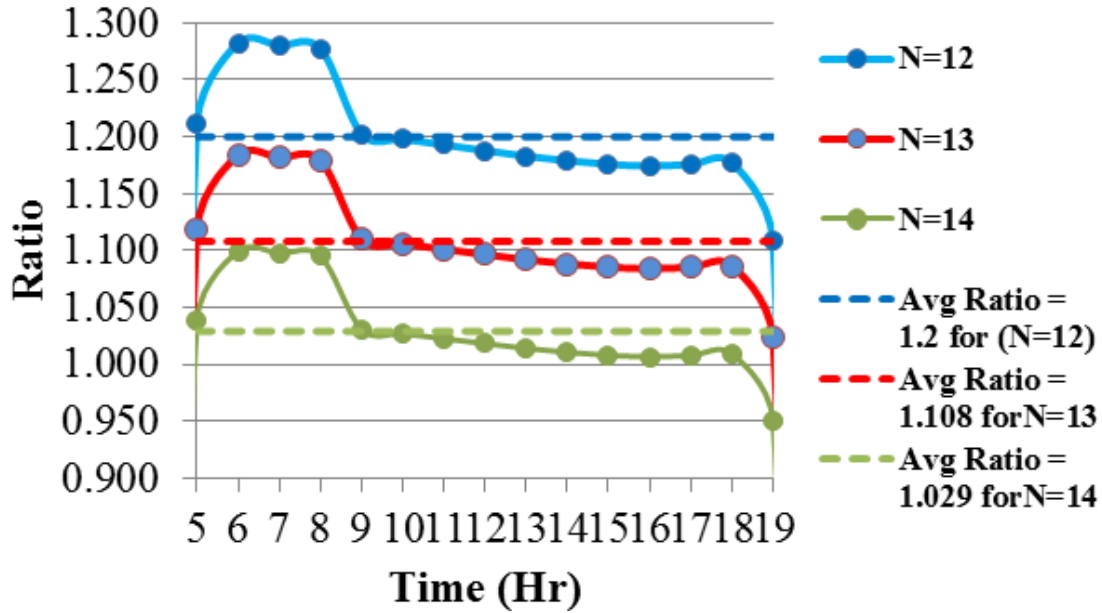


Figure 5. 56 Optimum ratio between V_{mp} and battery voltage

In general, the following rules used to choose the battery size [206]. If, the Battery voltage is equal optimum PV voltage (V_{mp}) then the charging efficiency is 100%. If, the Battery voltage is less than the optimum PV voltage (V_{mp}) then the charging efficiency is the ratio. If, the Battery voltage is larger than the optimum PV voltage (V_{mp}) then the charging efficiency dropping sharply. If the Battery voltage is larger than the open circuit PV voltage (V_{OC}) then no power is produced.

By using $n=14$, Figure 5.57 (a) show charging current generated by PV and used to charge battery and Figure 5.57 (b) battery voltage.

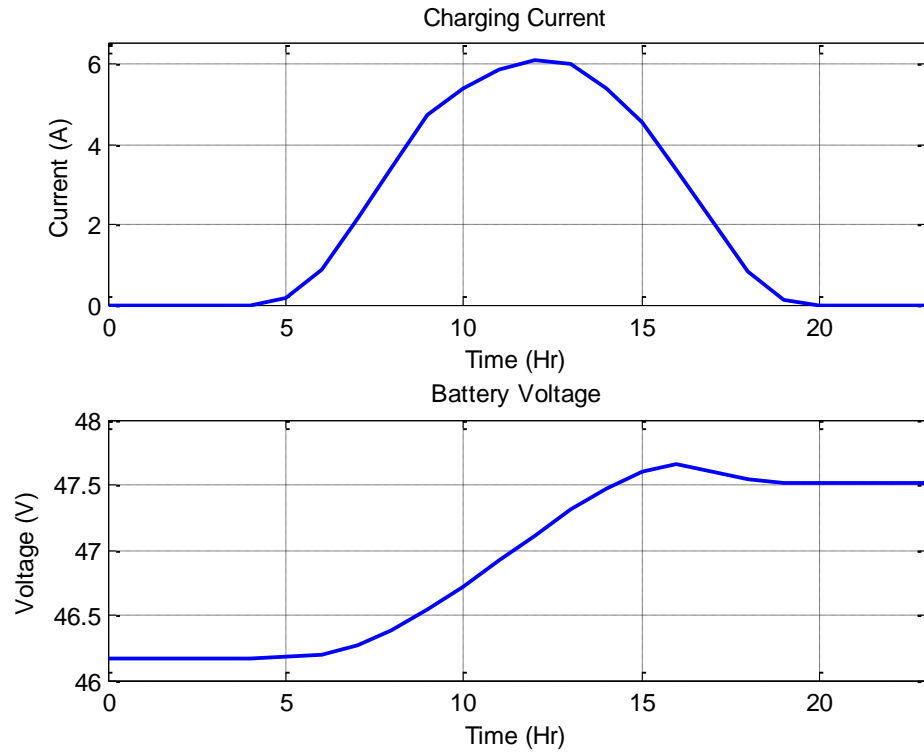


Figure 5. 57 (a) Charging current and (b) battery voltage

Figure 5.58 shows the estimated battery SOC as a function of time. The initial SOC is assumed 10%.

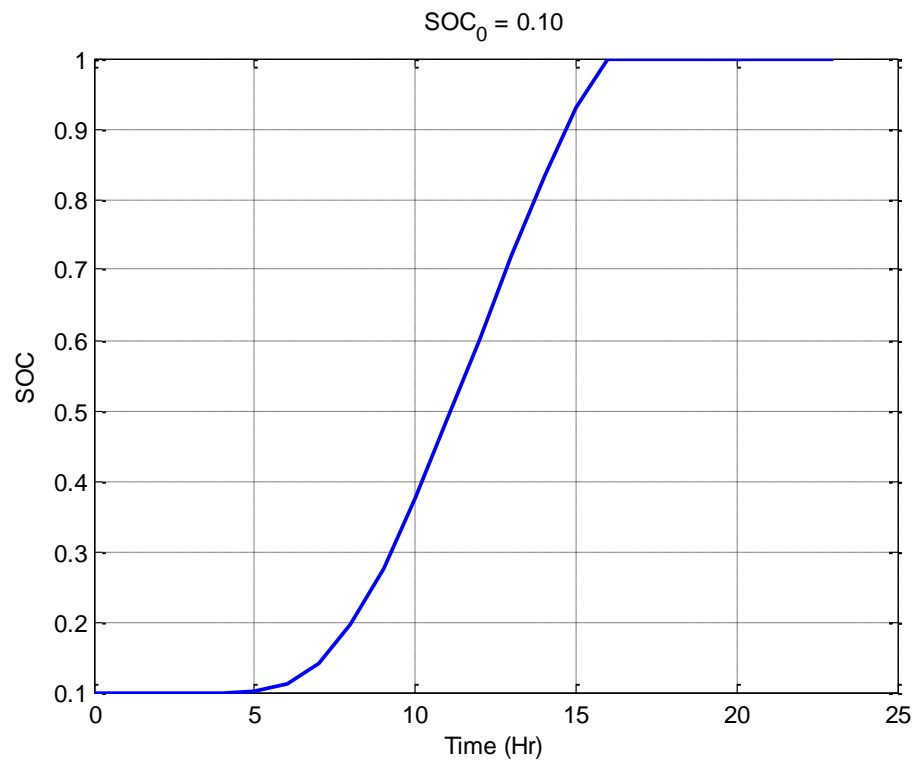


Figure 5. 58 Battery SOC with time by charging with PV module

Figures 5.59 shows the internal parameters estimation E, R in charge state.

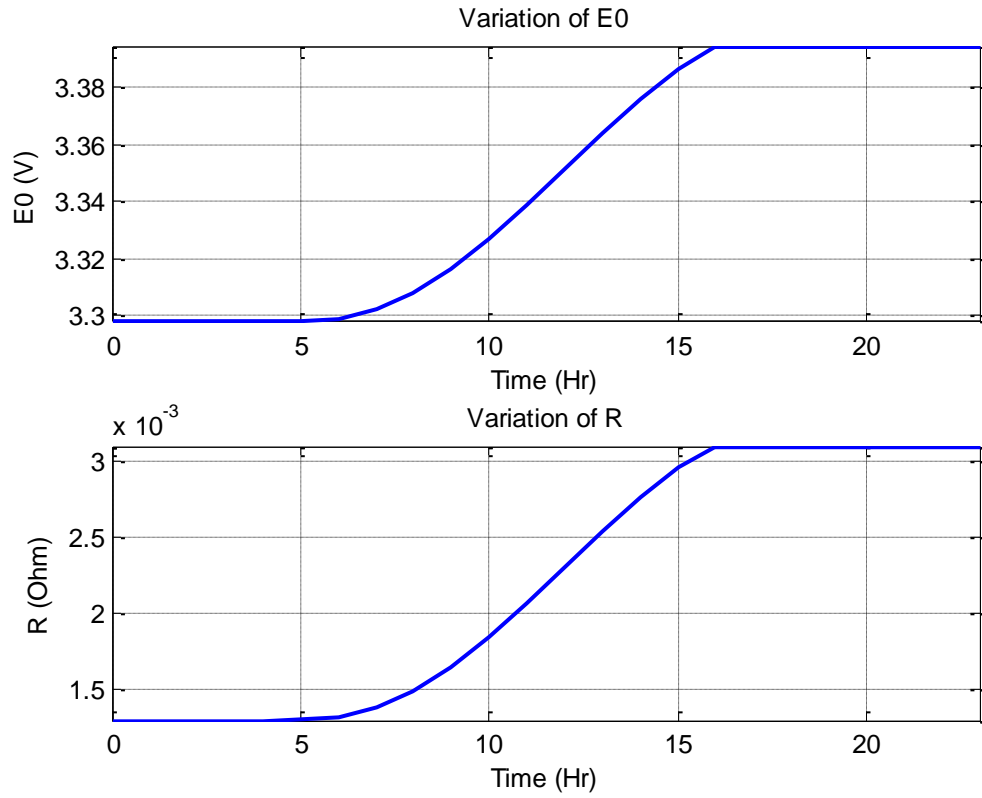


Figure 5. 59 Internal resistor (R) and open voltage (E) in battery charging mode as a functions of time

Figure 5.60 shows the estimated efficiency of charging above 99.7%, which is close to 100%, reported value in [227].

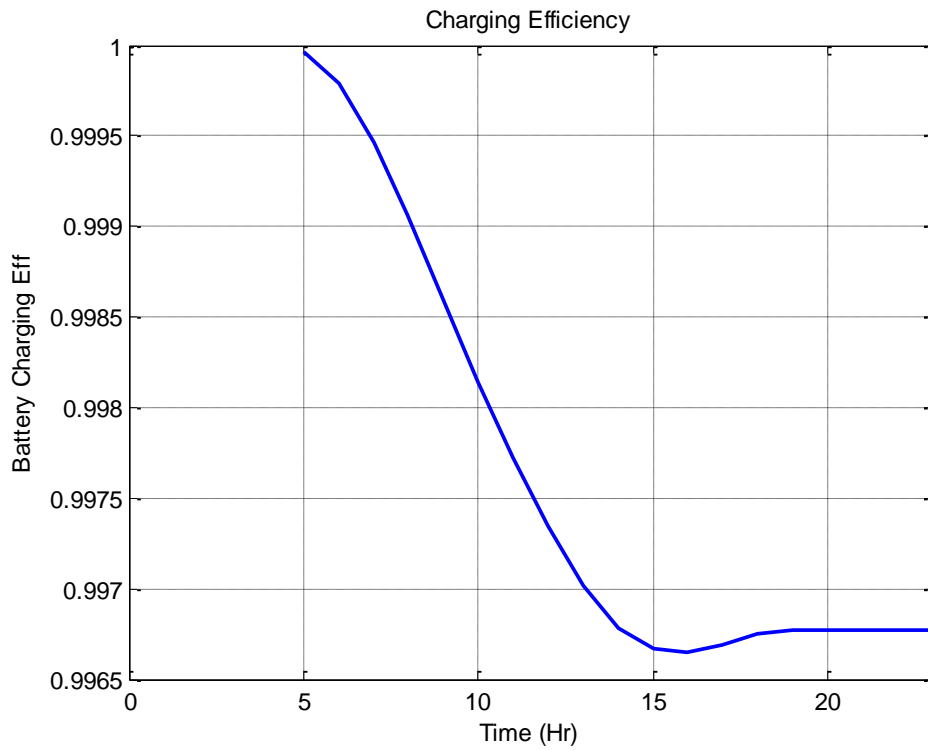


Figure 5. 60 Battery charging efficiency

The total estimated energy in kWh stored in battery with using typical PV module discussed previously in Figure (5. 6) (Area = 1.63 m²) in Phoenix, AZ in June is less than 2.5 kWh as shown in Figure 5.61.

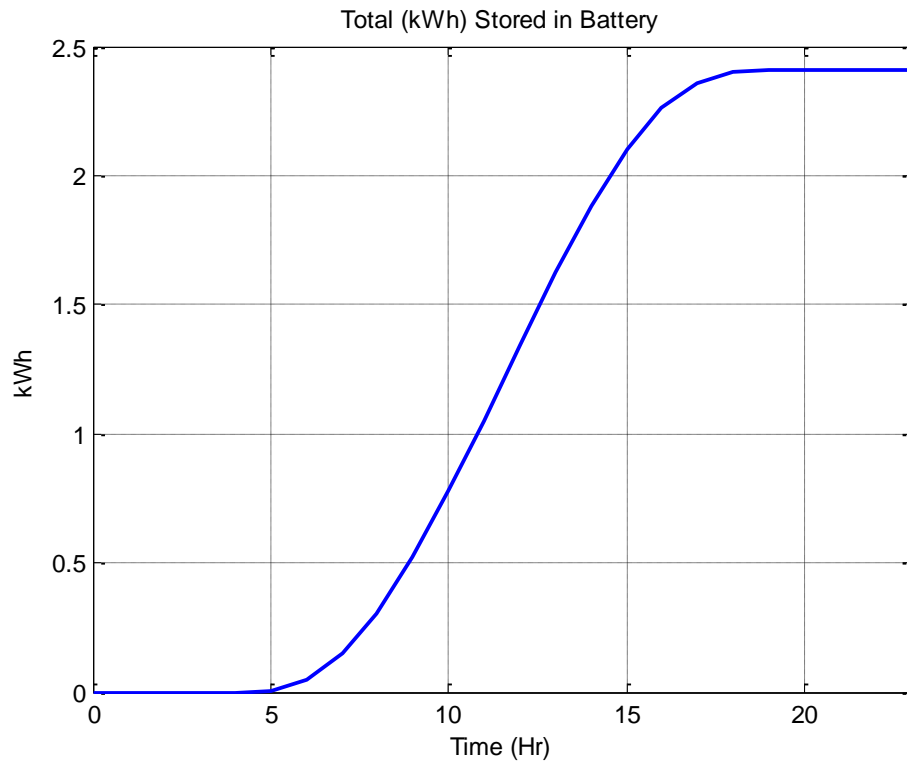


Figure 5. 61 Total energy in kWh stored in battery with using typical PV module in Phoenix, AZ in June

5.10 Modeling PV System Results

The Figures 5.62 and 5.63 show the total daily energy (Wh) stored in the battery for varying PV module areas in June and December, respectively. The base PV module area used with area 1.63 m^2 with the length is equal 1.559 m^2 and 1.046 m^2 widths (Figure 5.6). Typically, the vehicle surface can be fitted this PV module width. The various PV areas shown in Figure 5.62 with the assumption is the width is constant and the length is variable with series connection to perform the required PV area (with constraint the PV efficiency is constant).

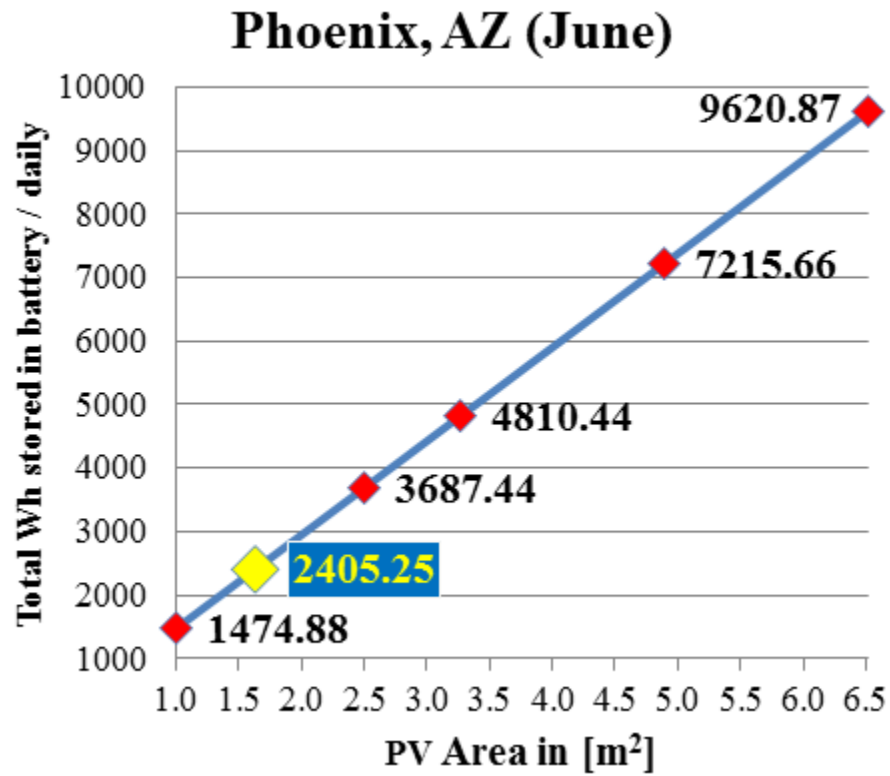


Figure 5. 62 Total daily Energy Stored (Wh) in Battery by PV module in Phoenix, AZ (June)

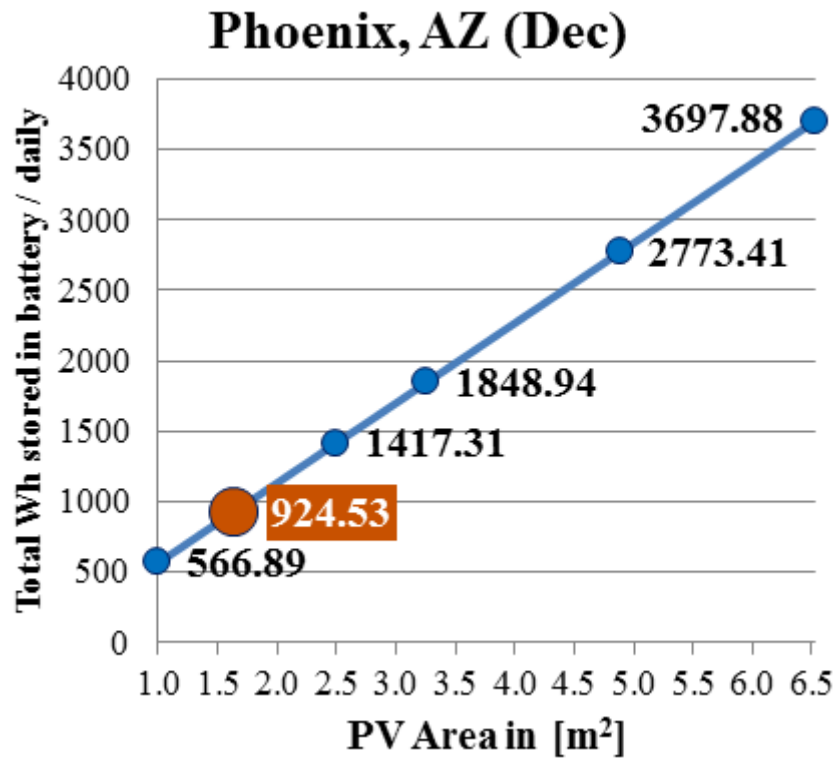


Figure 5. 63 Total daily Energy Stored (Wh) in Battery by PV module in Phoenix, AZ (December)

The above Figures showed that the energy stored in same place depends on module area and season (month). For example, in June with PV area equal 3.26 m^2 the daily stored energy is equal about 4.8 kWh. The maximum energy could be stored in December with much large module area (6.5 m^2) is equal to around 3,7 kWh.

The hourly energy stored in the battery (Wh) as a function of time and module area in Phoenix, AZ in June is shown in Figure 5.64. The color bar shows the energy region. For example, around the noon at 11 am-12 pm, the stored energy is 430 Wh with module area 2.5 m^2 , assumed the module on the sun and the sky is clear.

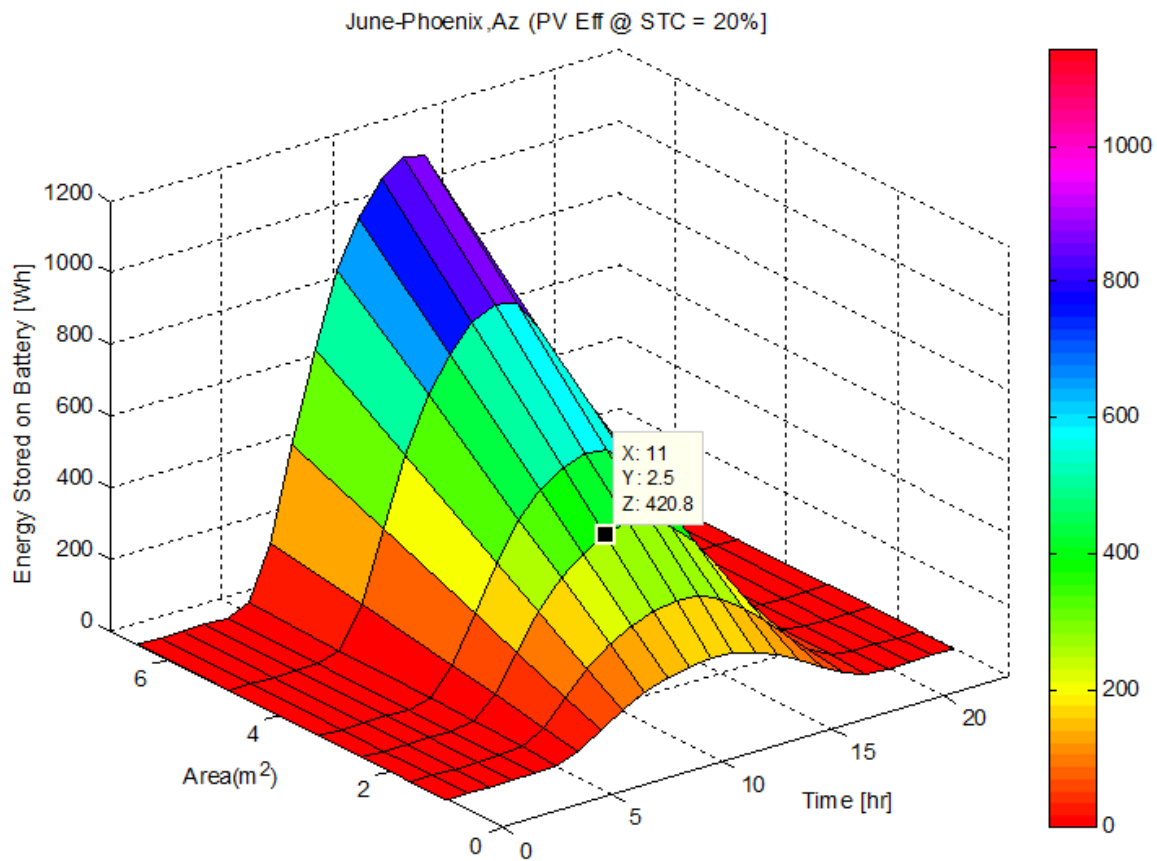


Figure 5. 64 Hourly Energy Stored (Wh) in Battery by PV module in Phoenix, AZ (June)

The stored energy also depends on the location and PV module efficiency as shown in the Figures 5.65 and 5.66. Assumed, the PV module area equal 3.261 m^2 and the PV module efficiency is varying from low (7%) to (29~30%), which is the maximum theoretical efficiency of this module type [238]. Figures 5.65 and 5.66 show results in Phoenix, AZ in June and December, respectively. While, Figures 5.67 and 5.68 show results in Boston, MA in June and December, respectively.

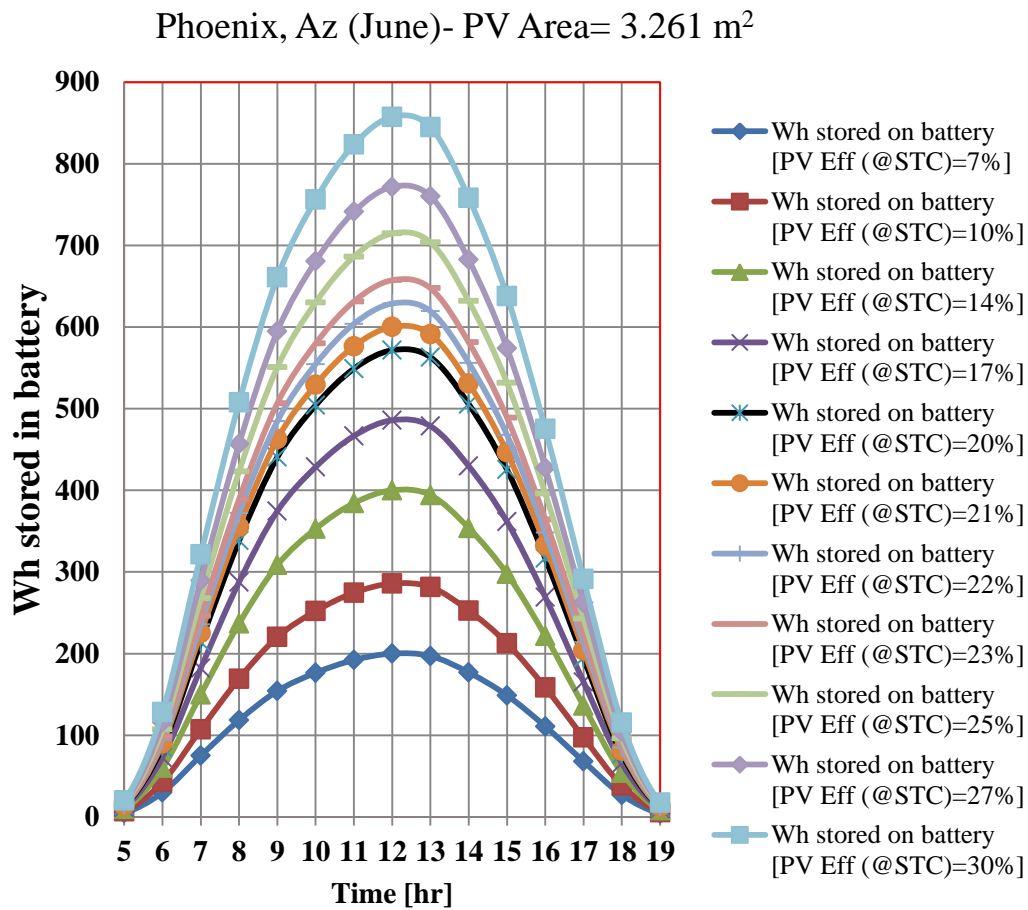


Figure 5. 65 Hourly Energy Stored (Wh) in battery (as function of time and efficiency) by PV module in Phoenix, AZ (June)

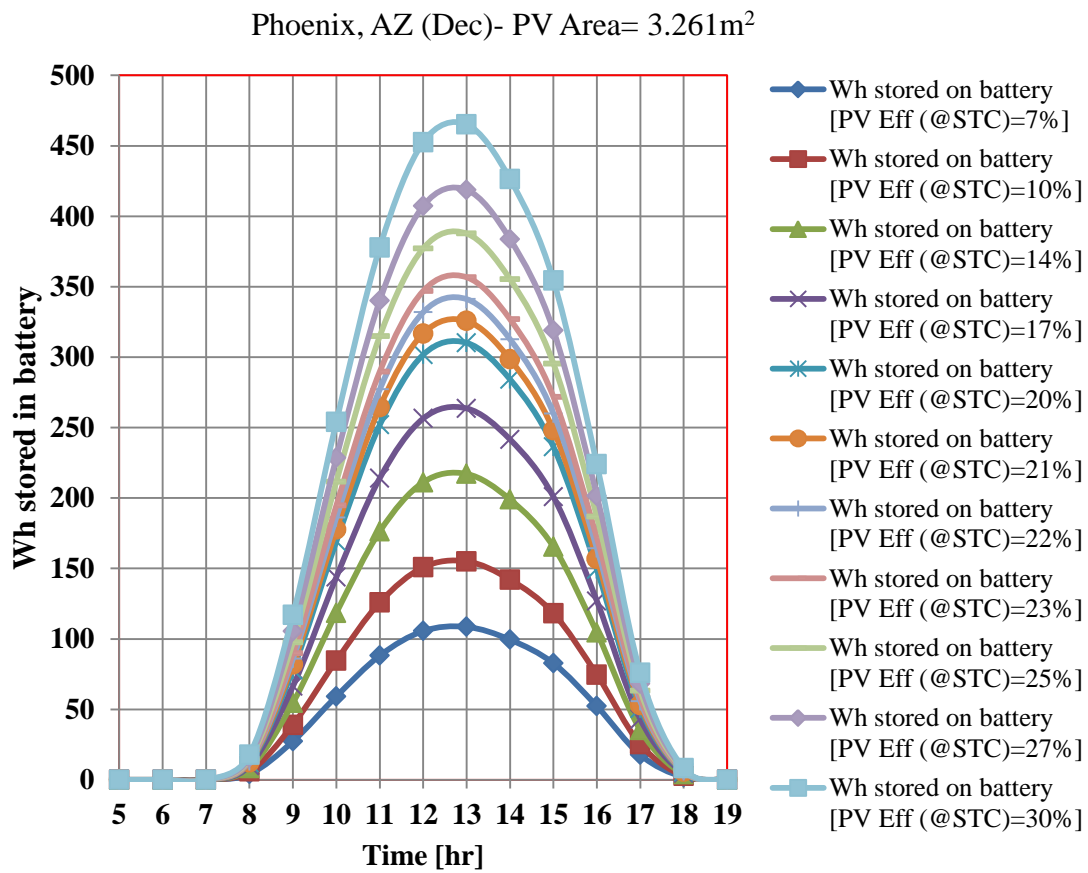


Figure 5. 66 Hourly Energy Stored (Wh) in battery (as function of time and efficiency) by PV module in Phoenix, AZ (December)

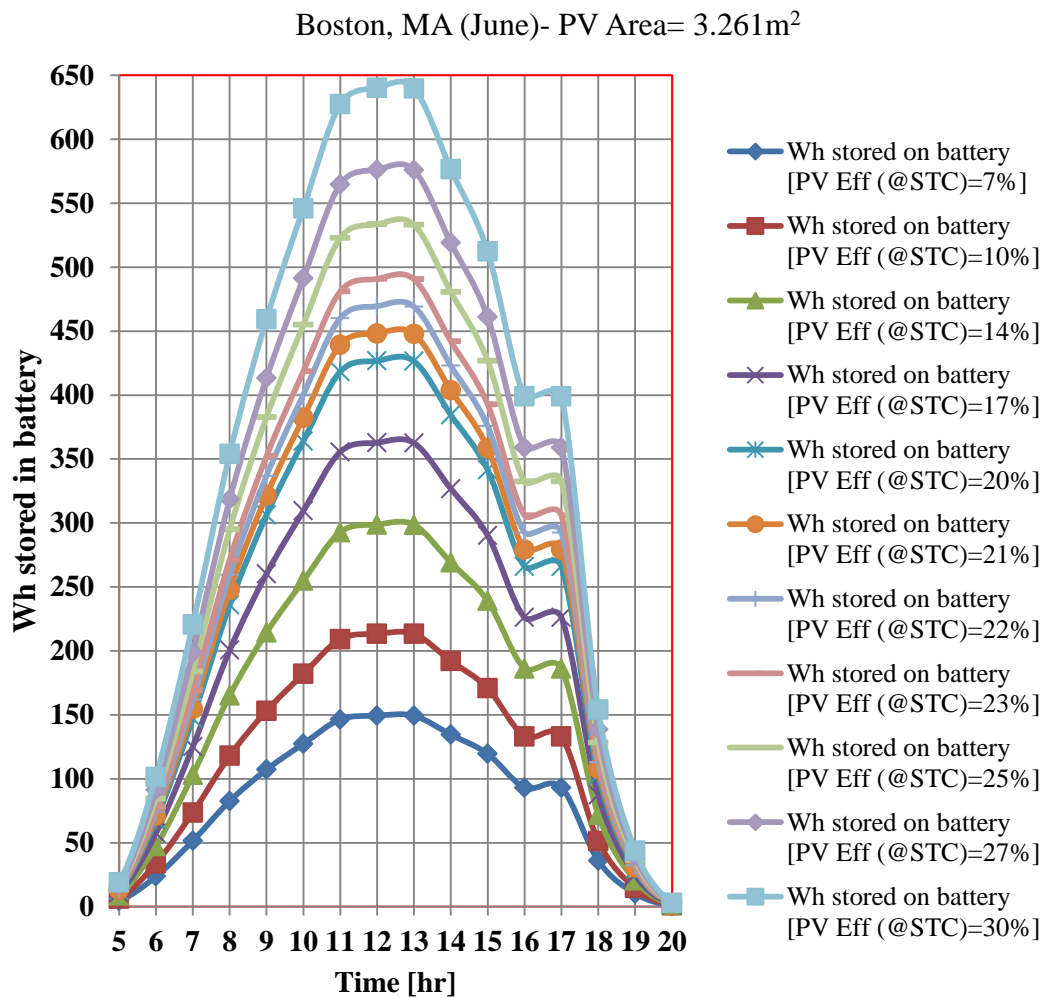


Figure 5. 67 Hourly Energy Stored (Wh) in battery (as a function of time and efficiency) by PV module in Boston, MA (June)

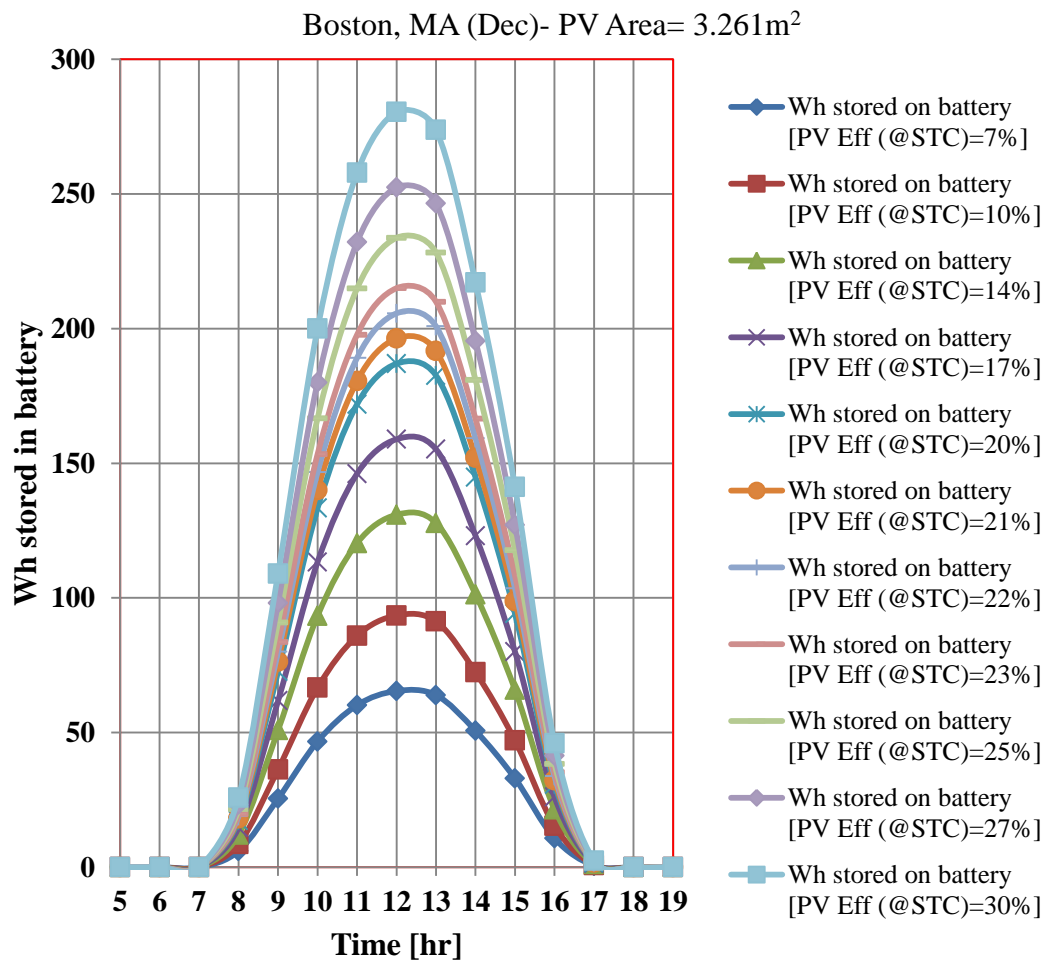


Figure 5. 68 Hourly Energy Stored (Wh) in battery (as function of time and efficiency) by PV module in Boston, MA (December)

The Figure 5.69 shows the proposed model output in terms of the total daily energy (Wh) stored in battery in different locations and months. In addition, the PV module efficiencies are varying to reflect future scenarios. The assumption here the PV module area is equal 3.261 m^2 .

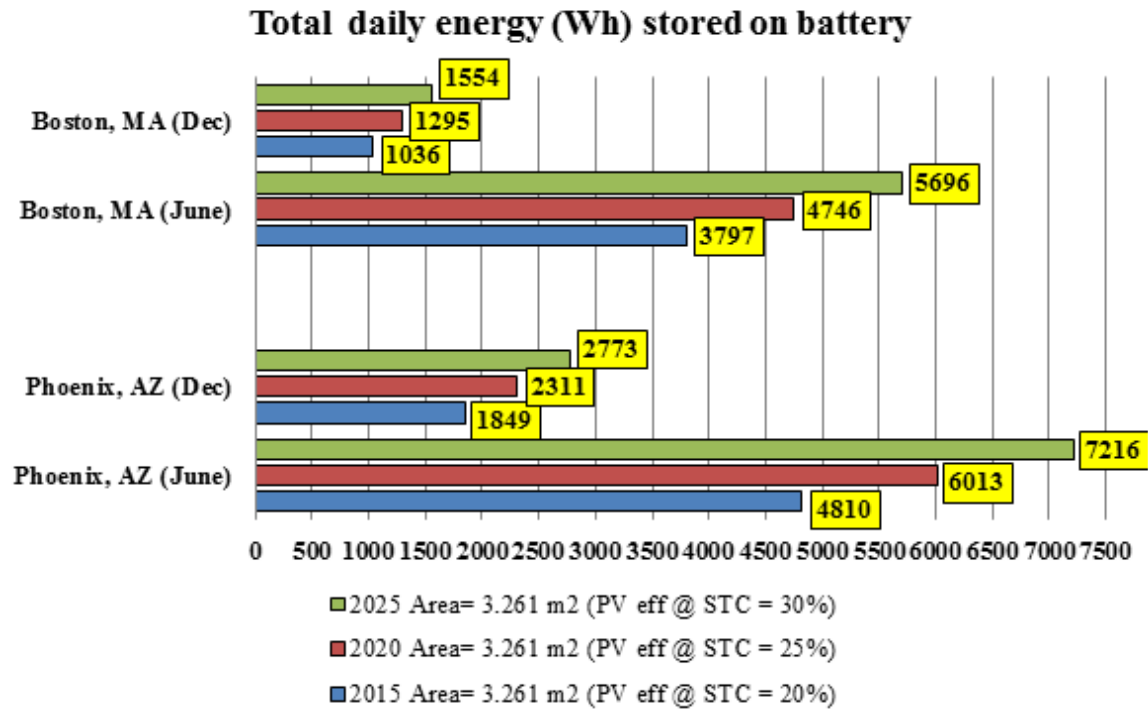


Figure 5. 69 Daily Energy (Wh) stored in battery for different scenarios

The Figure 5.70 shows the proposed model output in terms of the hourly energy (Wh) stored in battery in different locations and months. The assumption here the PV module area is equal 3.261 m^2 and PV module efficiency at STC equal 20%.

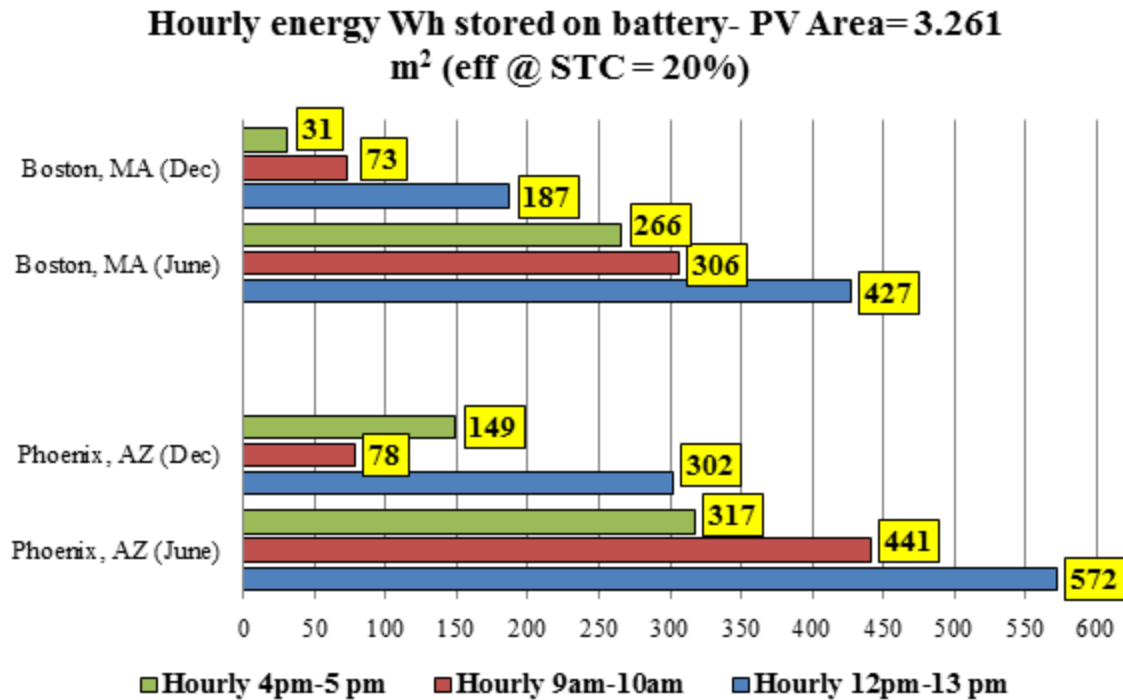


Figure 5. 70 Hourly energy (Wh) stored in battery for different scenarios

Mostly, in each state in the U.S. and in any month the results will be between December in Boston, MA in June in Phoenix, AZ. On the next stage, the best-case scenario depends on June in Phoenix, AZ and the worst-case scenario depends on December in Boston, MA are analyzed.

5.11 Summary

This chapter first presents the advantages of using solar PV on-board for vehicle application and the PV Structure is discussed. Then its focus on modeling the PV system on-board for vehicle application and optimizes the solar energy to the DC electrical power output ratio. The electrical and thermal performance of PV modules is modeled. In addition, the solar data, MPPT algorithm, and energy storage are modeled. The PV energy output is optimized to show the effects of mounting configuration, tilt option, angling on the vehicle surface, and the solar energy to battery voltage. Finally, the proposed model results are represented to reflect most all cases by changing PV module areas, efficiencies, installation locations, seasons, and times.

CHAPTER SIX

VEHICLE MODEL WITH ON-BOARD PV (TANK TO WHEEL ANALYSIS)

6.1 Introduction

In general, to model a specific vehicle, there are two main approaches; forward-looking model and backward-looking model. The former is called driver driven, the way this model works start from the driver by sending a command as an accelerator or brake pedal to the different Powertrain components to follow the desired driving cycle. In contrast, the latter is called vehicle driven and the desired vehicle speed goes from vehicle block to the Powertrain's components to find out how much each component should be used to follow the objective speed. In previous work a forward-facing model for a series hybrid compressed natural gas (CNG) vehicle configuration is developed [239].

There are many models have been used to predict vehicle performance as ADVISOR model [240], developed preliminary by NREL in 1994 with the help of the transportation industry and was made available free of charge from 1998 to 2003. ADVISOR is a backward-facing vehicle simulation used to predict how changes in vehicle component type and size affect fuel economy, performance, and emissions. Powertrain System Analysis Toolkit (PSAT) software [241], developed by Argonne National Laboratory, the first version was in 1999 with collaborative with Ford, General Motors, and DaimlerChrysler companies. The objective of this software assists the department of

energy (DOE) in identifying future research directions regarding plug-in hybrid electric vehicles (HEVs). In 2007, a new tool has developed by Argonne and General Motors called Autonomy [242], the new software is a plug-and-play Powertrain and vehicle model architecture. This model is a math-based simulation to predict the vehicle performance and analyze virtually the hardware models and algorithms.

Future Automotive Systems Technology Simulator (FASTSim) [243] is developed by NREL to estimate the performance, cost, and battery life of a vehicle with specified Powertrain components over standard drive cycles. High-level vehicle characteristics (Frontal area, drag coefficient, mass, engine power, etc.) for many light duty and heavy duty vehicles are included. This tool is used to compare powertrains based on a selected vehicle with modifications to a few high level inputs.

VISION [244] is a spreadsheet model has been developed by Argonne lab and the U.S. DOE to estimate the potential energy use, oil, and carbon emission impacts of vehicle technologies and alternative fuel through the year 2100. The estimations are done based on user input by defining the market share for each vehicle type and define fuel economy of each type. The fuel economy values match the projected values by annual energy outlook and the carbon emission values is based on the GREET model [245]. The GREET Model stands for The Greenhouse Gases, Regulated Emissions, and Energy Use in Transportation Model developed by the Argonne lab as a multi-dimensional spreadsheet. The first version was released in 1996 and the latest version is released on October 3, 2014. This tool is used to evaluate the energy and emission impacts of different vehicle technologies. The evaluations are done based on full fuel cycle and

vehicle cycle basis. The GREET model is a mathematical model evaluates the life cycle for different energy paths as shown in Figure 6.1. In Figure 6.1, the resources with the green background are the resources covered in GREET while the yellow background being processed. The resources with blue background are not calculated, e.g., solar energy has not included in this model yet.



Figure 6. 1 Snapshot from GREET Model: Energy Pathway [245]

Recently, many models are developed to evaluate the energy and emission impacts of different vehicle technologies and different energy paths. However, so far, none of these models investigate the incorporation of the on-board PV technologies to power vehicles.

6.2 Benchmarked Electric Vehicle (EV)

Figure 6.2 shows nine different EVs 2014 models used in this study for benchmarked, which Smart fortwo [246] is a two-seater car, Fiat 500e [247] is mini compact car, both Chevrolet Spark EV [248] and Mitsubishi i-MiEV [249] are subcompact size, Ford Focus [250] is a compact size vehicle, Nissan Leaf [251] is midsize car, Tesla Motor S [252] is large size car, Honda Fit [253] is small station wagon, and lastly Lastly, STELLA is the world first solar-powered family car developed by Solar team Eindhoven [254]. The reason Stella is included to compare the commercial EVs with solar vehicle.

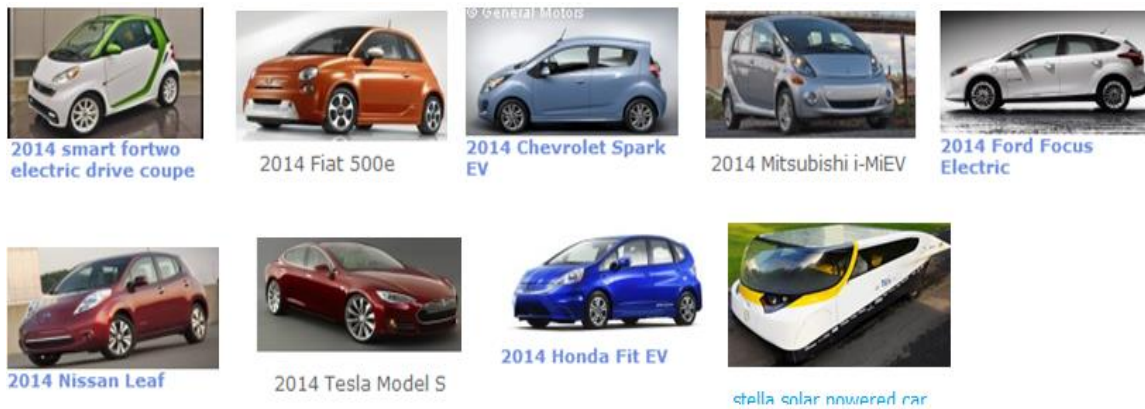


Figure 6. 2 Selected Electric vehicle for Benchmarked

All the previous vehicles are analyzed in many aspects. For example, the Figure 6.3 shows the curb weight in (kg) and the battery size for the above EV. The highest curb weight found in the case of Tesla Model around 2,108 kg with the lowest one in case of Stella, the solar car, around 380 kg. For other EVs, the curb weight between 950 kg to 1,651 kg. The battery size is varying between the minimum as in the case of Stella around

15 kWh to the most in case of Tesla 85 kWh. The battery sizes for the remaining EVs are varying between 16 kWh to 24 kWh.

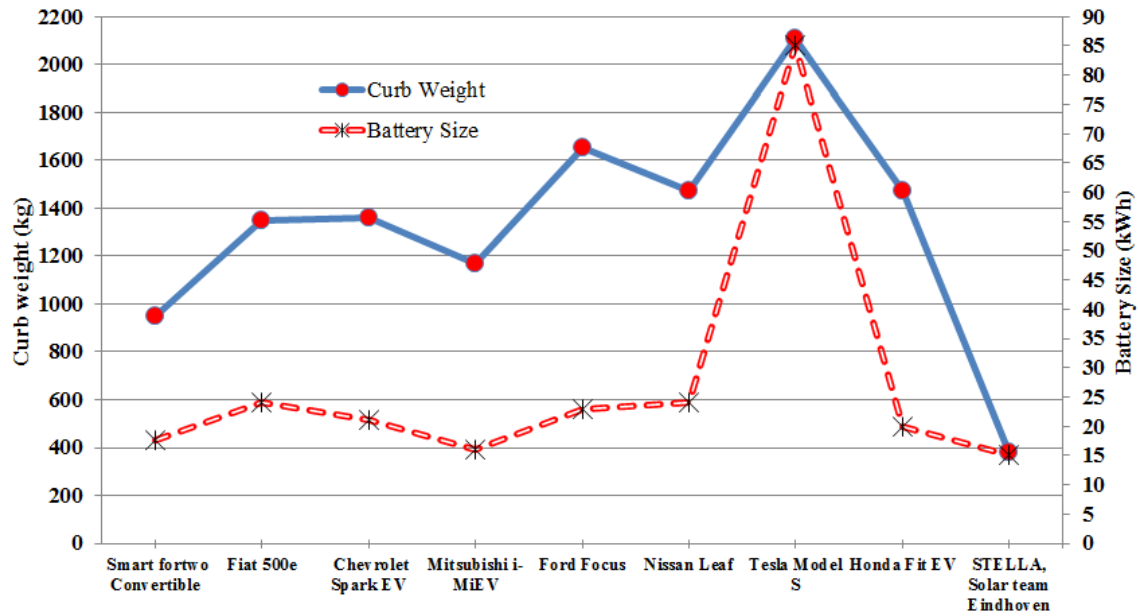


Figure 6. 3 Curb weight and battery size for selected EVs

Table 6.1 summarizes the combined miles on a charge, the time to charge the battery, and motor description for the selected EVs. The highest combined driving range on a single charge in both city and highway driving cycles is found in the case of Tesla Model S equal 265 miles. In case of Stella, there is no reported combined mile; however, the reported driving range is equal 373 miles. The remaining EVs have an average of 77 combined miles on a charge. This range is used as a proposed driving range for EV in this study.

Table 6. 1 Combined miles on a charge, the time to charge the battery, and motor description for selected EVs.

Vehicle (2014 Model)	Combined miles on a charge	Time to charge Battery	Motor descriptor
Smart fortwo Convertible	68	6 hrs, 240 V	Max Power :55 kW Water-cooled permanent 3-phase AC motor
Fiat 500e	87	4 hrs, 240 V	82 kW AC Induction Permanent Magnet
Chevrolet Spark EV	82	7 hrs, 240 V	104 kW AC Induction
Mitsubishi i-MiEV	62	7 hrs, 240 V	49 kW AC synchronous permanent magnetic motor
Ford Focus	76	3.6 hrs, 240 V	107 kW AC Permanent Magnet Synchronous
Nissan Leaf	84	8 hrs, 240 V (3.6 kW charger), 5 hrs, 240 V (6.6 kW charger)	80 kW AC synchronous electric motor
Tesla Model S	265	12 hrs, 240 V (single charger), 4.75 hrs, 240 V (dual charger)	270 kW AC Induction
Honda Fit EV	82	4 hrs, 240 V	92 kW AC Synchronous Permanent-Magnet Electric Motor
STELLA	-	-	DC 1.8 kW, efficiency 98.3%

In Figure 6.4, the driving efficiency in terms of energy consumption per mile (Wh/mile) is calculated and displayed. These values are based on reported combined kWh per 100 miles, except in case of Stella is based on driving range on a single charge. The Stella has a very efficient efficiency around 40 Wh per mile due to its light weight. In typical vehicle, the efficiency around 300 Wh per mile.

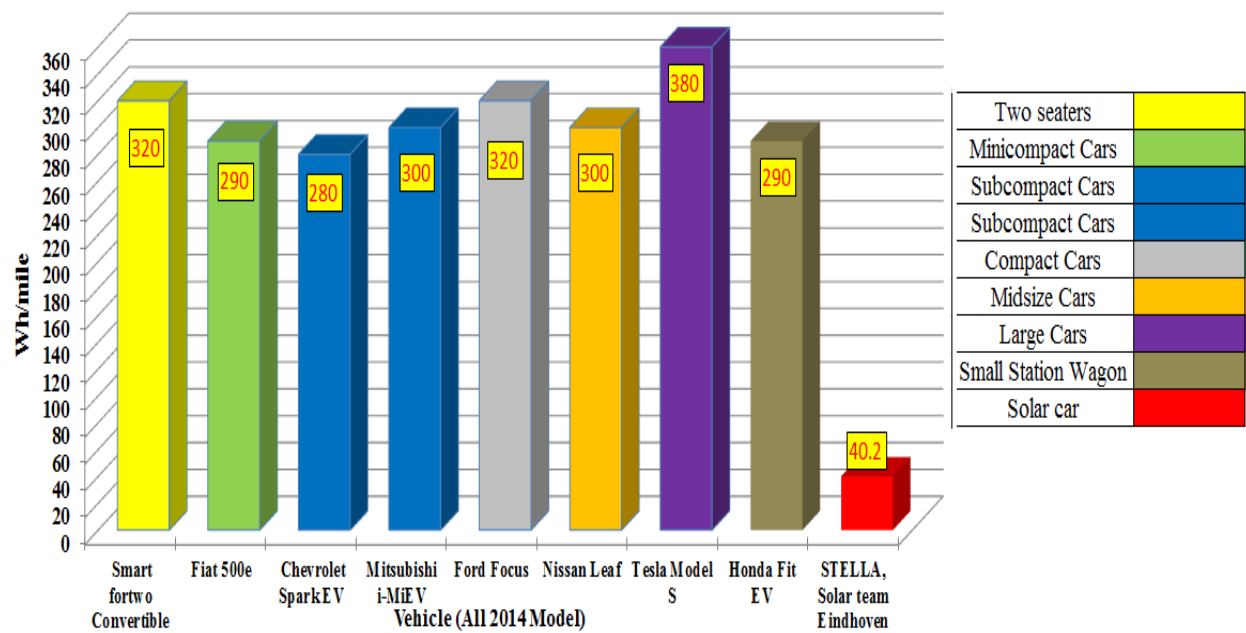


Figure 6. 4 Energy consumption per mile (Wh/mile) of selected EVs

6.3 Benchmarked Solar Vehicle

Some of the vehicles with on-board PV are discussed in chapters 2 and 3. In the previous section, Stella is discussed which is lightweight solar car has room for four people. Other solar vehicle as Tesseract, the MIT solar car [255], is lighter than Stella, with reported curb mass with driver as 254 kg and solar surface area is equal 7.5 m^2 , the drag coefficient and frontal surface are 0.12 and 0.85, respectively. The motor is 6 hp axial flux brushless DC motor. Nuna 7 [256], which is designed by Nuon Solar Team at Delft University of Technology has a curb weight slightly higher than Tessercat and equal 270 kg, the solar energy is stored in 5.3 kWh battery size. The reported rolling resistance is 10 times less than the average car and the drag coefficient is very low as 0.07.

Recently, Ford Motor Company has released C-MAX Solar Energi Concept [257], the plug-in hybrid EV that use concentrated photovoltaic (CPV) to recharge the battery. This concept is different from on-board PV to power vehicle. Here, the solar energy is concentrated using Fresnel lenses in a canopy-like a parking structure to focus sunlight, then transmit this energy to the solar which installed on the vehicle roof. This solar transmitter has the ability to track the sun and the vehicle has to be stopped at the solar concentrator transmitter spot to receive this energy. The concept is shown in Figure 6.5. The roof PV area is 1.5 m^2 with power output around 300-350 W with the intensity of light is boosted eight times using this concept. The estimated driving range of pure EV is 21 miles.

Elements of the C-MAX Solar Energi Concept

Ford C-MAX Solar Energi Concept is a first-of-its-kind sun-powered concept vehicle with the potential to deliver the best of a plug-in hybrid without depending on the electric grid for fuel. By using renewable power, the C-MAX Solar Energi Concept is estimated to reduce annual greenhouse gas emissions from a typical owner by four metric tons.

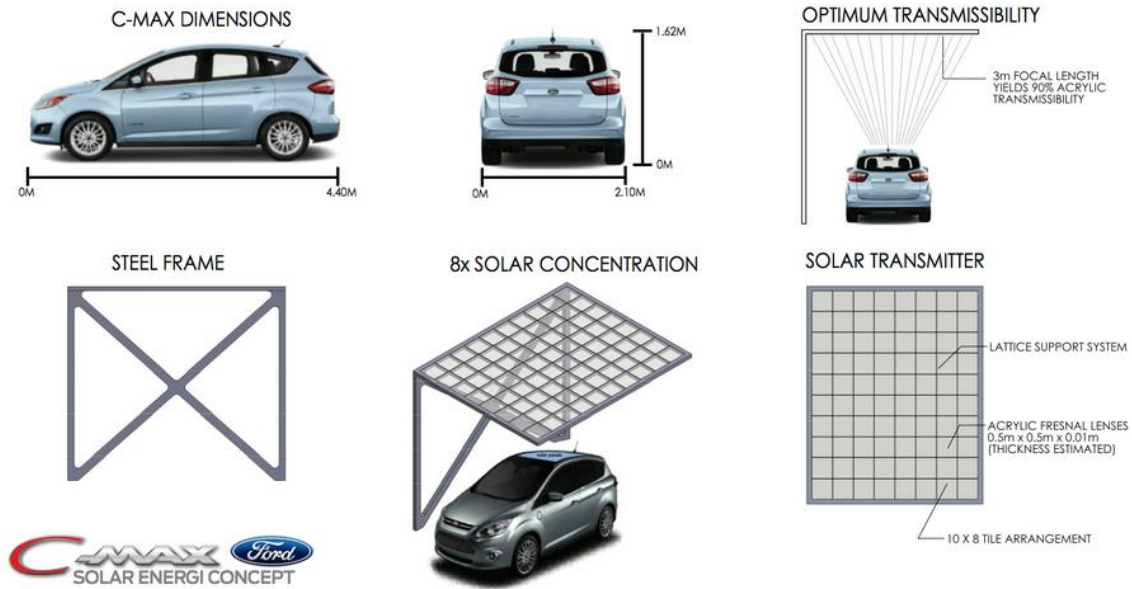


Figure 6. 5 C-MAX Solar Energi Concept, Ford Motor Company [257]

6.4 Modeling Vehicle Energy at Wheels

The certain energy demands at the wheels for a given driving cycle and given vehicle is calculated by first calculated the force at the wheel by using Equations (6.1)-(6.5) [258]:

$$F_w = F_a + F_r + F_g + F_I \quad (6.1)$$

Where,

F_w , is the forces at the wheel

F_a , Aerodynamics force

F_r , rolling force

F_g , grade force

F_I , is the inertia force

The above forces are calculated using equations

$$F_a = \frac{1}{2} \times \rho_a \times C_d \times A_f \times v_{eff}^2 \quad (6.2)$$

$$F_r = M_v \times g \times \cos(\alpha) \times C_r \quad (6.3)$$

$$F_g = M_v \times g \times \sin(\alpha) \quad (6.4)$$

$$F_I = (M_v + M_r) \cdot \frac{dV}{dt} \approx 1.1 \cdot M_v \cdot \frac{dV}{dt} \quad (6.5)$$

Where,

ρ_a , is the density of the ambient air, which typically assume as 1.225 kg/m³

C_D , is the dimensionless aerodynamic drag coefficient that depends upon the shape of the moving body. For example, $C_d = 0.24$ for 2012 Tesla Model S [259], $C_d=0.28$ Nissan Leaf 2014 [260], $C_d=0.159$ Volkswagen XL1 2015 [261].

A_f , is the frontal projected area in m², $A_f = 2.32$ m² for 2012 Tesla Model S and $A_f=1.02$ m² for Volkswagen XL1 2013.

V_{eff} , is the effective vehicle speed and is called (V) if the wind speed is ignored.

C_r , is the rolling resistance coefficient, which depends upon the tire pressure and tire type. The typical values of C_r are 0.008 to 0.012 and can be as low as 0.005 for special tires.

M_v , the vehicle mass in (kg) and Figure 6.3 showed some example of typical vehicle mass.

M_r , the rotational inertia estimated as 10% of M_v

g , is gravity constant acceleration equal 9.81 m/s^2

α , is the slope road, equal 0 if no grade is assumed.

The power at the wheels (P_w) is calculated by Equation (6.6):

$$P_w = F_w \times V \quad (6.6)$$

The certain energy demand at the wheels in a given driving cycle is calculated using Equations (6.7)-(6.9) [258] assumed there is no grade as below.

$$E_w = \int_{Cycle} P_w dt \quad (6.7)$$

$$E_w = \frac{1}{2} \cdot \rho_a \cdot C_d \cdot A_f \cdot \int_{Cycle} v^3 dt + M_v \cdot g \cdot C_r \cdot \int_{Cycle} v dt + 1.1 \cdot M_v \cdot \int_{Cycle} V \frac{dV}{dt} \quad (6.8)$$

The above integral can be approximated in discrete form as:

$$E_w \cong \Delta t \cdot \left[\alpha_A \cdot \sum_i V_i^3 + \alpha_R \cdot \sum_i V_i + \alpha_I \cdot \sum_i \left(V_i \cdot \frac{dV_i}{dt} \right)^* \right] \quad (6.9)$$

Where,

Δt is the time step for driving cycle

V_i is the velocity at time step i

α_A , α_R , and α_I are vehicle dependent only factors, called aerodynamics, rolling, and Inertia, respectively.

$\frac{dV_i}{dt}$ is the acceleration at time step i , this term could be positive or negative depends on

if the vehicle is on acceleration or braking phases.

The summation in the last term in Equation (5.9) denoted by a star is related to inertia. This summation depends on driving cycle, as well as the regeneration efficiency. The regeneration efficiency is the potential to recapture the waste heat during vehicle decelerating by converting kinetic energy to store it in the battery or use it for propulsion. if the regeneration ability is assumed 100%, then this summation is zero and the third term in Equation (6.9) is ignored. This is because the assumption is the system is strictly conservative. If there is no regeneration at all, then the summation is counted only on time sample i have $\frac{dV_i}{dt} > 0$ and in this case represents the maximum summation as for any remaining time sample $\frac{dV_i}{dt} < 0$ is wasted as a heat and absorbed by the brakes. If the regeneration efficiency is assumed other values (e.g., η %), then the energy at the wheel will be between the two extreme values and the third summation in Equation (6.9) is separated as shown in Equation (6.10).

$$\sum_{i \rightarrow \frac{dV}{dt} > 0} (V_i \cdot \frac{dV_i}{dt}) + \eta \cdot \sum_{i \rightarrow \frac{dV}{dt} < 0} (V_i \cdot \frac{dV_i}{dt}) \quad (6.10)$$

Figures (6.6) to (6.8) show the driving cycle considered in this study (Data source in [262]). The FUDS is the federal urban driving cycle or sometimes it is called urban

dynamometer driving schedule (UDDS), or called city cycle. The city cycle simulates a stop and go trip as shown in Figure 6.6. The duration for this cycle is 1372 seconds (less than 23 minutes) and the driving distance 12.368 km (7.685 miles) with maximum speed equal 25.26 m/s (56.5 mph) and average speed is 9.01 m/s (20.15 mph).

The FHDS is the federal highway driving schedule or it is called HWFET stands for highway fuel economy driving schedule, it is called highway cycle shown in Figure 6.7. This cycle relatively is shorter than UDDS with 765 seconds (duration is less than 13 minutes) with traveling distances, equal 17.027 km (10.58 miles). The maximum speed is 26.78 m/s (59.91 mph) and average speed 22.26 m/s (49.79 mph).

The last driving cycle is 10+15 mode Japanese driving cycle, which uses to simulate low speed traffic. The duration is 660 seconds (11 minutes) with maximum speed is 19.44 m/s (43.48 mph).

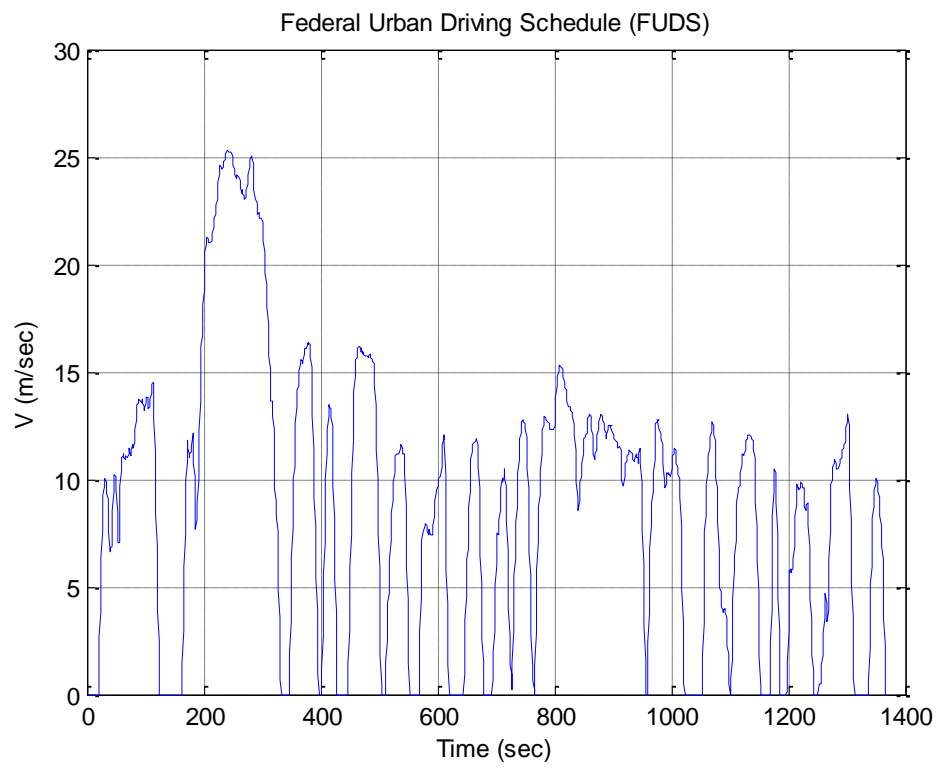


Figure 6. 6 Speed profile in FUDS driving cycle

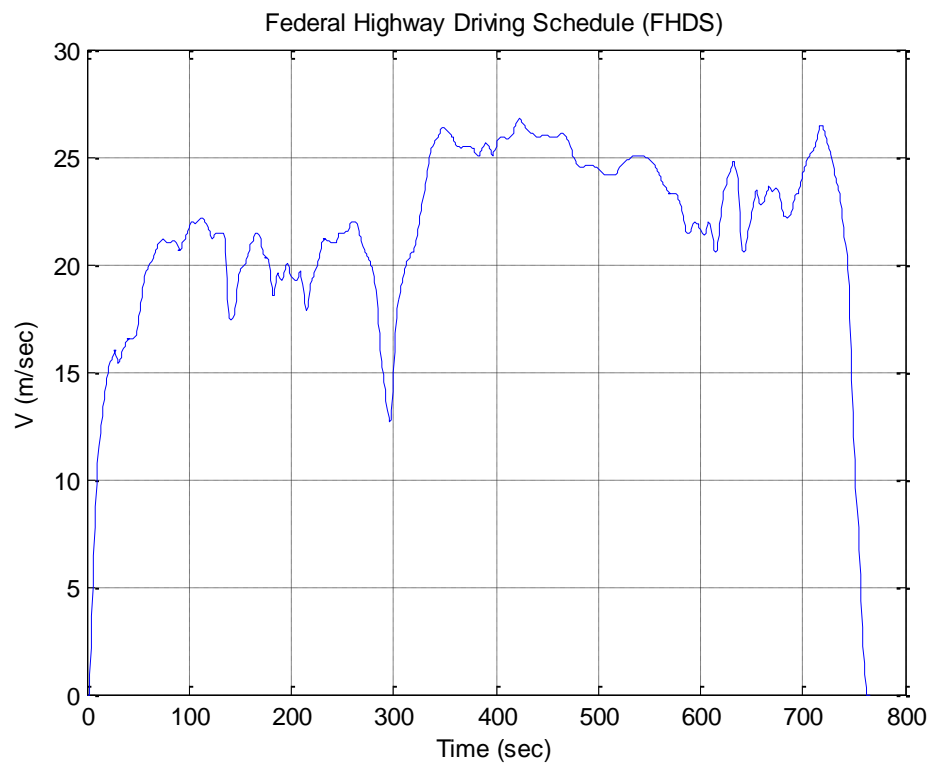


Figure 6. 7 Speed profile in FHDS driving cycle

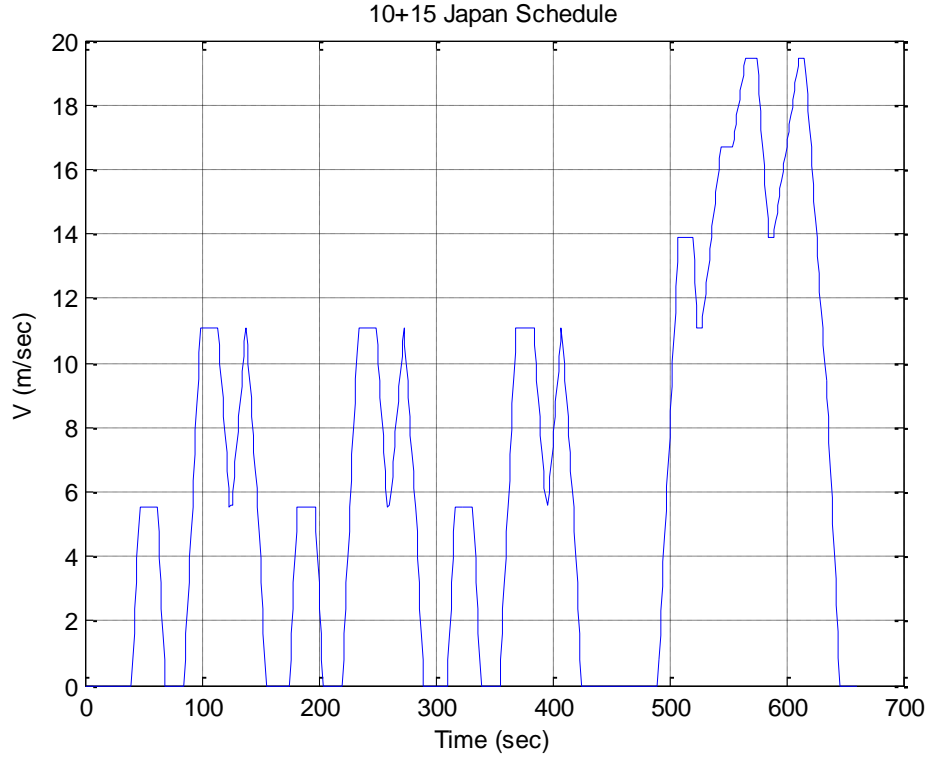


Figure 6. 8 Speed profile in 10+15 Japanese driving cycle

Another important parameter used in this study is the mean traction force. The mean traction force is defined as the total mechanical energy consumed per traveled distance in the given driving cycle and is calculated using Equation (6.11) [258].

$$\overline{F}_{traction} = \frac{1}{x_{tot}} \cdot \int_{t \in traction} F_w(t) \cdot v(t) dt \quad (6.11)$$

Where,

x_{tot} is defined as the total distance the vehicle traveled and calculated using Equation (6.12).

$$x_{tot} = \int_0^{t_{max}} v(t) dt \quad (6.12)$$

The mean traction force parameter relates to the traction mode. The traction mode is the mode in vehicle operation, when the vehicle needs to be provided by force to move. The other vehicle operation modes are braking or costing. As discussed previously, if the ideal recuperation is assumed, then the mean traction force (energy) is calculated only by considering aerodynamics and rolling friction losses but for all the time. But, if there is no recuperation, the mean traction force is calculated only at traction time, but includes all the losses (aerodynamics, rolling, and inertia). If the regeneration efficiency is assumed η %, mean traction force is calculated using Equation (6.13) as:

$$\bar{F}_{traction, \eta} = \frac{1}{x_{tot}} \left[\int_{t \in traction} P_w(t).dt - \eta \int_{t \in braking} P_w(t).dt \right] \quad (6.13)$$

By applying the previous equations with the assumption that there is no grade, the following mean traction force (energy in KJ per 100 km) Equations is calculated for the above three driving cycles for different cases:

- (i) In the case, the regenerative (recuperation) efficiency is 100%, then the mean traction force in kJ per 100 km is calculated as below Equation (6,14) to Equation (6.16).

$$\text{FUDS: } \bar{E}_{rec,100\%} = C_d A_f \rho \times 1.0962 \times 10^4 + M_v C_r \times 9.7984 \times 10^2 \quad \text{kJ/100km} \quad (6.14)$$

$$\text{FHDS: } \bar{E}_{rec,100\%} = C_d A_f \rho \times 2.5843 \times 10^4 + M_v C_r \times 9.7947 \times 10^2 \quad \text{kJ/100km} \quad (6.15)$$

$$\text{Japan: } \bar{E}_{rec,100\%} = C_d A_f \rho \times 5.5218 \times 10^3 + M_v C_r \times 6.4384 \times 10^2 \quad \text{kJ/100km} \quad (6.16)$$

ii. In the case, the regenerative (recuperation) efficiency is 80%, then the mean traction force in kJ per 100 km is calculated as shown in Equations (6.17) to (6.19)

$$\text{FUDS: } \bar{E}_{rec,80\%} = C_d A_f \rho \times 1.0962 \times 10^4 + M_v C_r \times 9.7984 \times 10^2 + M_{eff} \times 5.1301 \quad \text{kJ/100 km} \quad (6.17)$$

$$\text{FHDS: } \bar{E}_{rec,80\%} = C_d A_f \rho \times 2.5843 \times 10^4 + M_v C_r \times 9.7947 \times 10^2 + M_{eff} \times 5.1301 \quad \text{KJ/100km} \quad (6.18)$$

$$\text{Japan: } \bar{E}_{rec,80\%} = C_d A_f \rho \times 5.5218 \times 10^3 + M_v C_r \times 6.4384 \times 10^2 + M_{eff} \times 3.0546 \quad \text{KJ/100km} \quad (6.19)$$

Where, the effective mass $M_{eff} = 1.1. M_v$

The benefit of the above equations is given the general form for the estimation of the energy required at wheels for given driving cycle for given target distance and by substituting the given vehicle parameters in terms of mass, etc. the energy is calculated at wheels.

6.5 Sensitivity Analysis and MPG calculation

The sensitivity analysis is used to evaluate the effects of changes in a specific variable on energy consumption in giving driving cycle. This is used to understand the most promising approach to reduce energy consumption. The sensitivity is calculated using the Equation (6.20) [258].

$$S_p = \lim_{\delta p \rightarrow 0} \frac{(\bar{E}(p + \delta p) - \bar{E}(p)) / \bar{E}(p)}{\delta p / p} \quad (6.20)$$

Where,

\bar{E} , is the energy for a given driving cycle for example, \bar{E}_{FUDS} is the energy (same as mean traction force) for FUDS cycle.

p , is variable stands for any of the vehicle parameters (C_d , m_v , C_r , or A_f)

Equation (6.20) can be re-written as Equation (6.21) [258] to calculate the sensitivity for specific parameter change.

$$S_p = \frac{\partial \bar{E}(p)}{\partial p} \cdot \frac{p}{\bar{E}(p)} \quad (6.21)$$

The following is as an example of the model output, assumed the vehicle parameters are $C_r = 0.008$, $C_d=0.17$, $A_f=1.2 \text{ m}^2$, $M_v= 900 \text{ kg}$ and assumed ρ is equal 1.225 kg/m^3 . The calculated power (kW) demand at wheel is shown in Figure 6.9. This Figure showed also the traction and braking power.

The maximum positive power is found 21.36 kW and the maximum negative power is 16.38 kW. The average positive power needs at the wheel is found equal 2.16 kW. The positive energy requirement is 2.96 MJ.

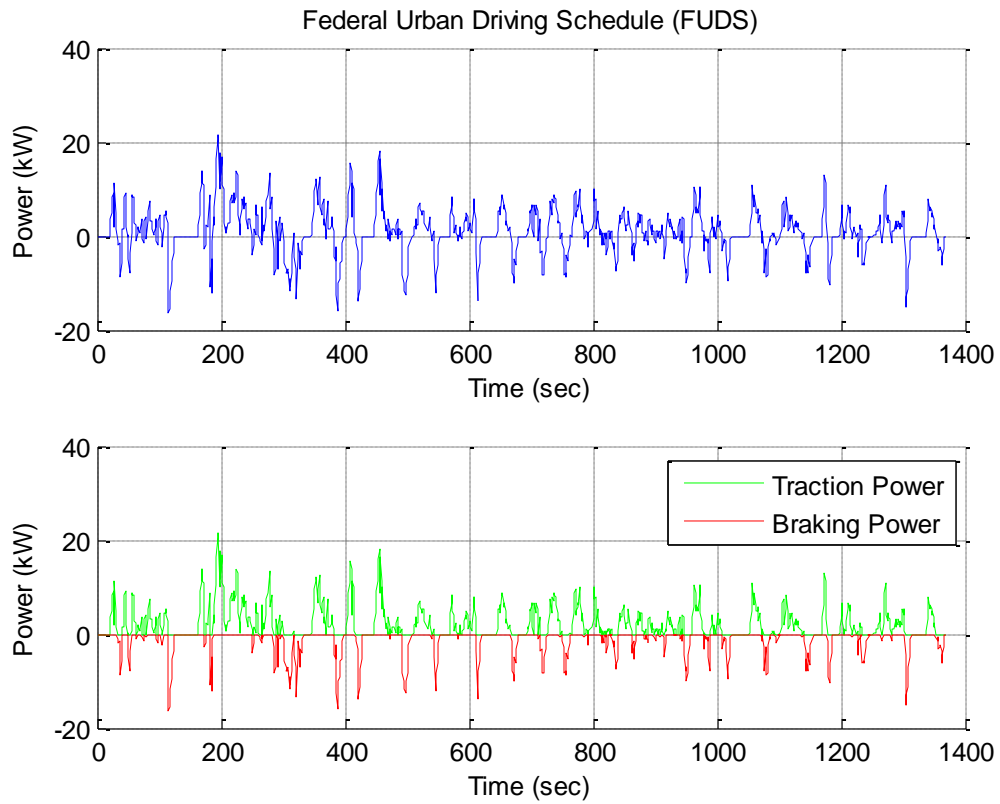


Figure 6. 9 Traction and braking power in FUDS for specific vehicle

For the same vehicle, Figure 6.10 shows the required power at wheels for FHDS cycle. The average positive power is 3.7 kW and the positive energy requirement is 2.84 MJ. The maximum positive power is 17.1 kW and the maximum negative power is 23.68 kW.

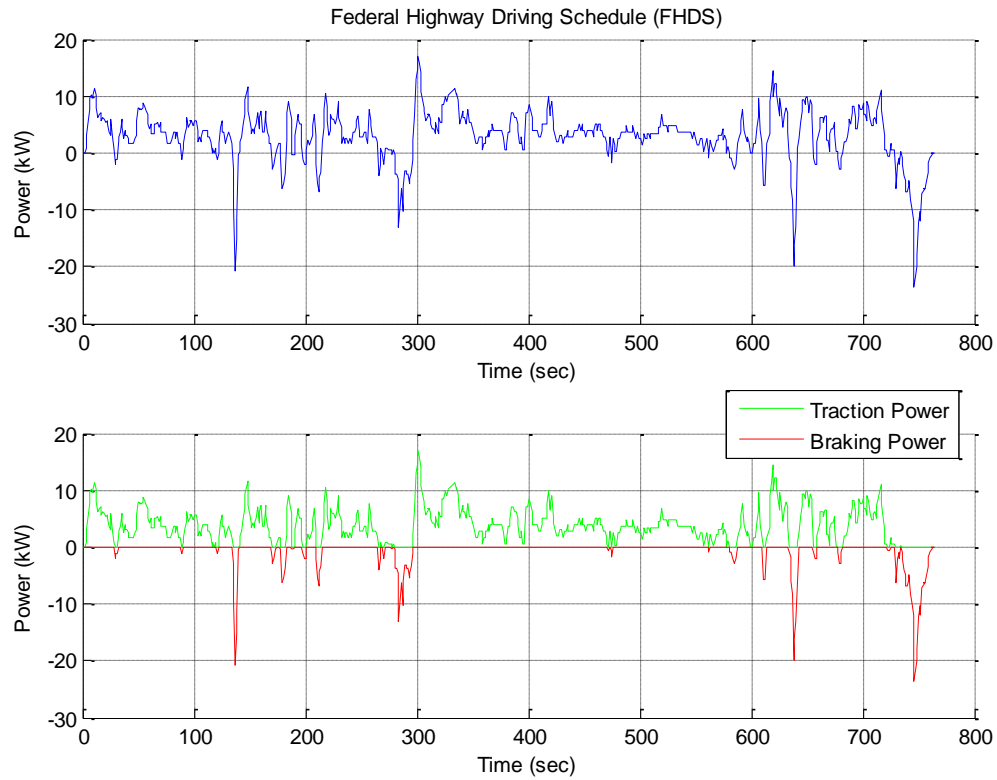


Figure 6. 10 Traction and braking power in FHDS for specific vehicle

If the 10+15 Japan schedule driving cycle is used, then the average positive power is relatively small and equal 1.51 kW and the maximum positive power 11.93 kW and the maximum negative power is -8.21 kW. The positive energy requirement is about 1 MJ. Figure 6.11 shows the power demands at wheels for 10+15 Japan cycle.

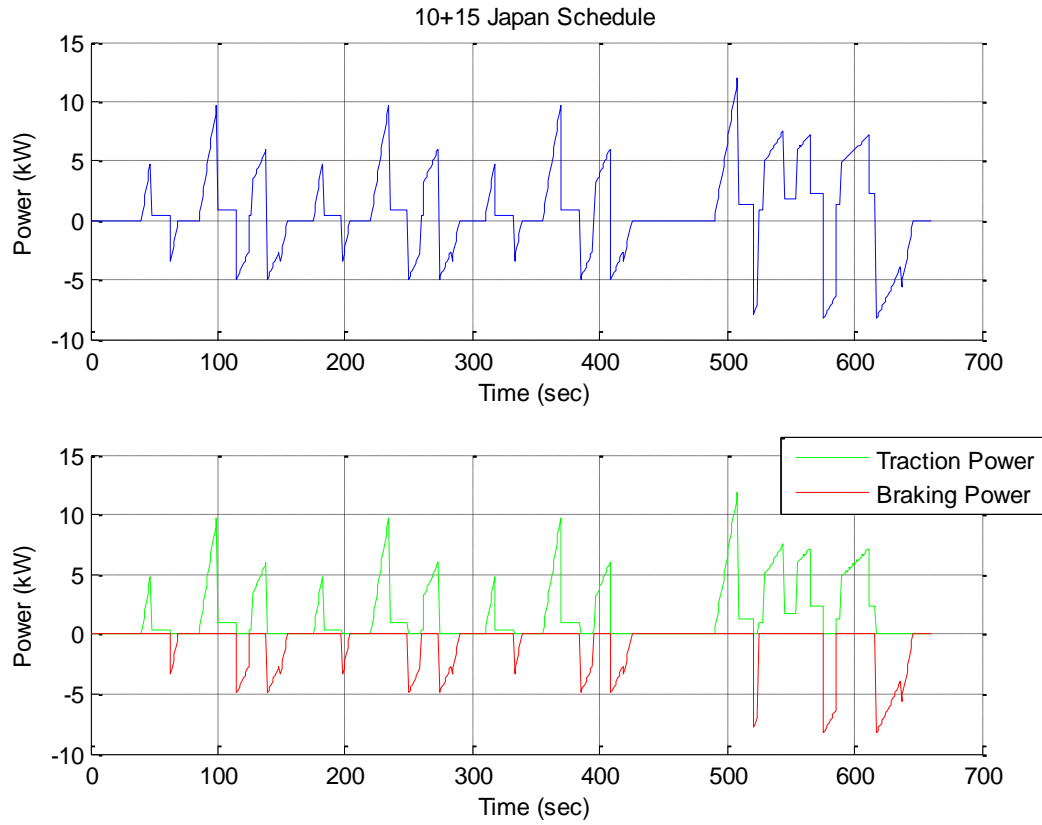


Figure 6. 11 Traction and braking power in 10+15 for specific vehicle

Figure 6.12 shows the energy (mean traction force) required at the wheels for the assumed vehicle in the three driving cycles with two cases no regeneration and ideal regeneration.

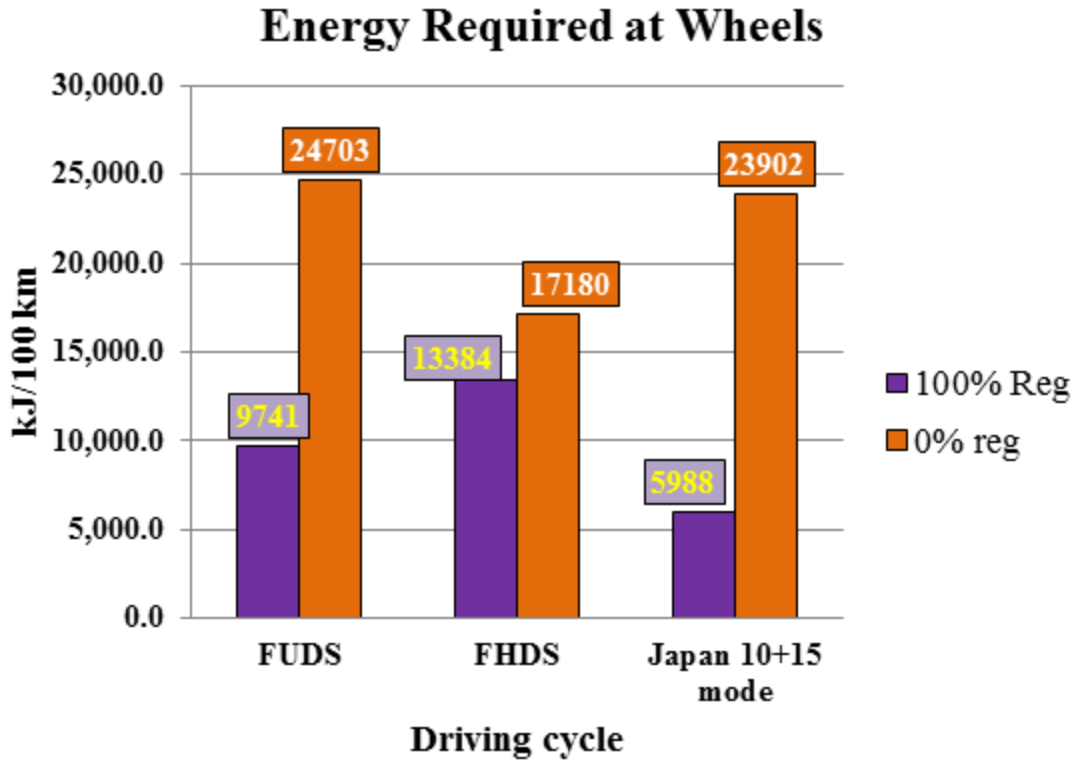


Figure 6. 12 Energy required at wheels per 100 km for different driving cycle for the assumed vehicle

The sensitivity results analysis of the required energy at the wheels are shown in Figures 6.13 and 6.14 for two scenarios 100% regeneration and 80% efficiency regeneration, respectively. The results (y-axis in the Figures 6.13 and 6.14) are based on the 5% reduction in parameter yields x% reduction consumption in the corresponding driving cycle. For example, with ideal regeneration, the rolling resistance C_r has same impact as vehicle mass, but in 80% regeneration efficiency case, the vehicle mass has a higher impact than C_r for all driving cycle. In addition, $C_d A$ has more impact in FHDS highway cycle than the other two cycles.

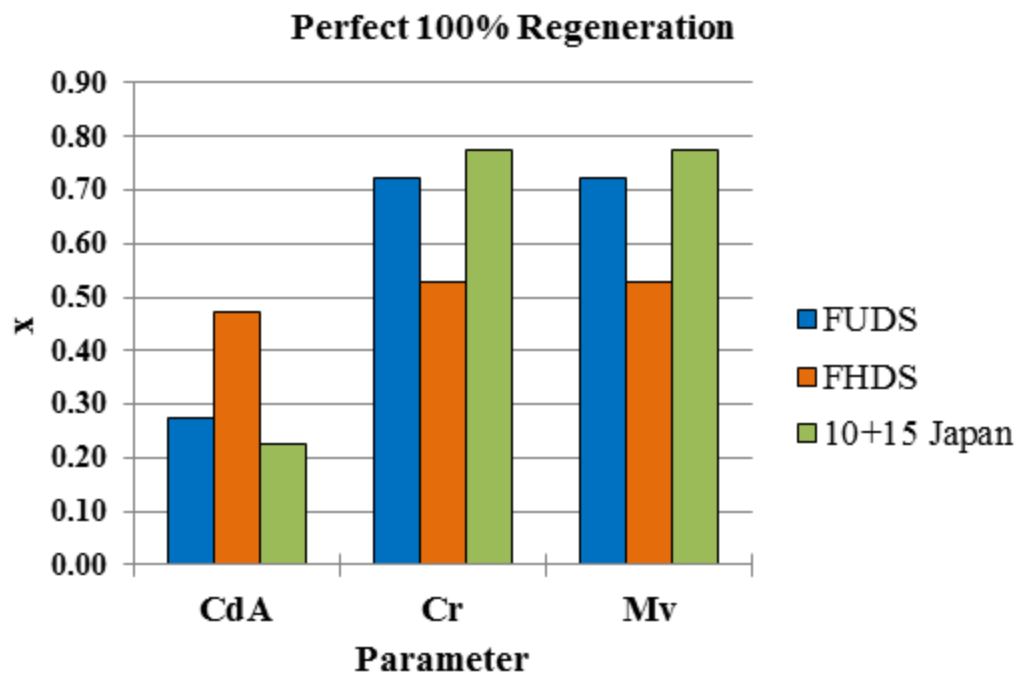


Figure 6. 13 Sensitivity analysis based on 5% reduction in parameter yields x% reduction in required energy consumption at wheels (perfect 100% regeneration)

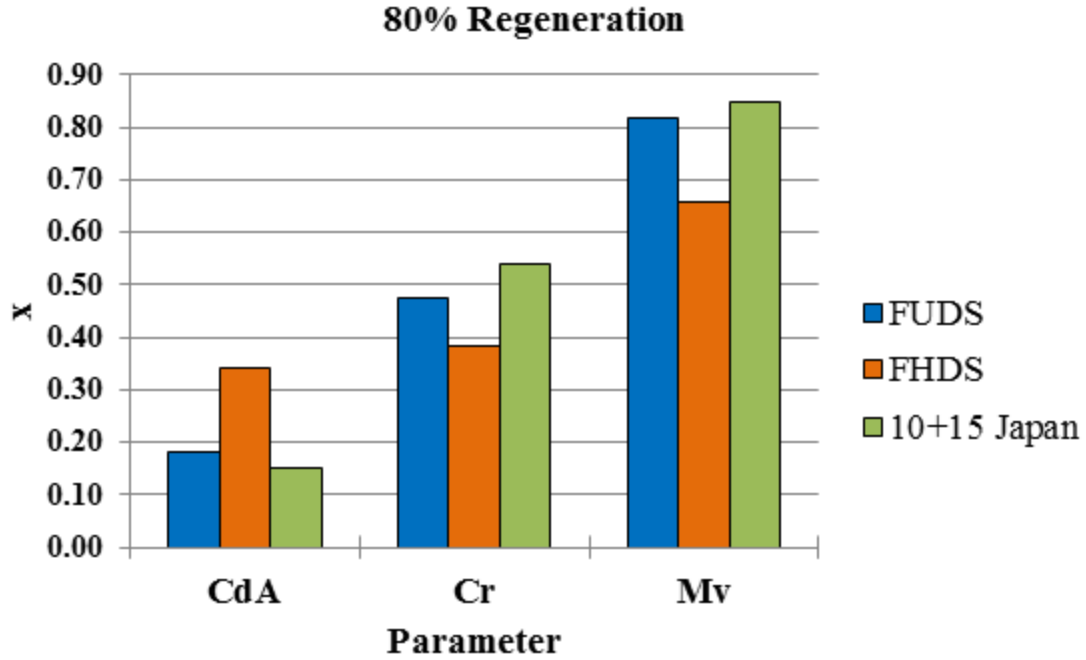


Figure 6. 14 Sensitivity analysis based on the 5 % reduction in parameter yields x% reduction in required energy consumption at the wheels (80% regeneration)

6.5 MPG Calculations

The fuel economy (FE) in terms of mile per gallon (MPG) in given driving cycles is calculated using Equation (6.22) [258].

$$\text{MPG} = \eta_{\text{T2W}} \times \frac{E_{\text{gasoline}}}{E_{\text{cycle}}} \times I_{\text{cycle}} \quad (6.22)$$

Where,

η_{T2W} : Tank to Wheel efficiency

E_{gasoline} : Energy in one gallon of gasoline

E_{cycle} : Energy need for given cycle in kWh

I_{cycle} : Driving cycle length in miles

$E_{gasoline}$ is assumed 33.7 kWh [263], I_{cycle} depends on the driving cycle, E_{cycle} depends on the vehicle parameters as well as driving cycle. The η_{T2W} is changed based on Powertrain configurations and driving cycle [264].

The combined fuel economy (FE) is calculated based on city and highway driving cycles (FE) using Equation (6.23). The weights of the city and highway driving cycles are considered as 55 percent and 45 percent, respectively.

$$FE (combined) = \frac{1}{\frac{0.55}{City FE} + \frac{0.45}{Hwy FE}} \quad (6.23)$$

For alternative fuel vehicles other than an internal compulsion vehicle, the mile per gallon gasoline equivalent (MPGe) is used to calculate the vehicle fuel economy based on Equation (6.24).

$$MPGE = \frac{\frac{\text{Total miles driven}}{\text{Total energy of all fuels consumed}}}{\text{Energy of one gallon of gasoline}} = \frac{33,700}{E_M} \quad (6.24)$$

Where, E_M is tank to wheel efficiency, electric energy consumed per mile (Wh/mile)

For example, assumed the very efficient vehicle parameters as $C_r = 0.008$, $C_d = 0.17$, and $A_f = 1.2 \text{ m}^2$ and no regeneration, the combined MPG/MPGe is calculated and displayed in Figure 6.15 based on various values of tank-to-wheel efficiency (η_{T2W}) and curb weight (M_v). The η_{T2W} is varying from low values typically 15-25 % in the case of gasoline vehicle to 27 -38 % in the case of hybrid Powertrain, and the maximum typically in the case of electric vehicle. For example, Tesla's electric powertrain with efficiency 88% [265]. The two lines in the Figure represented CAFE target 2020 and 2025.

The results showed for given η_{T2W} , the fuel economy depends heavily on curb weight and Vice Versa. The Figure 6.16 shows zooming to the region cannot meet CAFE target.

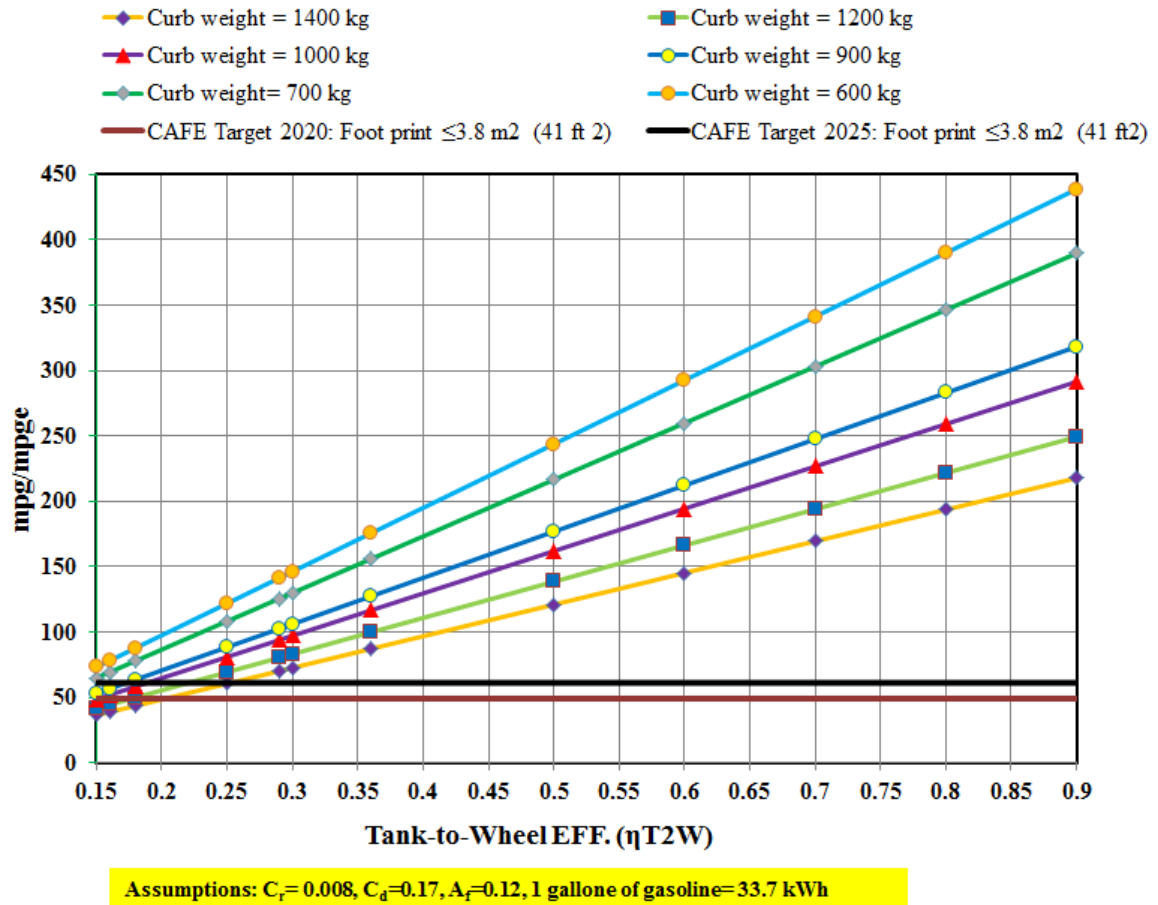


Figure 6. 15 Combined MPG/MPGe based on Tank to wheel efficiency and curb weight (No regeneration)

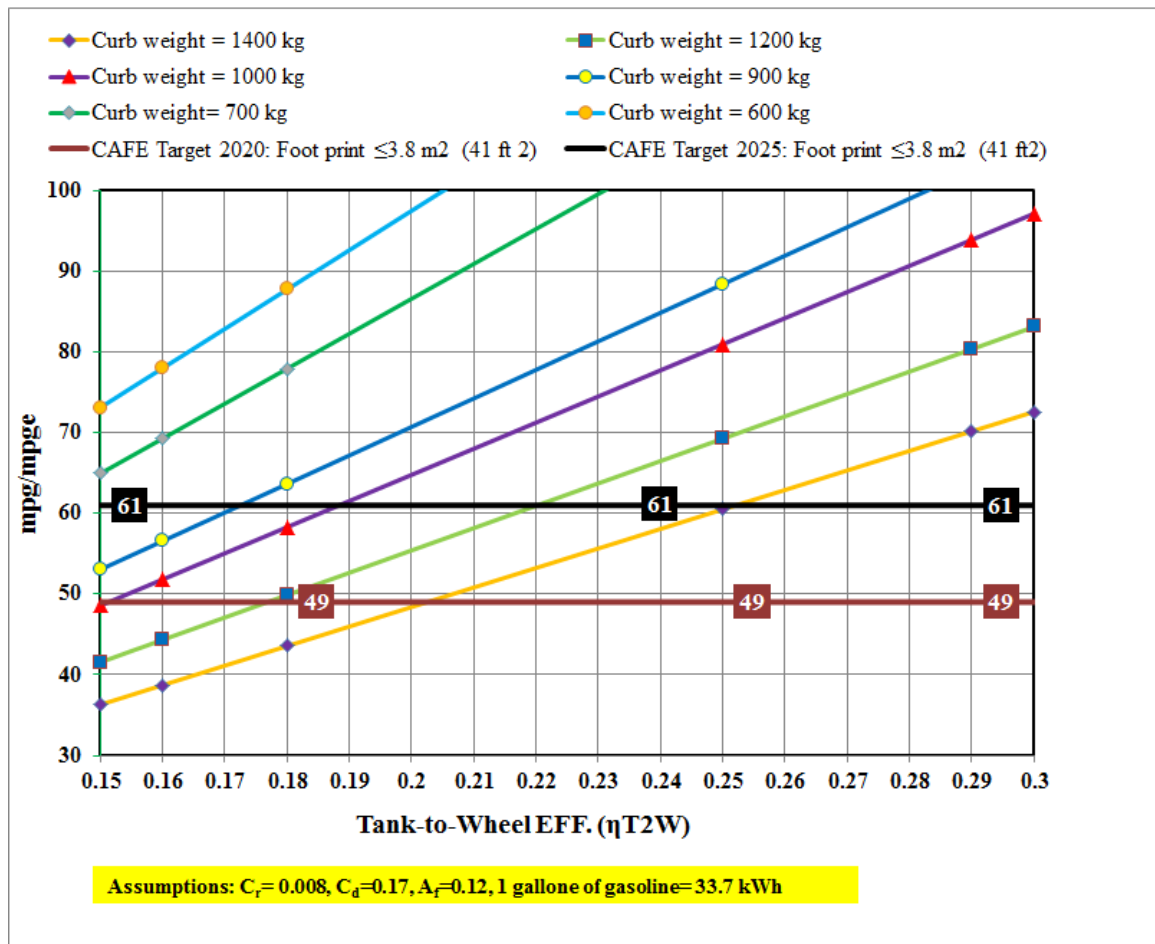


Figure 6. 16 Zooming snapshot of combined MPG/MPGe based on Tank to wheel efficiency and curb weight (No regeneration)

6.6 CAFE Standards with Projected Horizontal Vehicle Surface

The Figure 6.17 shows the CAFE standard curves for passenger car per vehicle footprint [266]. The x-axis represents the vehicle footprint in (ft²), the vehicle footprint is defined as the area consists of vehicle's wheelbase multiply by the average track width. For example, if the vehicle's footprint is equal 41 ft² (3.8 m²), this is similar to Honda Fit size, the fuel economy target has increased from around 38 mpg in 2014 to 61 mpg in 2025.

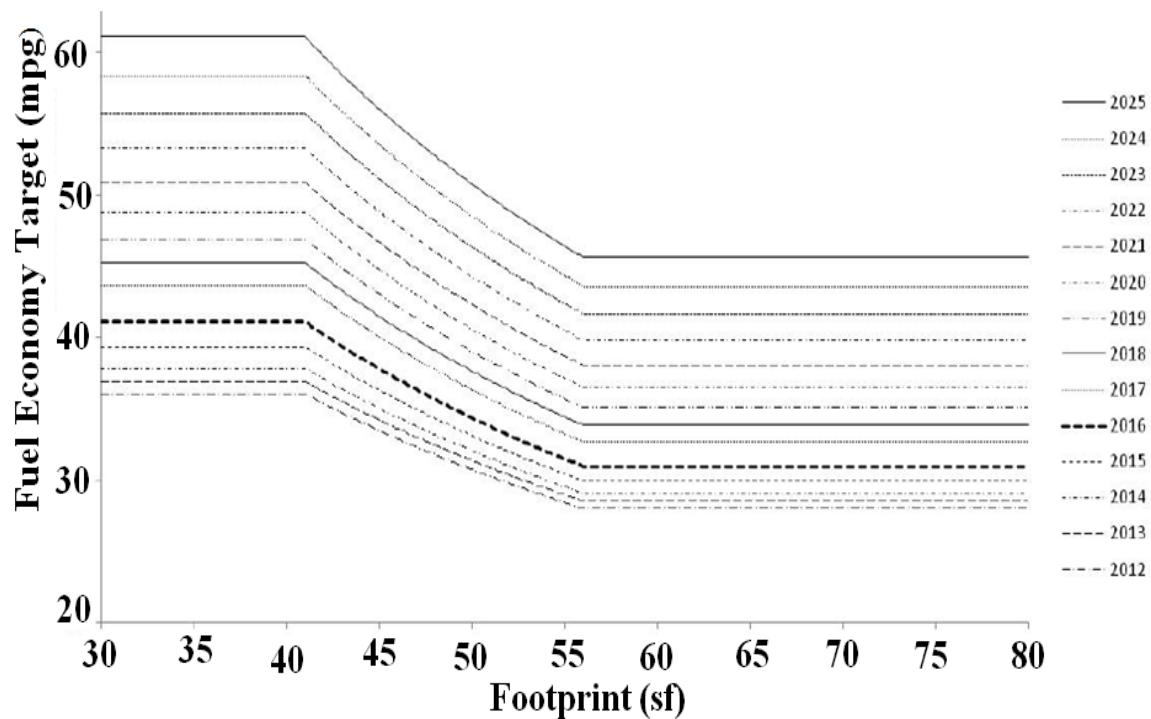


Figure 6. 17 CAFE (MPG) Standard Curves for Passenger Cars [266], edited for clearness

The CAFE target curves for year 2020 and 2025 can be re-written as criteria (6.25) and (6.26):

$$2020 : \begin{cases} ft \leq 3.8 \text{ m}^2 & \text{CAFE} = 49 \text{ MPG} \\ 3.8 \text{ m}^2 < ft < 5.1 \text{ m}^2 & \text{CAFE} = -0.9285714 \times ft^2 + 87.07143 \\ ft \geq 5.1 \text{ m}^2 & 36 \end{cases} \quad (6.25)$$

$$2025 : \begin{cases} ft \leq 3.8 \text{ m}^2 & \text{CAFE} = 61 \text{ MPG} \\ 3.8 \text{ m}^2 < ft < 5.1 \text{ m}^2 & \text{CAFE} = -1.0714286 \times ft^2 + 104.928571 \\ ft \geq 5.1 \text{ m}^2 & 46 \end{cases} \quad (6.26)$$

Where, ft in square feet.

Since, the CAFE target is based on the vehicle footprint and the PV output depends on the installation area typically on the surface. The next steps are done to relate the projected vehicle surface area with the CAFE 2020 and 2025 targets to investigate how much installation area is needed for given CAFE target.

First, for 2014 EV using for benchmarked in Figure 6.2. The relation between the reported vehicle footprint in (m^2) and projected horizontal surface in (m^2) are done as shown in Figure 6.18. Eight 2014 EVs are analyzed denoted from (a) to (h) in Figure 6.18. The projected horizontal surface is calculated by multiplying the reported vehicle length by width. The predicted relation is found with linear relationship with R^2 is too high equal 0.9637. The predicted horizontal area is found in the form (6.27).

$$\text{Predicted projected horizontal area} = 2.2807 \times \text{footprint} - 1.5638 \quad (6.27)$$

Where, the vehicle footprint in (m^2).

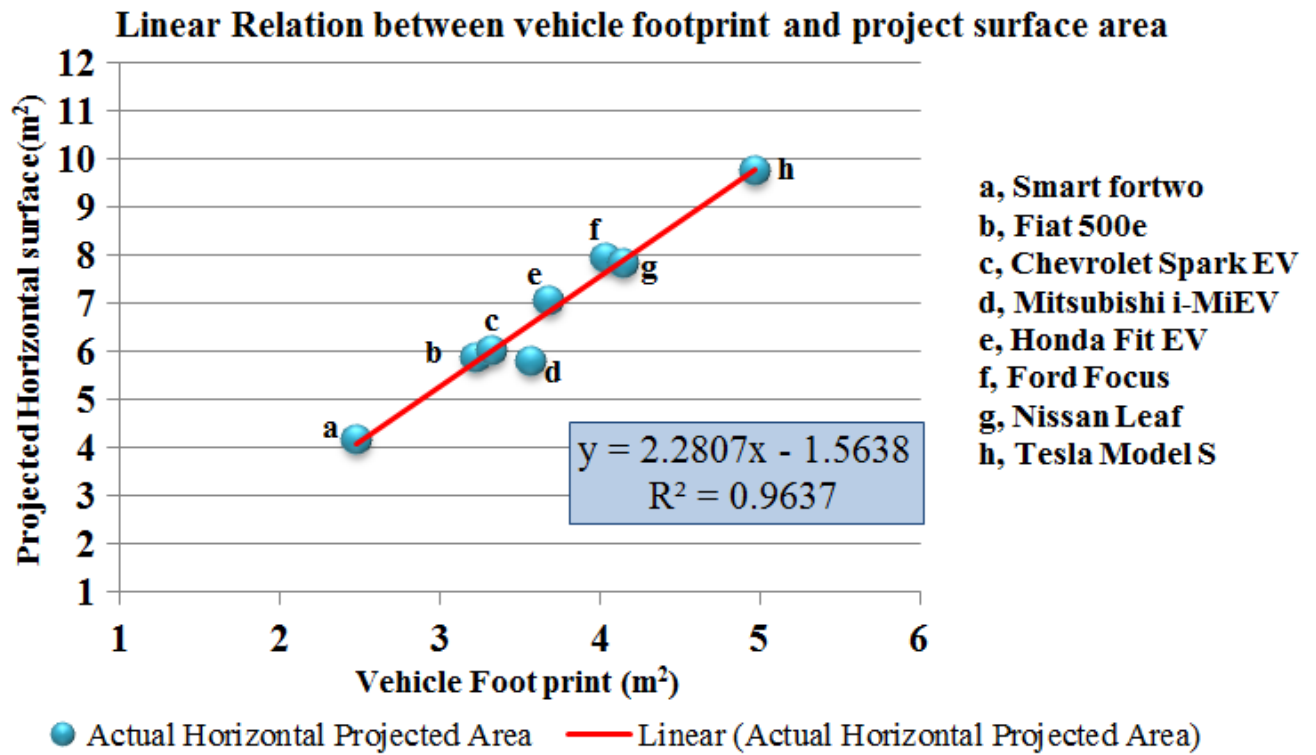


Figure 6. 18 Predicted projected horizontal surface based on vehicle footprint for selected 2014 EVs

The error in (m²) between (actual and predicted) projected horizontal surface areas is shown in Figure 6.19. The maximum error is found in the case of i-MiEV 2014 and Ford focus 2014 vehicle about 0.75 m² and 0.32 m², respectively. While for the most other vehicles with error less than 0.1 m².

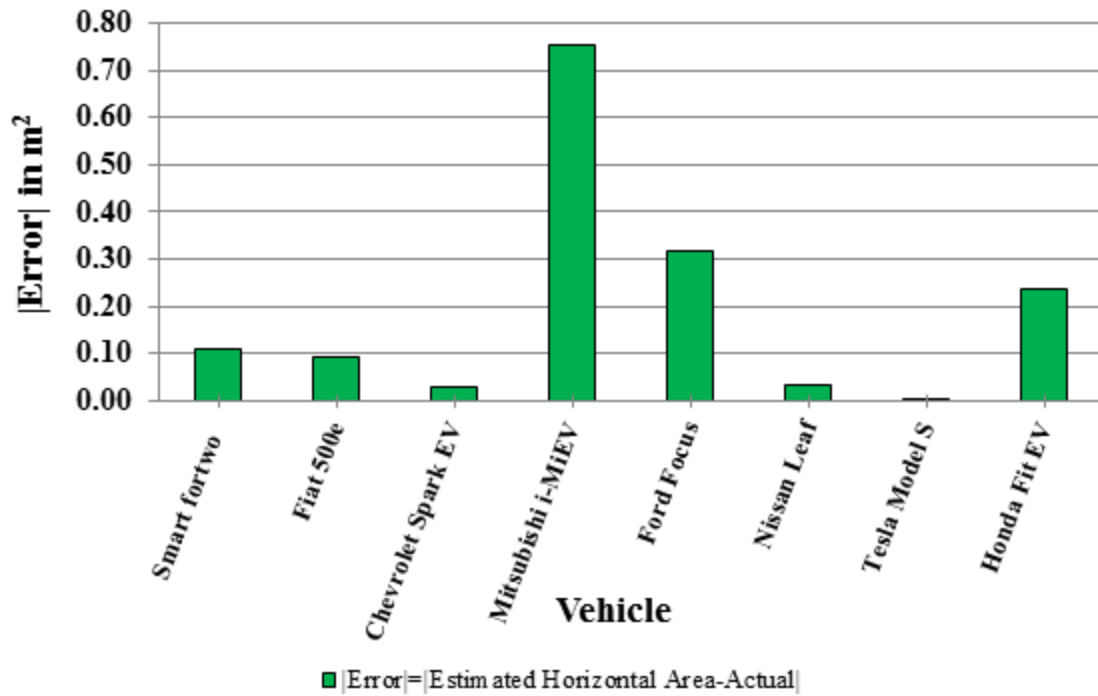


Figure 6. 19 Differences between projected horizontal surfaces (actual Vs. predicted) for selected EVs

The relation between vehicles projected horizontal surfaces and CAFE targets in 2020 and 2025 can be related using the proposed equation (6.28).

$$\left\{ \begin{array}{lll} \text{CAFE in 2020} & \text{CAFE in 2025} \\ \text{HS} \leq 7.1 \text{ m}^2 & 49 \text{ MPG} & 61 \text{ MPG} \\ 7.1 \text{ m}^2 < \text{HS} < 10 \text{ m}^2 & 36 \text{ MPG} - 49 \text{ MPG} & 46 \text{ MPG} - 61 \text{ MPG} \\ \text{HS} \geq 10 \text{ m}^2 & 36 \text{ MPG} & 46 \text{ MPG} \end{array} \right. \quad (6.28)$$

So, for the highest CAFE targets which is related to vehicle footprint less than 41 ft^2 (3.8 m^2) the horizontal projected surface is less than 7.1 m^2 . It is difficult to install all this area by PV for a typical vehicle since there is front windshield, rear windshield, etc. unless the vehicle design is optimized. For that, the assumption here is around 50% of the

projected horizontal surface area can be installed with PV. This is around 3.26 m² (two PV modules) as used in the previous chapter).

6.7 Driving Pattern Scenarios

The percent of person trips by time of day data is published in [267] and displayed in Figure 6.20.

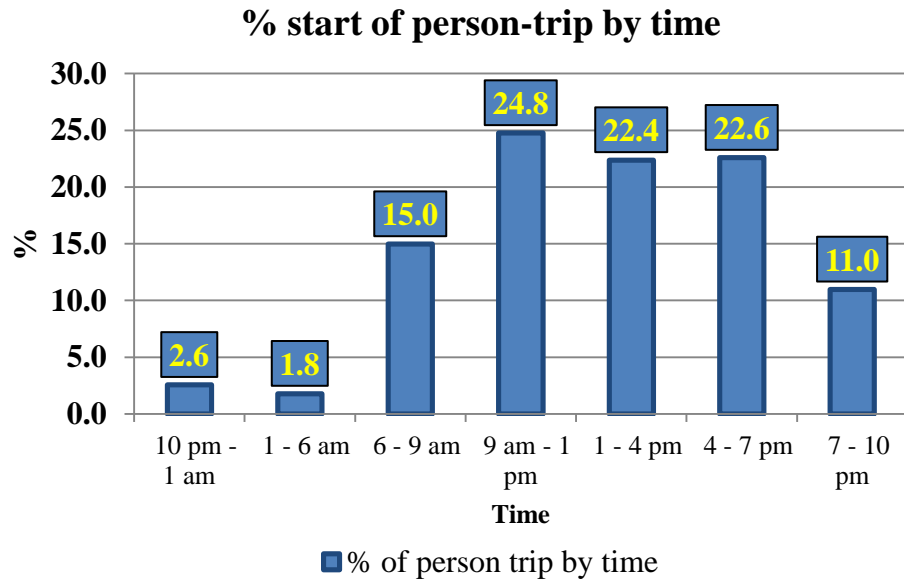


Figure 6. 20 The percent of trips by day [Data from [267]]

Therefore, around 85% of trips by day, started between 6 am to 7 pm, when typically the solar energy is available. Based on Figure 6.20, three driving time scenarios are assumed as from 9-10 am, 12-1 pm, and 4-5 pm since it showed the highest percent of trips in a typical day.

6.8 Summary

This chapter, first presents the vehicle model has been used to estimate energy and emission. Then it presents electric and solar vehicles use for benchmarked purposes. The vehicle energy at wheel modeling approach is discussed and the sensitivity analysis is presented. The energy required at the wheels (Tank-to-wheel analysis) and MPG calculations are discussed. Then, The CAFE standard curves in 2020 and 2025 are uniquely related to the projected horizontal vehicle surface area to estimate the maximum possible PV installation area for each CAFE target. Finally, the driving pattern scenarios are presented.

CHAPTER SEVEN

LIFE CYCLE ASSESSMENT MODEL (CRADLE-TO-GATE ANALYSIS)

7.1 Introduction

The PV cells/modules production by region in 1997 to 2013 in terms of total MW_p percentage produced is shown in Figure 7.1 [268].

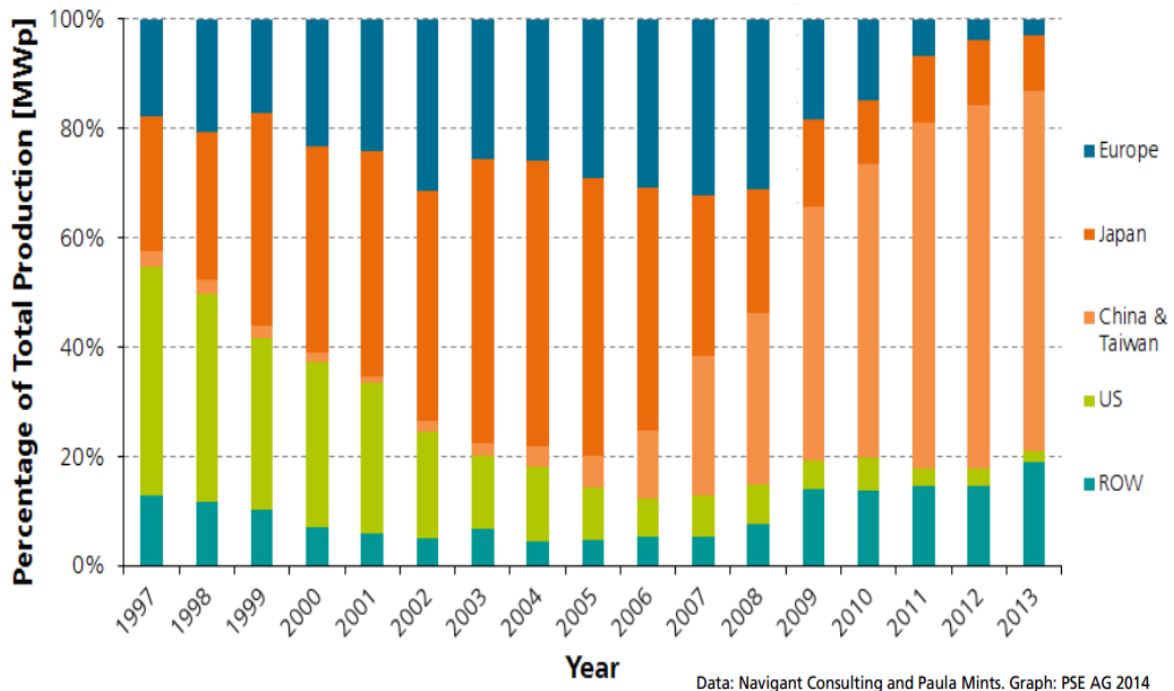


Figure 7. 1 Percentage of total PV cells/modules production per region [268]

The production of the current commercial PV market is dominated by Chinese products as shown in Figure 7.1. Figure 7.2 shows the global PV module production by

region in 2013 in MW [269]. The global PV module production in 2013 is around 40 GW and the Chinese PV modules represent around 64%, which equal around 26 MW. The second highest region manufactured PV is still in Asia, then Europe, then Japan. The U.S. as shown in Figure 7.2 manufactured around 943 MW (2.3% of the total) in 2013, which is the lowest region showed in Figure 7.2.

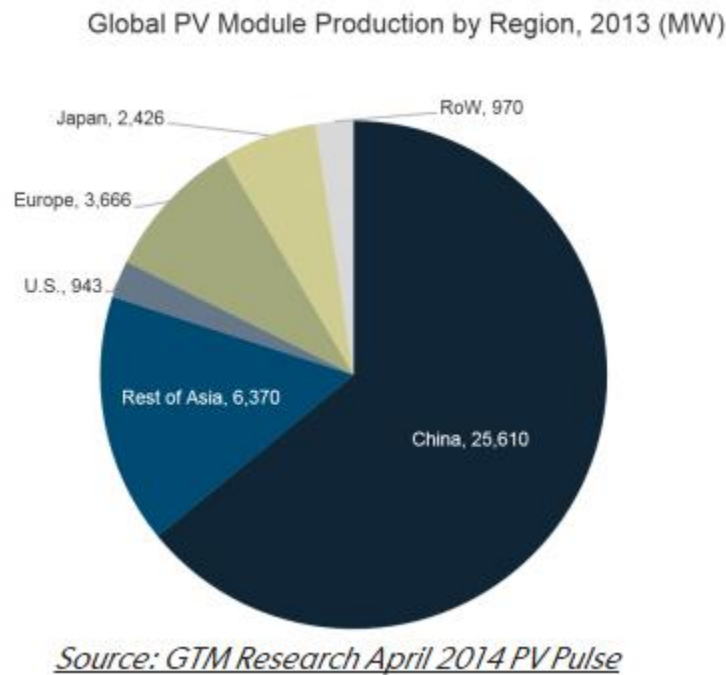


Figure 7. 2 Global PV Module Production by region (MW) in 2013 [269]

Figure 7.3 shows the percentages by the country to the total global PV installation [268]. The total cumulative PV installation at the end of the year 2013 were about 134 GWp but only 13% install in China and Taiwan and the most installed in Germany so far 27%. In the U.S. only 11% of PV have installed so far.

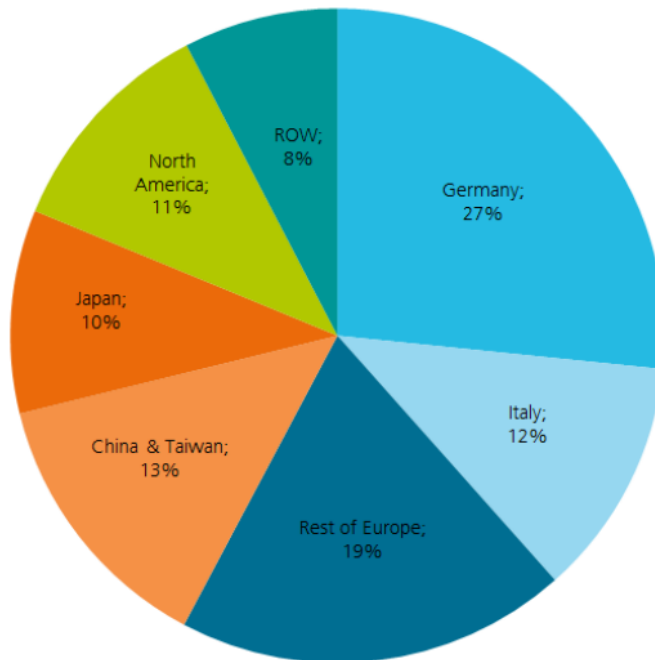


Figure 7. 3 Percentages by the country to the total global PV installation [268]

The reduced cost of PV modules is related to the cumulative installation which called the PV learning curve (see Figure 7.4 [270]). Figure 7.4 shows the PV module cost reduction per cumulative installation of PV module. From 1980 onwards, every doubling of the generation capacity of PV modules has been accompanied by a 20% reduction in the PV module-selling price [270], [271].

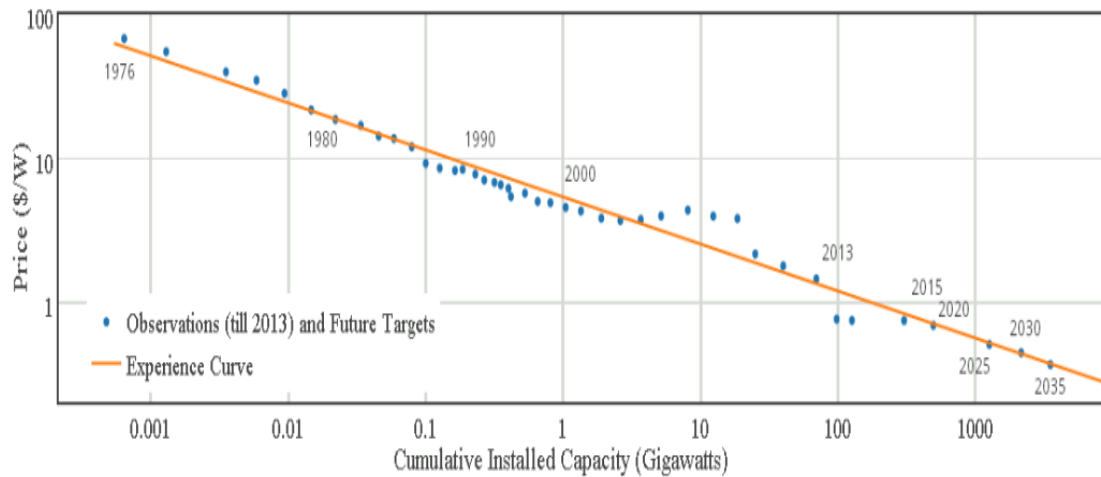


Figure 7. 4 Experience curve of doubling of PV module manufacturing and cost reduction by 20 % and extension to 2035 [270]

7.2 Defining LCA Study Methodology

The LCA or cradle-to-grave is a useful tool for quantifying the environmental performance of products taking into account the complete life cycle. The process starts from the extraction of raw material from the earth to create the product and ends when all material returned to the earth. LCA encompasses all environmental releases and the production of energy used to create the product through the raw material acquisition, manufacturing, use/reuse/maintenance, and recycle/waste management [272]. LCA study consists of four main phases (see Figure 7.5), which is covered through multiple ISO standards (International Organization for Standardization (ISO: 14040-14044) [273].

The first step is used to define the goal and scope of the study, while the second step is collecting and organizing the data to build a model, this step is called as life cycle inventory (LCI). The third step is to understand the relevance of all the inputs and

outputs, which is called a life cycle impact assessment (LCIA), fourth is the interpretation of the study, which is a systematic technique to identify, check, and evaluate information

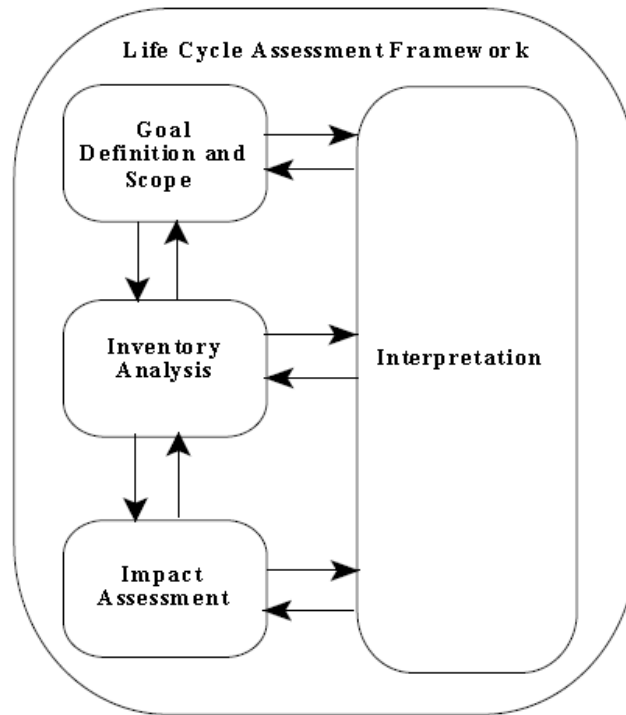


Figure 7. 5 Phases of an LCA (Source: ISO, 1997 [273])

The purpose of this study is to use the PV on-board for vehicle application. Beside PV, the system includes two other energy sources as gasoline fuel and grid electricity. The LCI in this study is based on extracting the data from the reliable literature and not for a specific manufacturer. The two important LCA indicators are included in this study, the greenhouse gases (GHG) emission rates and embodied energy.

The PV system consists of two parts as PV module and PV balance of system (BoS), the LCA of the two parts are discussed in the following sub-sections. To make the LCAs of PV system more consistent and to enhance the quality and reliability of the results, the

International Energy Agency (IEA) developed guidelines in (Alsema E., *et al.*, 2009 [274]) and revised in (Fthenakis, V., *et al.*, 2011 [275]) by providing consensus among assumptions. In Table 7.1, the main guidelines are summarized. The main parameters is the lifetime of PV assumed 30 years, with PV efficiency is reduced 0.7% per year.

Table 7. 1 IEA Guidelines for PV LCAs [274], [275]

Guidelines		Assumptions
Life Time	PV	30 years for mature module technologies (e.g., glass-glass or glass-Tedlar encapsulation), life expectancy may be lower for foil-only encapsulation; this life expectancy is based on typical PV module warranties.
	Inverter	Inverters: 15 years for small plants (residential PV); 30 years with 10% part replacement every 10 yrs (parts need to be specified) for large size plants utility PV
	Transformers and cabling	30 years
	Structure	30 years for rooftop and façades. Between 30- to 60-years for ground mount installations on metal supports.
Performance ratio (PR)		0.75 is recommended for rooftop and 0.80 for ground-mounted utility installations
Degradation		Linear degradation of the module efficiency reaching 80% of the initial efficiency at the end of a 30 year lifetime (i.e., 0.7% per year)
Functional unit		Functional unit "kWh electricity produced" or "m ² module" or "kWp rated power" depend on applications.
Greenhouse gas emissions (GHG)		GHG emissions during the life cycle stages of a PV system are estimated as an equivalent of CO ₂ using an integrated 100-year time horizon.
Cumulative Energy Demand (CED)		Represents the amount of primary energy use throughout the life cycle [MJ-eq.]

The boundary of the PV LCA study is summarized in Figure 7.6. The study includes the five main PV module types (mono-Si, multi-Si, a-Si, CdTe, and CIGS). The manufacturing PV stage is included in the study as well as BOS for vehicle

application. The transportation of the PV module from manufacturing place to installation place is not included in this study and in the next section will discuss the reasons. The installation stage (e.g., install PV on vehicle surface) is also excluded in this study. The reason is due to lack of information. Since, the proposed system is not commercially available. However, the impacts of the two stages are not significant in this study. In addition, the recycling stage is not included for two reasons, it has not covered well yet in the literature, especially for thin film PV, in addition the lifetime of a PV module is far greater than the life of the average automobile. The assumption is here reinstalling the PV module into another automobile or another application.

(e.g., PV efficiency), and LCA assumptions (e.g., system lifetime). For the same PV type, the LCAs results for rooftop and ground-mounted applications are different. The reason is the balance of system (BOS) is different in both applications. For a rooftop PV application, the BOS typically includes inverters, mounting structures, cable, and connectors. Ground-mounted PV requires additional equipment and facilities, such as grid connections, office facilities, and concrete. After screening more than 200 published LCA for PV application, the literature showed the following:

- Although the majority of PV modules produce in China, the life cycle inventory (LCI) for Chinese PV industry is not available [276], [277].
- Mainly the LCA studies related to PV done in Europe.
- Crystalline silicon PV mature and much process information is publicly available than thin films PVs.
- Most of LCA studies for crystalline PV are not based on real-world manufacturing data.
- Thin films LCAs are mainly based on empirical manufacturing data.
- The recycling stage for thin films has not been described in details yet.
- The BOS and tracker are not covered well in literature.
- Most of the LCA study is outdated

To the best of authors' knowledge, there is no LCA for On-board PV for vehicle application. The following criteria are proposed to collect and extract the LCA data from the literature:

Screened the published LCA environmental profile of Mono-Si, Multi-Si, a-Si, CdTe, and CIGS PV through 2014.

- The studies should be recent (only published after 2004).
- Complete assignments so that the equivalent CO₂ is reported.
- Reliable and original studies.
- Collected the studies that it is possible to separate the PV module contribution only from the PV system.
- Collected the studies that showed holistic manner, including initial materials extraction, manufacturing, use, and disposal/decommissioning.
- Studies reported functional units as a gram of CO₂ equivalent per kWh or MJ per m².

The most important issue, studies reported electricity source mix used for PV manufacturing.

- The electricity source mixes in specific country significantly affect the LCA result.

The differences because (i) every energy source could contribute differently in the total emission. The source of energy in many grid electricity countries will be presented in the following sections, (ii) every grid electricity has different primary energy to electricity conversion efficiency.

After screening about 200 LCA studies, the following Tables 7.2 to 7.6 summarized the LCA studies of different PV types passed the proposed criteria. In these Tables, the author reported the published g CO₂-eq per kWh for PV module manufacturing stage only. In addition, these tables include the most important LCA parameters and assumptions have taken through each study.

Table 7. 2 Summaries of published LCA estimated emission for multi-Si PV manufacturing

References	PV Type	Location	Life (Years)	Irradiance (kWh/m ² /year)	PR	Mounting	Eff.	Estimate (g CO ₂ -eq/kWh) PV module only	Note
[Beylot et al. (2014) [278]	Multi-Si	Europe	30	1700	0.855	30° tilt, fixed aluminum mount	14%	21.4	Ecoinvent v2.0/ French electricity mix for modules 5 MW/complete system .53.5 gCO ₂ /kWh (PV System)
Jungbluth et al. 2009 [279]	Multi-Si	Switzerland	30	1117	0.75	rooftop	13.2%	57	Electricity mix Switzerland Thickness 240 µm
Alsema et al., (2006) [280]	Multi-Si	Southern Europe	30	1700	0.75	roof mount	13.20%	32	285 µm crystal e European Commission's CrystalClear project from twelve European and US photovoltaic companies, 2004-2005
Fthenakis and Alsema (2006) [281]	Multi-Si	Europe	30	1700	0.75	roof mount	13.2%	37	crystal e European Commission's CrystalClear project from twelve European and US photovoltaic companies, 2004-2005
Alsema and de Wild-Scholten (2004) [282]	Multi-Si	Middle Europe Netherlands/Germany	30	1000	0.75	roof mount	13.2%	124	300 µm wafer
Pacca et al., 2007 [283]	Multi-Si Kyocera			1359	0.75	roof	12.92%	54.6	Based on European electricity. 72.4 (based on US grid). The difference is about 17.8 g CO ₂ /kWh.
D. Yue et al., 2014 [277]	Multi-Si	Southern Europe	30	1700	0.75		13.2%	31.8	

Table 7. 3 Summaries of published LCA estimated emission for mono-Si PV manufacturing

References	PV Type	Location	Life (Years)	Irradiance (kWh/m ² /Year)	PR	Mounting	Efficiency	Estimate (g CO ₂ -eq/kWh) for PV only	Note
Querini et al (2012) [284]	Mono-Si	-	30	1204	-	45 degree fixed mount	13.1%	92	Average electricity from various European countries
Jungbluth et al. 2009 [279]	Mono-Si	Switzerl and	30	1117	0.75	rooftop	14%	64	Electricity mix Switzerland Thickness 270 µm
Alsema et al., (2006) [280]	Mono-Si		30	1700	0.75	roof mount	14%	35	Thickness 300 µm
Fthenakis and Alsema (2006) [281]	Mono-Si	Europe	30	1700	-	roof mount	-	45	Average electricity from various European countries Thickness 270 µm 2004-2005 manufacturing data, from twelve European and US photovoltaic companies
D. Yue et al., 2014 [277]	Mono-Si	Southern Europe	30	1700	0.75		14%	37.3	

Table 7. 4 Summaries of published LCA estimated emission for a-Si PV manufacturing

References	PV Type	Data Year	Manufacture	Location	Life (Years)	Irradiance (kWh/m ² /Year)	PR	Mounting	Efficiency	Estimate (g CO ₂ -eq/kWh) PV modules only	
Wild-Scholten (2009) [285]	a-Si	2008	German producer	South Europe	30	1700	0.75	Roof mount	6.6	24	UCTE (European) electricity mix
Dominguez-Ramos et al., 2010 [286]	a-Si			Europe /Spain	30	1825	0.78	Ground	7	27	Europe Electricity mix
Sustainability Evaluation of Solar Energy Systems /SENSE (2008) [287]	a-Si	2003–2006	Free Energy Europe	Europe	20	1700	0.912	Ground	5.5%	31	UCTE mix Pilot/ A European Commission (EC) project, (SENSE)/ Commercial, 15 MWp/yr France electricity mix
Pacca, S., D. et al., 2006& 2007 [283], [288]	a-Si	2004	United Solar		20	1,359	0.95	Roof mount/ Building integrated case in Ann Arbor, MI	6.3%	34.3	Commercial, 28 MWp/yr

Table 7. 5 Summaries of published LCA estimated emission for CIGS PV manufacturing

References	Data Year	Actual Data	PV Type	Installation Location	Life (Years)	Irradiance (kWh/m ² /year)	Performance Ratio (PR)	Mounting	Efficiency	Estimate (g CO ₂ -eq/kWh)	
Dominguez-Ramos et al. (2010), [286]			CIGS	Spain	30	1825	0.78		10	33	German production/installed Spain
Wild-Scholten, 2009 [285]	2007		CIGS	South-European	30	1700	0.75	Roof-mount	10.5	21	UCTE (European) electricity mix German producer + ecoinvent 2.0 data for water & some metals
Raugei et al., 2007 [289]	2004	Würth Solar/Germany	CIGS	South-European	20	1700	0.75	-	11.0	70	Overestimated/ Based on pilot study. 95 gCO ₂ / kWh for PV System
Sustainability Evaluation of Solar Energy Systems (SENSE) (2008) [287]	2003–2006	Würth Solar/Germany	CIGS	South-European	20	1700	0.912	Ground-mount	11.5	37	UCTE mix /A European Commission (EC) project, Commercial, 15 MWp/yr 43 gCO ₂ / kWh for PV System/ Germany electricity mix

Table 7. 6 Summaries of published LCA estimated emission for CdTe PV manufacturing

References	PV Type	Location	Life (Years)	Irradiance (kWh/m ² /year)	Performance Ratio (PR)	Mounting	Efficiency	Estimate (g CO ₂ -eq/kwh)
Fthenakis. V. (2009) [290]	CdTe	Ohio, USA		1700	-	-	10.9%,	12.75
Alsema et al., (2006) [280]	CdTe	-	30	1700	0.80	Ground mount	9.00%	25
Fthenakis and kim (2006), [291]	CdTe	United states	30	1800	0.8	Ground mount	9.00%	24

The meta-model (see equation 7.1) for harmonizing the GHG_{PV} results is based upon similar assumptions as reported in (Hsu, D. D., 2012 [292]) and (Kim, H. C., 2012 [293]), which used to calculate GHG emission (W).

$$GHG_{rate} = \frac{W}{I \times \eta \times PR \times LT \times A'} \quad (7.1)$$

Where, the numerator (W) sums all of the GHG emissions from all components and life cycle phases and weighs each GHG by GWP, while the denominator calculates the power output over the lifetime of the PV system. Therefore, equation (7.1) is similar to equation (7.2) and (7.3).

$$W = GHG_{PV} + GHG_{BOS} \text{ (in unit g CO}_2\text{-eq)} \quad (7.2)$$

$$I \times \eta \times PR \times LT \times A' = E_{LCA-output} \quad (7.3)$$

Where,

I : is the irradiation (kWh/m²/yr);

η : is the lifetime average PV module efficiency;

LT : system lifetime (year);

PR : performance ratio; and

A : PV module area in (m²).

By using the above equations, the total emission (W) related to PV manufacturing stages are calculated for every study discussed previously in Tables 7.2 to 7.6. The results are summarized in Table 7.7. The GHG_{PV} is labeled as “estimated gCO₂-eq/kWh” and it

is based on published values in Tables 7.2 to 7.6. The “Calculated kg CO₂-eq” is same as “W ” and calculated based on the above discussion.

Table 7. 7 The calculated emission of PV manufacturing stage.

References	PV Type	Estimated gCO ₂ -eq/kWh [published in literature]	Calculated kgCO ₂ -eq [This study]
Beylot et al. (2014) [278]	Multi-Si	21.4	130.6
Jungbluth et al. 2009 [279]	Multi-Si	57	189.1
Alsema et al., (2006) [280]	Multi-Si	32	161.1
Fthenakis and Alsema (2006) [281]	Multi-Si	37	186.8
Alsema and de Wild-Scholten (2004) [282]	Multi-Si	124	368.3
Pacca et a., 2007 [283]	Multi-Si	54.6	215.7
D. Yue et al., 2014 [277]	Multi-Si	31.8	160.6
Querini et al (2012) [284]	Mono-Si	92	326.5
Jungbluth et al. 2009 [279]	Mono-Si	64	225.2
Alsema et al., (2006) [280]	Mono-Si	35	187.4
Fthenakis and Alsema (2006) [281]	Mono-Si	45	241.0
D. Yue et al., 2014 [277]	Mono-Si	37.3	199.7
Wild-Scholten (2009) [285]	a-Si	24	60.6
Dominguez-Ramos et al., (2010) [286]	a-Si	27	80.7
Sustainability Evaluation of Solar Energy Systems/SENSE (2008) [287]	a-Si	31	52.9
Pacca et al. (2006), (2007) [283], [288]	a-Si	34.3	55.8
Dominguez-Ramos et al. (2010) [286]	CIGS	33	140.9
Wild-Scholten, 2009 [285]	CIGS	21	84.3
Raugei et al., 2007 [289]	CIGS	70	196.4
Sustainability Evaluation of Solar Energy Systems (SENSE)/ (2008) [287]	CIGS	37	131.9
Fthenakis. V. (2009) [290]	CdTe	12.75	56.7
Alsema et al., (2006) [280]	CdTe	25	91.8
Fthenakis and kim (2006) [291]	CdTe	24	93.3

Figure 7.7 summarizes the results of GHG emission in PV manufacturing stage. The minimum, average, and maximum GHG for every PV type is displayed.

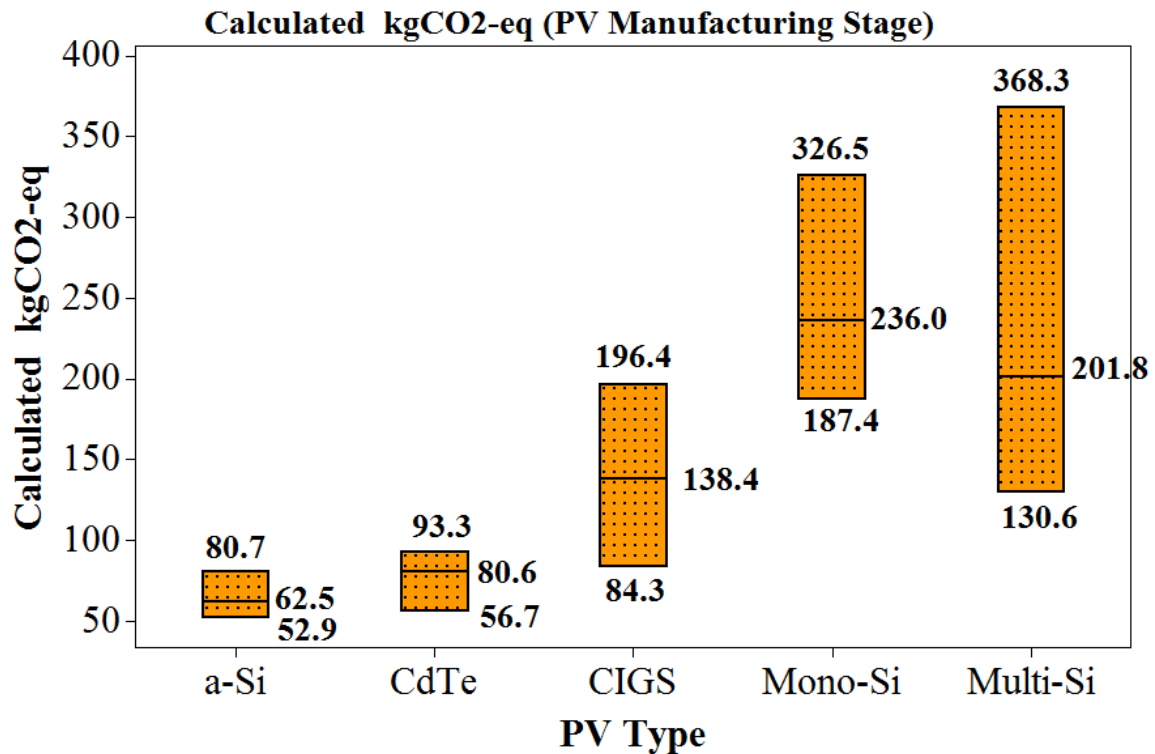


Figure 7. 7 GHG emission (kg CO₂-eq) in PV manufacturing stage.

Initially, the proposed selection criteria eliminated any LCA study has not used European electricity mix for PV production to reduce the data uncertainty. Table 7.8 shows the PV LCA studies passed the initial selection criteria, but excluded due to its use of the different electricity grid than Europe. Table 7.8 showed some results based on grids in the USA, China, Japan, Malaysia. However, the calculated emissions for all the studies in Table 7.8 are found located in the range, which is used in this study (Figure 7.7). So, for fair comparison the transportation stage of PV manufacturing to installation

is not included. However, the range of results (Figure 7.7) represents a global perspective of the PV manufacturing stage.

Table 7. 8 PV LCA studies are excluded in this study due to grid electricity not in Europe

References	PV Type	Life (Years)	Irradiance (kWh/m ² /year)	PR	Eff	Estimated gCO ₂ -eq/kWh	Calculated kgCO ₂ -eq [this study]	
Pacca et al., 2007 [283]	Multi-Si	30	1359	0.75	0.1292	72.4	286.0	USA grid
D. Yue et al., 2014 [277]	multi-Si	30	1700	0.75	0.132	69.2	349.4	China Grid
It, M., et al (2008) [294]	a-Si	30	2017	0.81	0.069	15.6	52.9	Japan Grid
It, M., et al (2008) [294]	CIGS	30	1702	0.787	0.11	44	194.5	Japan Grid
Kim, H. et al., (2014) [295].	CdTe	30	1810.4	0.8	0.112	15.1	73.5	Malaysia

7.4 Embodied Energy

The embodied energy is defined, as the total energy needs to produce the PV module from the life cycle point of view. For the scope of this work, the most recent LCA studies reported embodied energy are gathered until the PV module is manufactured in terms on MJ per m². Table 7.9 shows the embodied energy include in this study, for bulk-Si PV types, we include the most reliable and recent published results (after 2005) to be consistent with GHG results. However, there are fewer life-cycle studies of thin film PV technologies and we include the recent ones.

Table 7. 9 Embodied energy of PV manufacturing in terms of MJ/m²

Ref.	PV Type	Total (MJ/m ²)	Note
Battisti and Corrado (2005) [296]	Multi-Si	5150	Italian electricity Mix
Pacca, S. et al., (2006), (2008)[283] [288]	Multi-Si	4435	Based on European electricity. Kyocera type
Alsema and Wild-Scholten (2007) [297]	Multi-Si	3120	-
Wild-Scholten (2009) [285]	Multi-Si	2699	CrystalClear project Si feedstock = REC Siemens, multi wafers = REC. UCTE (European) electricity mix 13.2% eff (2007)
Jungbluth et al., (2009) [279]	Multi-Si	3065	Electricity mix Switzerland Thickness 240 μ m
Alsema and Wild-Scholten (2006) [280]	Mono-Si	5253	Efficiency 14% crystal e European Commission's CrystalClear project from twelve European and US photovoltaic companies,
Jungbluth and Stucki (2009) [279]	Mono-Si	3860	Electricity mix Switzerland Thickness 270 μ m
Wild-Scholten (2009) [285]	Mono-Si	2860	2008 (14%) UCTE (European) electricity mix/ CrystalClear project
Laleman (2011) [298]	Mono-Si	3513	-
Alsema and Nieuwlaar (2000), [299]	a-Si	1600	-
Pacca, S. et al., (2006), (2008)[283] [288]	a-Si	861	European) electricity mix
Wild-Scholten (2009) [285]	a-Si	989	2008 (6.6%) German producer UCTE (European) electricity mix
Knapp and Jester, 2001 [300]	CIGS	3150	Total MJ/m ² is converted as [55]
Wild-Scholten (2009) [285]	CIGS	1684	2009 (10.5%) UCTE (European) electricity mix German producer + ecoinvent 2.0 data for water & some metals
Wild-Scholten (2009) [285]	CIGS	1936	2007 (11%) UCTE (European) electricity mix German producer + ecoinvent 2.0 data for water & some metals
Fthenakis, V. et al., 2006, 2008 [281], [301]	CdTe	1200	actual 2005 production from First Solar's 25 MWp
Wild-Scholten (2009) [285]	CdTe	811	-
Kato K., et al., 2001 [302]	CdTe	1273	Annual production rate 100 MW

Figure 7.8 summarizes the gathered embodied energy of PV manufacturing stage in terms of MJ/m² in terms of minimum, average, and maximum values.

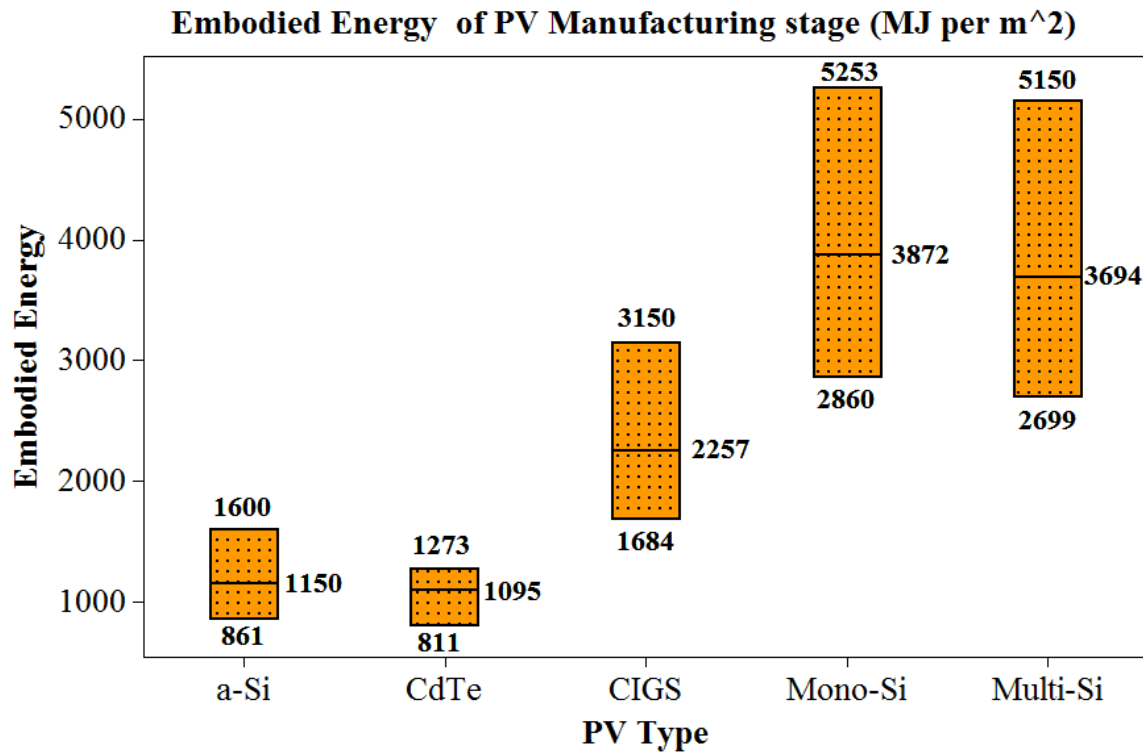


Figure 7. 8 Embodied energy of PV manufacturing in terms of MJ/m²

In [302], the reported embodied energy per m² is 1236 MJ for a-Si PV module, which manufactured in Japan with an annual production rate of 100 MW, this value is located in the range shown previously.

The challenges about LCA studies related to the PV industry are:

The majority of PV modules are manufactured in China, but the life cycle inventory (LCI) for Chinese PV industry is not available.

Even collected and analyzed the most reliable and recent LCA studies as done in this work, in Europe or US the age of the LCI are represented the current commercial PV module status is not guaranteed, since the duration between start collecting LCI to end of the work to be open in literature is time-consuming, beside, LCI data sometime is sensitive and not open for public. The improvements of PV module technology are rapid in terms of wafer thickness, cell efficiency, manufacturing process, etc. This causes the manufacturing of PV module to consume less energy and to emit less emission.

For example, the future PV wafer thickness for crystalline silicon solar cell shown previously in Figure 4.4 will be 120 μm by 2020, while all the reported LCA study in Tables 7.2 and 7.3 with thickness values 240-300 μm . In [280], the authors forecasted the manufacturing of future PV module with 19% efficiency and 150 μm thickness, will be with an emission rate equal 15.4 g $\text{CO}_2\text{-eq/kwh}$ with assumption life time 30 years, irradiation is 1700 $\text{kWh/m}^2\text{/year}$, and PR is 0.75. If the total emission (W) is calculated in this case, it will be 111.9 kg $\text{CO}_2\text{-eq}$ for future mono-Si PV module, which is around 50% lower than the current average LCA PV emission found in this study (See Figure 7.7).

The background data which typically is used for LCA model, could make data uncertainty in the results. Since, every LCA model software used different data.

7.5 LCA for PV Balance of System (BOS)

The balance of system (BOS) is all other components in the PV system besides PV module. The BOS depends on the type of application. In this study, the BOS includes mounting, batteries, and cables. The mounting is the structure to support the PV modules on the vehicle body. The cables are to interconnect PV modules to batteries. The battery is to store and deliver energy to the vehicle propulsion system. The proposed application is different from grid-connected application (roof-mounted) in the sense there is no inverter to convert DC-to-AC as well as different from standalone application (ground-mounted) in the sense there is no concrete to support the module and no office facilities.

7.5.1 Battery

In this work, the Li-ion batteries are used. There are various types of Li-ion batteries, using different compositions of cathode materials, such as LiMn_2O_4 (LMO), LiFePO_4 (LFP), $\text{Li}(\text{NiCoAl})\text{O}_2$, and $\text{Li}(\text{Ni}_x\text{Co}_y\text{Mn}_z)\text{O}_2$ (NCM), where x , y , and z denote different possible ratios. In Table 7.10, the most recent LCA studies of lithium-ion battery used in this study are summarized. The minimum, maximum, and average LCA emission battery results (Table 7.10) used in this study as 39.2, 250, 133 kg $\text{CO}_2\text{-eq/kWh}$, respectively. For other Li-ion battery types the estimated LCA emissions are 63.4, 121 kg $\text{CO}_2\text{-eq/kWh}$ for LiMnO_2 , Li-NCM respectively [304].

Table 7. 10 LCA Emission and Embodied Energy for Lithium-ion battery

LCA Study for Li-Ion Battery	(MJ/kWh) Cradle-to-gate energy	Kg CO ₂ - eq/kWh	Note
Ellingsen et al., (2014) [303]	586	172	Energy density is 0.174 kWh/kg (Manufactured in Norway)
USEPA (United States Environmental Protection Agency). (2013) [304]	-	151	-
Dunn et al. (2012b) [305]	576	39.2	Energy density is 0.13
Notter et al. (2010) [306]	-	54.4	-
Majeau-Bettez et al. (2011) [307]	371–473	200–250	Energy density is 0.110–0.140

7.5.2 Other BOS components

The LCA embodied energy and emission for silicon PV module are estimated based on [308]. The reported support structure frame mass is 30,906 kg/MW, the reported LCA energy and emission are 699 GJ/MW and 47 t CO₂-eq/MW, respectively [308]. By doing the conversion, the energy is 6.282 kWh/kg and the emission is estimated as 1.521 kg CO₂-eq/kg. The copper wire for installation is with LCA emission 3.4 kg CO₂/kg and energy is 12.678 kWh/kg based on GREET [309].

7.6 Estimation of PV Performance Ratio for On-board PV for Vehicle Application

Typically, the performance ratio (PR) of a PV system is the ratio between the annual electricity yields delivered to the application (typically AC electricity) to the theoretical annual production of PV model (DC electricity). The optimum PV system minimizes the losses, thus have high PR.

As shown previously in Tables 7.2 to 7.5, the estimated PR was varying from 0.75 to 0.95. Because of that and for a better comparison between the systems, the LCA guidelines (Table 7.1) recommends to use PR equal 0.75 for rooftop application and PR equal 0.80 for ground-mounted utility installations.

However, for this study, the PR does not depend on DC to AC efficiency as other applications, since the vehicle runs on direct current (DC) and there is no inverter. The proposed system depends on the efficiency from the PV module to the battery. The PR may be calculated by re-arranging equation (7.3) as the form in equation (7.4).

$$PR = \frac{E_{Output}}{I \times \eta \times LT \times A'} \quad (7.4)$$

The sophisticated proposed model, which was discussed in Chapter 5, estimated the actual energy stores in battery in both June and December for both Phoenix, AZ and Boston, MA places. To estimate PR, the annual actual yield is needed. For that, the study either should be done for all other months in a year, which is time consuming, or is to related the annual data with the data already available (June and December data). Here, the second approach is used with these steps:

The annual solar irradiation data (kWh/m^2) in Phoenix, AZ and Boston, MA cities are collected as shown in Table 7.11 [310]. Then, the average monthly irradiation is calculated by multiplying the average daily by the number of days in a month.

Figures 7.9 and 7.10 show the differences between the actual annual irradiation and estimated annual irradiation for both Phoenix, AZ and Boston, MA, respectively. The actual annual irradiation is the summation of average monthly irradiation (kWh/m^2) in Table 7.11. The estimated annual irradiation is based on the average between June and December, multiply by 12.

The results show that the differences are 3.9% and 3.7% in Phoenix, AZ and Boston, MA respectively. The differences between actual and estimated annual energy is added as “Bias” to the energy calculations for optimum PR estimation.

Table 7. 11 Average monthly irradiation in Phoenix, AZ and Boston, MA

Month	Jan	Feb	Mar	Apr	May	Jun	Jul	Aug	Sep	Oct	Nov	Dec
Number of days	31	28	31	30	31	30	31	31	30	31	30	31
Average daily (kWh/m ²), Phoenix, AZ [310]	3252	4302	5500	7206	8122	8281	7825	7176	6290	4982	3661	2927
Average monthly (kWh/m ²), Phoenix, AZ	100.812	120.456	170.5	216.18	251.782	248.43	242.575	222.456	188.7	154.442	109.83	90.737
Average daily (kWh/m ²), Boston, MA [310]	1852	2778	3792	4595	5571	6029	6031	5439	4259	3171	1898	1580
Average monthly (kWh/m ²), Boston, MA	57412	77784	117552	137850	172701	180870	186961	168609	127770	98301	56940	48980

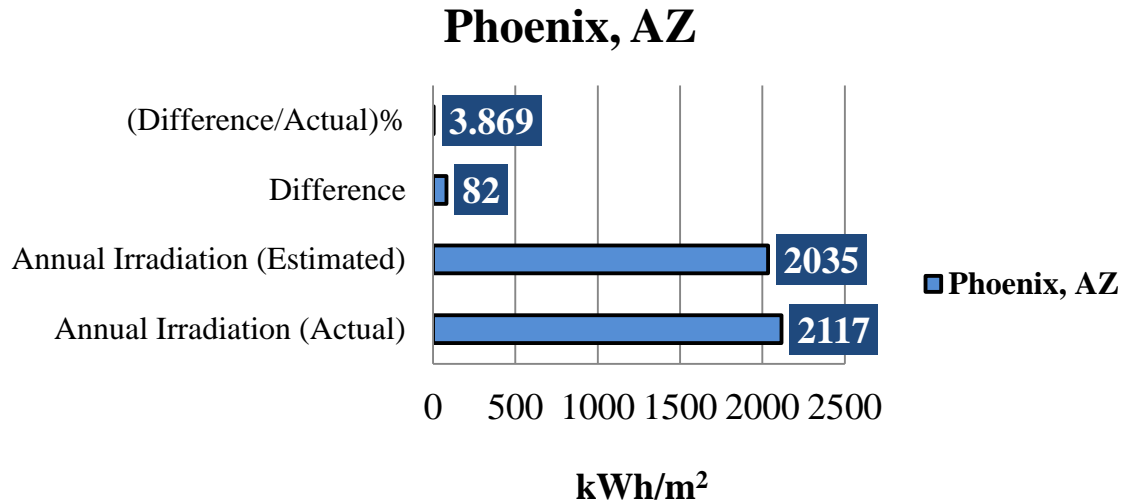


Figure 7. 9 Annual solar irradiation kWh/m² (Estimated and Actual) in Phoenix, AZ

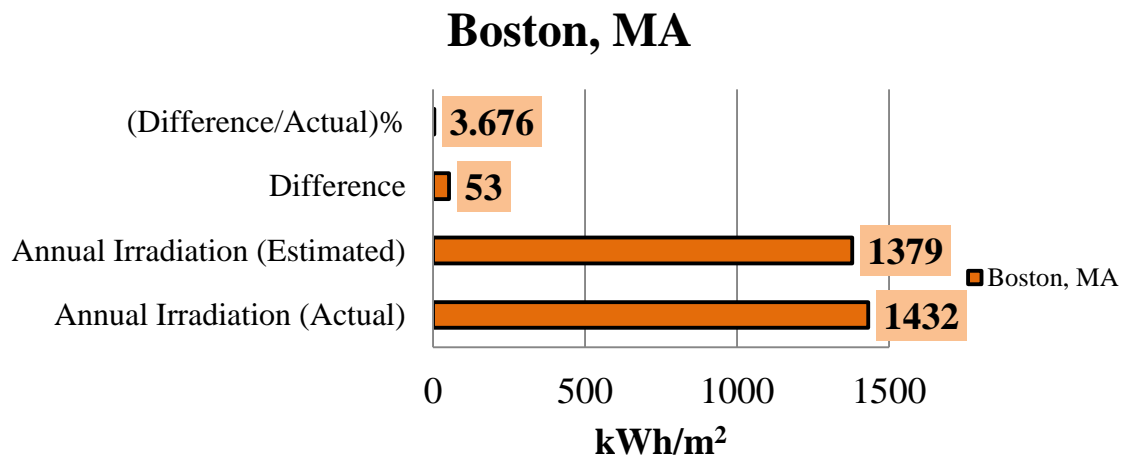


Figure 7. 10 Annual solar irradiation kWh/m² (Estimated and Actual) in Boston, MA

The calculations for estimations PR in Phoenix, AZ and in Boston, MA are summarized in Tables 7.12 and 7.13, respectively.

Table 7. 12 Estimated PR in Phoenix, AZ

	Total Irradiation (kWh/m ²)	PV Eff (%)	LT	A (m ²)	Energy (kWh)	Estimated PR
Phoenix, AZ (June)	248430	20.1	1	3.261	144,300	0.89
Phoenix, AZ (Dec)	90737	20.1	1	3.261	57,319	0.96
Phoenix, AZ (Estimated Annual)	2113736	20.1	1	3.261	125,653,0	0.91

Table 7. 13 Estimated PR in Boston, MA

	Total Irradiation (kWh/m ²)	PV Eff (%)	LT	A (m ²)	Energy (kWh)	Estimated PR
Phoenix, AZ (June)	248430	20.1	1	3.261	144,300	0.89
Phoenix, AZ (Dec)	90737	20.1	1	3.261	57,319	0.96
Phoenix, AZ (Estimated Annual)	2113736	20.1	1	3.261	125,653,0	0.91

Figure 7.11 shows the unique estimation of PR for using on-board PV for vehicle application compared to other applications. The estimated PR is 0.91 if the system is used in Phoenix, AZ and 0.97 in it is used in Boston, MA.

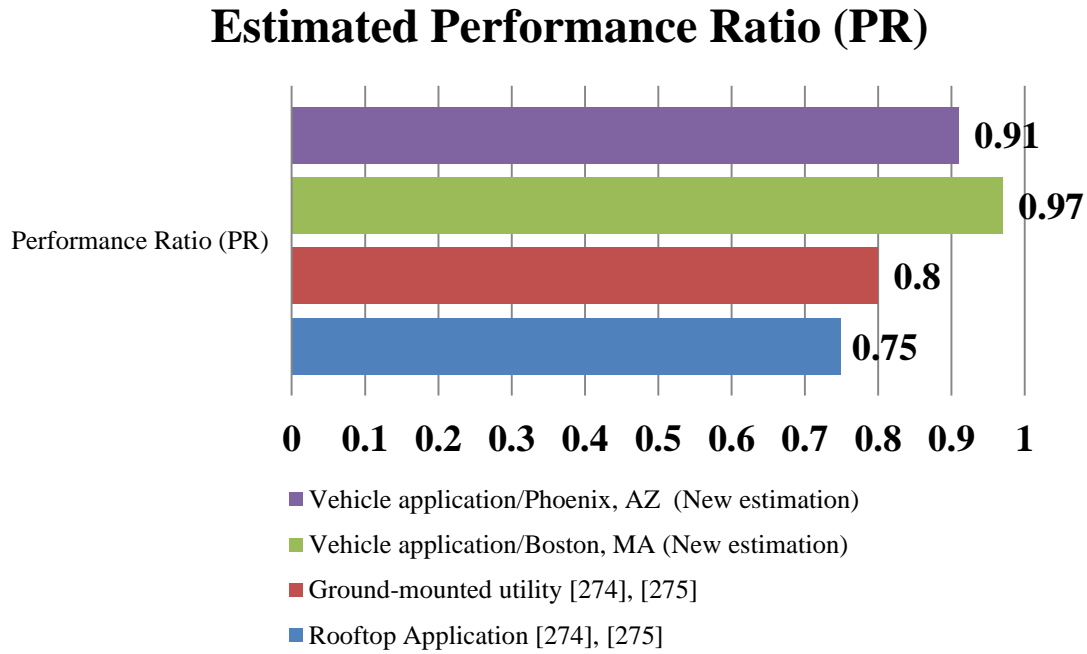


Figure 7. 11 Estimated PR for On-board PV system for Vehicle application

The estimated PR for the current application is found higher than ground-mounted and roof-mounted applications, since the current system using DC electricity and eliminated inverter losses. In addition, PR is found higher in the case of Boston, MA compared to Phoenix, AZ due to losses increase as ambient temperature increase. Therefore, PR has an inverse relationship with ambient temperature. For other cities, the PR is estimated equal 0.94 the average values of the two previous calculated values.

7.7 PV lifetime Energy in US and the World

The life span of PV modules is 30 years and the module efficiency is degraded linearly by 0.7% per year (Table 7.1). The assumed initial PV module efficiency is 20.1% (Figure 5.6). The average lifetime PV module efficiency is calculated as 18.09% as shown in Figure 7.12.

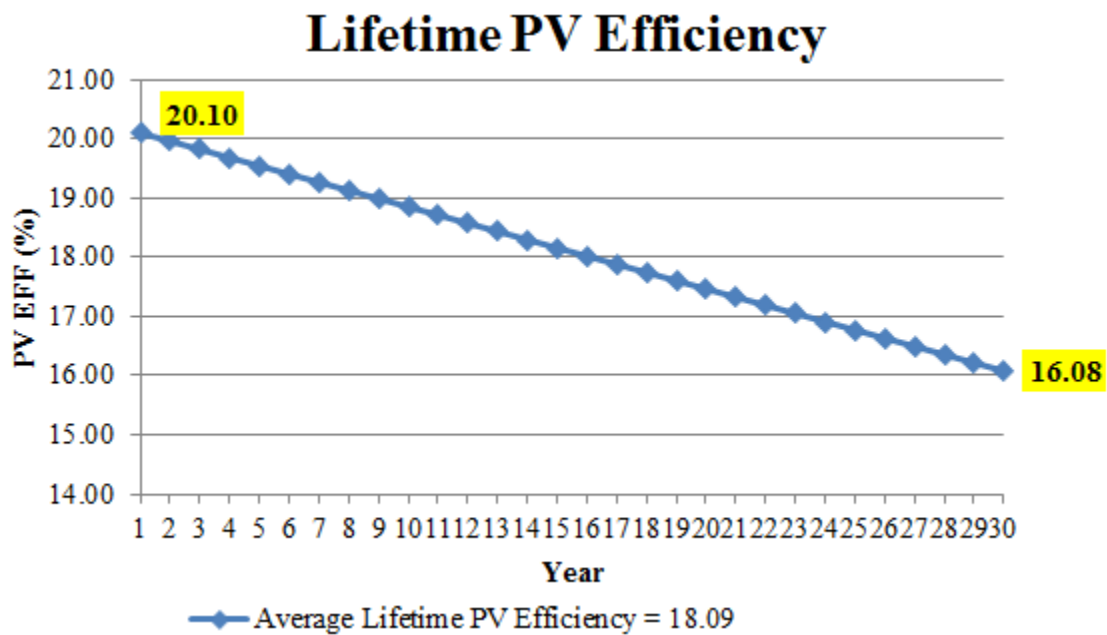


Figure 7. 12 Average lifetime PV efficiency (%)

In this section, the annual solar irradiations in different 12 U.S. states as well as 16 countries in the World are collected and analyzed. For all these locations, the generated PV lifetime energy by using a specific PV module with 3.261 m² area for vehicle application are calculated and displayed in Figures 7.13 and 7.14.

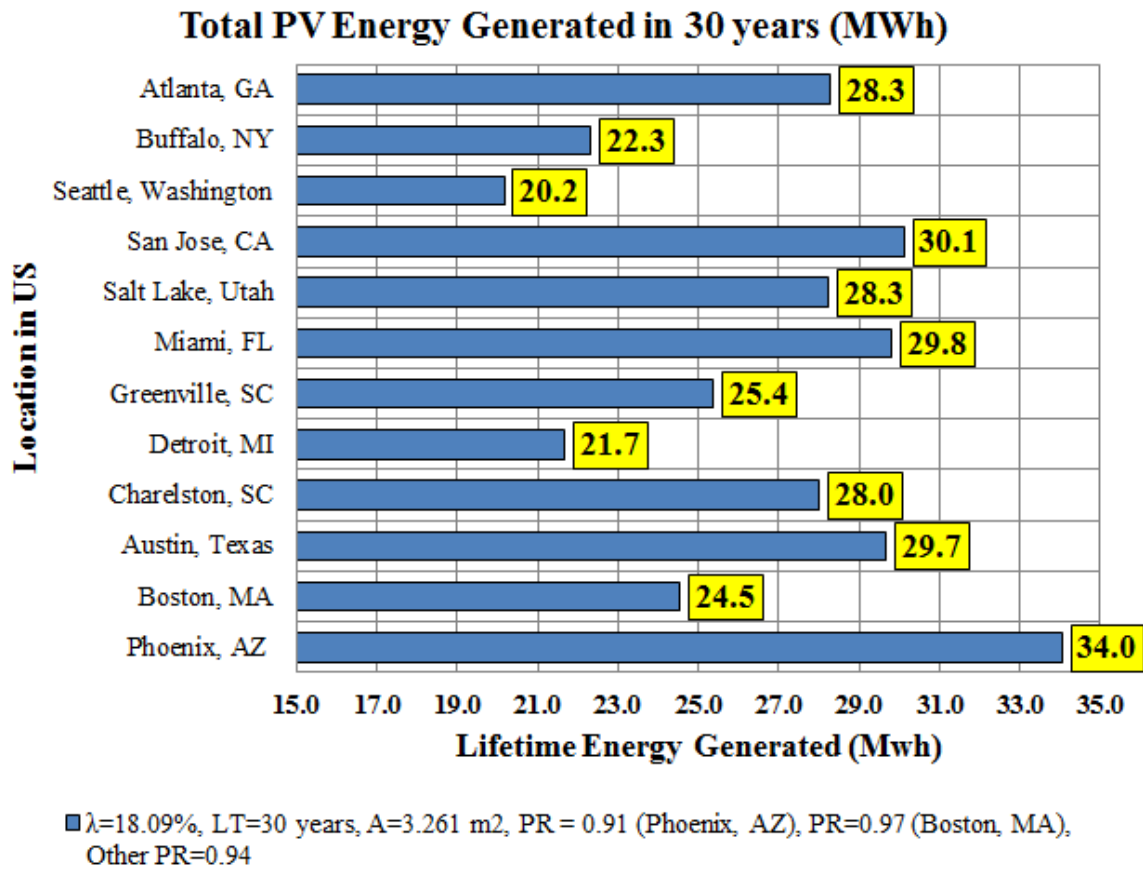


Figure 7. 13 Lifetime generated PV Energy in MWh in U.S. states

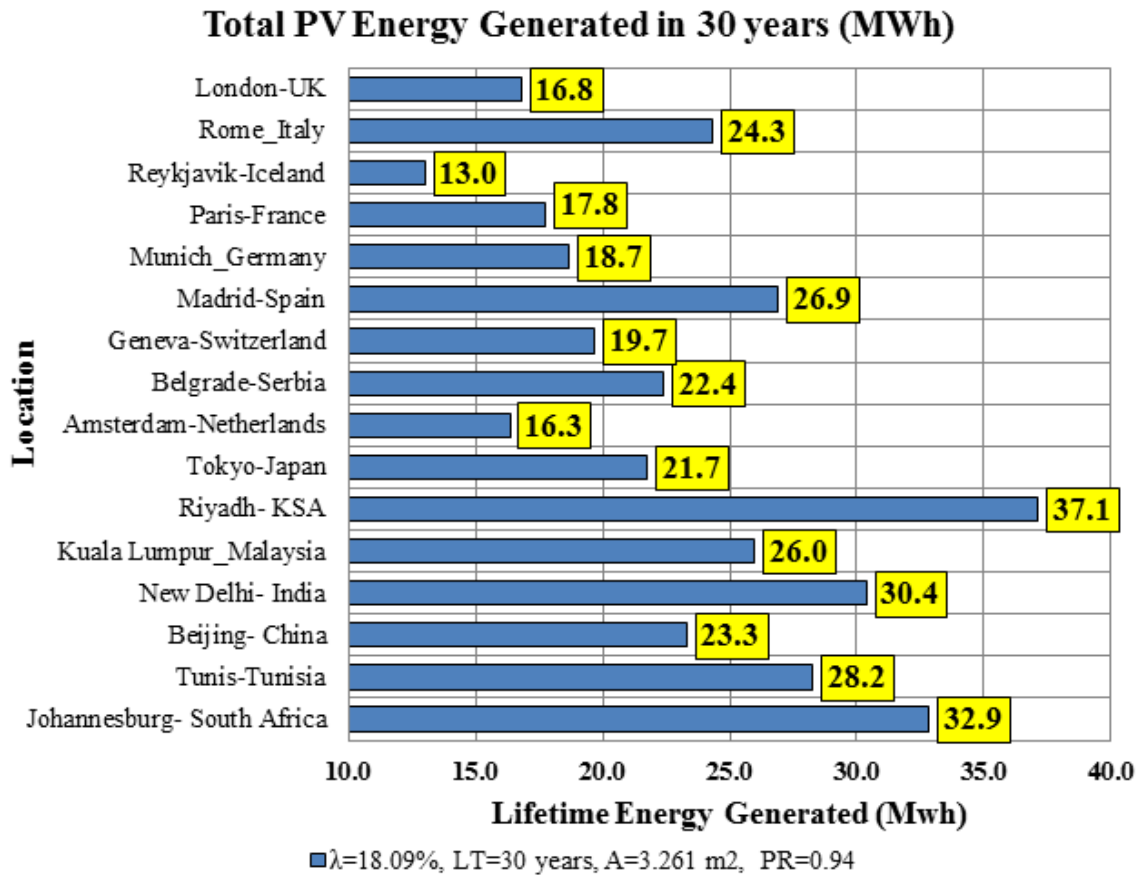


Figure 7. 14 Lifetime generated PV Energy in MWh in selected countries in the World

In the specific countries in the world (Figure 7.14), all the lifetime PV energy generated are lower than Phoenix, AZ (Figure 7.13) except in the case of Riyadh, KSA. In Riyadh, KSA, the calculated lifetime PV energy is the highest around 37.1 MWh and the related values in Johannesburg-South Africa and New Delhi-India are high and equal 32.9 MWh and 30.4 MWh, respectively. The lowest one found in case of Reykjavik-Iceland as 13 MWh since there is no much solar energy there.

The generated PV energy in Amsterdam-Netherland, Paris-France, and London-UK are lower than any of the U.S. states shown in Figure (e.g., lower than Seattle,

Washington). However, these countries invest in solar energy in terms of cumulative installation so far much higher than the U.S. (especially in Germany) as shown previously in Figure 7.3. The highest lifetime generated energy by PV in U.S. is found in Phoenix, AZ and San Jose, CA as 34 MWh and 30.1 MWh, respectively.

In 2012, the average annual electricity consumption for a U.S. household was 10,837 kWh, an average of 903 kWh per month. Louisiana had the highest annual consumption at 15,046 kWh and Maine the lowest at 6,367 kWh [311]. While the average annual household electricity use in India is much less around 900 kWh [312]. This means the lifetime generated energy by the proposed PV module in Phoenix, AZ is the equivalent of what an American household residential utility customer consumed in more than 3 years. If the proposed system is based on New-Delhi, India, the lifetime generated energy by the proposed PV module is equivalent of what Indian household residential utility customer consumed in more than 33 years.

7.8 LCA for Gasoline Fuel

The LCA data for gasoline fuel is based on GREET model data [309]. The gasoline include in this study is the U.S. conventional gasoline with additives (E10) with snapshot as the Figure 7.15 [309].

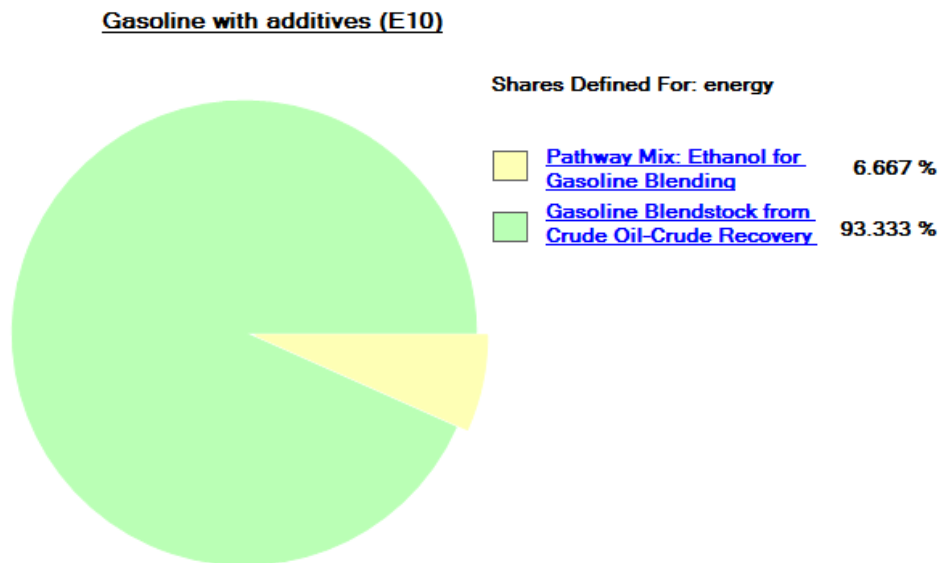


Figure 7. 15 Gasoline with additives (E10) [Source: GREET [309]]

The GHG emission by burning one gallon of gasoline (E10) results 2.582 kg from the life cycle point of view [309] as well as 8.887 kg in operation [313].

7.9 LCA for Electricity from Grid in US and the World

The grid electricity emissions in a specific country depends on the electricity production energy sources have used. In able 7.14 to Table 7.17, the source of electricity energy production is selected countries in Africa, America, Asia, and Europe, respectively are summarized [314], [315].

Table 7. 14 Electricity production energy sources in some countries in Africa [314], [315].

Africa		
South Africa	93% (Hard coal), Nuclear (5%), Hydro power (2%)	IEA 2010 for the year 2008,
Tanzania	Natural gas (36 %), hard coal (3 %), petroleum products (1 %) hydropower (61 %).	IEA 2010 for the year 2008,
Tunisia (TN)	Natural gas (87 %) and petroleum products (11 %), (2%) others	IEA 2010 for the year 2008,

Table 7. 15 Electricity production energy sources in some countries in America [314], [315].

America		
Brazil	Hydro power (73 %), biomass (4 %) and nuclear power (3 %)	IEA 2010 for the year 2008,
Mexico	Natural gas (50 %), petroleum products (19 %) and hard coal (8 %)hydropower (16 %) and nuclear power (4 %).	IEA (2011)
USA	Hard coal (46 %), natural gas (20 %) and lignite (2 %), nuclear power (19 %) and hydro power (7 %)	IEA (2011)

Table 7. 16 Electricity production energy sources in some countries in Asia [314], [315].

Asia		
India	hard coal (65 %), natural gas (10 %) and petroleum products (4 %) hydropower (14 %) and from nuclear power (2 %).	
Indonesia	lignite (41 %), petroleum products (29 %) and natural gas (17 %)hydropower (8 %) and from renewables, mainly geothermal (6 %).	
Japan	hard coal (24 %), natural gas (26 %) and petroleum products (12 %) nuclear power (24 %) and hydro power (8 %).	IEA 2011
People's Republic of China	hard coal (77 %), hydropower (19 %), nuclear power (2 %)	
Saudi Arabia	petroleum products (57 %) and natural gas (43 %)	
Malaysia	natural gas (64 %) and hard coal (27 %), hydro-power (8 %)	
South Korea	hard coal (40 %) and natural gas (18 %), nuclear power (34 %) and hydro power (1 %).	IEA 2011
Chinese Taipei	hard coal (47 %), natural gas (19 %), petroleum products (6 %) and lignite (4 %), nuclear power (17 %) and hydro power (3 %).	

Table 7. 17 Electricity production energy sources in some countries in Europe [314], [315].

Europe		
France	nuclear power source (75 %), hydro power (12 %), hard coal (4 %) and natural gas (4 %)	IEA 2011
Germany	lignite (22 %), hard coal (18 %) and natural gas (13 %), nuclear power (22 %), wind (6 %).	IEA 2011
Iceland	hydro power as main energy source (76 %).geothermal (24 %).	IEA 2011
Italy	natural gas (46 %) hard coal (12 %) and petroleum products (8 %)	IEA 2011
Netherlands	Natural gas (47 %) and hard coal (17 %),other (renewable energy and nuclear)	IEA 2011
Serbia	lignite (55 %), hydro power (23 %), 21% imported	IEA 2010
Spain	natural gas (37 %), hard coal (15 %) and petroleum products (6 %), other (nuclear and wind)	IEA 2011
United Kingdom	Hard coal (31 %) and natural gas (44 %), nuclear (13 %), wind (2 %).	IEA 2011

The emission also depends on the losses during electricity transmission and distribution in a specific grid. This depends on the infrastructure, voltage level, population density, etc. Table 7.18 shows some losses for low voltage level. The losses are varying from around 5% in cases of Netherland to around 34% in the case of Tanzania. The US electricity losses around 8%, while in India around 22%. These losses cost waste energy and increase both emission and cost.

Table 7. 18 Electricity losses on low voltage level for some countries [316]

Country	Cumulated losses LV (%)
Brazil	24.4
France	9.1
Germany	7.1
India	21.7
Indonesia	15.0
Italy	8.2
Japan	6.7
Netherland	5.3
Saudi Arabia	12.4
South Africa	13.6
Spain	7.1
Switzerland	9.7
Tanzania	33.6
United kingdom	10.3
US	8.1

LCA for electricity grid in three different voltage levels (high, medium, and low) is modelled in [316]. High voltage level above 24 kV (e.g., large-scale industry), medium voltage level between 1 kV and 24 kV (e.g., medium to small-scale industry, service sector and public buildings), and low voltage level below 1 kV (e.g., households). This study focus on low voltage level results since it is used to charge plug-in electric vehicle. The cumulative energy demand (CED) in terms of equivalent MJ-oil per kWh in Table 7.19 for low voltage at grid. The results show that at minimum 4.21 MJ-oil energy to most 15.7 MJ-oil energy need to produce 1 kWh electricity at grid low level in case of Iceland and Serbia and Montenegro, respectively.

Table 7. 19 CED at low level voltage at Grid [316]

low voltage, at grid		
	Country	CED Total (MJ-oil- eq/kWh)
Africa	South Africa	13.91
	Tanzania	9.06
	Tunisia	13.35
Americas	Brazil	6.44
	Mexico	13.66
	USA	13.57
Asia	China	11.71
	Chinese Taipei	12.90
	India	6.79
	Indonesia	13.50
	Japan	12.49
	Malaysia	11.32
	Saudia Arabia	13.35
	South Korea	12.93
Europe	France	13.05
	Germany	11.51
	Iceland	4.21
	Italy	10.64
	Netherlands	10.99
	Serbia and Montenegro	15.70
	Spain	10.63
	Switzerland	10.89
	UK	11.90

Table 7.20 shows the greenhouse gas emissions (GHG) at low voltage, grid in terms of grams of equivalent CO₂ per kWh. The CO₂ equivalent emission in grams release by consumed 1 kWh at the low level grid is varying from very low in case of Iceland around 4.21 to very high 1230 and 1272 in case of China and India, respectively.

However, there is uncertainty for the electricity emission at the grid. For example, from the table above (Table 7.20) in the U.S., the grid emission at low level is 808.4 g CO₂-eq per kWh [316], while in GREET model the estimated emission in U.S. average electricity is 614 g CO₂-eq per kWh [309]. In this study, the US Grid electricity life cycle emission is based on GREET for better comparison since the gasoline fuel is based also in GREET. For all other countries, the Grid emission is based on Table above (Table 7.20).

**Table 7. 20 GHG at low level voltage at Grid, calculated IPCC global warming potential 2007 100 ,
GWP) [316]**

low voltage, at grid		
	Country	GWP (g CO ₂ -eq/kWh)
Africa	South Africa	1126.8
	Tanzania	404.5
	Tunisia	805.1
Americas	Brazil	199.7
	Mexico	793.9
	USA	808.4 [49], 614 [GREET [42]
Asia	China	1229.6
	Chinese Taipei	997.4
	India	1272.2
	Indonesia	1025.4
	Japan	675.9
	Malaysia	758.7
	Saudia Arabia	897.4
	South Korea	708.9
Europe	France	109.0
	Germany	671.5
	Iceland	27.5
	Italy	621.2
	Netherlands	684.2
	Serbia and Montenegro	1143.0
	Spain	496.3
	Switzerland	135.0
	UK	684.7

7.10 Reduction of Life Cycle Grid Emission by using PV

The PV LCA GHG is estimated by using Equation (7.1). By dividing the calculated life cycle CO₂-eq emission (see Table 7.21) over lifetime energy generated (see section 7.7).

Table 7.21 shows the proposed LCA estimation for using the on-board PV system for vehicle application. The values of “Emission” column in Table 7.21 are based on the average values of mono-Si PV manufacturing, mounting, Li-ion battery, etc. as discussed previously. The contribution of the battery in total LCA system emission is around 1.7 times than PV module.

Table 7. 21 The proposed LCA emission estimation of on-board PV system for vehicle application

Component	Emission	Quantity	LCA Emission (kg CO ₂ -eq)	Note
PV Module [mono-Si]	236 kg CO ₂ -eq per m ²	3.261 m ²	770	No need for replacement
Mounting	1.521 kg CO ₂ -eq per kg	4 kg	6.084	No need for replacement
Battery	133 kg CO ₂ -eq per kWh	5 kWh	1,330	One time replacement
Other	-		-	Minor contributions: cables, etc.
Total System			2,106	

In Figure 7.16, the proposed estimation of the total LCA emission by consuming energy equal 1 kWh from PV versus the total LCA emission by consuming the same amount of energy from conventional grid is estimated and compared. The results mostly

showed huge reduction, from the LCA point of view, by using PV over conventional grid for most of the countries.

As an example, the LCA emission by consuming 1 kWh from the conventional grid at low voltage (e.g., household) in India is 1272.2 g CO₂-eq and for grid in China is equal 1229.6 g CO₂-eq.

If the same energy (e.g., 1 kWh) is generated using PV the LCA g CO₂-eq are reduced to 69.3 and 90.4 in New Delhi-India and Beijing-China, respectively. This means by using PV over conventional Grid, the life cycle emission could be reduced 18 times and 14 times in India and China, respectively.

On the other hand, In Reykjavik-Iceland and Paris-France, the results are opposite. For example, if the customer consumed 1 kWh using conventional grid in Iceland, from LCA it emits only 27.5 g CO₂-eq, however is the 1 kWh is generated from PV in Reykjavik-Iceland, the emission will be higher around 162.1 g CO₂-eq. The reasons these countries already using renewable energy to generate electricity at Grid, in addition, there is no enough solar energy there.

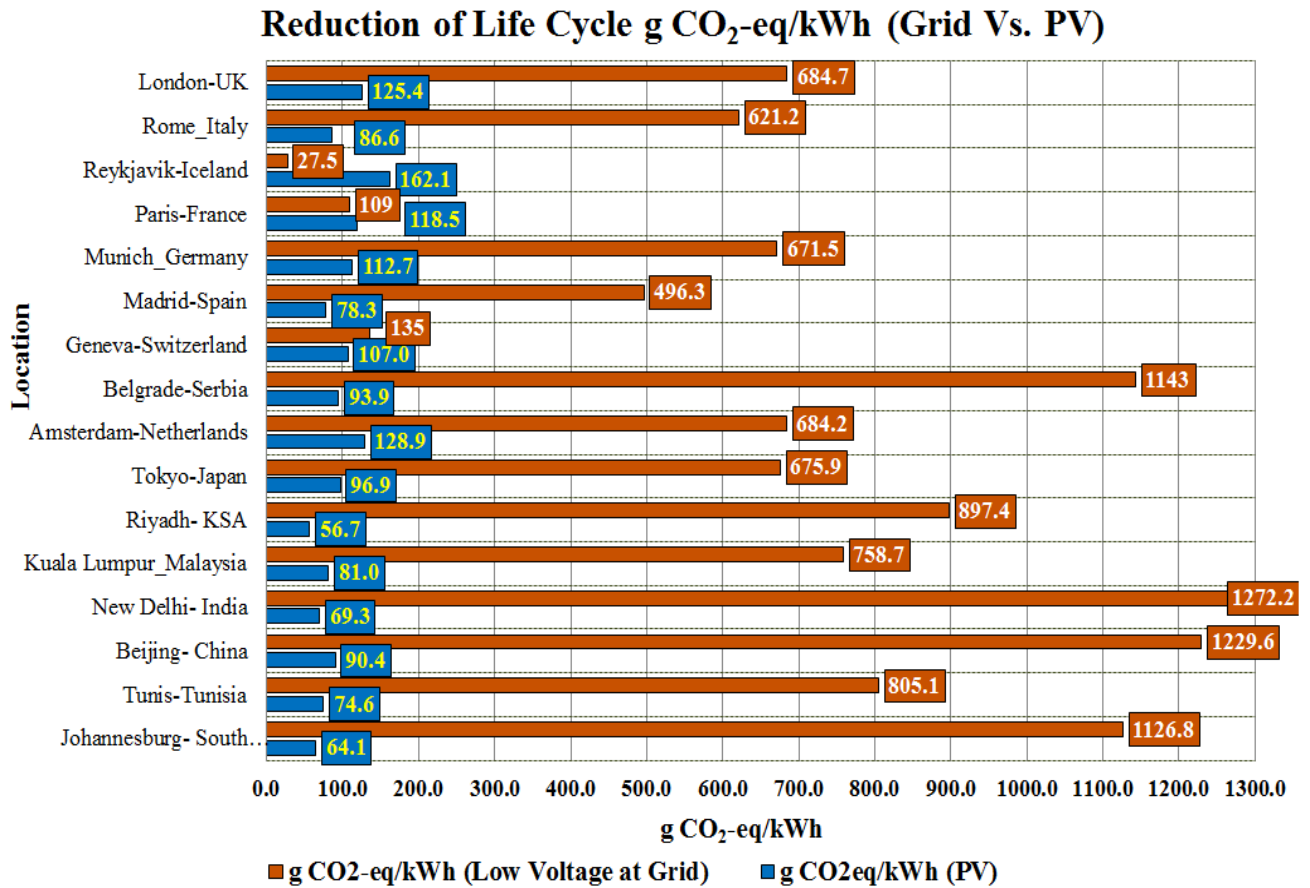


Figure 7. 16 Reduction of Life Cycle g CO₂-eq emission per kWh by using PV vs. Grid

7.11 Limitations and Data Uncertainty

In this work, the sources of uncertainties in the LCA data are found due:

- i) PV outputs are based upon historical solar irradiation, ambient temperature, and wind speed data.
- ii) The open LCI is very limited. For example, the most reliable and open PV LCI could be found in [280], [317], [318]. The study was conducted within the integrated project CrystalClear and funded by European Commission with ten largest PV companies [319], [320], [321]. This study represented the crystalline-silicon module production technology in Western Europe in the year 2005/2006 and Balance-of-System components of the year 2006. The challenges are in the purpose to protect the sensitivity of the data, this study hidden some values, aggregated results, or averaged many results. For example, mono-crystalline silicon wafer is based on average from three companies in North America, Europe, and Asia. Another example, the mono-crystalline cell data is an average of five specific companies.
- iii) Other challenges related to PV and Grid in the U.S summarized in the previous section
- iv) The majority of LCA studies comes from Europe, there is few come from US, but there is very limited for other countries. Especially, in China or India, there is limited information about the LCA emission for gasoline.

- v) The LCA published studies for batteries also have high uncertain as reported by EPA [322].

This study eliminated the uncertainty by proposing conservative selection criteria for the published LCA studies. By collecting the most recent and reliable LCA studies (the selection criteria are discussed in details in section 6.3). In addition, the minimum, maximum, and average emission values are reported. Since, only few studies are passed the proposed selection criteria. The LCA model is based on few sample data less than 10 samples for each PV type. Since, the mono-Si PV type is the one used for analysis here, and due to limited sample size and wide range the average values are used for analysis.

The recommendation here is to deal with uncertainty as below: If many reliable LCA data related to PV, battery, etc. are becoming available; the analyst may fit the related data under different distributions and select the best-fit function. Then the analyst can find the probability for each sample. Then, they can combine the LCA data from different stages by finding the distribution of the two, three, four, etc. (depends on the stages include in the study) random variables. In addition, for specific scenario the installation and transportation can be included.

7.12 Summary

This chapter first presents a historical PV production and cumulative installation data. The LCA methodology used in this study is defined. Then the proposed LCA selection criteria for evaluating and selecting the most reliable and recent LCA studies in literature are analyzed. Then after screening more than 200 LCA studies, the LCA data related to five main PV types and balance of system are presented. Next, a unique estimation of PV performance ratio for the current application is proposed. Then, lifetime PV generated energy is calculated and analyzed in 12 U.S. states as well as 16 different countries in the World. After that, the LCA data for gasoline fuel and Grid electricity is presented. In addition, this chapter presented the unique estimation of the reduction in LCA emission by having the source of energy from PV versus the conventional grid in many countries in the World. Lastly, the challenges in LCA studies, the limitation, and the recommendation uncertainty analysis are discussed.

CHAPTER EIGHT

ASSESSMENT METHODOLOGY RESULTS

8.1 Introduction

In this section, all the previous steps are integrated to present the novel comprehensive assessment methodology results. The results in this section will be presented based on the assumptions in Table 8.1.

Table 8. 1 The key assumptions used for assessment results

Description	Assumption
The usage of PV for vehicle	On-board
PV Types/Specifications	Mono-Si (Figure 5.3)
Area of PV installation	3.261 m ²
Shadow and sky clearness factor	Factor =1 (Optimum case)
Mounting option	Open rack: glass/cell/polymer sheet
MPPT implemented	Yes
Tilt option	No
Tracking option	No
Future scenarios	PV efficiency at STC= 25%-30%
Energy Storage	Li-ion Battery
Scenarios	Maximum related to June in Phoenix, AZ. Minimum related to December in Boston, MA
Driving pattern scenario	9-10 am, 12-1 pm, 4-5 pm
EV range	77 miles
Vehicle lifetime	160,000 miles
Regeneration option	No (energy at wheel is calculated for the worst case scenario)
Driving cycles	UDDS/ HWFET
Tank-to-Wheel Efficiency	15%, 20%, 90% are for gasoline vehicle (city cycle), gasoline vehicle (highway cycle), electric vehicle, respectively.
LCA guideline	ISO/IEA

8.2 Contribution of On-board PV toward CAFE 2025

The contribution of using on-board PV in increasing the fuel economy is calculated by using the proposed following Equation (8.1) and (8.2).

$$\text{MPG}_{\text{City}} = \eta_{\text{T2W}_{\text{city}}} \times \frac{E_{\text{gasoline}}}{(E_{\text{city cycle}} - E_{\text{PV at wheel-city cycle}})} \times I_{\text{city cycle}} \quad (8.1)$$

$$\text{MPG}_{\text{Hwy}} = \eta_{\text{T2W}_{\text{Hwy}}} \times \frac{E_{\text{gasoline}}}{(E_{\text{Hwy cycle}} - E_{\text{PV at wheel-Hwy cycle}})} \times I_{\text{Hwy cycle}} \quad (8.2)$$

$$\text{MPG}_{\text{Combined}} = \frac{1}{\frac{0.55}{\text{MPG}_{\text{City}}} + \frac{0.45}{\text{MPG}_{\text{Hwy}}}} \quad (8.3)$$

Where,

$E_{\text{PV at wheel-city cycle}}$, is the PV energy provided at the wheel in the duration of the city driving cycle.

$E_{\text{PV at wheel-Hwy cycle}}$, is the PV energy provided at the wheel in the duration of the highway driving cycle.

$\eta_{\text{T2W}_{\text{city}}}$ and $\eta_{\text{T2W}_{\text{Hwy}}}$, are tank to wheel efficiencies of the conventional vehicle (before the PV is added) in city and highway cycles, respectively.

The PV energy reaches the wheels in a given driving cycle is calculated using the proposed Equation (8.4).

$$E_{\text{PV at wheel}} = T_{\text{Cycle}} \times \eta_{\text{PV2W}} \times E_{\text{PV-hourly}} \quad (8.4)$$

Where,

$E_{PV-hourly}$ is the hourly energy estimated previously in chapter 5 for different locations and different driving patterns.

T_{cycle} , is the cycle duration (in hour), (e.g., $T_{cycle}=0.38$ in city cycle and $T_{cycle}=0.2125$ in highway cycle).

η_{PV2W} , is tank-to-wheel efficiency from PV module to wheels, assumed here 90%.

The sophisticated estimation for a tank to wheel efficiency of this application requires further optimization stage to run for specific vehicle component size and specific driving pattern. The idea here is to minimize energy conversions losses by using any available solar energy directly to the wheels without storing the energy in the battery unless if the system is forced to do that (e.g., SOC). However, this depends on many parameters as size of components, battery SOC, driving cycle, control strategy, etc..

Figures 8.1, 8.2, and 8.3 show the increase in the combined mpg after adding the proposed PV on-board for different conventional gasoline vehicles at 9-10 am, 12-1pm, 4-5pm, respectively. The analysis is done on five different vehicle specifications to cover a wide range of vehicles. The vehicle parameters are shown on the x-axis in Figures 8.1 to 8.3.

The vehicle 1 has ($C_d=0.17$, $A_f=1.2$, $C_r=0.008$, and curb weight (M_v) =900 kg), which is similar to Volkswagen XL1. While vehicle 2, is assumed very lightweight and aerodynamically very efficient (with $C_d=0.17$, $A_f=1.2$, $C_r=0.008$, and curb weight (M_v) =600 kg), which could be the target in 2025. The parameters for vehicle 3 is similar to Nissan Leaf 2012 as ($C_d=0.29$, $A_f=2.27$, $C_r=0.008$, and curb weight (M_v) =1532 kg). (Vehicle 4 with similar parameters as Toyota Camry 2014 as $C_d=0.28$, $A_f=2.25$,

$C_r=0.008$, and curb weight (M_v) =1447 kg). The last vehicle represents vehicle similar to Tesla 2013 S with ($C_d= 0.256$, $A_f = 2.36$, $C_r=0.008$, and curb weight (M_v) =2110 kg).

The increment in combined MPG is between a minor increase 0.11 mpg to a major increment by 34.15 mpg depends on vehicle specifications, time, location, and month.

The author calculated the combined fuel economy (mpg) (before the PV is added) for all the above vehicles as shown in the Figures x-axis by assuming all the vehicles are with conventional internal consumption engine with $\eta_{T2W_{city}}=15\%$ and $\eta_{T2W_{Hwy}}=20\%$.

The y-axis in Figures 8.1 to 8.3 show the minimum and maximum increase in mpg for three driving times at 9-10 am, 12-1 pm, and 4-5 pm. The minimum values refer to the vehicle driven in December in Boston, MA. The maximum values refer to the vehicle driven in June in Phoenix, AZ. For specific vehicle parameters and specific drive time, the increment in the fuel economy mostly between minimum and maximum values represented in the above Figures for any U.S. state in any month in a year.

As shown, the maximum PV contribution in vehicle 5 is 2.29 mpg, which due to the relative heaviest curb weight and the cycle time is relatively short compared to the number of total hours in a day when the sun is available. For vehicle 2, the fuel economy is increased by 1.33 mpg in December in Boston, MA at 4-5 pm. While, at 12-1 pm in Phoenix, AZ the fuel economy is increased up to 34.15 mpg. For typical Midsize car (Nissan Leaf or Toyota Camry), the fuel economy could be increased up to 4.2 MPG by using on-board PV at noon.

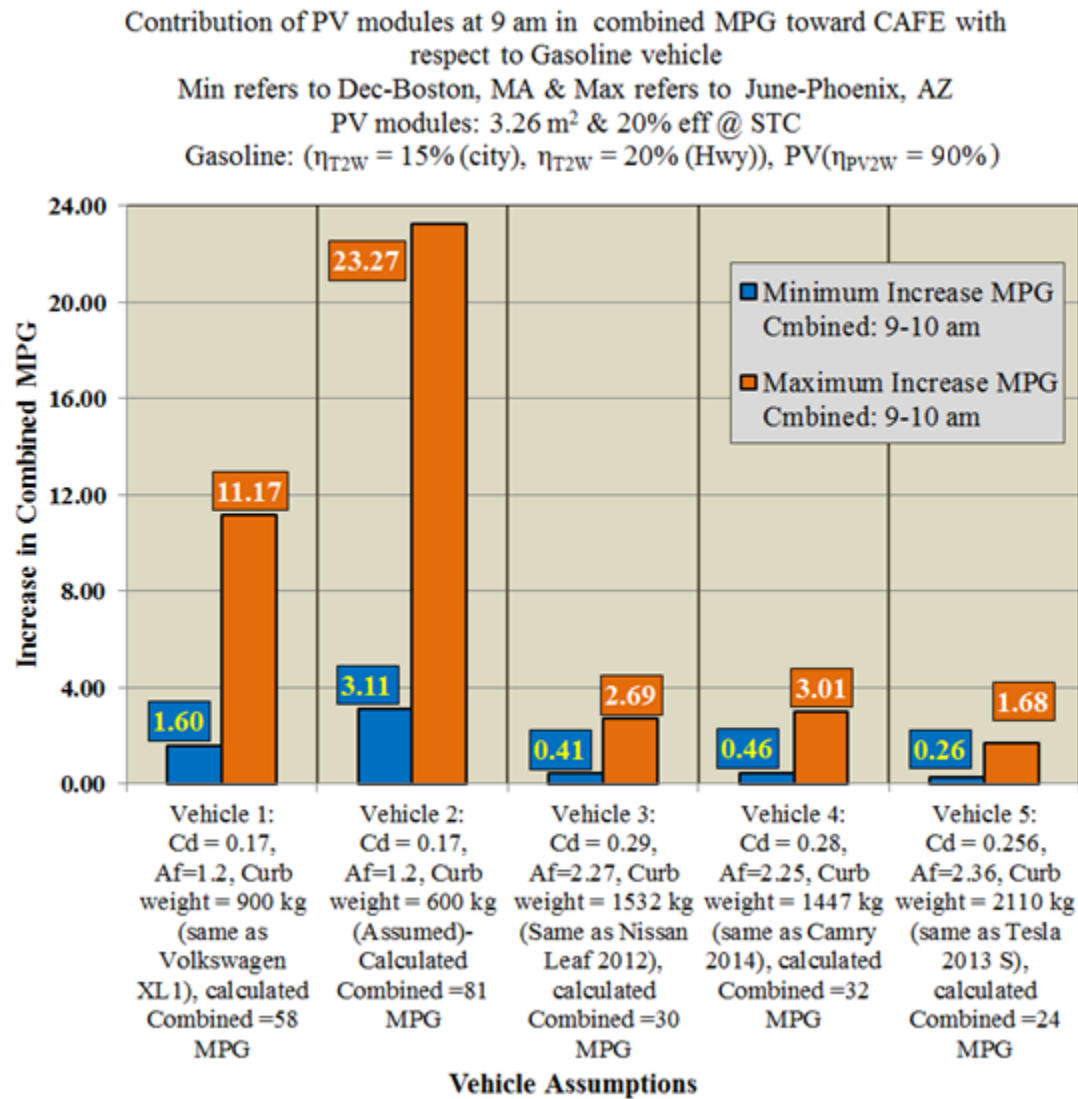


Figure 8. 1 On-board PV contribution in fuel economy (MPG) at 9-10 am scenario

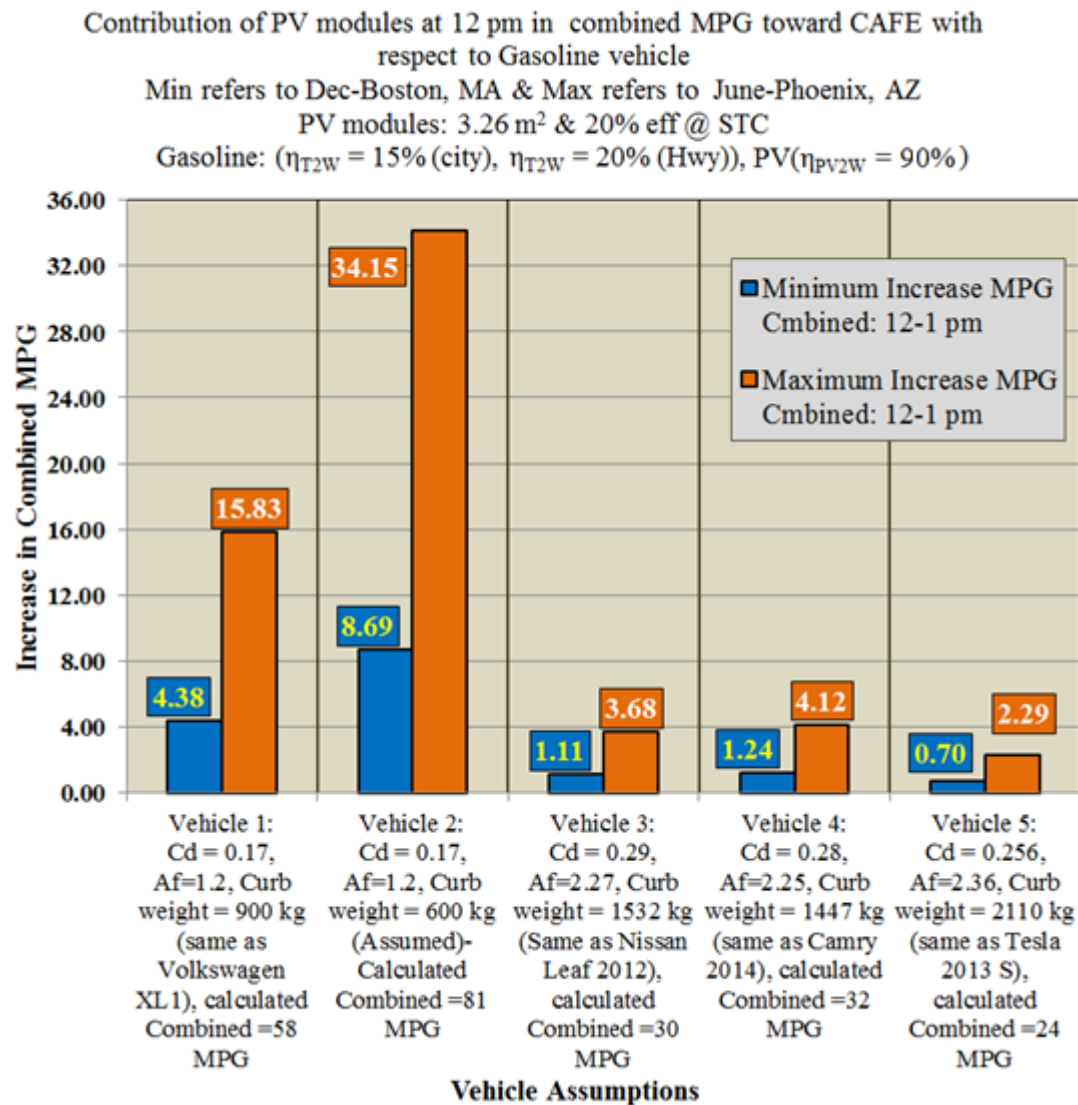


Figure 8. 2 On-board PV contribution in fuel economy (MPG) at 12-1 pm scenario

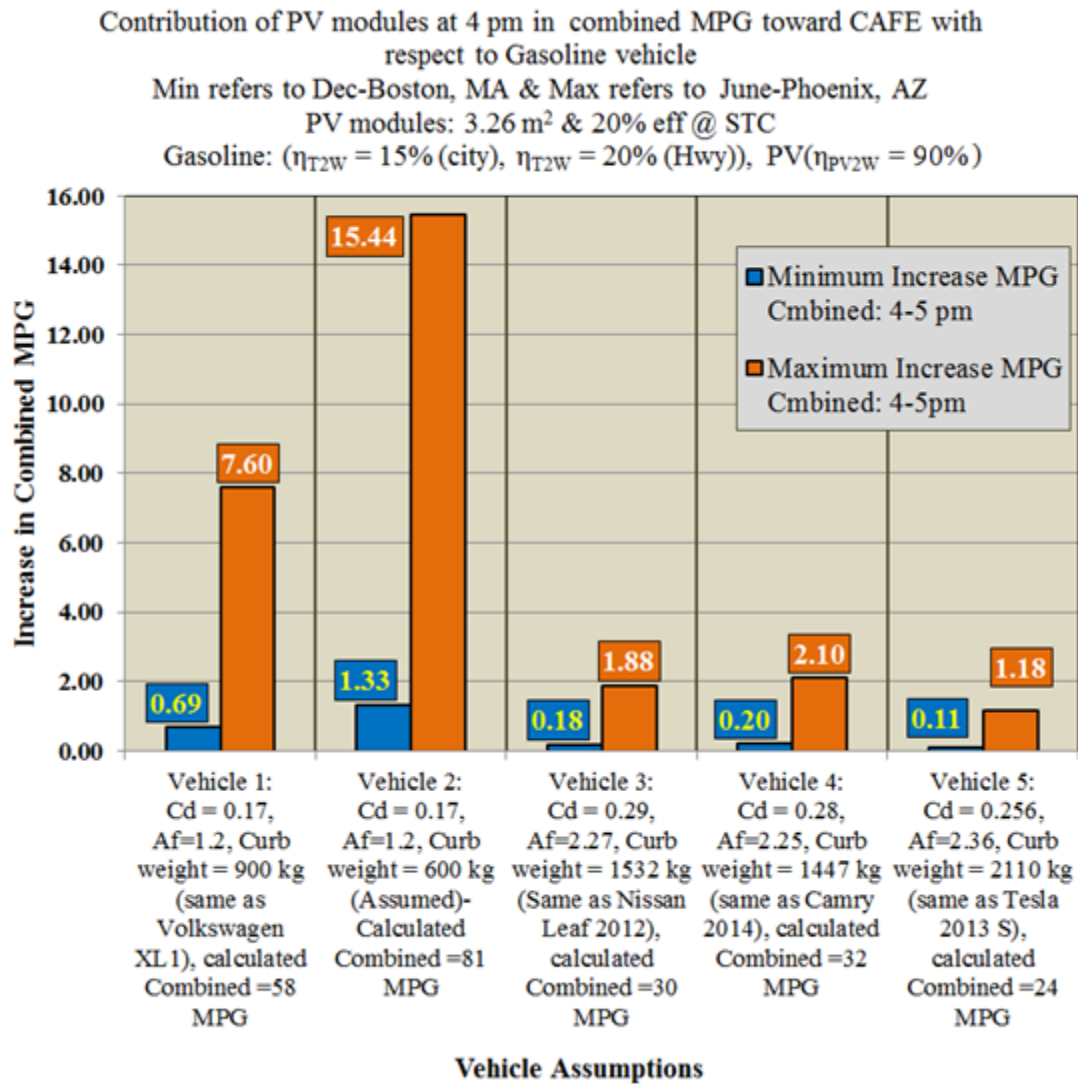


Figure 8. 3 On-board PV contribution in fuel economy (MPG) at 4-5 pm scenario

8.3 Pure PV Solar Daily Driving Ranges (PV Range Extender)

In this section, the daily pure PV solar driving ranges are estimated by adding the proposed PV module to 11 different vehicles (see Figure 8.4). The assumed vehicles 1 and 2 are same as discussed in section 8.2. The remaining vehicles also discussed in section 6.2. Here, all the vehicles are assumed electric and the vehicle efficiency (Wh per mile) is located in y-axis of Figure 8.4. These efficiencies are calculated based on the published combined MPGe. However, for vehicle 1 and 2, the MPGe is calculated using Equation 6.24 with $\eta_{T2W} = 90\%$ (see Figure 6.15 for details). The results with assumption are that the published vehicles curb weight remains constant. For, weight scenario analysis (see section).

Figure 8.4 shows the extended daily driving ranges are between 3 to 62.5 miles. For very efficient vehicle (e.g., vehicle 1) the PV can mostly daily drive between 13.5 to 62.5 miles in any of the U.S. From the results in Figure 8.4, up to 50% of the total daily miles travel by a person in the U.S. could be driven by solar energy if using typical mid-size vehicle and up to 174% if using a very lightweight and aerodynamically efficient vehicle.

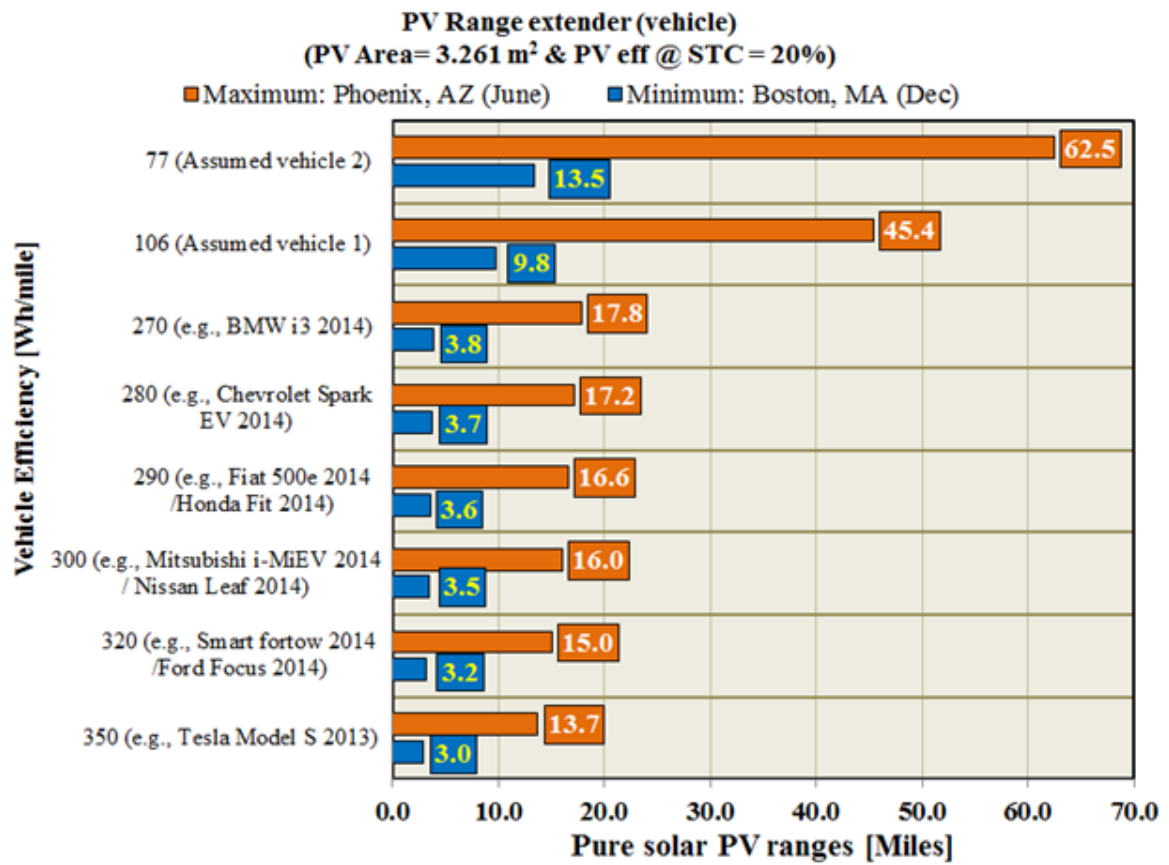


Figure 8. 4 Daily pure solar driving ranges

8.4 How green is Pure Solar Vehicle

The life cycle (well-to-wheels) emission of purely solar PV for driving the vehicle in different U.S. states (in terms of g CO₂-eq per mile) is estimated and displayed in Figures 8.5 to 8.8. The estimations are based on multiply the calculated GHG_{rate} by vehicle efficiency. The analyses are done in 12 U.S. states and 4 different vehicles titled previously (vehicle 1, vehicle 2, vehicle similar to Nissan Leaf 2014, or Mitsubishi i-MiEV 2014, and vehicle similar to Tesla Model S2013). For efficient vehicle (e.g., higher electrical efficiency or lower Wh per mile) the LCA emission per driven miles will be lower since the electricity consumption is less.

For vehicle 2, mostly in the U.S. the daily pure solar PV driven range is estimated between 13.5 and 62.5 miles with life cycle emission (CO₂-eq per driven mile) is estimated between 4.8 and 8.0 depends on the location. However, for vehicles with similar specifications as Nissan Leaf 2014 or Mitsubishi i-MiEV 2014, the estimated pure solar driven range is between 3.5 to 16.0 miles with LCA emission is between 18.6 to 31.3 g CO₂-eq per mile. For the last vehicle, which is similar to Tesla S 2013, the estimated pure driving ranges from 3 to 13.7 miles with 24.7 to 36.5 CO₂-eq/mile.

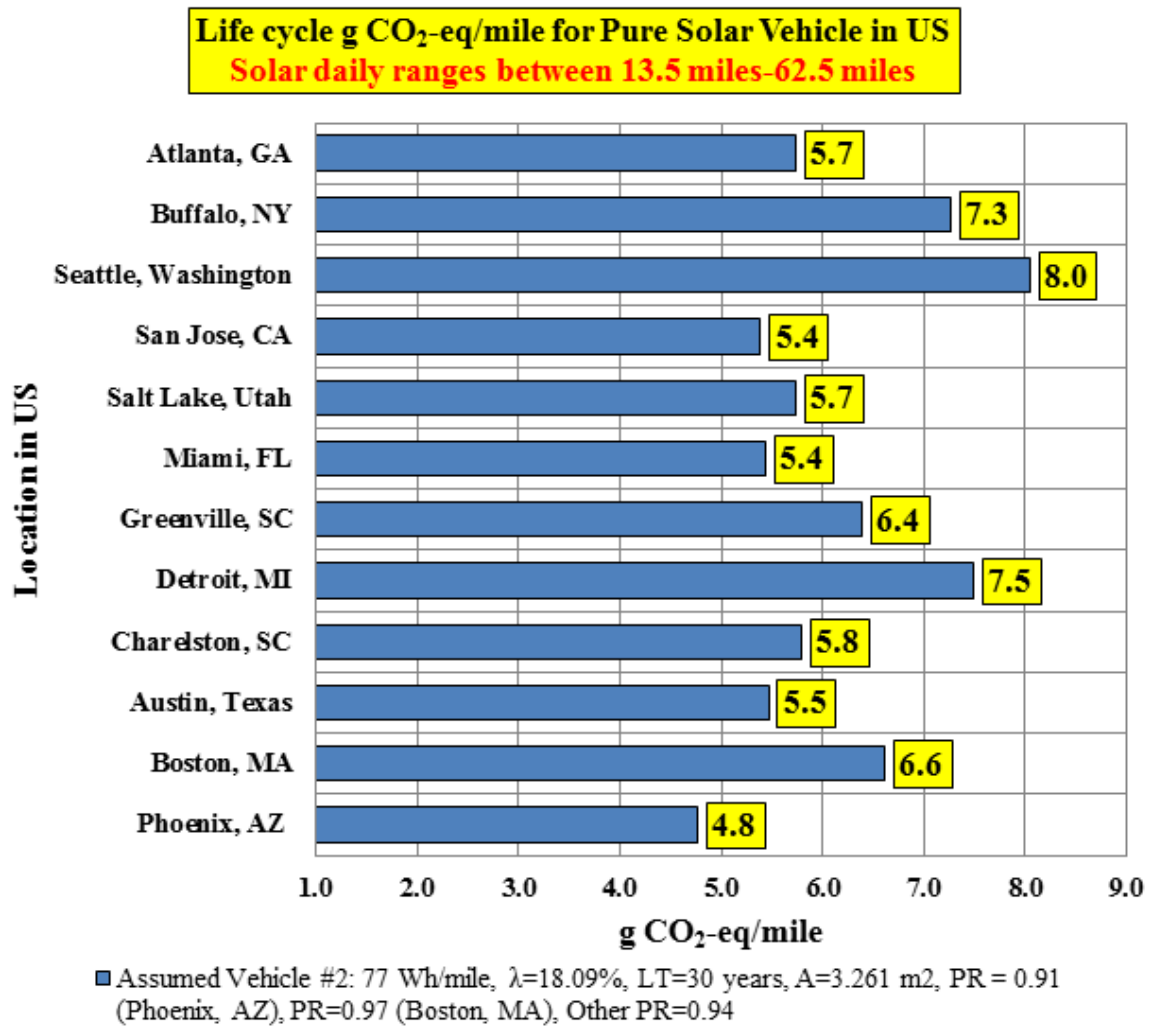
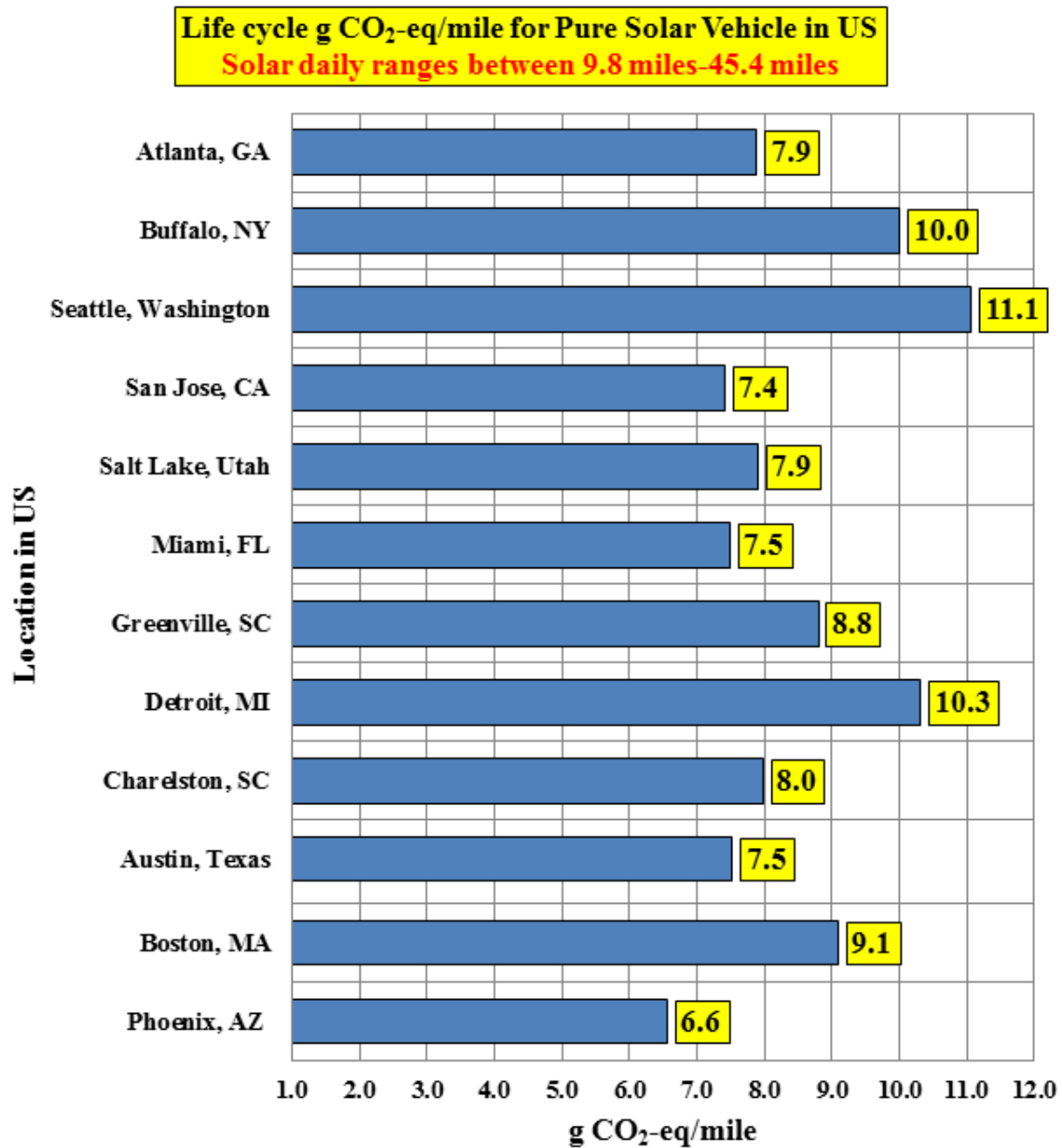


Figure 8. 5 Life cycle emission for pure solar vehicle in US (Assumed vehicle 2)



■ Assumed Vehicle #1: 106 Wh/mile, $\lambda=18.09\%$, LT=30 years, A=3.261 m², PR = 0.91 (Phoenix, AZ), PR=0.97 (Boston, MA), Other PR=0.94

Figure 8. 6 Life cycle emission for pure solar vehicle in US (Assumed vehicle 1)

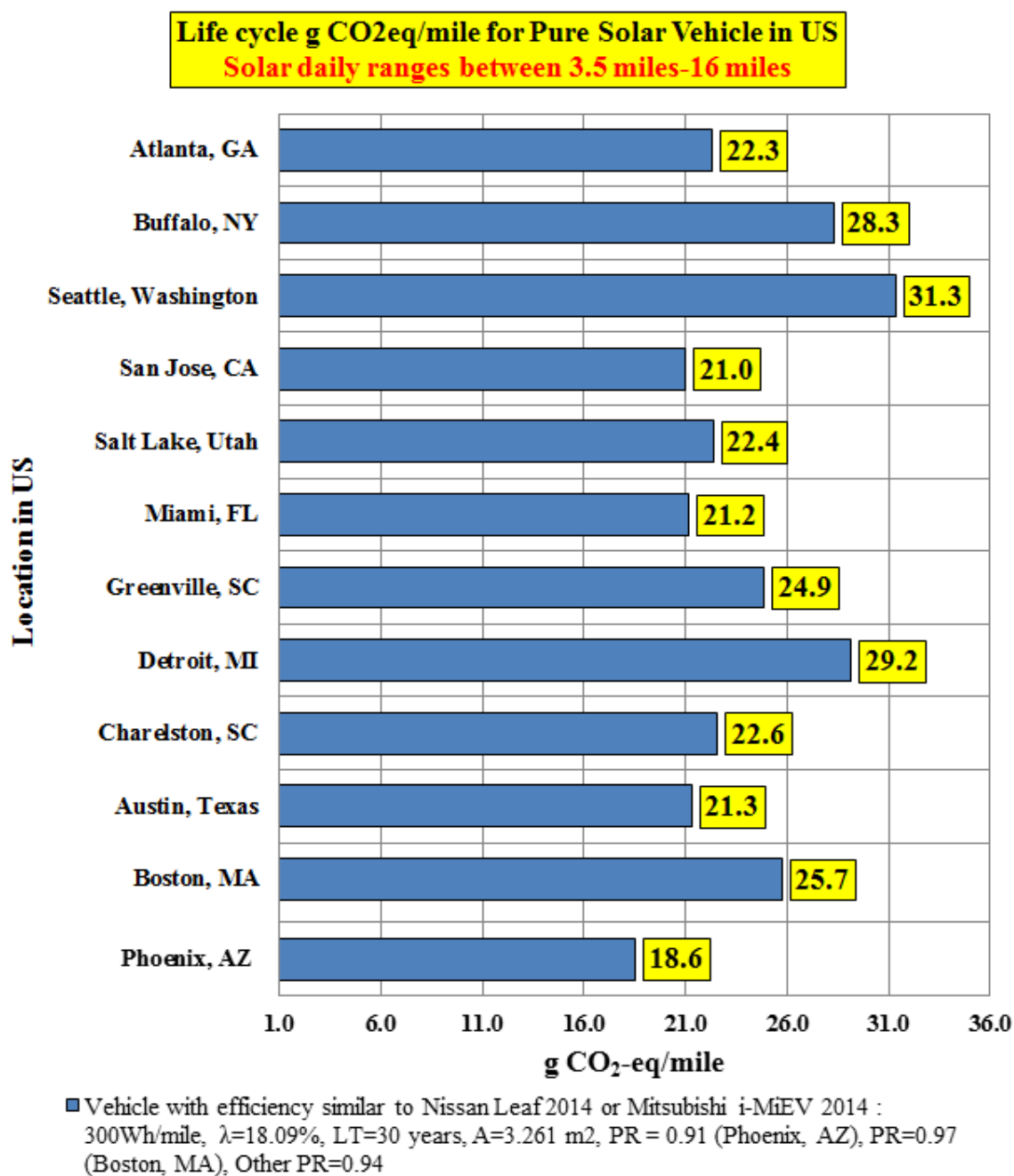


Figure 8. 7 Life cycle emission for pure solar vehicle in US (Vehicle with efficiency similar to Nissan Leaf 2014 or Mitsubishi i-MiEV 2014)

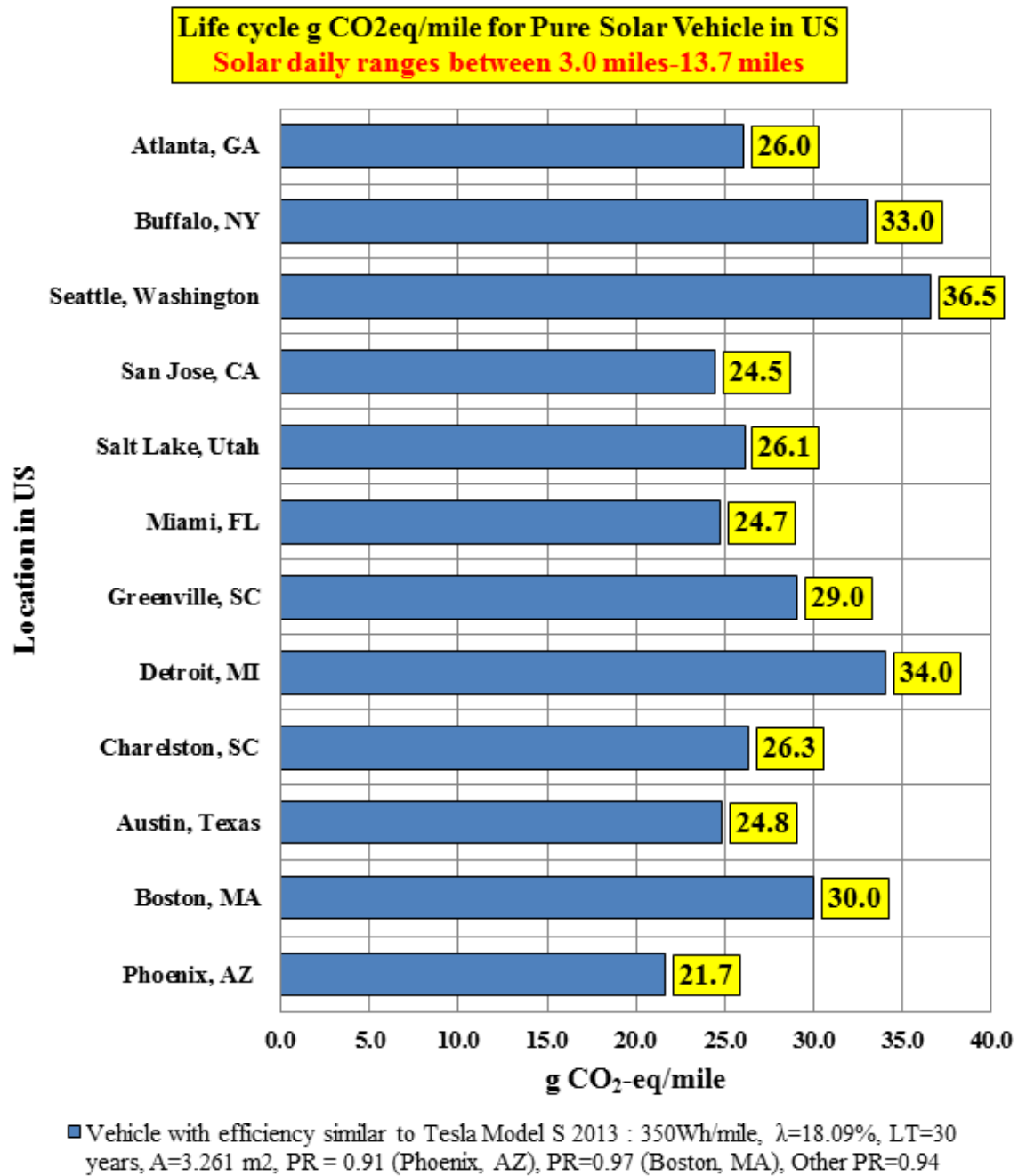


Figure 8. 8 Life cycle emission for pure solar vehicle in the US (Vehicle similar to Tesla Model S2013)

8.5 Life Cycle Emission Reduction for On-board PV with Gasoline Vehicle

The analysis of this section is done for the similar four base vehicles (Vehicle 1, 2, 3, and 5) with assumption daily driving range is 77 miles. Figure 8.9 shows the comparison between life cycle (well-to-wheels) emissions (g CO₂-eq/mile) for gasoline vehicles before and after adding the proposed on-board PV.

An example of the calculations, for vehicle number 1, the vehicle 1 with fuel economy is 58 mpg, this lead to life cycle g CO₂-eq per mile equal 197.7. Adding PV for vehicle 1 extend the driving ranges from the minimum daily range of 9.8 miles in the case of Boston, MA with 9.1 g CO₂-eq per mile to the maximum range of 45.4 miles in the case of Phoenix, AZ with 6.6 g CO₂-eq per mile. Therefore, by using assumed the driving range is 77 miles per day. The LCA emission of pure gasoline vehicle 1 can be reduced from 197.7 g CO₂-eq/mile to range from 85.0 to 173.7 g CO₂-eq/mile depending on the vehicle operating locations. This means that by adding PV, the reduction in CO₂ per mile can be from 24 to 112.7 grams.

For vehicle 2, without PV, the LCA emission is 141.6 g CO₂-eq per mile, but with adding the proposed PV the LCA emission could reduce to any value in the range 30.6 - 117.9 g CO₂-eq per mile. For vehicle 3, without PV will has emission 382.3 g CO₂-eq per mile and with PV the emission is reduced to a minimum value of 306.7 g CO₂-eq per mile or a maximum 366.1 g CO₂-eq per mile. Lastly, for vehicle number 5, for pure gasoline vehicle the emission is 477.9 g CO₂-eq per mile, while by adding PV it could be reduced to 369.7 (minimum) to 460.4 (maximum) g CO₂-eq per mile. All the results for

minimum and maximum reduction in LCA emission per mile by adding a PV on-board for gasoline vehicle can be found in Figure 8.9.

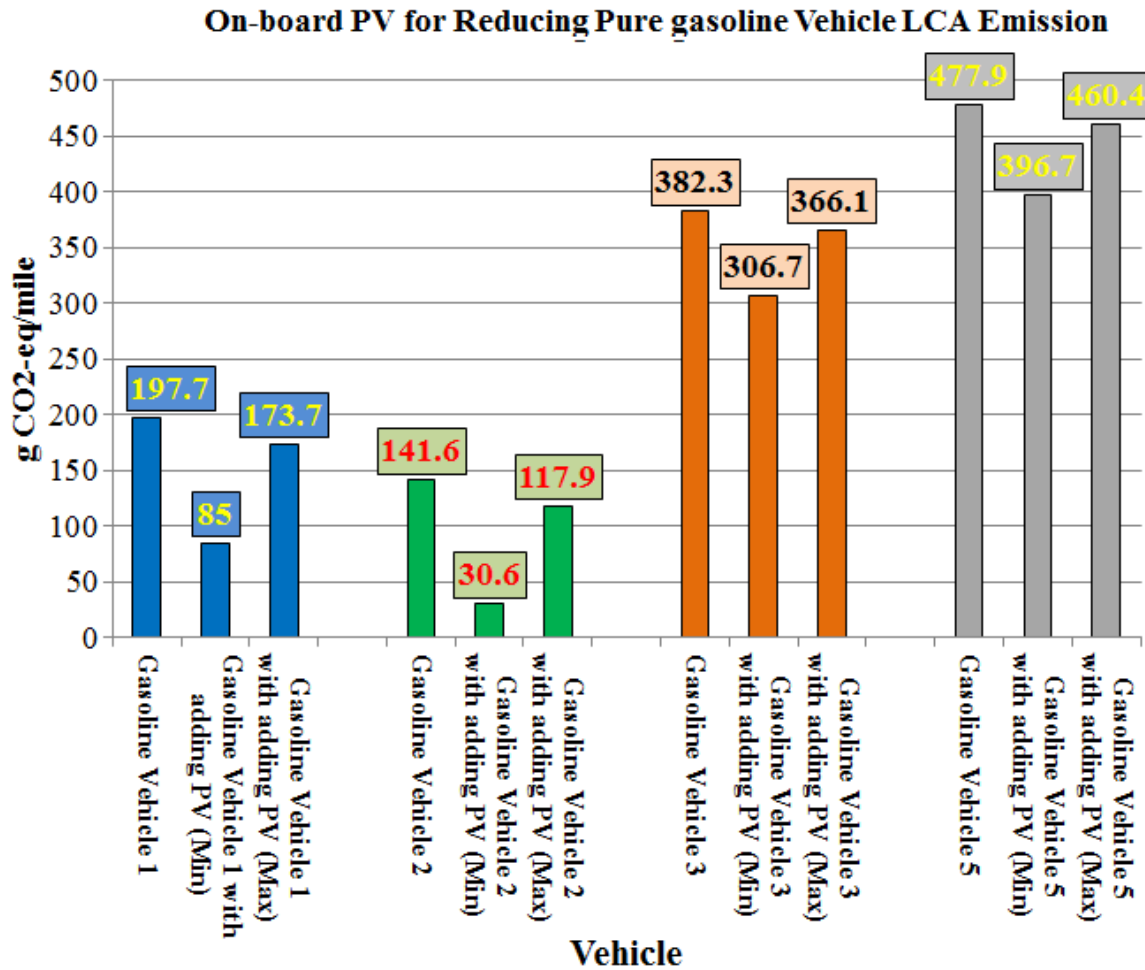


Figure 8. 9 LCA emission in terms of (g CO₂-eq per mile) for gasoline vehicle versus gasoline vehicle with PV

Figure 8.10 shows the minimum and the maximum lifetime ranges of LCA gCO₂-eq emission reduction by incorporating the proposed on-board PV to different gasoline

vehicles. The results are based on vehicle lifetime is 160,000 miles, since this range is used in GREET model [323].

For vehicle 1 and 2, the estimation is roughly from 4 to 18 metric tons of CO₂-eq per vehicle lifetime will be reduced. While, for vehicles 3 and 5, the maximum reduction is roughly 12-13 metric tons of CO₂-eq.

The annual CO₂ emission for energy use per average U.S. home is around 10.97 metric tons [324].

This means by using the proposed PV with a gasoline vehicle in the U.S. the system could be reduced 3 to 18 metric tons of CO₂-eq in vehicle lifetime—the equivalent of what an average U.S. home produces in 3 months to 20 months, respectively.

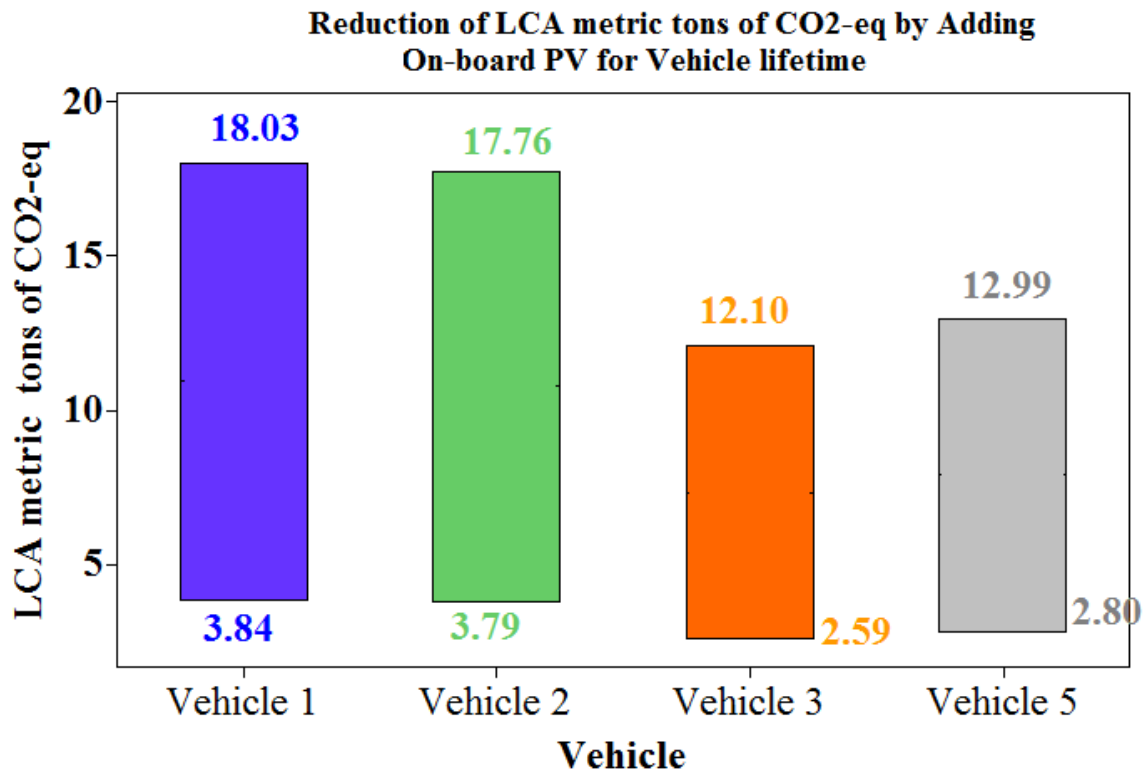


Figure 8. 10 LCA metric tons of CO₂-eq reduction ranges by incorporating the proposed on-board PV to different gasoline vehicles

8.6 Life Cycle Emission Reduction for On-board PV with Plug-in Electric Vehicle

In this section, the LCA (well-to-wheel) emission of pure plug-in vehicles in the U.S and India is estimated with and without adding the proposed on-board PV. Figure 8.11 shows the comparisons between grams of CO₂-eq per driven mile before and after adding the proposed on-board PV for different plug-in electric vehicles in the U.S. Here, the Battery and vehicle lifetime is assumed 160,000 miles as proposed in GREET [323].

The results showed the emission of pure plug-in electric vehicle 1 is 79.2 g CO₂-eq per mile, which could be minimized to 70.3 or further to 36.4 g CO₂-eq per mile by using the proposed PV on-board. For vehicle 2, pure EV configuration emits 58 g CO₂-eq per mile, while by adding PV the emission is reduced to 49 g CO₂-eq per mile or to very low 14.8 g CO₂-eq per mile. The highest emission is found in the case of the heavier vehicle (vehicle number 5), so the emission of its pure configuration is 263.7 g CO₂-eq/mile, while by using on-board PV the emission could be reduced to 220.6 or 254.6 g CO₂-eq per mile. This mean by adding PV for vehicle number 5 (similar to Tesla), the reduction in LCA emission can be between 9.1 and 43.1 g CO₂-eq for every driving mile, depends on the location and the time.

The results in this section are based on the following calculations: For example, the LCA emission for pure plug-in EV 1 is calculated as below:

- The total electricity needed is equal about 9 kWh based on vehicle efficiency 106 Wh per mile and 90% SOC.
- The total battery emission is equal 1,197 kg CO₂-eq based on 133 kg CO₂-eq/kWh

- The lifetime Grid electricity is equal 18,701 kWh
- The total lifetime electricity emission is 11,483 kg CO₂-eq based on U.S. Grid (assumed 614 g CO₂-eq/kWh).
- The total lifetime kg CO₂-eq = 11,483 + 1,197 = 12.68
- The lifetime emission of pure plug-in EV 1 (U.S. Grid) is equal 79.2 g CO₂-eq/mile.

Incorporating on-board PV with the above vehicle will reduce the emission as below:

- The minimum daily PV range of this vehicle is 9.8 miles with 9.1 g CO₂-eq/mile, the remaining range is 67.2 miles with emission as above 79.2 CO₂-eq/mile. The total emission for full range (77 miles) is calculated as 5,411 kg CO₂-eq, which corresponding to 70.3 g CO₂-eq/mile.
- The maximum daily PV range of this vehicle is 45.4 miles with 6.6 g CO₂-eq/mile, the remaining driving range is 31.6 miles with emission as above 79.2 CO₂-eq/mile. The total emission for full range (77 miles) is calculated as 2,802 kg CO₂-eq, which corresponding 36.4 g CO₂-eq/mile.
- If the same vehicle is operating in India, New Delhi, without PV the lifetime emission is calculated as 156.2 g CO₂-eq/mile that is based on India Grid (1,272.2 g CO₂-eq/kWh). Incorporating on-board PV will reduce the emission to 105.5 g CO₂-eq/mile. The average daily solar irradiation stored in the battery is 2,776 Wh. Therefore, the average estimated daily pure PV solar range is 26.2 miles with LCA emission of 7.34 g CO₂-eq/mile.

Figure 8.12 shows the potential LCA emission lifetime reduction after adding proposed PV to the plug-in EVs operating in India. The solar data are based on New Delhi area with average daily solar data is used. The results showed the following:

- The LCA CO₂-eq emission for plug-in EV in India emits almost double CO₂-eq emission compared to the similar plug-in EV operating in the U.S.
- For heavy vehicle (e.g., vehicle 5), the LCA emission of pure plug-in EV is estimated as 519.6 g CO₂-eq per mile, this is higher than the similar gasoline vehicle when operating in the U.S.
- The positive environmental impact of incorporating on-board PV for EV in India is higher than U.S, since India grid mainly depends on Coal.

Figure 8.13 shows the metric tons of CO₂-eq reduction by using on-board PV compared to pure EV in the U.S and India. As shown, the total emission reduction in the U.S. is roughly between 1.4 to 7 metric tons per vehicle lifetime. While, the average metric tons of CO₂-eq reduction if the vehicle based in India is around 8.2 metric tons.

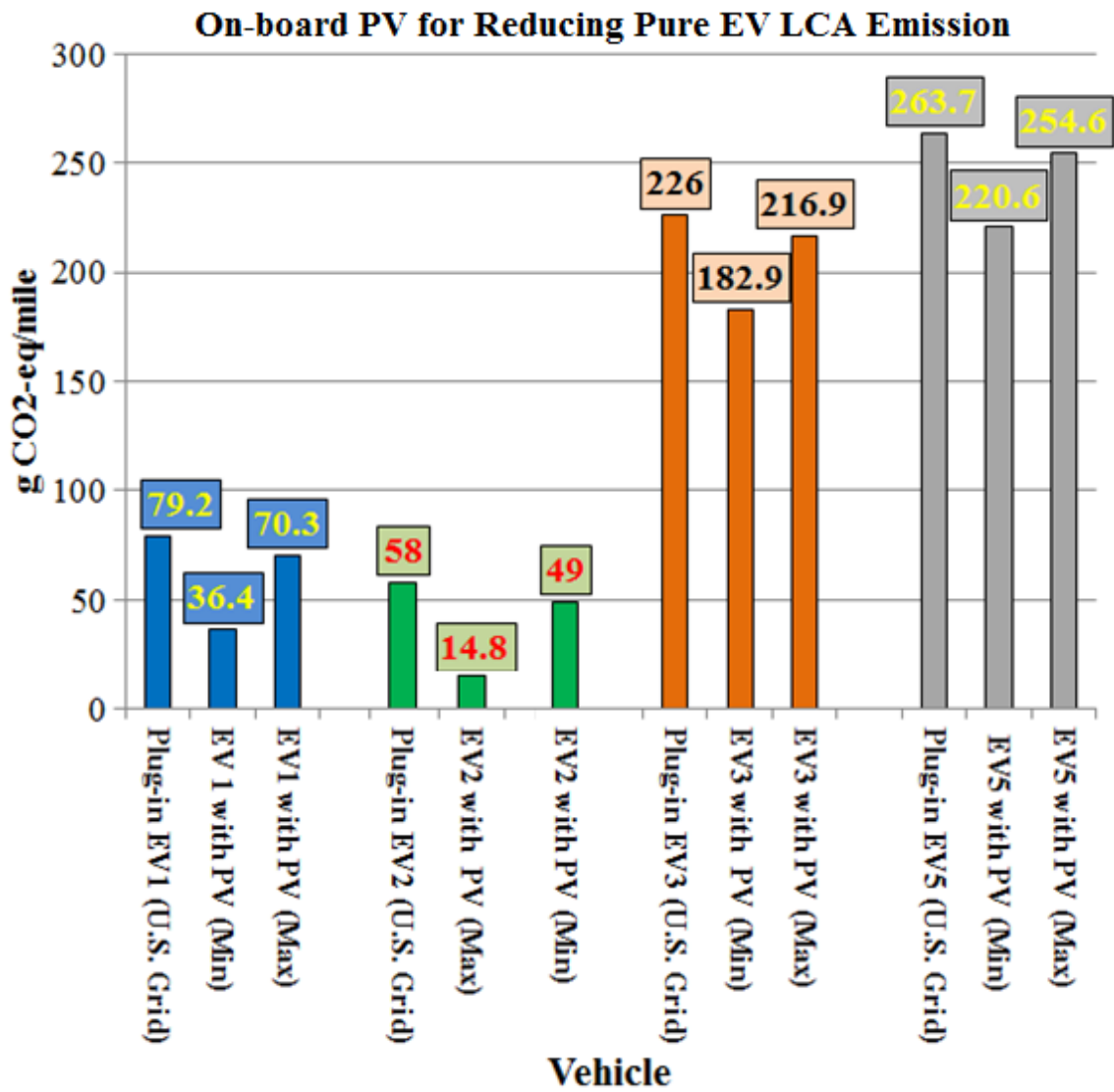


Figure 8. 11 grams CO₂-eq reduction by incorporating on-board PV to pure plug-in electric vehicle (U.S. Grid)

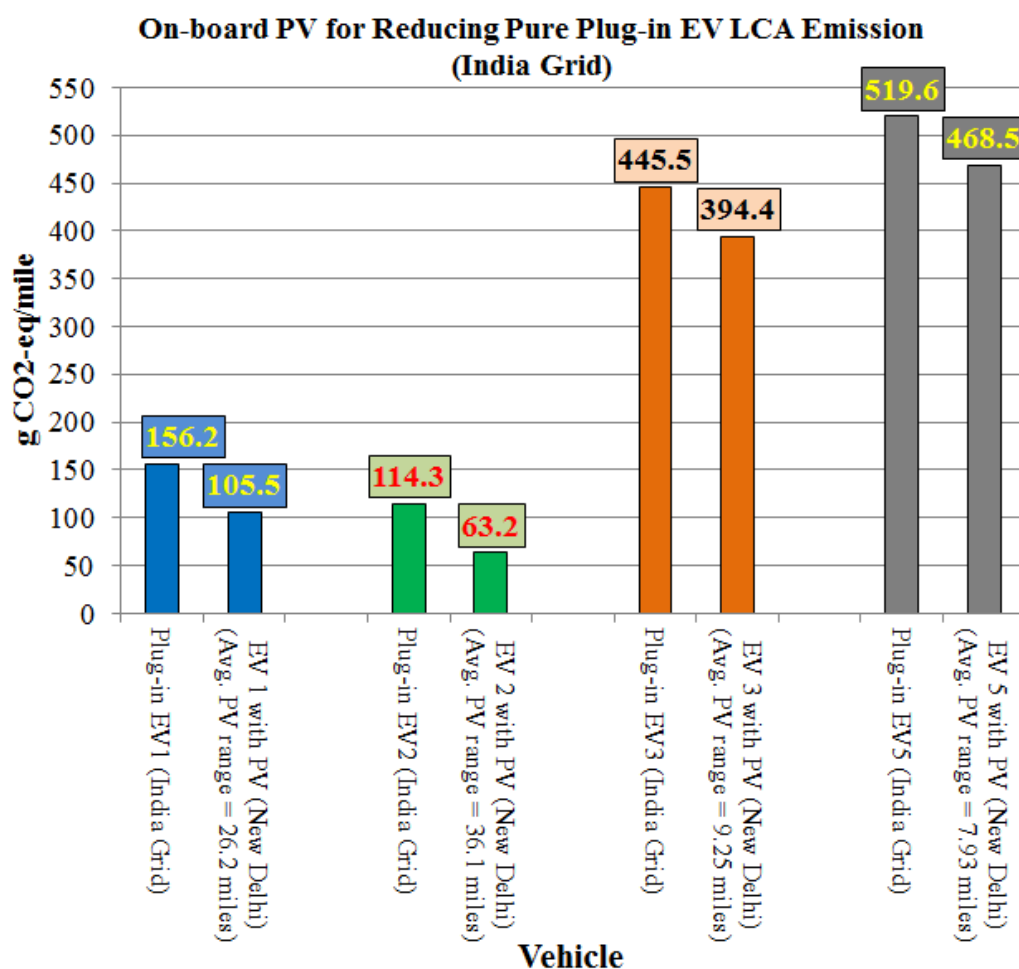


Figure 8. 12 grams CO₂-eq reduction by incorporating on-board PV to pure plug-in electric vehicle (India Grid)

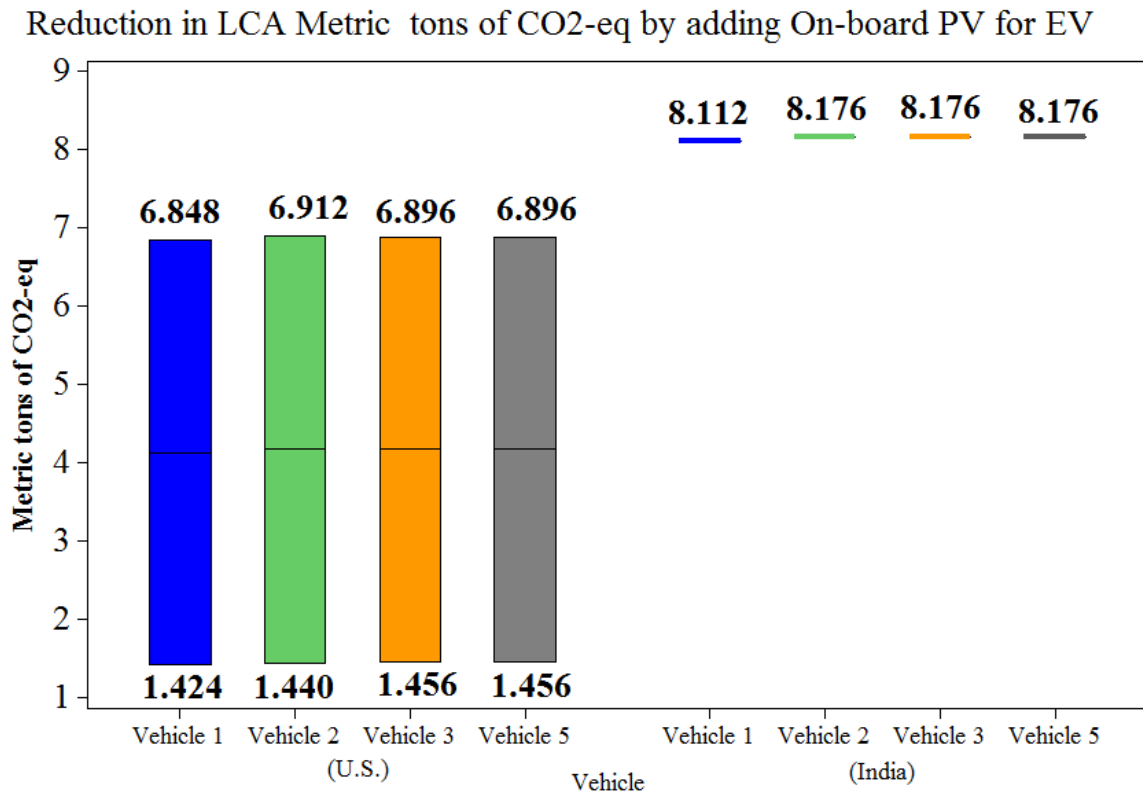


Figure 8. 13 Metric tons of grams CO₂-eq reduction by incorporating on-board PV to pure plug-in electric vehicle (U.S. Grid vs. India Grid)

8.7 Cost Analysis

In this section, the life cycle cost analysis (\$) for each driven mile are estimated. The following fuel types are analyzed; only pure solar PV, pure gasoline (U.S.), U.S. grid electricity (current scenario), U.S. grid electricity (future scenario), gasoline with PV solar, as well as grid electricity with PV solar.

8.7.1 Cost Analysis of Pure Solar PV Vehicle

The cost of the battery and motor are calculated using Equations (8.5) and (8.6), these equations already used in in Future Automotive Systems Technology Simulator – NREL [325], [326], [327].

$$\text{Motor and controller} = \$21.7/\text{kW} + \$425 \quad (8.5)$$

$$\text{Battery} = \$22/\text{kW} + \$500/\text{kWh} + \$680 \quad (8.6)$$

The cost of the battery was around 1000 \$/kWh in 2008, while it is dropped to 325 \$/kWh in 2014 and the price will further be dropped to 125 \$/kWh by 2022 with 100,000 annually production [328]. The cost of the battery based on Tesla Motor may be dropped faster since the goal of Tesla to increase the EV production to 500,000 vehicles by 2020 compared to 35,000 vehicles in 2014. The Figures 8.14 and 8.15 show the Tesla Motor's proposed battery Gigafactory and estimated cost reduction [329], [330].

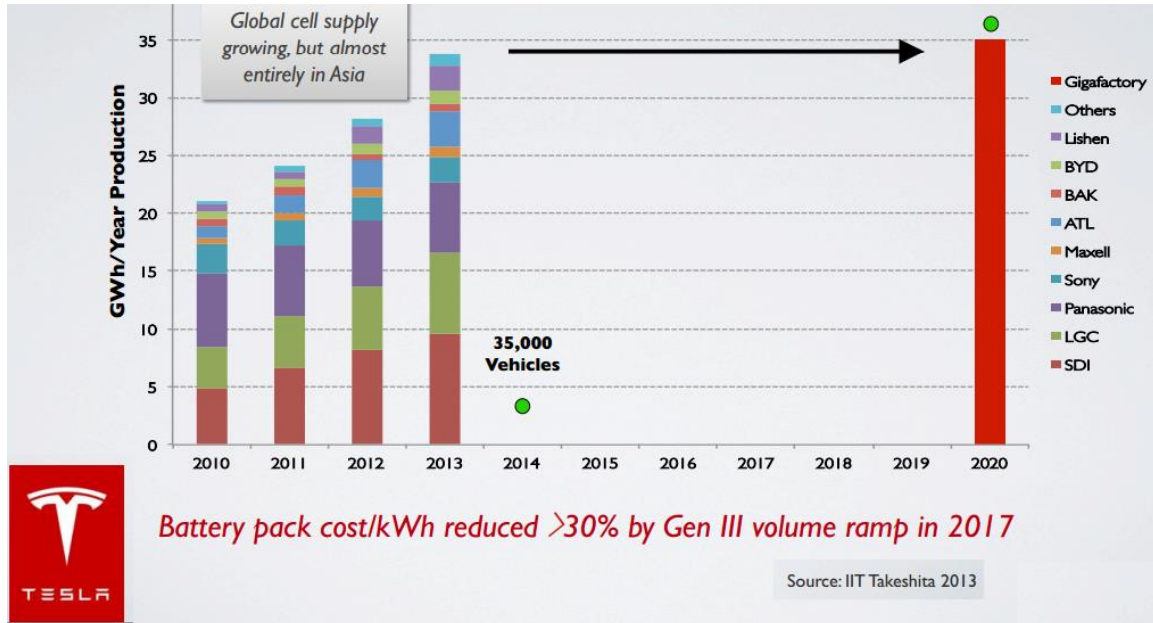


Figure 8. 14 Planned 2020 Gigafactory Production [329]

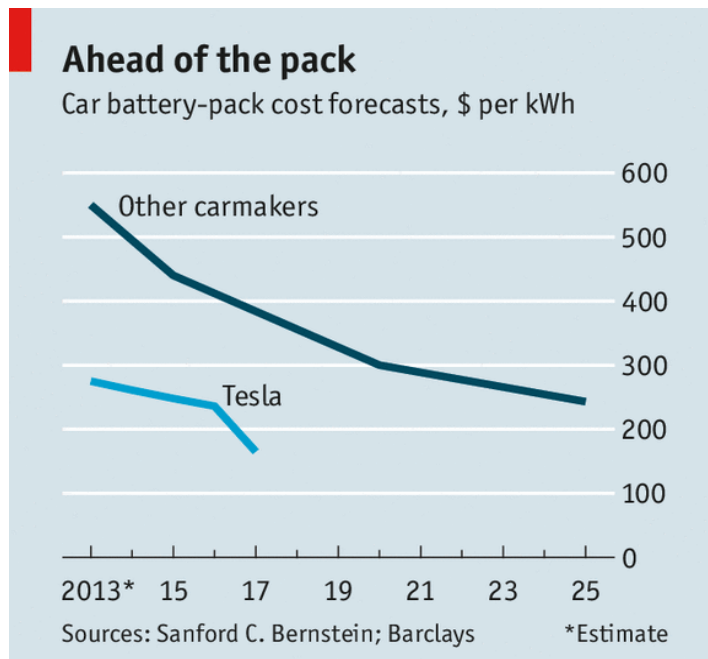


Figure 8. 15 The battery cost forecast based on Tesla Motor's proposed production [330]

The powertrain and the fuel life cycle costs of pure solar EV are estimated as \$ 5,758 in current price to drop to \$ 3,572 in the future. The key assumptions are tabulated in Table 8.2. The vehicle lifetime is considered 160,000 miles, which is same for the battery and the motor, however the life span of the PV module is around 30 years. The assumption here, the calculation just based on vehicle lifetime and the PV module could be transferred to another application after the vehicle is recycled.

Table 8. 2 Assumptions for cost analysis of pure solar vehicle

Component	Quantity	Life cycle Quantity for 160,000 miles	Current Price	Future Price	Note/Ref
PV Module (\$/W)	1 Watt	1	0.88	0.51	Prices for silicon PV module with no tax as the minimum and maximum market price [331]
PV Module (\$)	654 W	1	616	357	Proposed module with 7% tax
Mounting	1	1	100	50	Same as roof mounted cargo rack
Battery	5 kWh	1	3400	1525	Current price based on Equation 8.6. Future price based on equation 8.6 and DOE estimation in 2022
Motor and controller	10 kW	1	642	642	Equation 8.5
Maintenance	-	-	1000	1000	Assumed
Total life time Cost (\$)			5758	3572	

For example, if vehicle 2 is used, then the life cycle cost of driving will be between 2 to 4 ¢/mile with 13.5-62.5 daily driving ranges. However, this will be suitable for a low speed vehicle since the motor size is small.

8.7.2 Cost Analysis of Pure Gasoline Vehicle Vs. Gasoline vehicle with PV

The cost analysis of gasoline vehicle with and without PV is done for the three vehicles as vehicle 1 which is similar to Volkswagen XL 2015 (curb weight 900 kg), vehicle 2 (light weight, curb weight 600 kg), and vehicle 3, which is similar to Nissan Leaf (curb weight 1532 kg).

For fair estimation, the acceleration time 0-60 mph is set as a constraint for the purpose of calculating the net power needed. The net power is calculated using Equation (8.7)

$$P_{\max} = \frac{V_0^2 \times m_v}{t_0} \quad (8.7)$$

Where,

P_{\max} is the net power needed to accelerate the vehicle (e.g., 0-60 mph).

V_0 is the vehicle speed in m/s.

m_v is the curb weight in kg.

t_0 is the acceleration time needed (e.g., 0-60 mph).

Assuming, the 0-60 mph acceleration time is equal 12 seconds, then the P_{\max} is equal 54 kW, 36 kW, and 92 kW for vehicle 1, vehicle 2, and vehicle 3, respectively. The estimated pure gasoline lifetime cost is included the cost of the lifetime fuel, engine, and maintenance. The cost of the engine is calculated using Equation 8.8, which is already used in in Future Automotive Systems Technology Simulator – NREL [325], [326],

[327]. For pure gasoline vehicle, the key assumptions and the estimated values are tabulated in Table 8.3.

$$\text{Engine} = \$14.5/\text{kW} + \$531 \quad (8.8)$$

Table 8. 3 Assumptions for cost analysis of pure gasoline vehicle

Component	Vehicle 1	Vehicle 2	Vehicle 3	Note
Engine (\$)	1,314	1,053	1,865	Vehicle 1 (54 kW), vehicle 2 (36 kW), and vehicle 3 (92 kW)
Gasoline Fuel (\$)	11034.48	7901.235	21333.33	Vehicle 1 (mpg=58), vehicle 2 (mpg=81), and vehicle 3 (mpg=30). Vehicle lifetime = 160,000 miles. [Scenario 1: 4 \$ per gallon]
Gasoline Fuel (\$)	22069	15802	42667	Vehicle 1 (mpg=58), vehicle 2 (mpg=81), and vehicle 3 (mpg=30). Vehicle lifetime = 160,000 miles. [Scenario 2: 8 \$ per gallon]
Maintenance	3,000	3,000	3,000	Assumed same for all for fair comparison
Total lifetime Cost (\$) – (scenario 1)	15348	11954	26198	Added engine, gasoline fuel, and maintenance
Lifetime cost (¢) per mile (Scenario 1)	9.6	7.5	16.4	Total lifetime cost/lifetime mile
Total lifetime Cost (\$) – (scenario 2)	26383	19855	47532	Added engine, gasoline fuel, and maintenance
Lifetime cost (¢) per mile (Scenario 2)	16.5	12.4	29.7	Total lifetime cost/lifetime mile

For estimating the cost of gasoline vehicle with on-board PV, the total power required is divided between electric motor, which run by solar PV and need a battery for energy

storage and the remaining power is run by a smaller engine with gasoline fuel. The lifetime gasoline fuel price is reduced due to the number of gasoline gallons is reduced by incorporating PV.

For example, for vehicle 1 the pure solar PV ranges are between 9.8 to 45.4 miles depended on locations in the U.S. Without PV, the total number gallons of gasoline are 2,759 since the vehicle 1 MPG is 58. By incorporating PV, the total lifetime gasoline gallon is reduced to 1,132 given the minimum PV daily solar range or reduced to 2,408 gallons given the maximum PV daily ranges. So, the total saving gasoline gallons for vehicle 1 is from 351 to 1627.

Table 8.4 shows the proposed cost scenarios for gasoline vehicle with and without PV. For pure gasoline vehicle, there are two proposed scenarios, the first with gasoline price \$4.0 per gallon and the second with the high gasoline price at \$8.0 per gallon. For gasoline vehicle with PV, there are four different scenarios. The first scenario is based on current price of PV and battery with low gasoline price and assume it is operating in places with low solar energy (e.g., Boston, MA). The second scenario is based on similar assumptions used in scenario 1, except the gasoline price is high (\$8.0). The third scenario is based on future prices of PV and battery and current gasoline price (\$ 4.0), operating high solar energy location (e.g., Phoenix, AZ). The last scenario is based on similar assumptions used in scenario 3, with the exception is gasoline price is high (\$8.0).

Table 8. 4 Proposed cost scenarios of Gasoline vehicle with and without PV

Vehicle	Scenario Description
Pure Gasoline vehicle	Scenario 1: gasoline price 4.0 \$/gallon Scenario 2: gasoline price 8.0 \$/gallon
Gasoline vehicle with PV	Scenario 1: highest price PV, highest mounting, highest battery price, lowest PV location, gasoline price 4\$/gallon Scenario 2: highest price PV, highest mounting, highest battery price, lowest PV location, gasoline price 8\$/gallon Scenario 3: lowest price PV, lowest mounting, lowest battery price, best PV location, gasoline price 4\$/gallon Scenario 4: lowest price PV, lowest mounting, lowest battery price, best PV location, gasoline price 8\$/gallon

The following Tables 8.5,8.6,8.7, and 8.8 show the estimated lifetime cost of on-board PV with gasoline for scenario 1, scenario 2, scenario 3, and scenario 4, respectively.

Table 8. 5 Cost analysis of gasoline vehicle with PV (Scenario 1)

Component	Quantity	Vehicle 1	Vehicle 2	Vehicle 3	Note
PV Module (\$) Maximum	3 m ²	616	616	616	Same as Table 8.2
Mounting (\$) Max	1	100	100	100	Same as Table 8.2
Battery (Maximum)	5 kWh	3400	3400	3400	Same as Table 8.2
Motor and controller	10 kW	642	642	642	Same as Table 8.2
Maintenance	-	3000	3000	3000	Assumed for PV and gasoline powertrain
Engine (\$)	Vehicle 1 (44 kW), vehicle 2 (26 kW), and vehicle 3 (82 kW)	1169	908	1720	Minimized by 10 kW compared to pure gasoline (Table 8.3)
Gasoline Fuel (\$) Maximum		9632	6516	20364	Vehicle 1 (mpg=58), vehicle 2 (mpg=81), and vehicle 3 (mpg=30). Vehicle lifetime = 160,000 miles. 4 \$ per gallon (U.S.), Based on the minimum pure solar PV
Total life time Cost (\$) (Scenario 1)		18459	15082	29742	Adding maximum in every row
Life time cost (¢) per mile (scenario 1)		11.6	9.5	18.7	Lifetime cost/ lifetime mile

Table 8. 6 Cost analysis of gasoline vehicle with PV (Scenario 2)

Component	Quantity	Vehicle 1	Vehicle 2	Vehicle 3	Note
PV Module (\$) Maximum	3 m ²	616	616	616	Same as Table 8.2
Mounting (\$) Max		100	100	100	Same as Table 8.2
Battery (Maximum)	5 kWh	3400	3400	3400	Same as Table 8.2
Motor and controller	10 kW	642	642	642	Same as Table 8.2
Maintenance	-	3000	3000	3000	Assumed for PV and gasoline powertrain
Engine (\$)	Vehicle 1 (44 kW), vehicle 2 (26 kW), and vehicle 3 (82 kW)	1169	908	1720	Minimized by 10 kW compared to pure gasoline (Table 8.3)
Gasoline Fuel (\$) Maximum		19264	13032	40728	Vehicle 1 (mpg=58), vehicle 2 (mpg=81), and vehicle 3 (mpg=30). Vehicle lifetime = 160,000 miles. 4 \$ per gallon (U.S.), Based on the minimum pure solar PV
Total life time Cost (\$) (Scenario 2)		28191	21698	50206	Adding maximum in every row
Life time cost (¢) per mile (Scenario 2)		17.6	13.6	31.4	Lifetime cost/lifetime mile

Table 8.7 Cost analysis of gasoline vehicle with PV (Scenario 3)

Component	Quantity	Vehicle 1	Vehicle 2	Vehicle 3	Note
PV Module (\$) Minimum	3 m ²	357	357	357	Same as Table 8.2
Battery (Minimum)	5 kWh	1525	1525	1525	Same as Table 8.2
Mounting (\$) Min		50	50	50	Same as Table 8.2
Motor and controller	10 kW	642	642	642	Same as Table 8.2
Maintenance	-	3000	3000	3000	Assumed for PV and gasoline powertrain
Engine (\$)	Vehicle 1 (44 kW), vehicle 2 (26 kW), and vehicle 3 (82 kW)	1169	908	1720	Minimized by 10 kW compared to pure gasoline (Table 8.3)
Gasoline Fuel (\$) Minimum		4528	1488	16900	Vehicle 1 (mpg=58), vehicle 2 (mpg=81), and vehicle 3 (mpg=30). Vehicle lifetime = 160,000 miles. 4 \$ per gallon (U.S.), based on the maximum pure solar PV
Total life time Cost (\$) (Scenario 3)		11271	7970	24194	
Life time cost (¢) per mile (Scenario 3)		7.0	5.0	15.1	

Table 8. 8 Cost analysis of gasoline vehicle with PV (Scenario 4)

Component	Quantity	Vehicle 1	Vehicle 2	Vehicle 3	Note
PV Module (\$) Minimum	3 m ²	357	357	357	Same as Table 8.2
Battery (Minimum)	5 kWh	1525	1525	1525	Same as Table 8.2
Mounting (\$) Min		50	50	50	Same as Table 8.2
Motor and controller	10 kW	642	642	642	Same as Table 8.2
Maintenance	-	3000	3000	3000	Assumed for PV and gasoline powertrain
Engine (\$)	Vehicle 1 (44 kW), vehicle 2 (26 kW), and vehicle 3 (82 kW)	1169	908	1720	Minimized by 10 kW compared to pure gasoline (Table 8.3)
Gasoline Fuel (\$) Minimum		4528	1488	16900	Vehicle 1 (mpg=58), vehicle 2 (mpg=81), and vehicle 3 (mpg=30). Vehicle lifetime = 160,000 miles. 4 \$ per gallon (U.S.), based on the maximum pure solar PV
Total life time Cost (\$) (Scenario 4)		15799	9458	41094	
Life time cost (¢) per mile (Scenario 4)		9.9	5.9	25.7	

Figure 8.16 shows the estimated lifetime cost of driving (¢ per mile) of pure gasoline (the proposed scenario 1) and gasoline with PV (the proposed scenarios 1 and 3). All of these scenarios are proposed with current gasoline price in U.S. (\$4.0 per gallon).

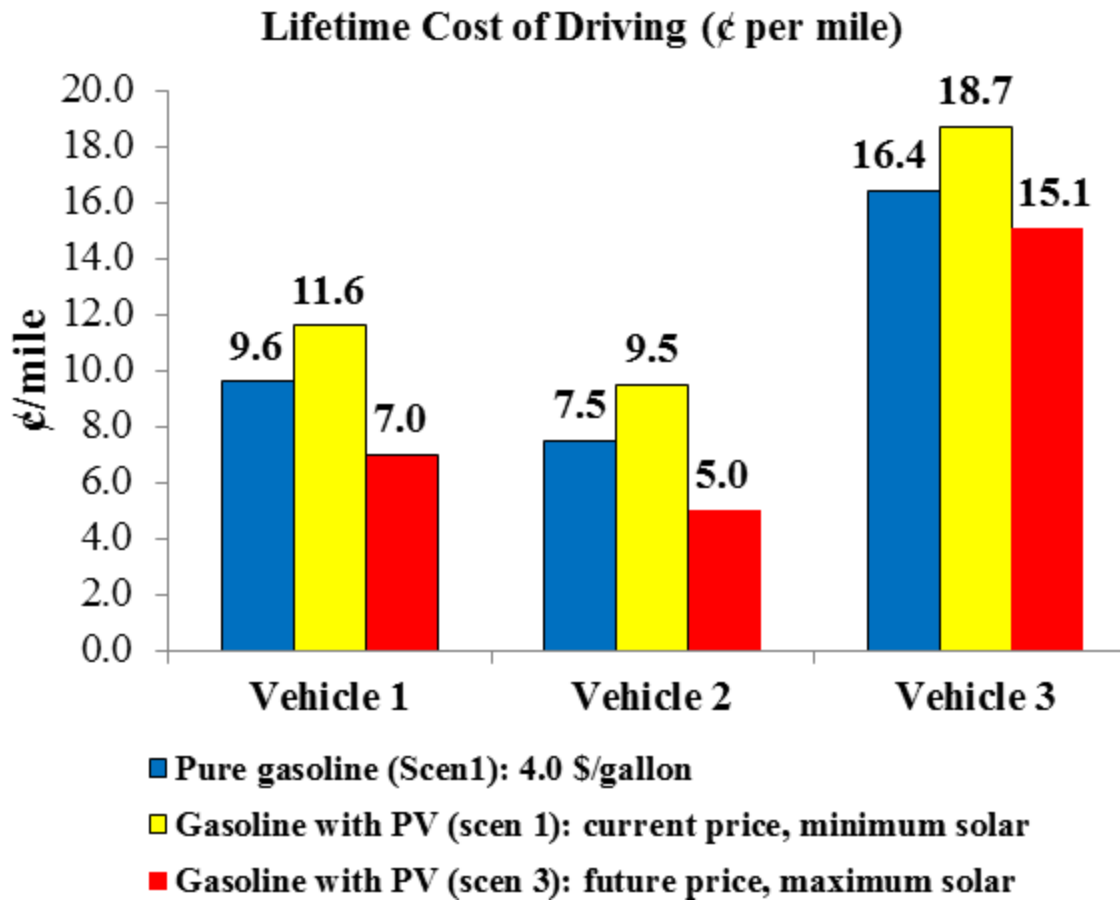


Figure 8. 16 Lifetime cost of driving (¢ per mile) for pure gasoline vehicle versus gasoline vehicle with PV [gasoline price 4 \$/gallon]

From Figure 8.16, the results showed that for the lifetime cost of gasoline vehicle with PV is better than pure gasoline only in the places there is plenty solar energy. This mean scenario 3 shows the biggest advantage in terms of reduction cost per mile for all

vehicles. For example, in using vehicle 2 the cost of driving after adding PV could be as low as 5 ¢ per mile around 33% lower than similar pure gasoline vehicle.

Figure 8.17 shows the estimated lifetime cost of driving (¢ per mile) of pure gasoline (the proposed scenario 2) and gasoline with PV (the proposed scenarios 2 and 4). All of these scenarios are proposed with current gasoline price in U.S. \$8.0 per gallon. In this case, the advantage in term of cost per mile of adding PV is much bigger. Future scenario (scenario 4) in plenty solar energy location shows that the lifetime cost per driving could be reduced by 40%, 52%, or 16 % for vehicle 1, 2, and 3, respectively.

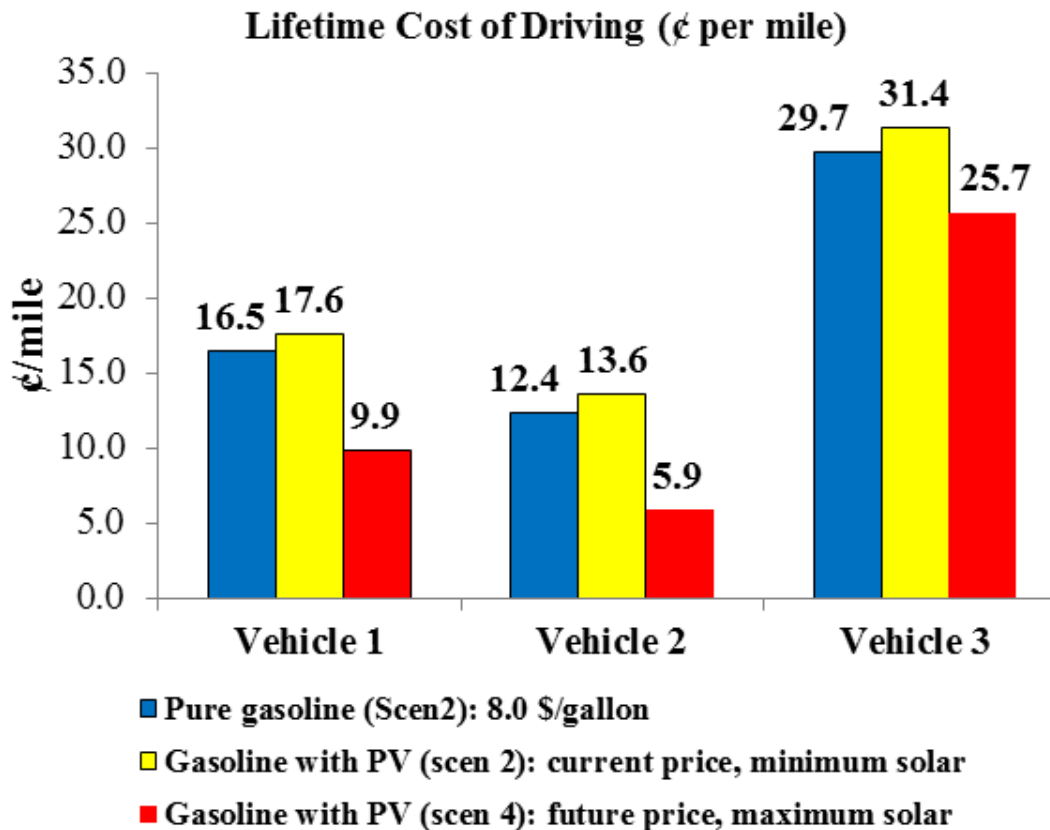


Figure 8. 17 Lifetime cost of driving (¢ per mile) for pure gasoline vehicle vs. gasoline vehicle with PV [gasoline price \$8/gallon]

8.7.3 Cost Analysis of Pure Plug-in EV vs. Plug-in EV with PV

In this section, the lifetime cost of a plug-in EV with and without PV is estimated for the similar vehicles used in section 8.7.2. The estimated electricity efficiency (Wh per mile) is 106, 77, and 300 for vehicle 1, vehicle 2, and vehicle 3, respectively.

For fair comparison, the estimated electric motor power is done with same 0-60 mph acceleration time used in the previous section. The battery sizes are assumed as 9.1 kWh, 6.6 kWh, and 25.7 kWh for vehicle 1, vehicle 2, and vehicle 3, respectively. The battery size is calculated based on the assumed driving range is equal 77 miles and 90% SOC. The electricity price is different from location to location, for that the three electricity prices are assumed around 18 ¢/kWh (California in July 2014), 13 ¢/kWh (Average U.S 2014), 35 ¢/kWh (Germany) [332], [333].

Table 8.9 shows the proposed scenarios for lifetime cost estimation of pure plug-in EV and plug-in EV with PV. Five different scenarios are proposed for pure plug-in EV, scenario 1 is based on current battery price with electricity price is low (13 ¢/kWh), scenario 2 is based on current battery price with electricity price is medium (18 ¢/kWh), while scenario 3 is based on current battery price with high electricity price (35 ¢/kWh). The scenarios 4 and 5 are based on future battery price with medium and high electricity prices, respectively.

In addition, six different scenarios are proposed for plug-in EV with PV as: scenario 1 is based on current prices of the battery and PV, with electricity price is low (13 ¢/kWh), operating in a low solar energy location (e.g., Boston, MA). scenario 2 is based on

current prices of the battery and PV, with electricity price is low (13 ¢/kWh), operating in high solar energy location (e.g., Phoenix, AZ). Scenario 3 is based on future prices of the battery and PV, with electricity price is medium (18 ¢/kWh), operating in a low solar energy location (e.g., Boston, MA). Scenario 4 is based on future prices of the battery and PV, with electricity price is medium (18 ¢/kWh), operating in a high solar energy location (e.g., Phoenix, AZ). Scenario 5 is based on future prices of the battery and PV, with electricity price is high (35 ¢/kWh), operating in a low solar energy location (e.g., Boston, MA). Finally, Scenario 6 is based on future prices of the battery and PV, with electricity price is high (35 ¢/kWh), operating in a high solar energy location (e.g., Phoenix, AZ).

Table 8. 9 Proposed scenarios of plug-in electric vehicle with and without PV

Vehicle	Scenario Description
Pure Plug-in EV vehicle	Scenario 1: current battery price, electricity price is low Scenario 2: current battery price, electricity price is medium Scenario 3: current battery price, electricity price is high Scenario 4: future battery price, electricity price is medium Scenario 5: future battery price, electricity price is high
Plug-in EV with PV	Scenario 1: current battery price, electricity price is low, high PV price, minimum solar range Scenario 2: current battery price, electricity price is low, high PV price, maximum solar range Scenario 3: future battery price, electricity price is medium, future PV price, minimum solar range Scenario 4: future battery price, electricity price is medium, future PV price, maximum solar range Scenario 5: future battery price, electricity price is high, future PV price, minimum solar range Scenario 6: future battery price, electricity price is high, future PV price, maximum solar range

Tables 8.10 shows the lifetime cost analysis of pure electric vehicles for the five different proposed scenarios.

Table 8. 10 Lifetime cost analysis for pure electric vehicles of different scenarios

Component	Vehicle 1	Vehicle 2	Vehicle 3	Note
Electric Motor (\$)	1597	1206	2421	Vehicle 1 (54 kW), vehicle 2 (36 kW), and vehicle 3 (92 kW)
Battery Current (\$)	6147	4907	14446	Vehicle 1 (9.1 kWh), vehicle 2 (6.6 kWh), and vehicle 3 (25.7 kWh)
Battery Future (\$)	2747	2436	4821	Vehicle 1 (9.1 kWh), vehicle 2 (6.6 kWh), and vehicle 3 (25.7 kWh)
Electricity: Low	2204.8	1601.6	6240	13 ¢/kWh
Electricity- Medium	3052.8	2217.6	8640	18 ¢/kWh
Electricity- High	5936	4312	16800	35 ¢/kWh
On-board Charger	500	500	500	
Maintenance	3,000	3,000	3,000	
Total lifetime cost (current price, electricity low) (Scenario 1)	13449	11215	26607	
¢/mile (current price, electricity low)/ (Scenario 1)	8.4	7.0	16.6	
Total lifetime cost (current price, electricity medium)/ (Scenario 2)	14297	11831	29007	
¢/mile (current price, electricity medium)/ (Scenario 2)	8.9	7.4	18.1	
Total lifetime cost (current price, electricity high)(Scenario 3)	17180	13925	37167	
¢/mile (current price, electricity high)/ (Scenario 3)	10.7	8.7	23.2	
Total lifetime cost (future price, electricity medium)/ (Scenario 4)	10897	9360	19382	
¢/mile (future price, electricity medium)/ (Scenario 4)	6.8	5.8	12.1	
Total lifetime cost (future price, electricity High)/ (Scenario 5)	13780	11454	27542	
¢/mile (future price, electricity High)/ (Scenario 5)	8.6	7.2	17.2	

Tables 8.11, 8.12, 8.13, 8.14, 8.15, and Table 8.16 summarize the lifetime cost analysis of plug-in electric vehicles with PV for scenario 1, scenario 2, scenario 3, scenario 4, scenario 5, and scenario 6.

Table 8. 11 Life cycle cost analysis of EV with PV (scenario 1)

Component	Vehicle 1	Vehicle 2	Vehicle 3	Note
PV Module (\$) -max	616	616	616	
Mounting (max)	100	100	100	
Battery (max)	6147	4907	14446	
Motor	1597	1206	2421	
Maintenance	3000	3000	3000	
Minimum solar: electricity low	1924.13	1320.8	5956.34	
On-board charging	500	500	500	
Lifetime cost (\$): (scenario 1)	13884	11650	27039	
Lifetime cost (¢/mile): (scenario 1)	8.7	7.3	16.9	

Table 8. 12 Life cycle cost analysis of EV with PV (scenario 2)

Component	Vehicle 1	Vehicle 2	Vehicle 3
PV Module (\$) -max	616	616	616
Mounting (max)	100	100	100
Battery (max)	6147	4907	14446
Motor	1597	1206	2421
Maintenance	3000	3000	3000
Minimum solar: electricity low	904.8	301.6	4943.38
On-board charging	500	500	500
Lifetime cost (\$): (Scenario 2)	12865	10631	26026
Lifetime cost (¢/mile): (Scenario 2)	8.0	6.6	16.3

Table 8. 13 Life cycle cost analysis of EV with PV (scenario 3)

Component	Vehicle 1	Vehicle 2	Vehicle 3
PV Module (\$) -min	357	357	357
Mounting - min	50	50	50
Battery -min	2747	2436	4821
Motor	1597	1206	2421
Maintenance	3000	3000	3000
Minimum solar: electricity medium	2664.18	1828.8	8247.24
On-board charging	500	500	500
Lifetime cost (\$):(Scenario 3)	10915	9378	19396
Lifetime cost (¢/mile): (Scenario 3)	6.8	5.9	12.1

Table 8. 14 Life cycle cost analysis of EV with PV (scenario 4)

Component	Vehicle 1	Vehicle 2	Vehicle 3
PV Module (\$) -min	357	357	357
Mounting - min	50	50	50
Battery -min	2747	2436	4821
Motor	1597	1206	2421
Maintenance	3000	3000	3000
Minumim solar: electircity medium	1252.8	417.6	6844.68
On-board charging	500	500	500
Lifetime cost (\$): (Scenario 4)	9504	7967	17994
Lifetime cost (¢/mile): (Scenario 4)	5.9	5.0	11.2

Table 8. 15 Life cycle cost analysis of EV with PV (scenario 5)

Component	Vehicle 1	Vehicle 2	Vehicle 3
PV Module (\$) -min	357	357	357
Mounting - min	50	50	50
Battery -min	2747	2436	4821
Motor	1597	1206	2421
Maintenance	3000	3000	3000
Minumim solar: electircity high	5180.35	3556	16036.3
On-board charging	500	500	500
Lifetime cost (\$): (Scenario 5)	13431	11105	27185
Lifetime cost (¢/mile): (Scenario 5)	8.4	6.9	17.0

Table 8. 16 Life cycle cost analysis of EV with PV (scenario 6)

Component	Vehicle 1	Vehicle 2	Vehicle 3
PV Module (\$) -min	357	357	357
Mounting - min	50	50	50
Battery -min	2747	2436	4821
Motor	1597	1206	2421
Maintenance	3000	3000	3000
Maximum solar: electricity high	2436	812	13309.1
On-board charging	500	500	500
Lifetime cost (\$): (Scenario 6)	10687	8361	24458
Lifetime cost (¢/mile): (Scenario 6)	6.7	5.2	15.3

Figure 8.18 shows the lifetime cost of driving of pure plug-in EV (Scenario 1) and plug-in EV with PV (Scenario 1 and 2). For all the electricity is assumed with low price

\$0.13/kWh. As shown, even with low electricity price, adding PV showed a positive impact from lifetime cost if the system is operating in high solar energy environment.

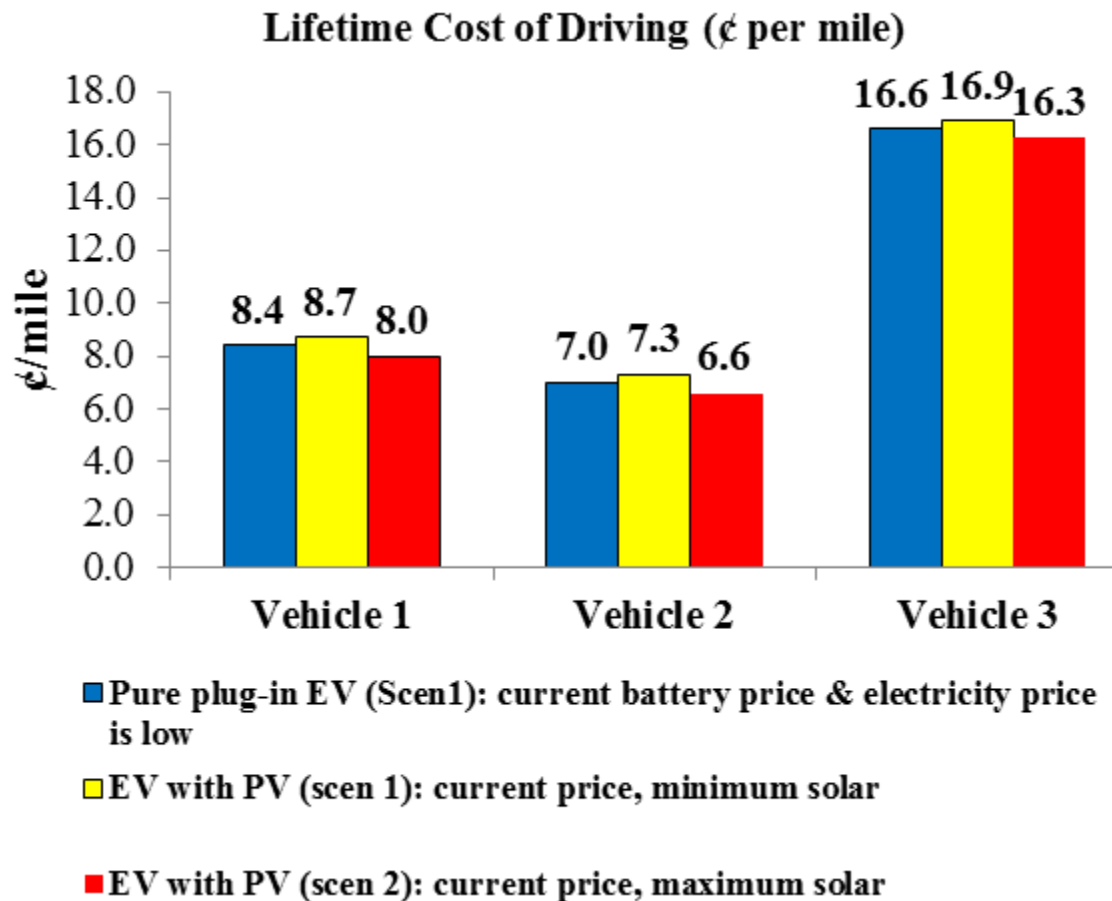


Figure 8. 18 Lifetime cost of driving (¢ per mile) of pure plug-in EV vs. plug-in EV with PV
 [Electricity price 0.13 \$/kWh]

Figure 8.19 shows the lifetime cost of driving of pure plug-in EV (Scenario 4) and plug-in EV with PV (Scenario 3 and 4). For all scenarios, the electricity price is assumed a medium price (\$0.18/kWh).

The results showed, in a medium electricity cost assumption even in low solar energy location, adding PV has a positive impact of lifetime cost.

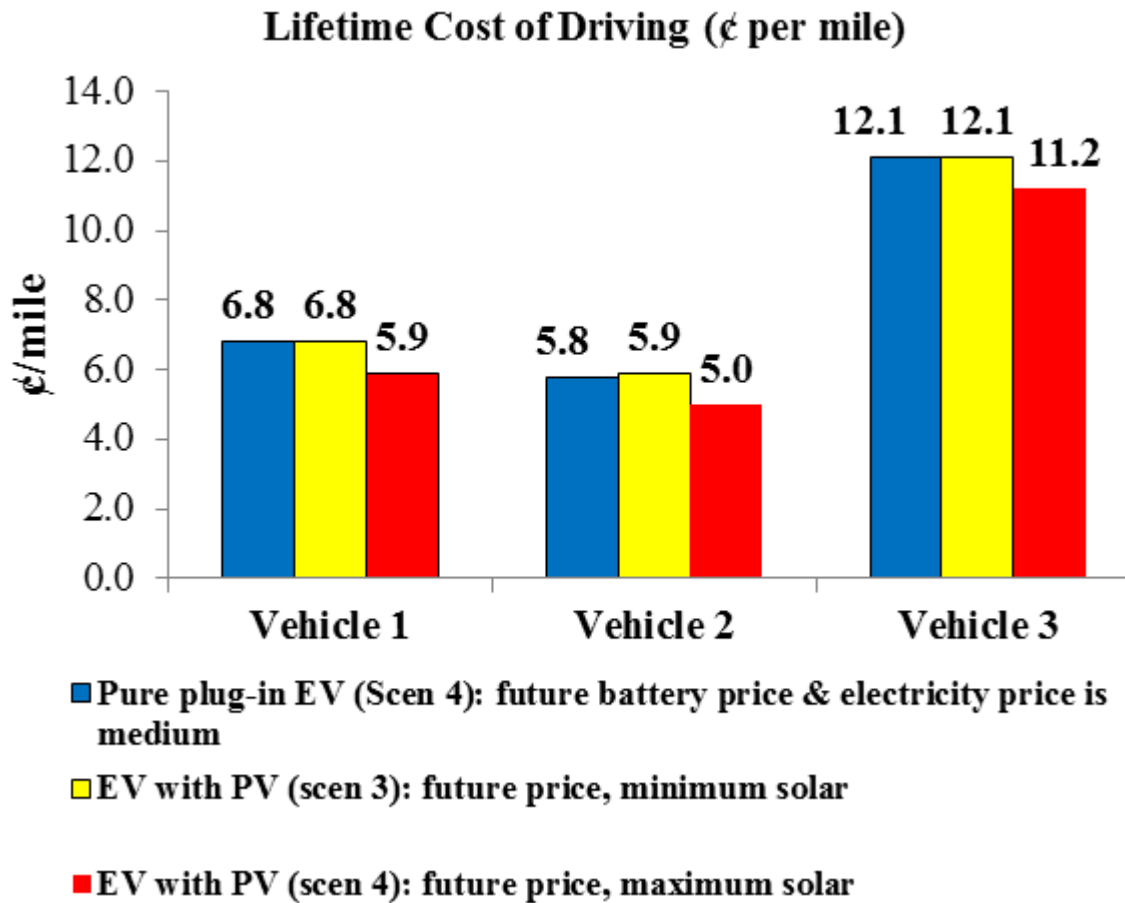


Figure 8. 19 Lifetime cost of driving (¢ per mile) for pure plug-in EV vs. plug-in EV with PV [Electricity price \$0.18/kWh]

Figure 8.20 shows the lifetime cost of driving of pure plug-in EV (Scenario 5) and plug-in EV with PV (Scenario 5 and 6). For all scenarios, the electricity price is assumed a high price (\$0.35/kWh). The results also showed a positive impact on cost for a low and a high solar energy region.

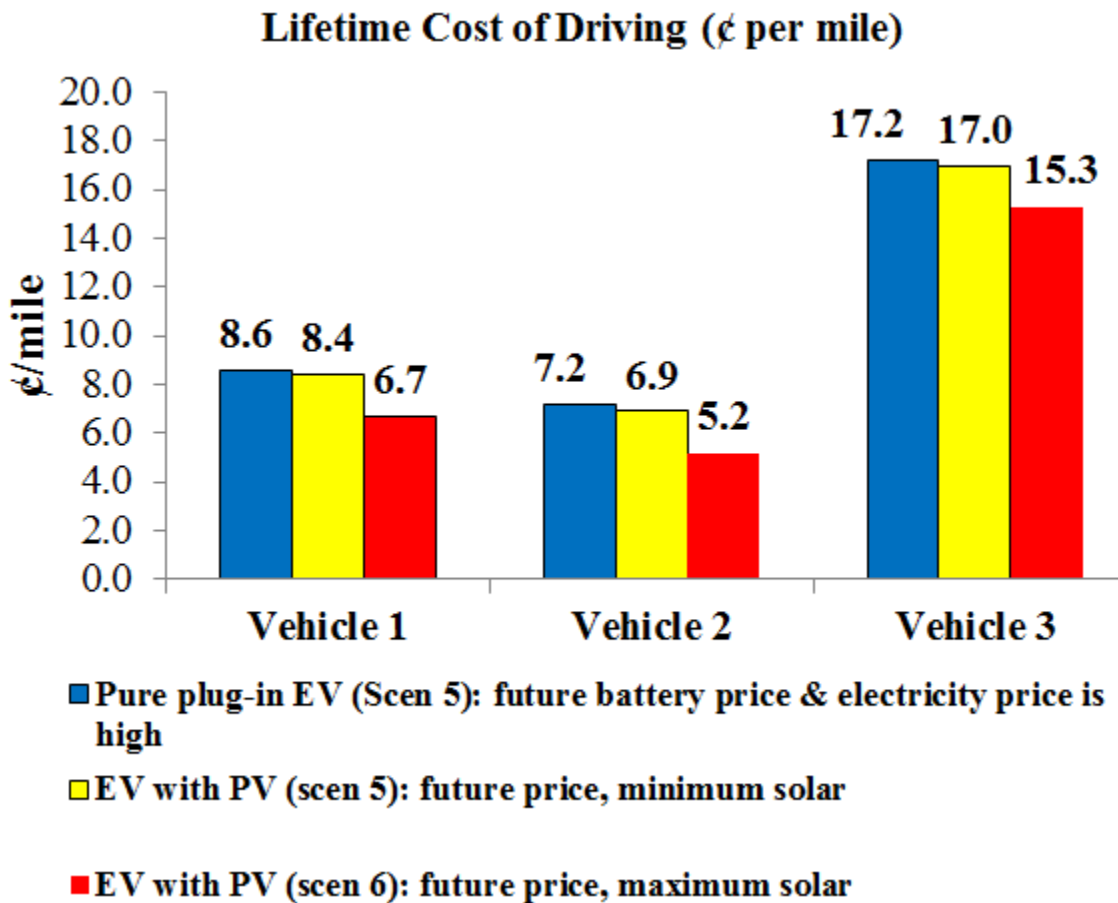


Figure 8. 20 Lifetime cost of driving (¢ per mile) for pure plug-in EV vs. plug-in EV with PV [Electricity price \$0.35/kWh]

Based on the above analysis, adding a PV on-board for plug-in EV have a positive impact of reducing lifetime cost per mile. For example, adding a PV for vehicle 3 (e.g., size Nissan Leaf or similar), the lifetime cost saving in the sunny-rich environment (e.g., Arizona) will be around \$1,440 given the current electricity price and the saving is around more than \$3,000 for high-electricity price scenario.

However, after the vehicle lifetime is ended, the PVs still have around 16 years of operating and can be plugged into different applications. This makes on-board more cost-effective solution, however this is not considered in the above analysis.

8.8 Comparison of On-board PV vs. Vehicle Lightweighting

The vehicle lightweighting aims to enhance fuel economy and reduce the emission to meet CAFE target. However, significant fuel economy improvements in terms of MPG will require large reductions in the vehicle weight. Previous studies have shown that 10% reduction in curb vehicle weight results in 6-8% improvement in fuel economy [334], [335]. The correlations (8.9) and (8.10) below have been proposed in the literature to relate fuel economy (MPG) with vehicle mass (curb weight in Lbs)

$$\text{MPG} = 895.24 \times (\text{mass})^{-0.463} \quad (8.9)$$

$$\text{MPG} = 8627.4 \times (\text{mass})^{-0.74584} \quad (8.10)$$

The results of Lightweighting in terms of emission per mile is investigated in in Figure 8.21 [336]. As shown in Figure 2.21, decrease the vehicle mass by 30% is equivalent to an 18 % to 24% CO₂ emission reduction. However, this emission is not reflected a well-to-tank analysis and only wheel to the mile.

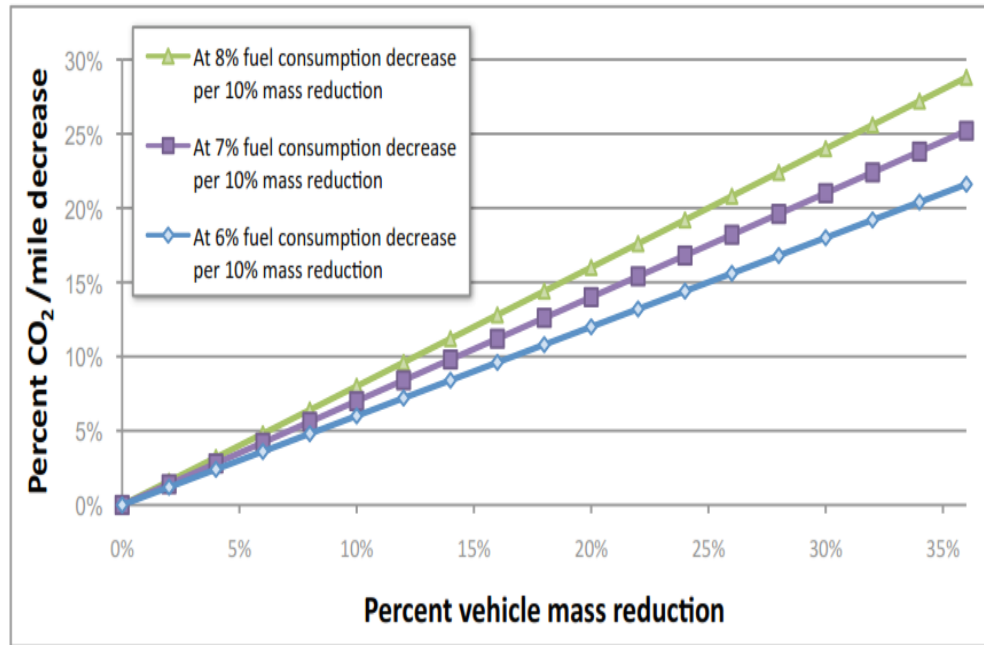


Figure 8. 21 Effect of mass-reduction technology on CO₂ emission rate for constant performance [336]

As discussed in previous sections, the author investigated how adding PV to the gasoline and EV vehicles will enhance fuel economy (MPG) and reduce CO₂ emission from well-to-mile perspective. In this study, vehicle 1 and vehicle 2 have similar specifications and the only differences are the curb weight. Vehicle 1 with 900 kg curb weight, while vehicle 2 with 600 kg curb weight. So vehicle 2 is lighter than vehicle 1 by 300 kg (33.3% mass reduction between the two vehicles).

Tables 8.17 shows the comparison between the lightweighting approach (Results of vehicle 2 compared to vehicle 1) versus adding PV on-board (Use vehicle 1 but added the proposed PV) for gasoline vehicle.

In terms of fuel economy, 33.3 % of mass reduction (lightweighting) enhances 40% of fuel economy, while only 7.55% to 27.3% fuel economy is increased by added PV for vehicle 1 at noon (no lightweighting).

On the other hand, the well-to- mile grams of CO₂-eq per mile with Lightweighting in reduced by 28.38%, while with added PV to vehicle 1 (no mass reduction) the emission is reduced from 12.14% to 57%, which is higher than lightweighting in some locations.

The life cycle CO₂-eq emission reduction with Lightweighting is around 8.98 metric tons, while with on-board PV is from 3.84 to 18.03 metric ton reduction.

Table 8. 17 Lightweighting approach vs. adding on-board PV (gasoline vehicle)

	Pure gasoline: Without PV /Lightweighting Differences: 300 kg	Gasoline vehicle with PV
Fuel Economy	Vehicle 1: 58 MPG Vehicle 2: 81 MPG Enhance MPG= 40% by reduced (33.3% mass reduction between vehicle 1 and vehicle 2)	Fuel economy of Vehicle 1 increase by 4.38 to 15.83 MPG at noon. Fuel economy of Vehicle 2 increase by 8.69 to 34.15 MPG at noon. Without mass reduction: vehicle 1 fuel economy increased from 7.55% to 27.3%
Well-to-tank grams of CO ₂ -eq per mile	Vehicle 1: 197.7 grams of CO ₂ -eq/mile Vehicle 2: 141.6 grams of CO ₂ -eq/mile Enhance CO ₂ -eq/mile by 28.38% by reduced (33.3% mass reduction between vehicle 1 and vehicle 2)	Vehicle 1 with PV emission is between 85 to 173.7 grams of CO ₂ -eq/mile Vehicle 2 with PV emission is between 30.6 to 117.9 grams of CO ₂ -eq/mile Without mass reduction: vehicle 1 well-to-tank CO ₂ emission reduced between 12.14% to 57%
Life cycle CO ₂ -eq emission reduction (160,000 miles)	8.976 metric tons of CO ₂ -eq reduction (lightweighting 33.3%)	Without mass reduction: vehicle 1 is reduced by 3.84 to 18.03 metric tons

Tables 8.18 shows the comparison between the lightweighting approach (Results of vehicle 2 compared to vehicle 1) and adding a PV on-board (Use vehicle 1 but added proposed PV) for plug-in electric vehicle. After adding on-board PV, the life cycle emission using U.S. Grid is reduced by 11.24% to 54.0% (without mass reduction), while it reduced by around 26.77% with lightweighting.

However, if the India grid is used, the advantage of adding PV versus Lightweighting in terms of life cycle emission is significant. Since, the life cycle CO₂ emission is reduced by 32.46% by added PV compared to 26.82% with Lightweighting.

Table 8. 18 Lightweighting approaches Versus adding on-board PV (electric vehicle)

	Pure plug-in EV: Without PV /Lightweighting Differences: 300 kg	Plug-in EV with PV
Well-to-tank grams of CO ₂ -eq per mile U.S. (Grid)	Vehicle 1: 79.2 grams of CO ₂ -eq/mile Vehicle 2: 58.0 grams of CO ₂ -eq/mile Enhance CO ₂ -eq/mile by 26.77% by reduced (33.3% mass reduction between vehicle 1 and vehicle 2)	Vehicle 1 with PV emission is between 36.4 to 70.3 grams of CO ₂ -eq/mile Vehicle 2 with PV emission is between 49.0 to 14.8 grams of CO ₂ -eq/mile Without mass reduction: vehicle 1 well-to-tank CO ₂ emission reduced between 11.24 % to 54.0 %
Well-to-tank grams of CO ₂ -eq per mile India (Grid)	Vehicle 1: 156.2 grams of CO ₂ -eq/mile Vehicle 2: 114.3 grams of CO ₂ -eq/mile Enhance CO ₂ -eq/mile by 26.82% by reduced (33.3% mass reduction between vehicle 1 and vehicle 2)	Vehicle 1 with PV emission is 105.5 grams of CO ₂ -eq/mile Vehicle 2 with PV emission is 63.2 grams of CO ₂ -eq/mile Without mass reduction: vehicle 1 well-to-tank CO ₂ emission reduced by 32.46%

8.9 Challenges of Vehicle Design with On-board PV

Some of the design issues are discussed previously to optimize energy from sun to the wheels as surface area, mounting, orientations, etc. Here, the weight issue of incorporating PV on-board for gasoline vehicle is investigated. The engine mass scaling and battery mass scaling are based on Equations (8.11) and (8.12) [337].

$$\text{Engine mass} = 0.47 \times \text{Engine Power} + 61 \quad (8.11)$$

$$\text{Lithium battery mass} = 8.5 \times \text{Battery Energy} + 58 \quad (8.12)$$

Where, engine mass and battery mass are in (kg), engine power in (kW), and battery energy in (kwh).

The electric motor is assumed similar to the one used in Stella solar [338]. Table 8.19 shows the weight analysis for adding PV to a gasoline vehicle. In Table 8.19, the current and future scenarios showed that there is extra weight around 86 kg or 23 kg, respectively. The extra weight of Powertrain component should be balanced by removing some other components in the vehicle to keep the curb weight constant.

Table 8. 19 Weight analysis by added PV on-board to gasoline vehicle

Component	Quantity	Weight (kg): current	Weight (kg): Future
PV Module	3.26 m ²	37	25 (Estimated)
Mounting		4	3
Battery	5 kWh	100	50
Electric motor	10 kW	11	11
Total (Add weight)		+152	+89
Remove weight from the engine	10 kW	-66	-66
Powertrain weight will increase by:		~ Extra 86 kg	~ Extra 23 kg

8.10 Summary

This chapter integrated the results from all previous chapters and presented the novel results. First, the analyses of adding PV on-board to enhance fuel economy (MPG) toward CAFE 2025 are represented for five different proposed vehicles. Next, the pure daily solar ranges for 11 proposed vehicles are estimated. Then, the author estimated how green is pure solar vehicle for four assumed vehicles in 12 different U.S. states. Next, the

well to wheel life cycle emission reduction by adding on-board PV for gasoline vehicle in the U.S., plug-in vehicles in the U.S., and plug-in vehicle in India are estimated. Subsequently, the cost analysis by adding PV for both gasoline and electric vehicles are discussed. The economic analyses are done for current and future scenarios, where 19 different cost scenarios are investigated. Then, the comparisons of adding on-board PV versus Lightweighting approach are assessed in terms of fuel emission reduction and enhance fuel economy. Finally, some challenges (e.g., weight) for adding a PV on-board to the existing gasoline vehicle are discussed.

CHAPTER NINE

CONCLUSION

9.1 Conclusion

This dissertation presented a novel comprehensive assessment methodology of on-board photovoltaic (PV) solar technologies in vehicle applications. This work provided a greater understanding of the usefulness and the challenges inherent in using on-board PV solar technologies for automotive applications based on life cycle (well-to-wheels) analysis from a unique energy, environmental, and economic perspective.

In this work, more than 25 PV types screened, 10 Inspection techniques are reviewed, and more than 200 LCA studies screened. In addition, more than 14 different vehicles are analyzed with two Powertrain configurations; pure gasoline and pure plug-in electric vehicles. The proposed assessment methodology includes 3 different travel patterns in 12 U.S. states and 16 countries covering 19 different cost analysis scenarios for current and future prices.

First, a comprehensive assessment study between different PV solar technologies is performed to develop a quantitative and qualitative analysis of different PV module options for on-board vehicle application. Then, two decisions-support systems are proposed to evaluate and select the optimal PV module type for this application by reconciling the conflicting objectives and multi-attribute restraints to solve the problem. The first approach involves a combination of quality function deployment (QFD) and an

analytical hierarchy process (AHP) and the second approach entails the use of a fuzzy axiomatic design. By using this two proposed approaches, a unique application for the proposed support systems is created and a unique method for benchmarking both approaches that compose this transformative application is proposed. The results showed that for on-board vehicle applications, the most suitable PV module option is Monocrystalline Silicon and the least suitable is Cadmium Telluride.

Second, for the optimum selected PV type, crystalline silicon modules, the main defects caused from manufacturing to installation stages are reviewed. Specifically, these are the micro-crack defects that occur in wafer, cell, and module levels, which greatly decrease the field-reliability and performance of the PV module. The non-destructive techniques, which have been used in detecting the micro crack defect, are intensively reviewed and analyzed. Then, this analysis is used to develop a novel decision-support system based on analytical hierarchy process (AHP) to evaluate the suitability of different non-destructive testing systems for use in an automated PV production line. The results showed that the micro-crack detection system based upon the photoluminescence (PL) imaging system was superior to all others and ideally suited for automated PV production lines.

Third, the PV module structure and the efficiency loss mechanisms are discussed for purposes of modeling the entire PV system for on-board vehicle application. Then, a comprehensive PV system model is developed for on-board vehicle application. The proposed model is optimized for the optimum solar energy-to-direct current (DC) electrical power ratio. This modeling entails analyzing the geographical solar location,

thermal performance, MPPT algorithm, energy storage, tilt option, shadow and sky clearness, angling on the vehicle surface, mounting configuration, and tracking options. The results of the dynamic model, which can reflect the various PV module areas, efficiencies, installation locations, times, and weather are applicable both nationwide and year-round.

Fourth, the vehicle model with on-board PVs is developed to determine the energy required for the vehicle wheels (tank-to-wheel analysis). Many commercial electric vehicles and solar vehicles are used for benchmark issue. Then, the required energy at vehicle' wheel is modelled for different driving cycles and conducted a sensitivity analysis of the main parameters. Then both 2020 and 2025 CAFE standard curves are uniquely related to the projected horizontal vehicle surface area to estimate the maximum possible PV installation area for each CAFE target. Finally, the three assumed driving pattern scenarios are discussed.

Fifth, a life cycle assessment (LCA) model is developed for cradle-to-gate analysis. The historical and current PV production and installation data are presented, followed by a definition of the methodology of current LCA study to follow both international organization for standardization (ISO) and international energy agency (IEA) guidelines. Then, the boundary of the system is defined to include the five top commercial PV module types (mono-Si, multi-Si, a-Si, CdTe, and CIGS) using the raw material until the system is installed and generating electricity.

The proposed LCA model is developed that included both emission in terms of equivalent CO₂ and embodied energy. Then, the proposed LCA selection criteria are

created for evaluating and selecting the most reliable and recent LCA studies in literature. After screening more than 200 LCA studies, we then the passed LCA data related to five main PV types and balance of system are summarized. The results showed that the GHG emission released and the embodied energy consumed from manufacturing crystalline PV module types was the highest, with the a-Si and CdTe modules the lowest. However, there is a huge window of improvement for crystalline silicon modules by the new manufacturing techniques and thickness reduction trends in crystalline silicon modules.

Next, unique estimation of the PV performance ratio (PR) for the current application is proposed, which showed the PR for this application is higher than ground-mounted and roof-mounted applications, since the system using DC electricity eliminated inverter losses. In addition, the results showed that PR is greater in Boston, MA compared to Phoenix, AZ due to an increase loss with a corresponding increase in ambient temperature. Therefore, PR has an inverse relationship to ambient temperature.

Then, the lifetime PV generated energy is calculated and analyzed in 12 U.S. states and 16 different countries. The results showed that the estimated lifetime energy of 3.2 m² generated by the proposed PV module in Phoenix, AZ was 34 MWh, the equivalent of what an average US residence consumed in a three year period. Moreover, the energy generated from the same system in New Delhi, India was 30.4 MWh, the equivalent of what an average Indian residence consumed over a 33 year period.

In addition, the results showed that in most US states the lifetime PV energy generated from the proposed PV system is higher than most of the selected countries in the world. For example, the lifetime energy generated in Phoenix, AZ was 103%, 112%,

and 146% greater than Johannesburg-South Africa, New Delhi-India, and Beijing-China, respectively. In addition, the lifetime energy generated in Seattle, Washington is 120%, 113%, 108%, 113% higher than London-UK, Paris-France, Munich-Germany, and Tokyo-Japan, respectively. However, until now PVs have been mostly manufactured in China, Japan, and Europe and used mostly in Europe, especially Germany, but there is a substantive availability of solar power in the US, which should be the next large market.

Next, an LCA model for analyzing the use of gas and grid electricity is presented. Then, the estimation of LCA emission via the use of PV in lieu of the conventional grid is presented in many countries. The results showed greater reduction in the use of the PV over a conventional grid for most of the countries in this study. For example, the life cycle emissions could be reduced 18 times and 14 times in New Delhi-India and Beijing-China, respectively. However, the results showed the opposite to be true in Reykjavik, Iceland and Paris, France. Specifically, in Reykjavik, Iceland, the results showed that the conventional grid emits 27.5 g of CO₂-eq, which is the equivalent to the consumption of 1 kWh energy. Generating this level of energy using the proposed PV system will yield a higher LCA g CO₂-eq emission of approximately 162.1. The reasons that these countries are using renewable sources to generate electricity at the grid and there is a low solar energy in these places. However, the context here is the comparison is done in regards emission only, but for complete comparison, another factors should be included as water consumptions, land, etc. Finally, the challenges and limitations of current LCA studies are discussed, and the proposed recommendation of uncertainty analysis.

Six, the proposed comprehensive methodology, which includes tank-to-wheel and wheel-to-mile analysis are presented. Next, the maximum contribution of on-board PV for enhancing fuel economy in the driving cycle for different travel patterns and for five different vehicle sizes are presented. The results showed that an increase in combined MPG at noon in a vehicle similar to Tesla 2013 S was between 2.9% to 9.5%, while there was a very significant increase for lightweight and aerodynamic efficient vehicles, with a range of 10.7% to 42.2%. The ranges depend on location and time in a year. The short duration of the driving cycle, as little as 0.38 hours in the city cycle and 0.2125 hours on the highway cycle made a comparison of the hours in a day where solar energy is available difficult, however.

Next, the estimation of the pure PV solar range (PV range extender) for 11 vehicle types are presented, the results showed that the addition of an on-board PV to cover less than 50% (3.2 m^2) of the projected horizontal surface area of a typical vehicle, was effective in extending the pure solar PV ranges to 50% of the total daily drive time by a person in the U.S. of a mid-size vehicle. In addition, if the lightweight and aerodynamically efficient vehicle combined with the proposed PVs could increase up to 174% of the total person miles of travel per day in the U.S. could be driven by solar energy.

The results showed that the daily driving range could be extended from 3.0 miles to 62.5 miles based on vehicle specifications, locations, and time. For example, the addition of the proposed PV module to very lightweight and aerodynamically efficient vehicles could extend the daily range between 13.5 miles to 62.5 miles. In specific tests

of vehicle similar to the BMW i3 2014, the range was extended to 3.8 miles as a minimum to 17.8 miles (maximum), and in similar tests with the heavier vehicle similar to Tesla Model S 2013, a totally solar powered PV extended the driving range between 3 to 13.7 miles.

Next, the model estimated how green is a pure solar vehicle from well-to-mile analysis (in terms of g CO₂-eq per mile) in 12 U.S. states and 4 different vehicles. For very lightweight and efficient vehicle, mostly in the U.S., the emissions (CO₂-eq) per driven mile were estimated between 4.8 and 8.0 depending on the location. However, for vehicles with similar specifications such as the Nissan Leaf 2014 or Mitsubishi i-MiEV 2014, the estimated pure solar driven range fell between 3.5 to 16.0 miles with LCA emissions between 18.6 to 31.3 g CO₂ -eq per mile. For vehicles similar to the Tesla S 2013, the estimated pure driving ranges were between 3 to 13.7 miles with 24.7 to 36.5 CO₂-eq per mile.

Then, estimated the reduction in LCA CO₂-eq lifetime emission by adding the proposed PV into a gasoline vehicle for comparison with a total gas powered vehicle for four base vehicle is presented. The results showed, for vehicles similar to Volkswagen XL1 2015, the estimated reductions in vehicle lifetime were between 4 to 18 metric tons, and between 2.59 to 13 metric tons of CO₂-eq for vehicles similar to the Nissan Leaf 2012 and Tesla 2013 S. Based upon these results, the addition of the proposed PV system with a gasoline vehicle in the U.S. will result in a reduction of between 3 to 18 metric tons of CO₂-eq in vehicle lifetime or the equivalent emissions from an average U.S. residence over a three-month to 20-month period.

The same vehicles and same PV used with plug-in electric powertrain configuration will yield a reduction in the estimated lifetime emission of between 1.4 to 7.0 metric tons of CO₂-eq for the average U.S. mix grid. If the same vehicles are operating in India-New Delhi, the estimated emission reduction is higher which approximates 8.0 metric tons in vehicle lifetime. Since, the grid emission per kWh in India is higher.

The LCA well-to-mile results showed that pure plug-in electric vehicles do not always yield lower GHG emissions per mile compared to a similar gasoline powered vehicles since they are not autonomous (i.e. They require an external electrical power source). The result showed that each mile driven by plug-in electric vehicle in India emits about 36 g CO₂-eq and 42 g CO₂-eq greater than similar gasoline vehicle in the U.S. for similar vehicle to Nissan Leaf 2012 and Tesla 2013 S, respectively.

Later on, the proposed cost analysis of more than 19 scenarios of both gasoline and electric vehicles using PVs is discussed. The results showed, the lifetime driving cost (\$ per mile) of a gasoline vehicle compared to a gasoline vehicle with PV, was lower in regions with more sunlight (e.g., Arizona) even if the price of gas was \$4.0 per gallon, because of the assumption that battery cost will decline eventually. As an example, the lifetime driving cost for vehicles like the Volkswagen-XL 2015 and Nissan Leaf 2012 was lower by 27 % and 8%, respectively.

A comparison of the lifetime driving cost (\$ per mile) of a pure plug-in EV versus a plug-in EV with PV was at least similar (mostly lower), even in regions with less sunlight (e.g., Boston) with the assumption is the electricity price is at least 0.18 \$/kWh.

In places with low electricity prices (0.13 \$/kWh), and with more sunlight the costs of operating an EV with PV were naturally lower, however.

The PV modules did, however outlive their vehicle hosts, however, having nearly 16 years of operation left for use in different applications. Although this indicates the addition of the PV to the vehicle a value added alternative, we did not consider this criterion in this study.

Then, a unique comparison between on-board PV solutions versus vehicle Lightweighting is discussed. Although the comparison of on-board PV solutions and vehicle lightweighting found that on-board PV did result in less emission in terms of fuel cycle-well-to-mile per vehicle lifetime, lightweighting does yield better fuel economy. The results showed 33% reduction of vehicle curb weight in gasoline vehicle enhanced the fuel economy in terms of combined MPG by around 40%, while without weight reduction, the proposed on-board PV (3.26 m²) increased the combined MPG between 7.55% to 27.3% depending upon the location and weather. The CO₂-eq life cycle emission did decrease by 9 metric tons if with a 33.3% mass reduction of the vehicle. The lack of mass reduction and the addition of the PV reduced emissions from 3.84 to 18 metric tons per vehicle lifetime.

The analyses for plug-in EV also found that when the EV mass was reduced by 33%, the well-to-tank CO₂-eq/mile emission also dropped by 26.8%, and the addition of a PV without mass reduction still reduced the well-to-tank CO₂-eq emission per mile between 11.24% to 54%. Both of these scenarios however, depended upon their location in the U.S. However, if the same scenarios are repeated in India, the well-to-wheels CO₂-

eq emission per mile was reduced by 26.8% (using lightweighting) as compared to 32.5% (using only PV). Finally, the challenges in the design are discussed.

9.2 Contribution

A novel comprehensive assessment methodology based on well-to-wheel life cycle analysis is proposed for using on-board photovoltaic (PV) solar technologies in vehicles. The proposed work provided a greater understanding of the usefulness and the challenges inherent in using on-board PV technologies for automotive applications based on a unique energy, environmental, and economic perspective.

This work is developed two decisions-support systems for selecting and evaluating the most appropriate PV module option for vehicle applications, which is currently unavailable.

This research is among the first few researchers to study and review the occurrence of defects (mainly micro-cracks) and its inspection techniques in PV technology. It is also novel in that a unique decision-support system is proposed for selecting and evaluating the best micro-crack non-destructive system for use in an automated PV production line to increase the reliability and the efficiency of PV modules, as well as reducing their manufacturing cost.

The proposed PV system model for on-board vehicle applications is a novel in three respects: First, a comprehensive PV system model for on-board vehicle application is proposed and is optimized the solar energy to the DC electrical power output ratio. Through which the study investigated how well the model functions by studying it's

geographical solar location, thermal performance, the use of the MPPT algorithm, energy storage, the tilt option, the effect of weather, the angle on the vehicle surface, the mounting configuration, the installation area, and the tracking option.

Second, predicted the actual contribution of the on-board PV in reducing fuel consumption, particularly in meeting corporate average fuel economy (CAFE) standards in different scenarios, and for estimating how well on-board PVs extend the vehicle range. The study will be useful in elucidating the applicability and effective use of on-board PV modules in individual automobiles. Third, developed a well-to-wheels LCA model for this application. This enables a comprehensive assessment of the effectiveness of an on-board PV vehicle application from energy consumption, greenhouse gas (GHG) emission, and economic life-cycle perspective.

The significance of the study is the first study to do a comprehensive analysis of using the solar energy on-board to enhance automotive fuel economies to meet CAFE standards and reduce energy consumption. The study develops a tool for decision-makers to use during the conceptual design stage, since its results are capable of reflecting the changes in fuel consumption, greenhouse gas emission, and cost for different locations, technological, and vehicle sizes. Finally, the study provides a reference framework for future research on other Powertrain configurations and different energy paths and facilitates the deployment of a sustainable transportation system.

9.3 Limitation and Future Works

Although the available life cycle inventory data used in this study did not represent the top PV manufacturing countries, the proposed analysis does propose valid selection criteria for the published LCA studies to collect the most recent and reliable data. The LCA data limitation and data uncertainty are discussed in detail in section 7.10.

This research presented a series of design requirements and promising results for the implementation of on-board PV in automobiles. This work also optimized the solar energy to the DC electrical power ratio for this application. However, there is a need to go to the product level and implement this proposed system for a specific vehicle under a specific scenario. For example, there is a need to implement sophisticated control strategy for specific vehicles to optimize the use of available solar energy. This includes maximizing the use of solar energy directly to the wheels and eliminates the energy stored in battery to eliminate any losses in the battery (e.g., charging efficiency and discharging efficiency). The engine operating points, battery SOC, and driving patterns must also be considered.

In addition, when a vehicle is parked, if there is no window to store the DC electricity in the on-board battery, the extra energy can be returned to the grid (e.g., vehicle to grid integration). This makes the rule of automobile is a multi-purpose not only use for driving, but also serve as a flexible energy generation system that can be fed into the grid and used to power electrical devices in homes and offices.

In addition, this work discussed the main defects in PV from manufacturing to installation stages, which may lead to decrease the PV efficiency and reliability in the field (e.g., vehicle application) and suggested the best non-destructive system to eliminate this error from the initial steps. However, there is a need to test the reliability and integrity of on-board PV modules for vehicle application to improve the on-road safety. Other issues the effects of road vibration on the reliability and the performance of the PV module are still other areas for research.

REFERENCES

- [1] 2009 National Household Travel Survey (NHTS), [Online]
<http://nhts.ornl.gov/2009/pub/stt.pdf> , 2011.
- [2] United States Energy Flow Trends in 2013, Lawrence Livermore National Lab,
[Online]https://flowcharts.llnl.gov/content/energy/energy_archive/energy_flow_2013/2013USEnergy.png
- [3] United States Carbon Emission in 2013, Lawrence Livermore National Lab, [Online]
https://flowcharts.llnl.gov/content/carbon/carbon_emissions_2013/2013USCarbon.png
- [4] CAFE (MPG) Standard Curves for Passenger Cars, [Online]
<http://www.nhtsa.gov/fuel-economy>
- [5] CAFE Fines NHTSA, (April, 2013), [Online],
www.nhtsa.gov/staticfiles/rulemaking/pdf/cale/cale_fines-040913.pdf
- [6] G. Rizzo. (2013, Dec. 01). Automotive Applications of Solar Energy. [Online].
Available:http://www.dimec.unisa.it/leonardo_new/documents/Survey_Paper_AAC10_GRizzo.pdf
- [7] Zap Electric Cars. (2013, Dec. 01). [Online]. Available:
<http://www.roperld.com/science/zapelectriccars.htm>
- [8] STELLA. (2014, May. 30). [Online]. Available:
<http://www.solarteameindhoven.nl/en/pages/#!/car>
- [9] Solar powered truck. (2014, May. 30). [Online]. Available: <http://solarenergy-usa.com/2013/12/solar-powered-trucks-coming-in-2014/>
- [10] A. Yoji, "History of Quality Function Deployment in Japan," The Best on Quality, IAQ Book Series Vol. 3. pp. 183-196. International Academy for Quality, 1990.

- [11] T. L. Saaty, "How to make a decision: the analytic hierarchy process," *European Journal Operational Research*, vol. 48, no. 1, pp. 9–26, 1990.
- [12] E. W. Stein, "A comprehensive multi-criteria model to rank electric energy production technologies," *Renewable and Sustainable Energy Reviews*, vol. 22, pp. 640-654, 2013.
- [13] V. Chandrasekhar, M. Marthuvanan, M. M. Ramkumar, R. Shriram, V.M. Manickavasagam, and B.V. Ramnath, "MCDM approach for selecting suitable solar tracking system," *Intelligent Systems and Control (ISCO)*, 2013 7th International Conference on , pp. 148-152, 4-5 Jan. 2013.
- [14] F. Ahammed, A. Azeem, "Selection of the most appropriate package of Solar Home System using Analytic Hierarchy Process model in rural areas of Bangladesh", *Renewable Energy*, Vol. 55, pp. 6-11, 2013.
- [15] P. Aragonés-Beltrán, F. Chaparro-González , J. Pastor-Ferrando ,and A. Pla-Rubio, "An AHP (Analytic Hierarchy Process)/ANP (Analytic Network Process)-based multicriteria decision approach for the selection of solar-thermal power plant investment projects", *Energy*, 2014.
- [16] D.P. Bernardon, A.P.C. Mello, L.L. Pfitscher, L.N. Canha, A.R. Abaide, A.A.B. Ferreira, "Real-time reconfiguration of distribution network with distributed generation", *Electric Power Systems Research*, Vol. 107, pp. 59-67, 2014.
- [17] D. Scannapieco, V. Naddeo, V. Belgiorno, "Sustainable power plants: A support tool for the analysis of alternatives", *Land Use Policy*, Vol. 36, pp. 478-484, 2014.
- [18] M. Abdelhamid, R. Singh, M. Omar, "Review of Microcrack Detection Technique for Silicon Solar Cells", *Photovoltaics, IEEE Journal of*, Vol. 4, No. 1, pp. 514-524, 2014.
- [19] J. A. Carnevalli and P. C. Miguel, "Review, analysis and classification of the literature on QFD—Types of research, difficulties and benefits", *International Journal of Production Economics*, Vol. 114, no. 2, pp. 737-754, 2008

- [20] W. Ho," Integrated analytic hierarchy process and its applications – A literature review", European Journal of Operational Research, Vol. 186, no. 1, pp. 211-228, 2008
- [21] A. Mayyas , Q. Shen , A. Mayyas , M. Abdelhamid , D. Shan , A. Qattawi, and M. Omar," Using Quality Function Deployment and Analytical Hierarchy Process for material selection of Body-In-White," Materials and Design, Vol. 32, pp. 2771–2782, 2011.
- [22] A. Qattawi, A. Mayyas, M. Abdelhamid, and M. Omar," Incorporating quality function deployment and analytical hierarchy process in a knowledge-based system for automotive production line design," International Journal of Computer Integrated Manufacturing, 2013.
- [23] D. Bouyssou, T. Marchant, M. Pirlot, P. Perny, A. Tsoukias, P. Vincke, "Evaluation and decision models: a critical perspective", Kluwer Academic Publishers, Dordrecht (2000)]
- [24] M. A. Green, K. Emery, Y. Hishikawa, W. Warta, and E. D. Dunlop," Solar cell efficiency tables (version 43)", Prog. Photovolt: Res. Appl., Vol. 22, pp. 1–9, 2014.
- [25] Mehta, S. (2014, April 23). GTM Research April 2014 PV Pulse. [Online]. Available: <http://www.greentechmedia.com/articles/read/Global-2013-PV-Module-Production-Hits-39.8-GW-Yingli-Leads-in-Production-a>
- [26] R. Singh and J. D. Leslie, "Economic requirements for new materials for solar photovoltaic cells," Solar Energy, vol. 24, pp. 589-592, 1980.
- [27] R. Singh, "Why Silicon is and Will Remain the Dominant Photovoltaic Material," Journal of Nanophotonics., vol. 3, 032503, 16 July 2009.
- [28] R. Singh, G. F. Alapatt, and M. Abdelhamid, "Green energy conversion & storage for solving India's energy problem through innovation in ultra large scale manufacturing and advanced research of solid state devices and systems," Emerging Electronics (ICEE), 2012 International Conference on , vol., no., pp. 1-8, 15-17 Dec. 2012. doi: 10.1109/ICEmElec.2012.6636220

[29] R. Singh, N. Gupta, and K.F. Poole, “Global green energy conversion revolution in 21st century through solid state devices”, Proc. 26th International Conference on Microelectronics, Nis, Serbia, May 11-14, 2008, vol. 1, pp. 45-54, IEEE, New York, NY.

[30] R. Singh, G. F. Alapatt, and A. Lakhtakia,” Making Solar Cells a Reality in Every Home: Opportunities and Challenges for Photovoltaic Device Design,” Electron Devices Society, IEEE Journal of the, Vol. 1, no. 6, pp. 129-144, 2013.

[31]C. H. Peters, I. T. Sachs-Quintana, J. P. Kastrop, S. Beaupr’e, M. Leclerc, M. D. McGehee,” High efficiency polymer solar cells with long operating lifetimes”, Adv. Energy Mater, Vol. 1, no. 4, pp. 491–494, 2011.

[32]R. Lakhani, D. Ganesh D., and B. Joule,” Internalizing land use impacts for life cycle cost analysis of energy systems: A case of California’s photovoltaic implementation,” Applied Energy, vol. 116, pp. 253-259, 2014.

[33] Solar PV Snapshot (2014, May 28). [Online]. Available:
<http://pvinsights.com/index.php>

[34] V. Fthenakis, R. Frischknecht, M. Raugei, H. C. Kim, E. Alsema, M. Held and M. de Wild-Scholten, 2011, Methodology Guidelines on Life Cycle Assessment of Photovoltaic Electricity, 2nd edition, IEA PVPS Task 12, International Energy Agency Photovoltaic Power systems Programme

[35] Saurat, M., and Ritthoff, M. Photovoltaics and the RoHS Directive,” Position Paper, Wuppertal Institute (2014, July 29) [Online]. Available:
http://engineering2.dartmouth.edu/~cushman/courses/engs171/SauratRittoff-Photovoltaics_and_RoHS-2010.pdf

[36] TL. Saaty,” Fundamentals of decision making and priority theory with the Analytic Hierarchy Process. 1st ed. RWS Publications; 1994.

[37] L. Guzzella and A. Sciarretta, Vehicle Propulsion Systems: Introduction to Modeling and Optimization, Springer; 2nd ed. 2007 edition (October 19, 2010. ISBN-10: 3642094155, Springer-Verlag Berlin Heidelberg 2005 Printed in Germany.

[38] C. J. Rydh, B. A. Sanden, "Energy analysis of batteries in photovoltaic systems. Part I: performance and energy requirements", *Energy Conversion and Management*, Vol. 46, pp. 1957–1979, 2005.

[39] B. Alzuwayer, M. Abdelhamid, P. Pisu, P. Giovenco, P. Venhovens, "Modeling and Simulation of a Series Hybrid CNG Vehicle, 2014, *SAE Int. J. Alt. Power*, Vol. 3, no. 1, pp. 20-29, doi: 10.4271/2014-01-1802

[40] Greenhouse Gas Emissions from a Typical Passenger Vehicle. (2013, Dec. 01). EPA, Office of Transportation and Air Quality, EPA420-F-05-004 February 2005 [Online]. Available: [http://yosemite.epa.gov/oa/EAB_Web_Docket.nsf/Filings%20By%20Appeal%20Number/D67DD10DEF159EE28525771A0060F621/\\$File/Exhibit%2034%20EPA%20GHG%20Emissions%20Fact%20Sheet...3.18.pdf](http://yosemite.epa.gov/oa/EAB_Web_Docket.nsf/Filings%20By%20Appeal%20Number/D67DD10DEF159EE28525771A0060F621/$File/Exhibit%2034%20EPA%20GHG%20Emissions%20Fact%20Sheet...3.18.pdf)

[41] Cleantech market intelligence firm Pike Research forecast. (2011, June 23). [Online]. Available: <http://www.navigantresearch.com/newsroom/695000-neighborhood-electric-vehicles-to-be-on-the-road-by-2017>

[42] Estimated Energy Use in 2013. (n.d.). Retrieved May 12, 2014, from <https://flowcharts.llnl.gov/#>

[43] The Outlook For Energy: A View to 2040. (n.d.). Retrieved May 01, 2014, from <http://cdn.exxonmobil.com/en/energy/energy-outlook>

[44] EPA Greenhouse Gas Emissions from a Typical Passenger Vehicle. (n.d.). Retrieved December 01, 2013, from <http://www.epa.gov/otaq/climate/documents/420f11041.pdf>

[45] Mints, P. (2013, March 20). Solar PV profit's last stand. *Renewable Energy World.com*. Retrieved February 04, 2014, from <http://www.renewableenergyworld.com/rea/news/article/2013/03/solar-pv-profits-last-stand?cmpid=SolarNL>

[46] The U.S. Department of Energy (DOE), Photovoltaics. (n.d.). Retrieved February 08, 2014, from <http://energy.gov/eere/sunshot/photovoltaics>.

[47]Martínez-Duart, J. M., & Hernández-Moro, J. (2013). Commentary: Photovoltaics Firmly Moving to the Terawatt Scale. *Journal of Nanophotonics*, 7(1), 078599-078599.

[48]Singh, R., Gupta, N., & Poole, K. F. (2008). Global Green Energy Conversion Revolution in 21 st Century through Solid State Devices. *Proceedings of the 26th International Conference on Microelectronics*, (pp. 45-54). NIŠ, SERBIA.

[49]Singh, R., Alapatt, G. F., & Lakhtakia, A. (2013). Making Solar Cells a Reality in Every Home: Opportunities and Challenges for Photovoltaic Device Design. *Electron Devices Society, IEEE Journal of the*, 1(6), 129-144.

[50]Singh, R., Alapatt, G. F., & Abdelhamid, M. (2012). Green Energy Conversion & Storage for Solving India's Energy Problem through Innovation in Ultra Large Scale Manufacturing and Advanced Research of Solid State Devices and Systems. Proceeding in *International Conference of Emerging Electronics (ICEE)*, (pp. 1-8). IIT bombay, Mumbai.

[51]Singh, R., Asif, A. A., Venayagamoorthy, G. K., Lakhtakia, A., Abdelhamid, M., et al. (2014). Emerging Role of Photovoltaics for Sustainably Powering Underdeveloped, Emerging, and Developed Economies. *Proceeding of the 2nd International Conference on Green Energy and Technology (ICGET)*. Dhaka, Bangladesh

[52]Green, M. A., Emery, K., Hishikawa, Y., Warta, W., & Dunlop, E. D. (2014). Solar Cell Efficiency Tables (version 43). *Progress in Photovoltaics: Research and Applications*, 22(1), 1–9.

[53]Tariq, M., Abdelhamid, M., Li, Y., Omar, M., & Zhou, Y. (2012). Fusion of Thermal and Visible Acquisitions for Evaluating Production-borne Scratches and Shunts in Photovoltaic PV Cells. *Journal of Materials Science Research*, 1(4), 57-72.

[54]Fujnaka, M. (1992). Solar Cars Free of Environmental Pollution—Prototype of Practically Usable Car Completed. *Renewable Energy*, 2(1), 57-64.

[55]Seal, M. R. (1994). Viking 23-zero Emissions in the City, Range and Performance on the Freeway. *Proceedings of the Northcon/94 Conference Record*, (pp. 264-268). Seattle, WA.

- [56]Sasaki, K., Yokota, M., Nagayoshi, H., & Kamisako, K. (1997). Evaluation of Electric Motor and Gasoline Engine Hybrid Car using Solar Cells. *Solar Energy Materials and Solar Cells*, 47(1), 259-263.
- [57]Astrolab. (n.d.). Retrieved January 10, 2014, from <http://www.venturi.fr/vehicules/la-gamme-venturi/astrolab/overview>
- [58]STELLA. (n.d.). Retrieved September 20, 2014, from <http://www.stellagoesusa.com/>
- [59]Saaty, T. L. (1990). How to Make a Decision: the Analytic Hierarchy Process. *European Journal of Operational Research*, 48(1), 9-26.
- [60]Suh, N. P. (1990). *The Principles of Design*. Oxford University Press.
- [61]Suh, N. P. (2001). *Axiomatic Design: Advances and Applications*. Oxford University Press.
- [62]Chan, L. K., & Wu, M. L. (2002). Quality function deployment: a literature review. *European Journal of Operational Research*, 143(3), 463-497.
- [63]Hwang, C. L., & Yoon, K. (1981). *Multiple Attribute Decision Making: Methods and Application – A State of the Art Survey*. Springer-Verlags.
- [64]Stein, E. W. (2013). A Comprehensive Multi-criteria Model to Rank Electric Energy Production Technologies. *Renewable and Sustainable Energy Reviews*, 22, 640-654.
- [65]Ahammed, F., & Azeem, A. (2013). Selection of the Most Appropriate Package of Solar Home System using Analytic Hierarchy Process Model in Rural Areas of Bangladesh. *Renewable Energy*. 55, 6-11.
- [66]Aragonés-Beltrán, P., Chaparro-González, F. Pastor-Ferrando, J., & Pla-Rubio, A. (2014). An AHP (Analytic Hierarchy Process)/ANP (Analytic Network Process)-based Multicriteria Decision Approach for the Selection of Solar-thermal Power Plant Investment projects. *Energy*, 66, 222-238.

- [67]Scannapieco, D., Naddeo, V., & Belgiorno, V. (2014). Sustainable Power Plants: a Support Tool for the Analysis of Alternatives. *Land Use Policy*, 36, 478-484.
- [68]Abdelhamid, M., Singh, R., Omar, M. (2014). Review of Microcrack Detection Techniques for Silicon Solar Cells. *Photovoltaics, IEEE Journal of*, 4(1), 514-524.
- [69]Kahraman, C., Cebi, S., & Kaya, İ. (2010). Selection among Renewable Energy Alternatives Using Fuzzy Axiomatic Design: The Case of Turkey. *Journal of Universal Computer Science*, 16(1), 82-102.
- [70]Boran, F. E., Boran, K., & Dizdar, E. (2012). A Fuzzy Multi Criteria Decision Making to Evaluate Energy Policy Based on an Information Axiom: A Case Study in Turkey. *Energy Sources, Part B: Economics, Planning, and Policy*, 7(3), 230-240.
- [71]Maldonado, A., García, J. L., Alvarado, A., & Balderrama, C. O. (2013). A Hierarchical Fuzzy Axiomatic Design Methodology for Ergonomic Compatibility Evaluation of Advanced Manufacturing Technology. *The International Journal of Advanced Manufacturing Technology*, 66(1-4), 171-186.
- [72]Kannan D., Govindan K., & Rajendran S. (2014). Fuzzy Axiomatic Design Approach Based Green Supplier Selection: a Case Study from Singapore. *Journal of Cleaner Production*.
- [73]Carnevalli, J. A., & Miguel, P. C. (2008). Review, Analysis and Classification of the Literature on QFD—Types of Research, Difficulties and Benefits. *International Journal of Production Economics*, 114(2), 737-754.
- [74]Ho, W. (2008). Integrated Analytic Hierarchy Process and its Applications—a Literature Review. *European Journal of operational research*, 186(1), 211-228.
- [75] Mayyas, A., Shen, Q., Mayyas, A., Abdelhamid, M., Shan, D., Qattawi, A., et al. (2011). Using Quality Function Deployment and Analytical Hierarchy Process for Material Selection of Body-in-White. *Materials & Design*, 32(5), 2771-2782.

- [76]Qattawi, A., Mayyas, A., Abdelhamid, M., & Omar, M. A. (2013). Incorporating Quality Function Deployment and Analytical Hierarchy Process in a Knowledge-based System for Automotive Production Line Design. *International Journal of Computer Integrated Manufacturing*, 26(9), 839-856.
- [77]Kahraman, C., Kaya, İ., & Cebi, S. (2009). A Comparative Analysis for Multiattribute Selection among Renewable Energy Alternatives using Fuzzy Axiomatic Design and Fuzzy Analytic Hierarchy Process. *Energy*, 34(10), 1603-1616.
- [78]Bouyssou, D., Marchant, T., Pirlot, M., Perny, P., Tsoukias, A., & Vincke, P., (2000). *Evaluation and Decision Models: a Critical Perspective*. Kluwer Academic Publishers
- [79]Mehta, S. (2014). GTM Research April 2014 PV Pulse, Retrieved April 23 from <http://www.greentechmedia.com/articles/read/Global-2013-PV-Module-Production-Hits-39.8-GW-Yingli-Leads-in-Production-a>
- [80]Singh, R., & Leslie, J. D. (1980). Economic Requirements for New Materials for Solar Photovoltaic Cells. *Solar Energy*, 24, 589-592.
- [81]Singh, R. (2009). Why Silicon is and Will Remain the Dominant Photovoltaic Material. *Journal of Nanophotonics*, 3, 032503.
- [82]Peters, C. H., Sachs-Quintana, I. T., Kastrop, J. P., Beaupre, S., Leclerc, M., & McGehee, M. D. (2011). High Efficiency Polymer Solar Cells with Long Operating Lifetimes. *Advanced Energy Materials*, 1(4), 491-494.
- [83]Saurat, M., & Ritthoff, M. (2010). Photovoltaics and the RoHS Directive,” Position Paper, Wuppertal Institute, from http://engineering2.dartmouth.edu/~cushman/courses/engs171/SauratRitthoff-Photovoltaics_and_RoHS-2010.pdf
- [84]Ito, M., Kato, K., Komoto, K., Kichimi, T., & Kurokawa, K. (2008). A Comparative Study on Cost and Life-cycle Analysis for 100 MW Very Large-scale PV (VLS-PV) Systems in Deserts using m-Si, a-Si, CdTe, and CIS modules. *Progress in Photovoltaics: Research and Applications*, 16(1), 17-30.

[85]Lakhani, R., Ganesh, D., & Joule, B. (2014). Internalizing Land Use Impacts for Life Cycle Cost Analysis of Energy Systems: A Case of California's Photovoltaic Implementation. *Applied Energy*, 116, 253-259.

[86]Aly, A. M., & Bitsuamlak, G. (2013). Aerodynamics of Ground-mounted Solar Panels: Test Model Scale Effects. *Journal of Wind Engineering and Industrial Aerodynamics*, 123, 250-260.

[87]Aly, A. M., & Bitsuamlak, G. (2013). Wind-induced Pressures on Solar Panels Mounted on Residential Homes. *Journal of Architectural Engineering*, 20(1). 04013003-1, 04013003-12

[88]PVinsights Grid the World. (n.d.). Retrieved May 5, 2014, from <http://pvinsights.com/index.php>

[89]Fthenakis, V., Frischknecht, R., Raugei, M., Kim, H. C., Alsema, E., Held, M., et al. (2011). *Methodology Guidelines on Life Cycle Assessment of Photovoltaic Electricity*, 2nd edition, IEA PVPS Task 12, International Energy Agency Photovoltaic Power systems Programme.

[90]Saaty, T. L. (1994). *Fundamentals of Decision Making and Priority Theory with the Analytic Hierarchy Process*. RWS Publications

[91]Kaufmann, A., & Gupta, M. M. (1991). *Introduction to Fuzzy Arithmetic: Theory and Applications*. Van Nostrand Reinhold.

[92]Shannon, C. E. (1948). The Mathematics Theory of Communication. *The Bell System Technical Journal*, 27(3-4), 373-423.

[93]Kulak O., & Kahraman C. (2005a). Multi-attribute Comparison of Advanced Manufacturing Systems using Fuzzy vs. Crisp Axiomatic Design Approach. *International Journal of Production Economics*, 95, 415–424.

[94]J. Montgomery (2013, February 12). 100 GW of Solar PV Now Installed in the World Today [Online]. Available: <http://www.renewableenergyworld.com/rea/news/article/2013/02/100-gw-of-solar-pv-now-installed-in-the-world-today>

[95]S. Clara (2013, March 11). Solar Photovoltaic Demand to Reach 31 Gigawatts in 2013: According to NPD Solarbuzz [Online]. Available: <http://www.prweb.com/releases/2013/3/prweb10514041.htm>

[96]S. Staff (2013, May 21). Global Solar PV Market Poised To 'Rise From The Ashes' Of 2011 [Online]. Available: http://www.solarindustrymag.com/e107_plugins/content/content.php?content.12701.

[97]R. Singh and G. F. Alapatt, (2012, October 11). Innovative Paths for Providing Green Energy for Sustainable Global Economic Growth”, Proc. SPIE 8482, Photonic Innovations and Solutions for Complex Environments and Systems (PISCES), 848205; doi:10.1117/12.928058. Available: <http://dx.doi.org/10.1117/12.928058>.

[98]P. Mints (2013, March 20). Solar PV Profit's Last Stand [Online]. Available: <http://www.renewableenergyworld.com/rea/news/article/2013/03/solar-pv-profits-last-stand?cmpid=SolarNL-2013-03-22>

[99]Z. Shahan (2013, May 11). Solar Module Manufacturing Trends in 2012 [Online]. Available: <http://cleantechnica.com/2013/05/11/solar-module-manufacturing-trends-in-2012/>

[100]R. Singh, “Why Silicon is and Will Remain the Dominant Photovoltaic Material,” *Journal of Nanophotonics*, vol. 3, no. 1, pp. 032503, 2009.

[101]J. M. Martimez-Duart and J. Hernandez-Moro, “Commentary: Photovoltaics Firmly Moving to the Terawatt Scale,” *Journal of Nanophotonics*, vol. 7, pp. 078599, March 22, 2013.

[102]M. Green, K. Emery, Y. Hishikawa, W. Warta, and E. Dunlop, “Solar cell efficiency tables (Version 40),” *Progress in Photovoltaics: Research and Applications*, vol. 20, pp. 606–614, 2012.

[103]SunPower® Residential Solar Panels [Online]. Available:
<http://us.sunpowercorp.com/homes/products-services/solar-panels/>

[104]O. Breitenstein, J. P. Rakotoniaina, M. H. Al Rifai MH, and M. Werner, “Shunt types in crystalline silicon solar cells,” *Progress in Photovoltaics: Research and Applications*, vol. 12, pp. 529-538, 2004.

[105] S. A. Correia, J. Lossen, and M. Bahr, “Eliminating Shunts from Industrial Silicon Solar Cells by Spatially Resolved Analysis,” *Proceeding of the 21st European Photovoltaic Solar Energy EPVSEC Conference*, 2006; 1297-1300

[106] O. Breitenstein, J. Bauer, and J. P. Rakotoniaina, “Material- Induced Shunts in Multicrystalline Silicon Solar Cells,” *Journal of Semiconductors*, vol. 41, no. 4, pp. 440–443, 2007.

[107] Z. Lucheng, X. Xinxiang, Y. Zhuojian, S. Xiaopu, X. Hongyun, L. Haobin, and S. Hui, ” An efficient method for monitoring the shunts in silicon solar cells during fabrication processes with infrared imaging,” *Journal of Semiconductors*, vol. 30, no. 7, pp. 076001, 2009.

[108] G. Acciani, O. Falcone, and S. Vergura, “Typical defects of PV-cells, “*Proceeding on International Symposium on Industrial Electronics (ISIE) Conference*, pp. 2745 – 2749, 2010.

[109] J. Rakotoniaina, S. Neve, M. Werner, O. Breitenstein, “Material induced shunts in multicrystalline silicon solar cells, “*Proceedings of the Conference on PV in Europe*, Rome, pp. 24-27, 2002.

[110] M. Kusko, M. Perný, and V. Šály, “Dark and under illumination electric PV parameters of modified solar cells,” *ELEKTROENERGETIKA*, vol. 4, no. 2, pp. 5-7, 2011.

[111] B. Gao, S. Nakano, and K. Kakimoto, “Effect of crucible cover material on impurities of multicrystalline silicon in a unidirectional solidification furnace, “*Journal of Crystal Growth*, vol. 318, pp. 255–258, 2011.

[112] S. Riepe, I. E. Reis, W. Kwapil, M. A. Falkenberg, J. Schön, H. Behnken, J. Bauer, D. Kreßner-Kiel, W. Seifert, and W. Koch, “Research on efficiency limiting defects and defect engineering in silicon solar cells - results of the German research cluster Solar Focus,” *Physica Status Solidi* ©, vol. 8, no. 3, pp. 733–738, 2011.

DOI: 10.1002/pssc.201000338.

[113] A. Schieferdecker, J. Sachse, T. Mueller, U. Seidel, L. Bartholomaeus, S. Germershausen, R. Perras, R. Meissner, H. Hoebbel, A. Schenke, K. Bhatti, K. H. Küsters, and H. Richter, “Material effects in manufacturing of silicon based solar cells and modules,” *Physica Status Solidi* ©, vol. 8, no. 3, pp. 871–874, 2011. DOI 10.1002/pssc.201000279.

[114] P. Rupnowski and B. Sopori, “Strength of Silicon Wafers: Fracture Mechanics Approach,” *International Journal of Fracture*, vol. 155, no. 1, pp. 67-74, 2009.

[115] S. Wansleben (2011, March). Not Falling Through the Crack [Online], Available: http://www.pv-magazine.com/archive/articles/beitrag/not-falling-through-the-cracks_100002343/#ixzz2XlDuI4Bt

[116] M. Israil, S. A. Anwar, and M. Z. Abdullah, “Automatic detection of micro-crack in solar wafers and cells: a review,” *Transaction of the institute of measurement and control*, vol. 0, no. 0, 2012. DOI. 10.1177/0142331212457583.

[117] B. Lawn, *Fracture in Brittle Solids*. Cambridge University Press, 2nd Edition, 1975.

[118] R. Perez and P. Gumbsch, “Directional anisotropy in the cleavage fracture of silicon,” *Physical Review Letters*, vol. 84, no. 23, pp. 5347-5350, 2000.

[119] J. Hauch, D. Holland, M. P. Marder, and H. L. Swinney, “Dynamic fracture in single crystal silicon,” *Physical Review Letters*, vol. 82, no. 19, pp. 3823-3826, 1999.

[120] M. J. Buehler, H. Tang, V. Duin, and W. A. Goddard, “Threshold Crack Speed Controls Dynamical Fracture of Silicon Single Crystals,” *Physical Review Letters*, vol. 99, pp. 165502, 2007.

[121] M. F. Hafiz and T. Kobayashi, “Fracture toughness of eutectic Al–Si casting alloy with different microstructural features,” *Journal of Materials Science*, vol. 31, pp. 6195–6200, 1996.

[122] I. Chasiotis, S. W. Cho, and K. Jonnalagadda, “Fracture toughness and subcritical crack growth in polycrystalline silicon,” *Journal of Applied Mechanics*, vol. 73, pp. 714–722, 2006.

[123] L. Johnsen, T. Bergstrom, M. M'Hamdi, and K. Kay Gastinger, “The importance of temperature control during crystallization and wafering in silicon solar cell,” *Photovoltaics International 7th Edition*, February 2010.

[124] Y. K. Park, M. C. Wagener, N. Stoddard, M. Bennett, and G. A. Rozgonyi GA, “Correlation between wafer fracture and saw damage introduced during cast silicon cutting,” Proceeding of the 15th Workshop on Crystalline Silicon Solar Cells and Modules: Materials and Processes, Vail, CO, USA, August 7-10 2005, pp. 178-181.

[125] H. Park H, S. Kwon, J. SungLee, H. Lim, S. Yoon, and D. Kim, “Improvement on surface texturing of single crystalline silicon for solar cells by saw-damage etching using an acidic solution,” *Solar Energy Materials & Solar Cells*, vol. 93, pp. 1773–1778, 2009.

[126] H. Larsson H, J. Gustafsson, H. J. Solheim, and T. Boström, “The Impact of Saw Damage Etching on Microcracks in Solar Cell Production,” Proceeding of the 23rd European Photovoltaic Solar Energy Conference, 2008.

[127] A. Schneider, G. Bühler, F. Huster, K. Peter, P. Fath, “Impact of Individual Process Steps on the Stability of Silicon Solar Cells Studied with a Simple Mechanical Stability Tester,” in Proc. of the PV in Europe from PV Technology to Energy Solutions Conference, Rome, Italy, 2002.

[128] T. Geipel, S. Pingel, J. Dittrich, Y. Zemen, G. Kropke, M. Wittner, J. Berghold, “Comparison of Acidic and Alkaline Textured Multicrystalline Solar Cells in a Solar Panel Production,” 24th European Photovoltaic Solar Energy Conference, 21-25 September 2009, Hamburg, German, pp. 3248-3252.

- [129] M. Köntges, S. Kajari-Schröder, I. Kunze, and U. Jahn, “Crack Statistic of Crystalline Silicon Photovoltaic Modules,” Proceeding of the 26th European Photovoltaic Solar Energy Conference and Exhibition, 5 to 6 September 2011 Hamburg, German.
- [130] X. F. Brun and S. N. Melkote, “Analysis of stresses and breakage of crystalline silicon wafers during handling and transport,” *Solar Energy Materials & Solar Cells*, vol. 93, pp. 1238–1247, 2009.
- [131] M. Sander, B. Henke, S. Schweizer, M. Ebert, and J. Bagdahn, “PV Module Defect Detection by Combination of Mechanical and Electrical Analysis Methods,” Proceeding of the 35th IEEE Photovoltaic Specialists Conference (PVSC), 20 - 25 June 2010: Honolulu, Hawaii, USA.
- [132] Y. Chiou and J. Liu J,” Micro crack detection of multi-crystalline silicon solar wafer using machine vision techniques,” *Sensor Review*, vol. 31, no. 2, pp. 154 – 165, 2011.
- [133] O. Breitenstein, J. Bauer, P. P. Altermatt, and K. Ramspeck, “Influence of Defects on Solar Cell Characteristics,” *Solid State Phenomena*, vol. 156-158, pp.1-10, 2010.
- [134] J. Wohlgemuth and W. Herrmann, "Hot spot tests for crystalline silicon modules," *Photovoltaic Specialists Conference, 2005. Conference Record of the Thirty-first IEEE* , vol., no., pp.1062,1063, 3-7 Jan. 2005. doi: 10.1109/PVSC.2005.1488317
- [135] P. Grunow, P. Clemens, V. Hoffmann, B. Litzenburger, and L. Podlowski, “Influence of Micro Cracks in Multi-Crystalline Silicon Solar Cells on the Reliability of PV Modules,” Proceeding at the 20th European Photovoltaic Solar Energy Conference, 6 –10 June 2005, Barcelona.
- [136] M. Köntges, S. Kajari-Schröder, I. Kunze, and U. Jahn, “Crack Statistic of Crystalline Silicon Photovoltaic Modules,” Proceeding of the 26th European Photovoltaic Solar Energy Conference and Exhibition, 5 to 6 September 2011 Hamburg, German.

[137] S. Kajari-Schroder, I. Kunze, U. Eitner, and M. Kontges, “ Spatial and orientational distribution of cracks in crystalline photovoltaic modules generated by mechanical load tests,” *Solar Energy Materials & Solar Cells*, vol. 95, pp.3054–3059, 2011.

[138] M. Köntges, S. Kajari-Schröder, I. Kunze, and U. Jahn U,” The risk of power loss in crystalline silicon based photovoltaic modules due to micro-cracks,” *Solar Energy Materials & Solar Cells*, vol. 95, pp. 1131–1137, 2011.

[139] S. Pingel, Y. Zemen, O. Frank, T. Geipel, and J. Berghold, “ Mechanical stability of solar cells within solar panels,” Proceeding of 24th EUPVSEC (WIP, Dresden, Germany, 2009), pp. 3459-3464.

[140] A. M. Gabor, M. M. Ralli, L. Alegria, C. Brodonaro, J. Woods, and L. Felton, “ Soldering induced damage to thin Si solar cells and detection of cracked cells in modules,” Proceeding of 21st EUPVSEC (WIP, Dresden, Germany, 2006), pp. 2042-2047.

[141] P. Chaturvedi, B. Hoex, and T. M. Walsh, “ Broken metal fingers in silicon wafer solar cells and PV modules,” *Solar Energy Materials and Solar Cells*, vol. 108, pp. 78 – 81, 2013, Available: <http://dx.doi.org/10.1016/j.solmat.2012.09.013>

[142] V. A. Popovich, T. Amstel, I. J. Bennett, M. Janssen, and I. M. Richardson, “ Microstructure and mechanical properties of aluminum back contact layers,” Proceedings of 24th (EPSEC) Hamburg, Germany, 2009.

[143] V. A. Popovich, A. Yunus, M. Janssen, I. J. Bennett, and I. M. Richardson,” Effect of silicon solar cell processing parameters and crystallinity on mechanical strength,” *Solar Energy Materials & Solar Cells*, vol. 95, pp. 97–100, 2011.

[144] J. Gustafsson, H. Larsson, H. J. Solheim, and T. Boström, “ Mechanical Stress Tests on Mc-Si Wafers with Microcracks,” Proceeding on the 23rd European Photovoltaic Solar Energy Conference, Valencia, Spain, 2008.

[145] G. Coletti, C. J. Tool, L. J. Geerligs, “Mechanical strength of silicon wafers and its modeling,” Proceeding on the 15th Workshop on Crystalline Silicon Solar Cells and Modules: Materials and Processes, Vail, CO, USA, August 7-10, 2005, pp. 117-20.

[146] G. Coletti, V. D. Borg, S. D. Iuliis, C. J. Tool, and L. J. Geerligs, "Mechanical Strength of Silicon Wafers Depending on Wafer Thickness and Surface Treatment," Presented at the 21st European Photovoltaic Solar Energy Conference and Exhibition, 4-8 September 2006, Dresden, Germany.

[147] M. Fischer (2012, March), International Technology Roadmap for Photovoltaic (ITRPV) - 3rd Edition - Results 2011 [Online]. Available: http://www.semi.org/eu/sites/semi.org/files/docs/05PVFMF2012_Markus%20Fischer_Q-Cells_ITRPV-Results_2011.pdf

[148] B. Li, H. Xianghao, and F. Shuai, "Automatic Inspection of Surface Crack in Solar Cell Images," Chinese Control and Decision Conference (CCDC), 2011.

[149] A. H. Aghamohammadi, A. S. Prabuwno, S. Sahran, and M. Mogharrebi, "Solar Cell Panel Crack Detection using Particle Swarm Optimization Algorithm," Proceeding on International Conference on Pattern Analysis and Intelligent Robotics, 28-29 June 2011, Putrajaya, Malaysia, 2011.

[150] E. Rueland, A. Herguth, A. Trummer, S. Wansleben, and P. Fath, "Micro-Crack detection an other optical characterization techniques for in-line inspection of wafers and cells," Proceedings of 20th EU PVSEC, Barcelona 2005, pp. 3242–3245.

[151] M. Xu, H. Wang, and Z. Gui, "Solar panel surface crack extraction using curve fitting," Proceedings at the 2nd International Conference on Education Technology and Computer, 2010, vol. 3, pp. 90-94.

[152] F. Zhuang, Z. Yanzheng, L. Yang, C. Qixin, C. Mingbo, Z. Jun, and J. Lee, "Solar Cell Crack Inspection by Image Processing," Proceeding on the International Business of Electronic Product Reliability and Liability Conference, April 27-30, 2004, pp. 77-80.

[153] S. Ke, K. Lin, Y. Lin, J. Chen, Y. Wang, and C. Liu, "High-performance Inspecting System for Detecting Micro-crack Defects of Solar Wafer," Proceeding at IEEE Sensors Conference, 1-4 Nov. 2010, pp. 494-497.

[154] S. Ko, C. Liu, and Y. Lin, "Optical inspection system with tunable exposure unit for micro-crack detection in solar wafers," *Optik - International Journal for Light and Electron Optics*, [Online], Available online 8 March 2013, <http://dx.doi.org/10.1016/j.ijleo.2012.12.024>

[155] D. Tsai, C. Chang, and S. Chao, "Micro-crack inspection in heterogeneously textured solar wafers using anisotropic diffusion," *Image and vision computing*, vol. 28, no. 3, pp. 491-501, 2010.

[156] W. Yang, "Short-Time Discrete Wavelet Transform for Wafer Microcrack Detection," IEEE International Symposium on Industrial Electronics (ISIE 2009) Seoul Olympic Parktel, Seoul, Korea July 5-8, 2009.

[157] J. P. Rakotoniaina, O. Breitenstein, M. H. Al Rifai, D. Franke, and A. Schnieder, "Detection of cracks in silicon wafers and solar cells by lock-in ultrasound thermography," Proceedings of PV Solar conference, Paris 2004: 640-643.

[158] A. Belyaev, O. Polupan, S. Ostapenko, D. P. Hess, and J. P. Kalejs, "Resonance ultrasonic vibration diagnostics of elastic stress in full-size silicon wafers," *Semiconductor Science and Technology*, vol. 21, pp. 254-260, 2006.

[159] C. Hilmersson, D. P. Hess, and W. Dallas, "Crack detection in single-crystalline silicon wafers using impact testing," *Applied Acoustics*, vol. 69, no. 8, pp. 755-760, 2008.

[160] A. Belyaev, O. Polupan, W. Dallas, S. Ostapenko, and D. Hess, "Crack detection and analyses using resonance ultrasonic vibrations in full-size crystalline silicon wafers," *Applied Physics Letters*, vol. 88, no. 11, pp. 111907, 2006.

[161] W. Dallas, O. Polupan, and S. Ostapenko, "Resonance ultrasonic vibrations for crack detection in photovoltaic silicon wafers," *Measurement Science and Technology*, vol. 18, pp. 852-858, 2007.

[162] T. Wen and C. Yin, "Crack detection in photovoltaic cells by interferometric analysis of electronic speckle patterns," *Journal Solar Energy Materials & Solar Cells*, vol. 98, pp. 216-223, 2012.

- [163] S. K. Chakrapani, M. J. Padiyar, and K. Balasubramaniam, "Crack Detection in Full Size Cz-Silicon Wafers Using LambWave Air Coupled Ultrasonic Testing (LAC-UT)," *Journal of Nondestructive Evaluation*, vol. 31, pp. 46–55, 2012.
- [164] M. J. Padiyar, S. K. Chakrapani, C. V. Krishnamurthy, and K. Balasubramaniam, "Crack Detection in Polycrystalline Silicon Wafers Using Air-coupled Ultrasonic Guided Waves," *Proceedings of the National Seminar & Exhibition on Non-Destructive Evaluation NDE 2009*, December 10-12, pp. 341-345.
- [165] O. Breitenstein, M. Langenkamp, O. Lang, and A. Schirmacher, "A. Shunts due to laser scribing of solar cell evaluated by highly sensitive lock-in thermography," *Solar Energy Materials and Solar Cells*, vol. 65, no. 1, pp. 55-62, 2001.
- [166] O. Breitenstein, M. Langenkamp, *Lock-in Thermography - Basics and Use for Functional Diagnostics of Electronic Components*, Springer, Berlin (2003)
- [167] Lock-in Thermography Imaging Workstation,
http://www.nrel.gov/pv/pdil/samc_thermography.html
- [168] O. Breitenstein, Illuminated versus dark lock-in thermography investigations of solar cells, *Int. J. Nanoparticles*, Vol. 6, Nos. 2/3, 2013
- [169] L.St-Laurent, M. Genest, C. Simon, and X. Maldague," Micro-cracks detection in Photo-Voltaic Cells by Infrared Thermography," *Proceeding at 7th International Conference of Quantitative Infrared Thermography (QIRT)*, July 5-8, 2004.
- [170] T. Fuyuki, H. Kondo, T. Yamazaki, Y. Takahashi, and Y. Uraoka," Photographic surveying of minority carrier diffusion length in polycrystalline silicon solar cells by electroluminescence," *Applied Physics Letters*, vol. 86, 262108. 2005 DOI: 10.1063/1.1978979.
- [171] T. Trupke, R. A. Bardos, M.C. Schubert, and W. Warta, "Photoluminescence imaging of silicon wafers," *Applied Physics Letters*, vol.89, no.4, pp.044107, 044107-3, Jul 2006doi: 10.1063/1.2234747
- [172] T. Trupke, R. A. Bardos, M. D. Abbott, P. Würfel, E. Pink, Y. Augarten, F. W. Chen et al., "\ " *Proceeding of the 22nd EPVSC*, Milan, Italy (2007).

- [173] O. Breitenstein, J. Bauer, K. Bothe, D. Hinken, J. Muller, W. Kwapil, M. C. Schubert, and W. Warta, "Can Luminescence Imaging Replace Lock-in Thermography on Solar Cells," *IEEE Journal of Photovoltaics*, vol. 1, no. 2, pp. 159-167, 2011.
- [174] J. Jean, C. Chen, and H. Lin, "Application of an Image Processing Software Tool to Crack Inspection of Crystalline Silicon Solar Cells," Proceedings of the 2011 International Conference on Machine Learning and Cybernetics, Guilin, 10-13 July, 2011.
- [175] W. J. Lin, Y. H. Lei, and C. H. Huang, "Automatic Detection of Internal defects in Solar Cells," Instrumentation and Measurement Technology Conference (I2MTC), 10-12 May 2011, Binjiang: 1-4.
- [176] D.M. Tsai, S. C. Wu, and W. C. Li, "Defect detection of solar cells in electroluminescence images using Fourier image reconstruction," *Solar Energy Materials and Solar Cells*, vol. 99, pp. 250-262, 2012.
- [177] W. Niblack, *An Introduction to Digital Image Processing*, Prentice Hall, pp. 115-116, 1986.
- [178] BT Imaging, <http://www.btimaging.com/>
- [179] RUV Systems, <http://www.ruvsystems.nl/>
- [180] T. L. Saaty. Decision Making with Feedback: The Analytical Network Process, (RWS Publications, Pittsburg, PA, 1996).
- [181] D. H. Byun, "The AHP approach for selecting an automobile purchase model," *Information & Management*, vol. 38, pp. 289-297, 2001.
- [182] A. Bhattacharyay, B. Sarkar, and S. Mukherjee, "Integrating AHP with QFD for robot selection under requirement perspective," *International Journal of Production Research*, vol. 43, no. 17, pp. 3671-3685, 2005.

[183] A. Mayyas, Q. Shen, A. Mayyas, M. Abdelhamid, D. Shan, A. Qattawi, and M. Omar, "Using Quality Function Deployment and Analytical Hierarchy Process for material selection of Body-In-White," *Materials and Design*, vol. 32, pp. 2771–2782, 2011.

[184] A. Qattawi, A. Mayyas, M. Abdelhamid, and M. Omar, "Incorporating quality function deployment and analytical hierarchy process in a knowledge-based system for automotive production line design," *International Journal of Computer Integrated Manufacturing*, 2013. DOI:10.1080/0951192X.2013.799780.

[185] Perez, R., and Perez, M. (2009a). "A fundamental look at energy reserves for the planet," *The IEA SHC, Solar Update*, vol. 50, pp. 2-3.

[186] Clean& Green: Best Practices in Photovoltaic's Report, 2012, [Online], <http://www.asyousow.org/publications/2012/Clean&Green-Photovoltaics.pdf>

[187] Tatsuo Saga, "Advances in crystalline silicon solar cell technology for industrial mass production", Sharp Corporation, Japan, *NPG Asia Mater.* Vol.3, No.3, PP. 96–102, 2010.

[188] Singh, R.; Alapatt, G.F.; Lakhtakia, A., "Making Solar Cells a Reality in Every Home: Opportunities and Challenges for Photovoltaic Device Design," *Electron Devices Society, IEEE Journal of the*, vol.1, no.6, pp.129,144, June 2013

[189] Villalva, M. G., & Gazoli, J. R. (2009). Comprehensive approach to modeling and simulation of photovoltaic arrays. *Power Electronics, IEEE Transactions on*, 24(5), 1198-1208.

[190] Open-circuit Voltage, PV Education, [Online] <http://pveducation.org/pvcdrom/solar-cell-operation/open-circuit-voltage>

[191] Reference Solar Spectral Irradiance: ASTM G-173, Renewable Resource Data Center (RReDC), [Online], <http://rredc.nrel.gov/solar/spectra/am1.5/ASTMG173/ASTMG173.html>

[192]E20/327 Solar Panel, SUNPOWER, [Online]
<http://www.rectifier.co.za/Solar/sunpower/pdf/DATASHEET%20-%20SPR-327NE-WHT-D%20FOR%20NORTH%20AMERICA.pdf>

[193]F. Lasnier and T. G. Ang, *Photovoltaic Engineering Handbook*. New York: Adam Hilger, 1990.

[194]C. Carrero, J. Amador, and S. Arnaltes, "A single procedure for helping PV designers to select silicon PV module and evaluate the loss resistances," *Renewable Energy*, vol. 32, no. 15, pp. 2579–2589, Dec. 2007.

[195]N. Pongratananukul and T. Kasparis, "Tool for automated simulation of solar arrays using general-purpose simulators," in *Proc. IEEE Workshop Comput. Power Electron.*, 2004, pp. 10–14.

[196]S. Chowdhury, G. A. Taylor, S. P. Chowdhury, A. K. Saha, and Y. H. Song, "Modelling, simulation and performance analysis of a PV array in an embedded environment," in *Proc. 42nd Int. Univ. Power Eng. Conf. (UPEC)*, 2007, pp. 781–785.

[197]J. Hyvarinen and J. Karila, "New analysis method for crystalline silicon cells," in *Proc. 3rd World Conf. Photovoltaic Energy Convers.*, 2003, vol. 2, pp. 1521–1524.

[198]Kashif Ishaque, Zainal Salam, Syafaruddin, comprehensive MATLAB Simulink PV system simulator with partial shading capability based on two-diode model, *Solar Energy* 85 (2011) 2217–2227.

[199]K. Nishioka, N. Sakitani, Y. Uraoka, and T. Fuyuki, "Analysis of multicrystalline silicon solar cells by modified 3-diode equivalent circuit model taking leakage current through periphery into consideration," *Solar Energy Mater. Solar Cells*, vol. 91, no. 13, pp. 1222–1227, 2007.

[200]Marcelo Gradella Villalva, Jonas Rafael Gazoli, and Ernesto Ruppert Filho, Comprehensive Approach to Modeling and Simulation of Photovoltaic Arrays, *IEEE Transactions on Power Electronics*, Vol. 24, no. 5, May 2009.

- [201]PV module series resistance, PVsyst 6 Help, [Online]
http://files.pvsyst.com/help/index.html?module_seriesresistance.htm
- [202]W. Xiao, W. G. Dunford, and A. Capel, "A novel modeling method for photovoltaic cells," in Proc. IEEE 35th Annu. Power Electron. Spec. Conf. (PESC), 2004, vol. 3, pp. 1950–1956.
- [203]G. Walker, "Evaluating MPPT converter topologies using a matlab PV model," J. Elect. Electron. Eng., Australia, vol. 21, no. 1, pp. 45–55, 2001.
- [204] M. Veerachary, "PSIM circuit-oriented simulator model for the nonlinear photovoltaic sources," IEEE Trans. Aerosp. Electron. Syst., vol. 42, no. 2, pp. 735–740, Apr. 2006
- [205]Francisco M. González-Longatt, Model of Photovoltaic Module in Matlab™, 2DO CONGRESO IBEROAMERICANO DE ESTUDIANTES DE INGENIERÍA ELÉCTRICA, ELECTRÓNICA Y COMPUTACIÓN (II CIBELEC 2005).
- [206]Douglas R. Carrol, The winning solar car: A design guide for solar race car teams, SAE International, 2003. ISBN: 0-7680-1131-0, USA
- [207]Eicker U. Solar technologies for buildings. New York: Wiley; 2003.
- [208]Viorel B. Dynamic model of a complex system including PV cells, electric battery, electrical motor and water pump. Energy 2003; 28:1165–81.
- [209]Y. T. Tan, D. S. Kirschen, and N. Jenkins, "A model of PV generation suitable for stability analysis," IEEE Trans. Energy Convers., vol. 19, no. 4, pp. 748–755, Dec. 2004.
- [210]N. D. Benavides and P. L. Chapman, "Modeling the effect of voltage ripple on the power output of photovoltaic modules," IEEE Trans. Ind. Electron., vol. 55, no. 7, pp. 2638–2643, Jul. 2008.

[211]W. De Soto, S.A.Klein, andW. A. Beckman, "Improvement and validation of a model for photovoltaic array performance," Solar Energy, vol. 80,no. 1, pp. 78–88, Jan. 2006.

[212]D.L. King, W.E. Boyson, J.A. Kratochvill Photovoltaic Array Performance Model, SANDIA National Laboratories, [Online] <http://prod.sandia.gov/techlib/access-control.cgi/2004/043535.pdf>

[213]Weather Data, EnergyPlus Energy Simulation Software, U.S. Department of Energy, [Online] http://apps1.eere.energy.gov/buildings/energyplus/cfm/weather_data2.cfm/region=4_north_and_central_america_wmo_region_4

[214]Duffie, John A., and William A. Beckman. Solar engineering of thermal processes. 4th Edition, John Wiley & Sons, 2013, ISBN: 978-0-470-87366-3.

[215]Cooper, P I., Solar Energy, 12, 3 (1969). "The Absorption of Solar Radiation in Solar Stills.

[216]Klein, S. A. "Calculation of monthly average insolation on tilted surfaces." Solar energy 19.4 (1977): 325-329.

[217]Solargis, [Online] <http://solargis.info/>

[218]Spencer. J. W., Search, 2 (5), 172 (1971). "Fourier Series Representation of the Position of the Sun.

[219]Iqbal, M., An Introduction to Solar Radiation, Academic Press, Toronto (1983).

[220]Hussein, K. H., Muta, I., Hoshino, T., & Osakada, M. (1995). Maximum photovoltaic power tracking: an algorithm for rapidly changing atmospheric conditions. *IEE Proceedings-Generation, Transmission and Distribution*, 142(1), 59-64

[221]Electrical energy storage, White paper, IEC, December 2011 [Online]
<http://www.iec.ch/whitepaper/pdf/iecWP-energystorage-LR-en.pdf>

[222]Source: Johnson Control Saft

[223]Chatzivasileiadi, Aikaterini, Eleni Ampatzi, and Ian Knight. "Characteristics of electrical energy storage technologies and their applications in buildings." *Renewable and Sustainable Energy Reviews* 25 (2013): 814-830.

[224]Lukic, S.M.; Cao, J.; Bansal, R.C.; Rodriguez, F.; Emadi, A, "Energy Storage Systems for Automotive Applications," *Industrial Electronics, IEEE Transactions on* , vol.55, no.6, pp.2258,2267, June 2008

[225]Tie, Siang Fui, and Chee Wei Tan. "A review of energy sources and energy management system in electric vehicles." *Renewable and Sustainable Energy Reviews* 20 (2013): 82-102.

[226] vA123 Systems, Proper Operation of A123 Systems High Power Lithium-ion Battery Strings, 2008.

[227]Thomas L. Gibson, Nelson A. Kelly, Solar photovoltaic charging of lithium-ion batteries, *Journal of Power Sources* 195 (2010) 3928–3932.

[228]Alzuwayer, B., Abdelhamid, M., Pisu, P., Giovenco, P. et al., "Modeling and Simulation of a Series Hybrid CNG Vehicle," *SAE Int. J. Alt. Power.* 3(1):20-29, 2014, doi:10.4271/2014-01-1802.

[229]Alzuwayer, B., Abdelhamid, M., Pisu, P., Giovenco, P., & Venhovens, P. (2014). Modeling and Simulation of a Series Hybrid CNG Vehicle (No. 2014-01-1802). SAE Technical Paper.

[230]Odeh S, Behnia M. Improving photovoltaic module efficiency using water cooling. *Heat Transfer Eng* 2009;30:499–505.

[231] Earle Wilson, Theoretical and operational thermal performance of a 'wet' crystalline silicon PV module under Jamaican conditions, *Renewable Energy* 34 (2009) 1655–1660

[232] Stefan Krauter, Increased electrical yield via water flow over the front of photovoltaic panels, *Solar Energy Materials & Solar Cells* 82 (2004) 131–137

[233] Xiao Tang, Zhenhua Quan, Yaohua Zhao, Experimental Investigation of Solar Panel Cooling by a Novel Micro Heat Pipe Array, *Energy and Power Engineering*, 2010, 2, 171-174.

[234] Valerie Evely, Peter Rodgers and Shrinivas Bojanampati, Enhancement of Photovoltaic Solar Module Performance for Power Generation in the Middle East, 28th IEEE SEMI-THERM Symposium, 2012

[235] Erdem Cuce, Tulin Bali and Suphi Anil Sekucoglu, "Effects of passive cooling on performance of silicon photovoltaic cells", *International Journal of Low-Carbon Technologies* 2011, 6, 299–308

[236] Performance enhancement of solar module by cooling: An experimental investigation, P G Nikhil, M Premalatha, *International Journal of Energy and Environment*, Vol 3, No 1, pp.73-82 (2012).

[237] Coraggio, G., Pisanti, C., Rizzo, G., & Senatore, A. (2010, July). A moving solar roof for a Hybrid solar vehicle. In *6th IFAC Symposium "Advances in Automotive Control"*, AAC10.

[238] W. Shockley & H. J. Queisser, "Detailed Balance Limit of Efficiency of PN Junction Solar Cells", *Journal of Applied Physics*, Vol. 32, PP.510–519, 1961.

[239] Alzuwayer, Bashar, Mahmoud Abdelhamid, Pierluigi Pisu, Pietro Giovenco, and Paul Venhovens. "Modeling and Simulation of a Series Hybrid CNG Vehicle." *SAE International Journal of Alternative Powertrains* 3, no. 1 (2014): 20-29.

[240]ADVISOR® Advanced Vehicle Simulator, Big Ladder software , (last updated May, 03 2013), [Online] <http://bigladdersoftware.com/advisor/>

[241]PSAT Software, Argonne National Laboratory, (last updated May 2012) , [Online] http://www.transportation.anl.gov/modeling_simulation/PSAT/

[242]Autonomy Software, Argonne National Laboratory (Last updated October 2012), [Online] <http://www.autonomie.net/>

243]Future Automotive Systems Technology Simulator (FASTSim), (Last updated May 02, 2013), [Online] <http://www.nrel.gov/vehiclesandfuels/vsa/fastsim.html>.

[244]VISION Model, Argonne National Laboratory, (September 2013), [Online] http://www.transportation.anl.gov/modeling_simulation/VISION/.

[245]GREET Model, Argonne Lab, (Last updated October 25, 2013), [Online] <http://greet.es.anl.gov/>.

[246]Smart fortwo electric drive coupe 2014, [Online] <http://www.smartusa.com/models/electric-drive/overview.aspx>

[247]Fiat 500e 2014, [Online], <http://www.motortrend.com/cars/2014/fiat/500e/specifications/exterior.html>

[248]Chevrolet Spark EV 2014, [Online], <http://www.gmfleet.com/chevrolet/spark-ev-mini-car/features-specs/dimensions.html>

[249]Mitsubishi i-MiEV 2014, [Online], <http://www.mitsubishicars.com/imiev/specifications>

[250]Ford Focus 2014, [Online], <http://www.ford.com/cars/focus/trim/electric/>

[251]Nissan Leaf 2014, [Online] <http://www.nissanusa.com/electric-cars/leaf/versions-specs>

[252]Tesla Model S , <http://www.teslamotors.com/models/specs>

[253]Honda Fit EV, [Online] <http://automobiles.honda.com/fit-ev/>

[254]STELLA , [Online], <http://www.designboom.com/technology/worlds-first-electricity-producing-solar-powered-family-car/>

[255]Tesseract, MIT solar car , <http://www.mit.edu/~solar-cars/flash/vehicles/present.shtml>

[256]Nuna 7, Nuon Solar Team 2013, [Online]
<http://www.nuonsolarteam.nl/nuna/?lang=en>

[257]Ford C-MAX Solar Energi Concept, [Online]
<https://media.ford.com/content/fordmedia/fna/us/en/news/2014/01/02/let-the-sun-in--ford-c-max-solar-energi-concept-goes-off-the-grid.html>

[258]Guzzella, Lino, and Antonio Sciarretta. *Vehicle propulsion systems*. Vol. 1. Springer-Verlag Berlin Heidelberg, 2007

[259]Tesla Model S, [Online] <http://www.autoblog.com/2012/09/11/2012-tesla-model-s-first-drive-review-video/>

[260]Nissan Leaf 2014, [Online], <http://www.nissanusa.com/electric-cars/leaf/versions-specs/>

[261]Volkswagen XL1 2015 , http://en.wikipedia.org/wiki/Volkswagen_1-litre_car

[262]Driving cycles, United States Environmental Protection Agency (EPA), [Online]
<http://www.epa.gov/otaq/sftp.htm>

[263]U.S. Environmental Protection Agency EPA, [Online]
<http://www.fueleconomy.gov/feg/evsbs.shtml>, U.S. Department of Energy, September 17
2014

[264]Tank to Wheel Efficiency, Devin Serpa , [Online]
http://www.afteroilev.com/Pub/EFF_Tank_to_Wheel.pdf
,Where the Energy Goes, <http://www.fueleconomy.gov/feg/atv.shtml>

[265]Using Energy Efficiency, Tesla Motor [Online]
<http://www.teslamotors.com/goelectric/efficiency>

[266]CAFE (MPG) Standard Curves for Passenger Cars
, [Online] <http://www.nhtsa.gov/fuel-economy>

[267]2009 National Household Travel Survey, <http://nhts.ornl.gov/2009/pub/stt.pdf>

[268] Photovoltaics Report, [Online] [http://www.ise.fraunhofer.de/de/downloads/pdf-](http://www.ise.fraunhofer.de/de/downloads/pdf-files/aktuelles/photovoltaics-report-in-englischer-sprache.pdf)
[files/aktuelles/photovoltaics-report-in-englischer-sprache.pdf](http://www.ise.fraunhofer.de/de/downloads/pdf-files/aktuelles/photovoltaics-report-in-englischer-sprache.pdf), July 28, 2014

[269] [http://www.greentechmedia.com/articles/read/Global-2013-PV-Module-](http://www.greentechmedia.com/articles/read/Global-2013-PV-Module-Production-Hits-39.8-GW-Yingli-Leads-in-Production-a)
[Production-Hits-39.8-GW-Yingli-Leads-in-Production-a](http://www.greentechmedia.com/articles/read/Global-2013-PV-Module-Production-Hits-39.8-GW-Yingli-Leads-in-Production-a)

[270] W. Rickerson, et al. “Residential Prosumers - Drivers and Policy Options” IEA-
Renewable Energy Technology Deployment, June 2014. [Online] [http://iea-retd.org/wp-](http://iea-retd.org/wp-content/uploads/2014/09/RE-PROSUMERS_IEA-RETD_2014.pdf)
[content/uploads/2014/09/RE-PROSUMERS_IEA-RETD_2014.pdf](http://iea-retd.org/wp-content/uploads/2014/09/RE-PROSUMERS_IEA-RETD_2014.pdf)

[271] Emerging Role of Photovoltaics for Sustainably Powering Underdeveloped,
Emerging, and Developed Economies, Rajendra Singh, Amir A. Asif, Ganesh K.
Venayagamoorthy, Akhlesh Lakhtakia, Mahmoud Abdelhamid, Githin F. Alapatt, and
David A. Ladner

[272] Curran, M., (May 2006), Life Cycle Assessment: Principles and Practice, The U.S.
Environmental Protection Agency (EPA), [Online]
<http://www.epa.gov/nrmrl/std/lca/lca.html>.

[273] International Organization for Standardization (ISO) standards, Life cycle assessment, [Online] <https://www.iso.org/obp/ui/#iso:std:iso:14004:ed-2:v1:en>

[274] Alsema E., Fraile, D., Frischknecht, R., Fthenakis ,V., Held, M., Kim, H.C., Pölz, W., Rauegi, M., and deWild-Scholten, M., (2009), Methodology Guidelines on Life Cycle Assessment of Photovoltaic Electricity, Subtask 20 "LCA", IEA PVPS Task 12.

[275] Fthenakis, V., Frischknecht, R., Rauegi, M., Kim, H. C., Alsema, E., Held, M., and deWild-Scholten, M., (2011), Methodology Guidelines on Life Cycle Assessment of Photovoltaic Electricity, 2nd edition, IEA PVPS Task 12, International Energy Agency Photovoltaic Power systems Programme

[276] <http://www.esu-services.ch/fileadmin/download/publicLCI/jungbluth-2012-LCI-Photovoltaics.pdf>

[277] D. Yue et al., Domestic and overseas manufacturing scenarios of silicon-based photovoltaic: life cycle energy and environmental comparative analysis, solar energy 105 (2014) 669-678

[278] Beylot,A.,Payet,J.,Puech,C.,Adra,N.,Jacquin,P.,Blanc,I.,Beloin-Saint-Pierre,D.,2014. Environmental impacts of large-scale grid-connected ground-mounted, PV installations. Renewable Energy 61,2–6.

[279] Jungbluth, N, Stucki, M, Frischknecht, R. (2009) Photovoltaics. In Dones, R , et al, editors, Sachbilanzen von Energiesystemen: Grundlagen für den ökologischen Vergleich von Energiesystemen und den Einbezug von Energiesystemen in Ökobilanzen für die Schweiz. ecoinvent report No. 6-XII, Swiss Centre for Life Cycle Inventories, Dübendorf, CH, 2009.

[280] Alsema, E.A.,deWild-Scholten,M.J.,Fthenakis,V.M, 2006. Environmental impacts of PV electricity generation—a critical comparison of energy supply options. In: 21st European Photovoltaic Solar Energy Conference, Dresden, Germany, September 4-8.

[281] Fthenakis, V., Alsema, E., 2006. Photovoltaics energy pay back times, greenhouse gas emissions and external costs : 2004-early 2005 status. Prog. Photovoltaics Res. Appl. 14, 275–280.

[282] Alsema E.A., deWild-Scholten, M.J., 2004. Environmental life cycle assessment of advanced silicon solar cell technologies. In: 19th European Photovoltaic Solar Energy Conference, Paris, France, June 7–11.

[283] Pacca, S., D. Sivaraman, and G. A. Keoleian. 2007. Parameters affecting the life cycle performance of PV technologies and systems. *Energy Policy* 35(6): 3316–3326

[284] Querini, F., Dagostino, S., Morel, S., Rousseaux, P., 2012. Greenhouse gas emissions of electric vehicles associated with wind and photovoltaic electricity. *Energy Procedia* 20, 391–401

[285] Wild-Scholten, M J. Energy pay back times of PV modules and systems. In: Workshop Photovoltaik- Modultechnik. Köln, 26–27 November 2009

[286] Dominguez-Ramos, A., M. Held, R. Aldaco, M. Fischer, and A. Irabien. 2010. Prospective CO₂ emissions from energy supplying systems: Photovoltaic systems and conventional grid within Spanish frame conditions. *International Journal of Life Cycle Assessment* 15(6):557–566.

[287] Sustainability Evaluation of Solar Energy Systems
SENSE. 2008. LCA analysis: Sustainability evaluation of solar energy systems revised version. Stuttgart, Germany: University of Stuttgart [Online] http://www.sense-eu.net/fileadmin/user_upload/intern/documents/Results_and_Downloads/SENSE_LCA_results.pdf

[288] Sergio Pacca, Deepak Sivaraman and Gregory A. Keoleian, Life Cycle Assessment of the 33 kW . Photovoltaic System on the Dana Building at the University of Michigan: Thin Film Laminates, Multi-crystalline Modules, and Balance of System Components, June 1, 2006, Report No. CSS05-09. Center of Sustainable systems: University of Michigan [Online] http://css.snre.umich.edu/css_doc/CSS05-09.pdf

[289] Raugei M, Bargigli S, Ulgiati S. Life cycle assessment and energy pay-back time of advanced photovoltaic modules: CdTe and CIS compared to poly-Si. *Energy* 2007; 32: 1310–8.

[290] Vasilis Fthenakis, Sustainability of photovoltaics: The case for thin-film solar cells, *Renewable and Sustainable Energy Reviews*, Volume 13, Issue 9, December 2009, Pages 2746-2750, ISSN 1364-0321, <http://dx.doi.org/10.1016/j.rser.2009.05.001>

[291] Fthenakis V.M., Kim. H.C., 2006. Energy use and greenhouse gas emissions in the life cycle of CdTe Photovoltaics. In: *Material Research Society Symposium Proc.* 895, 6.1–6.6.

[292] Hsu, D. D., O'Donoghue, P., Fthenakis, V., Heath, G. A., Kim, H. C., Sawyer, P., Choi, J.-K. and Turney, D. E. (2012), Life Cycle Greenhouse Gas Emissions of Crystalline Silicon Photovoltaic Electricity Generation. *Journal of Industrial Ecology*, 16: S122–S135. doi: 10.1111/j.1530-9290.2011.00439.x

[293] Kim, H. C., Fthenakis, V., Choi, J.-K. and Turney, D. E. (2012), Life Cycle Greenhouse Gas Emissions of Thin-film Photovoltaic Electricity Generation. *Journal of Industrial Ecology*, 16: S110–S121. doi: 10.1111/j.1530-9290.2011.00423.x

[294] Ito, M., Kato, K., Komoto, K., Kichimi, T. and Kurokawa, K. (2008), A comparative study on cost and life-cycle analysis for 100 MW very large-scale PV (VLS-PV) systems in deserts using m-Si, a-Si, CdTe, and CIS modules. *Prog. Photovolt: Res. Appl.*, 16: 17–30. doi: 10.1002/pip.770

[295] Hyoungseok Kim, Kyoungsoon Cha, Vasilis M. Fthenakis, Parikhit Sinha, Tak Hur, Life cycle assessment of cadmium telluride photovoltaic (CdTe PV) systems, *Solar Energy*, Volume 103, May 2014, Pages 78-88, ISSN 0038-092X, <http://dx.doi.org/10.1016/j.solener.2014.02.008>

[296] Battisti, R. Corrado, Evaluation of technical improvements of photovoltaic systems through life cycle assessment methodology, *Energy*, 30 (2005), pp. 952–967

[297] Alsema and Wild-Scholten, 2007, Reduction of the environmental impacts in crystalline silicon module manufacturing. In: *Proceedings of the 22nd European Photovoltaic Solar Energy Conference and Exhibition. Milan Italy, 2007*; p. 829–836.

[298] R Laleman, J Albrecht, J. Dewulf, Life cycle analysis to estimate the environmental impact of residential photovoltaic systems in regions with a low solar irradiation, *Renewable and Sustainable Energy Reviews*, 15 (2011), pp. 267–281

[299] Alsema and Nieuwlaar, 2000) EA Alsema, E. Nieuwlaar, Energy viability of photovoltaic systems, *Energy Policy*, 28 (2000), pp. 999–1010

[300] K Knapp, T. Jester, Empirical investigation of the energy payback time for photovoltaic modules, *Solar Energy*, 71 (3) (2001), pp. 165–172

[301] Fthenakis, V.M., H.C. Kim, and E. Alsema, Emissions from photovoltaic life cycles. *Environmental Science & Technology*, 2008. 42(6): p. 2168-2174

[302] Kazuhiko Kato, Takeshi Hibino, Keiichi Komoto, Seijiro Ihara, Shuji Yamamoto, and Hideaki Fujihara, A life-cycle analysis on thin-film CdS/CdTe PV modules, *Solar Energy Materials & Solar Cells* 67 (2001) 279-287

[303] Life Cycle Assessment of a Lithium-Ion Battery Vehicle Pack
Linda Ager-Wick Ellingsen, Guillaume Majeau-Bettez, Bhawna Singh, Akhilesh Kumar Srivastava, Lars Ole Valøen, and Anders Hammer Strømman. Volume 18, Number 1, Feb 2014, *Journal of Industrial Ecology*. DOI: 10.1111/jiec.12072

[304] Application of life-cycle assessment to nanoscale technology: Lithium-ion batteries for electric vehicles. Nanotechnology. EPA 744-R-12-001. Washington, DC: National Service Center for Environmental Publications.
<http://www.epa.gov/dfe/pubs/projects/lbnp/final-li-ion-battery-lca-report.pdf>. Accessed June, 02, 2014

[305] Dunn, J. B., L. Gaines, J. Sullivan, and M. Q. Wang. 2012b. Impact of recycling on cradle-to-gate energy consumption and greenhouse gas emissions of automotive lithium-ion batteries. *Environmental Science & Technology* 46(22): 12704–12710.

[306] Notter, D. A., M. Gauch, R. Widmer, P. Wäger, A. Stamp, R. Zah, and H.-J. Althaus. 2010. Contribution of Li-ion batteries to the environmental impact of electric vehicles. *Environmental Science & Technology* 44(17): 6550–6556.

[307] Majeau-Bettez, G., T. R. Hawkins, and A. H. Strømman. 2011. Life cycle environmental assessment of lithium-ion and nickel metal hydride batteries for plug-in hybrid and battery electric vehicles. *Environmental Science & Technology* 45(10): 4548–4554.

[308] J. E. Mason, V. M. Fthenakis, T. Hansen and H. C. Kim, “Energy Payback and Life-cycle CO₂ Emissions of the BOS in an Optimized 35 MW PV Installation” *Prog. Photovolt: Res. Appl.* 2006; 14:179–190.

[309] GREET Life-cycle Model, Argonne National Laboratory, [Online]
<https://greet.es.anl.gov>

[310] Weather Data, EnergyPlus Energy Simulation Software, U.S. Department of Energy, [Online]
http://apps1.eere.energy.gov/buildings/energyplus/cfm/weather_data2.cfm/region=4_north_and_central_america_wmo_region_4

[311] How much electricity does in American home use, [Online]
<http://www.eia.gov/tools/faqs/faq.cfm?id=97&t=3>, Last updated January, 10 2014

[312] Average Household Electricity Use, [Online]
<http://shrinkthatfootprint.com/average-household-electricity-consumption>

[313] Greenhouse Gas Emissions from a Typical Passenger Vehicle, U.S. Environmental Protection Agency (EPA) [Online]
<http://www.epa.gov/otaq/climate/documents/420f14040.pdf>

[314] IEA 2010, Energy Statistics for different countries, IEA 2010 for the year 2008,
<http://www.iea.org/stats/prodresult.asp?PRODUCT=Electricity/Heat>

[315] IEA (2011) OECD - Electricity and heat generation. International Energy Agency (IEA) Electricity information statistics (database), retrieved from: <http://www.oecd-ilibrary.org/energy/>

[316] Itten R., Frischknecht R. and Stucki M., 2012, Life Cycle Inventories of Electricity Mixes and Grid. ESU-services Ltd., Uster, CH.(available in ecoinvent v3.01) [<http://www.esu-services.ch/fileadmin/download/publicLCI/itten-2012-electricity-mix.pdf>], updated [June 2014].

[317] M.J. de Wild-Scholten, E.A. Alsema, E.W. ter Horst, M. Bächler, V.M. Fthenakis, A cost and environmental impact comparison of grid-connected rooftop and ground-based PV systems, 21th European Photovoltaic Solar Energy Conference, Dresden, Germany, 4-8 September 2006.

[318] E.A. Alsema and M.J. de Wild-Scholten, Environmental impacts of crystalline silicon photovoltaic module production, Presented at Materials Research Society Fall 2005 Meeting, November 2005, Boston, USA [Online] <http://www.ecn.nl/docs/library/report/2006/rx06010.pdf>

[319] THE CRYSTALCLEAR INTEGRATED PROJECT, [Online] <http://www.ecn.nl/docs/library/report/2005/rx05001.pdf>

[320] <http://www.ecn.nl/publicaties/default.aspx?au=44649>

[321] <http://www.ipcrystalclear.info>

[322] <http://www.epa.gov/dfe/pubs/projects/lbnp/final-li-ion-battery-lca-report.pdf>

[323] GREET Life-cycle Model, Argonne National Laboratory, [Online] <https://greet.es.anl.gov>

[324] Home energy use, U.S. Environmental Protection Agency (EPA), [Online] <http://www.epa.gov/cleanenergy/energy-resources/refs.html>

[325] Markel, T., and A. Simpson. *Cost-Benefit Analysis of Plug-In Hybrid Electric Vehicle Technology*. No. NREL/JA-540-40969. National Renewable Energy Laboratory (NREL), Golden, CO., 2006.

[326] Analytical Modeling Linking FASTSim and ADOPT Software Tools,
http://www4.eere.energy.gov/vehiclesandfuels/resources/meritreview/sites/default/files/van004_brooker_2013_o.pdf, May 16, 2013

[327] Howell, D. (2009). Annual Merit Review: Energy Storage R&D Overview. US Department of Energy, Energy Efficiency and Renewable Energy.

[328] Argonne National Laboratory, Energy Storage and Battery Advances, presented at Edison Electric Institute 2014 Spring Transmission, Distribution, and Metering Conference Glendale, AZ April 6-9, 2014
http://www.eei.org/about/meetings/Meeting_Documents/Miller,%20James.pdf

[329] Planned 2020 Gigafactory Production Exceeds 2013 Global Production, [Online]
http://www.teslamotors.com/sites/default/files/blog_attachments/gigafactory.pdf

[330] Tesla's Gigafactory, Driving ahead [Online]
<http://www.economist.com/blogs/schumpeter/2014/03/teslas-gigafactory>, March, 03 2014

[331] PVinsights Grid the World, <http://pvinsights.com/index.php>, Last updated October, 01 2014

[332] http://www.eia.gov/electricity/monthly/epm_table_grapher.cfm?t=epmt_5_6_a

[333] <http://cleantechnica.com/2013/09/30/average-electricity-prices-around-world/>

[334] Pagerit, S., Sharer, P., and Rousseau, A. (2006), Fuel Economy Sensitivity to vehicle mass for advanced powertrain", Society of Automotive Engineers, 2006-01-0665, [Online], http://www.autonomie.net/docs/6%20-%20Papers/Light%20duty/fuel_econom_sensitivity.pdf

[335] Anrico Casadei and Richard Broda, (April, 2008), Impact of Vehicle Weight Reduction on Fuel Economy for Various Vehicle Architectures, Research Report Prepared for: The Aluminum Association, Inc. Project FB769: RD.07/71602.2. [Online] <http://www.drivealuminum.org/research-resources/PDF/Research/2008/2008-Ricardo-Study.pdf>

[336] Lutsey, Nicholas P.(2010). Review of technical literature and trends related to automobile mass-reduction technology.*Institute of Transportation Studies*. UC Davis: Institute of Transportation Studies (UCD). Retrieved from: <https://escholarship.org/uc/item/9t04t94w>

[337] Aaron David Brooker, Jacob Ward, Lijuan Wang, Lightweighting Impacts on Fuel Economy, Cost, and Component Losses, 2013-01-0381, SAE International

[338] Marand Electric Solar Car In-Wheel Motors, [Online] <http://lati-solar-car.wikispaces.com/file/view/Surface+Mount+Kit+Motor+Information+Sheet.pdf>